UNIVERSITÉ
DE LORRAINE

THÈSE

Pour l'obtention du titre de :

DOCTEUR de L'UNIVERSITÉ DE LORRAINE

Spécialité: Science des matériaux, mécanique

Présentée par :

ARTEM ARLAZAROV

Evolution des microstructures et lien avec les propriétés mécaniques dans les aciers 'Médium Mn'

Thèse soutenue publiquement le 29 mai 2015 à Metz devant le jury composé de :

M. Alexis Deschamps	Professeur au SIMAP, Université de Grenoble	Président
M. Philippe Maugis	Professeur à IM2NP, Université d'Aix-Marseille	Rapporteur
M. Pascal Jacques	Professeur à l'Université Catholique de Louvain, Belgique	Rapporteur
Mme. Astrid Perlade	Ingénieur de recherche, ArcelorMittal Maizières Research	Examinateur
M. Gregory Ludkovsky	Directeur de la Recherche et Développement d'ArcelorMittal	Invité
M. Olivier Bouaziz	Professeur au LEM3, Université de Lorraine	Invité
M. Alain Hazotte	Professeur au LEM3, Université de Lorraine	Directeur de thèse
M. Mohamed Gouné	Professeur à l'ICMCB, Université de Bordeaux,	Co-directeur de thèse

LEM3 UMR CNRS 7239, Ile du Saulcy, 57045 METZ

Université de Lorraine – Pôle M4 : matière, matériaux, métallurgie, mécanique

ACKNOWLEDGEMENTS

Окружающий нас мир столь многогранен и сложен, что познавая его, мы всё больше и больше осознаём, что процес познания бесконечен как и сам мир.

Le monde autour de nous est tellement varié et complexe qu'en l'étudiant, le processus de découverte et d'apprentissage nous apparaît de plus en plus sans fin, comme le monde lui-même.

The world around us is so multifaceted and complex that when perceiving it, we realize more and more that discovering and learning processes are infinite as the world itself.

Sergey OLADYSHKIN

Résumé

La perspective d'une hausse durable du prix de l'énergie fossile et les exigences réglementaires accrues vis-à-vis des émissions de CO_2 nécessitent de développer des véhicules plus légers. L'utilisation d'aciers à Très Haute Résistance (THR) est une voie possible pour répondre à ces exigences, car ceux-ci permettent une réduction significative d'épaisseur sans affecter la rigidité des pièces. Le développement d'un acier qui combine à la fois une très haute résistance et une bonne formabilité constitue à l'heure actuelle un thème central chez les sidérurgistes. Une des solutions envisagées est de développer une nouvelle nuance d'aciers THR dits « Medium Manganèse » dont la teneur en Mn est située entre 4 et 12 %. Les premiers résultats publiés montrent un intérêt évident au développement de telles nuances. En effet, pour des teneurs en carbone relativement faibles, il est possible de stabiliser une fraction élevée d'austénite résiduelle à température ambiante grâce à la taille ultra fine de la microstructure et à l'enrichissement en Mn. Cette austénite résiduelle se transforme en martensite sous la charge mécanique (effet TRIP), ce qui procure une combinaison très attractive entre la résistance et la ductilité. Une des voies pour obtenir ce type de microstructure est d'effectuer un recuit inter-critique d'un acier complètement martensitique (issu d'austénitisation et trempe). Lors d'un tel recuit, la formation de l'austénite obéit à un mécanisme spécifique qui porte le nom d'ART – Austenite Reverted Transformation (transformation inverse de l'austénite). La compréhension et la modélisation des phénomènes en jeu pendant le recuit ART ont un grand intérêt scientifique.

Ainsi, l'objectif de ce travail de thèse était d'étudier et de modéliser les évolutions microstructurales en lien avec les propriétés mécaniques lors d'un recuit ART. Dans un premier temps, une étude de type « alloy design » a été menée pour déterminer la composition chimique de l'acier et le traitement thermique adapté à cette nuance. Une double approche, numérique et expérimentale, a été utilisée. Ensuite, des recuits inter-critiques (à 650°C) avec des temps de maintien variables (entre 3min et 30h) ont été réalisés sur l'acier laminé à froid et contenant 0.098%C et 4.7%Mn (mas.). Après chaque traitement, deux types de caractérisations ont été menés : analyse microstructurale et évaluation des propriétés mécaniques.

L'évolution de la microstructure lors du recuit a été étudiée en se basant sur deux types d'approches : expérimentale à l'échelle des phases (MEB, MET,..) et en utilisant la modélisation thermodynamique. Il a été déterminé que la microstructure finale se compose de phases de nature (ferrite, austénite résiduelle et martensite de trempe) et morphologie (en forme d'aiguille et polygonale) différentes. Une attention particulière a été accordée aux cinétiques de dissolution des carbures et de formation de l'austénite. Une vision complète de ces processus a été construite. De plus, un effet important de la taille de grains ultra fine sur les cinétiques globales a été démontré en comparant les résultats des calculs numériques avec les données expérimentales. En outre, le mécanisme de stabilisation de l'austénite résiduelle à la température ambiante a été étudié et discuté. Les deux contributions à la stabilité de l'austénite résiduelle, composition chimique et taille des grains, ont été analysées sur la base de l'évolution temporelle de l'austénite résiduelle. Enfin, une formulation adaptée pour le calcul de la température Ms des aciers « Medium Manganèse » avec une microstructure ultrafine a été proposée.

Des essais de traction ont été réalisés afin d'évaluer le comportement mécanique de l'acier après différents recuits ART. Les liens entre la réponse mécanique de l'acier et sa microstructure ont été établis. Une analyse plus détaillée du comportement de chaque constituant de la microstructure (ferrite, austénite résiduelle et martensite de trempe) a été effectuée. Elle a révélé que le Mn a un effet très important sur la résistance et sur l'écrouissage de la martensite de trempe. Cette observation a conduit à proposer un modèle spécifique pour décrire la courbe contrainte vraie – déformation vraie de la martensite de trempe. En revanche, les comportements de la ferrite et de l'austénite résiduelle ont été modélisés en s'appuyant sur des approches existant déjà dans la littérature. A l'issue de cette thèse, un modèle complet est disponible pour calculer les courbes de contrainte vraie – déformation vraie d'un acier « Medium Mn » après un recuit ART. Il s'appuie sur l'approche ISO-W pour décrire ce matériau multiphasé évolutif.

Abstract

Reduction of fuel consumption and CO_2 emission is one of the key concerns of the worldwide car makers today. The use of high-strength high-formability steels is one of the potential solutions to lighten a car. The so-called "Medium Mn" steels, containing from 4 to 12 wt.% Mn, are good candidates for such applications. They exhibit an ultra-fine microstructure with a significant amount of retained austenite. This retained austenite transforms during mechanical loading (TRIP effect), which provides a very attractive combination of strength and ductility. Such ultra-fine microstructure can be obtained during the intercritical annealing of fully martensitic Medium Mn steel. In that case, the formation of austenite happens through the so-called "Austenite Reverted Transformation" (ART) mechanism. Consequently, the understanding and modeling of phenomena taking place during ART-annealing is of prime interest.

In this PhD work, the evolution of both microstructure and tensile properties was studied as a function of holding time in the intercritical domain. First, an "alloy design" procedure was performed to select the chemical composition of steel and the thermal treatment adapted to this grade. It was based on both computational and experimental approaches. Then, the elaborated cold-rolled 0.098C – 4.7Mn (wt.%) steel was subjected to ART-annealing at 650°C with various holding time (from 3min to 30h). Two types of characterization were applied on the treated samples: analysis of microstructure evolution and evaluation of mechanical behavior.

Microstructure evolution was studied using a double experimental and modeling approach. The final microstructure contains phases of different natures (ferrite (annealed martensite), retained austenite and fresh martensite) and of different morphologies (lath-like and polygonal). A particular attention was paid to the kinetics of austenite formation in connection with cementite dissolution and to the morphology of the phases. A mechanism was proposed to describe the formation of such microstructure. Furthermore, the importance of taking into account the size distribution on the overall transformation kinetics was evidenced through the comparison between experimental and simulated austenite growth. The critical factors controlling thermal austenite stability, including both chemical and size effects, were determined and discussed, based on the analysis of the retained austenite time-evolution. At last, an adapted formulation of Ms temperature law applicable to the medium Mn steels with ultra-fine microstructure was proposed.

Tensile properties of the steel were measured as a function of holding time and the relation between microstructure and mechanical behavior was analyzed. Advanced analysis of the individual behavior of the three major constituents (ferrite (annealed martensite), retained austenite and fresh martensite) was performed. An important influence of Mn content on the strength and strain hardening of fresh martensite was revealed. Therefore, a specific model was proposed to describe true-stress versus true-strain curves of fresh martensite. On the other hand, mechanical behavior of retained austenite and ferrite was described with the adapted approaches already existing in the literature. At last, a complete model for predicting the true-stress versus true-strain curves of medium Mn steels was proposed based on the ISO-W mixture model.

TABLE OF CONTENTS

INTRODUCTION

Background of this study

Since more than 20 years, the worldwide car makers are in permanent progress in the field of material selection in order to decrease the weight of the vehicles. The goal of car weight reduction is to minimize fuel consumption and CO_2 emission. In the same time, passengers safety should be preserved or even improved. Vehicle lightening, especially for the passenger cars, is also stipulated by the European Union (EU) legislation. In 2009 was approved the mandatory emission reduction targets for new cars [EC]. These days, the average CO_2 emissions from the car fleet in the EU are precisely observed and reported. The evolution of CO_2 emissions and the targets for 2015 and 2020 are presented in Figure 1.
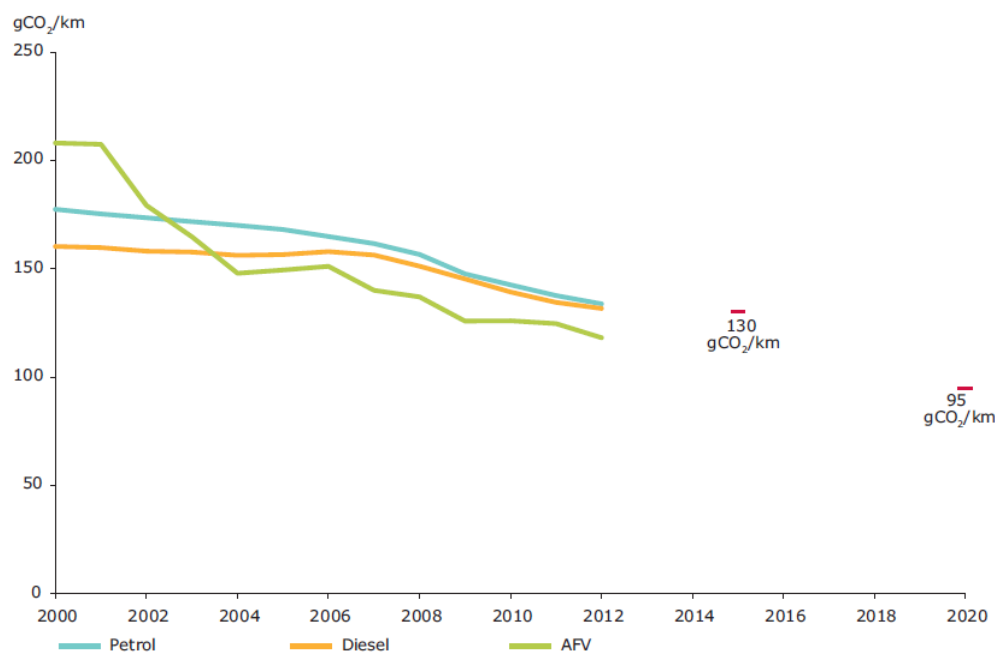
Figure 1 – Evolution of average CO_2 emissions from the car fleet in the EU.

The presented 2015 and 2020 targets are 130 grams of CO_2 per kilometre (g/km) and 95g/km, respectively. Compared with the 2007 fleet average of 158.7g/km these targets represent reductions of 18% and 40%, respectively [MON'12]. To achieve these quite ambitious targets, the car markers are constrained to use the most innovative solutions in terms of materials and design.

Car body and many other pieces of vehicles are made of different steels. Hence, there are two strategies for the weight reduction:
   a)   use permanently improved steel solutions;
   b)   use alternative materials: aluminum, magnesium, plastics and others.
Till now, steel stays a very attractive and functional material as it combines a wide range of mechanical properties and low production cost. That's why the research and development in the field of steels is quite important and has its place in the near future.

For many years, steel researchers were working on the conventional Advanced High Strength Steels (AHSS) grades: Dual Phase (DP), TRansformation Induced Plasticity (TRIP), Complex Phase (CP) and Martensitic (M) steels. These steels were classified as the 1st Generation AHSS.

Then, the TWinning Induced Plasticity (TWIP) steels were discovered and investigated as the 2nd Generation AHSS. Production of these steels is inhibited due to the high level of alloying elements that stipulates an important cost increase and a lot of problems on the process route. Finally, these days the researchers are trying to develop the 3rd Generation AHSS. The objective of this development is to propose steels with an intermediate strength-ductility balance (better than 1st Generation AHSS, but probably lower than the 2nd Generation AHSS) but with reasonable costs and production issues. Positions of this target in terms of tensile strength/total elongation balance as well as the already developed 1st and 2nd Generations of AHSS are illustrated in Figure 2.
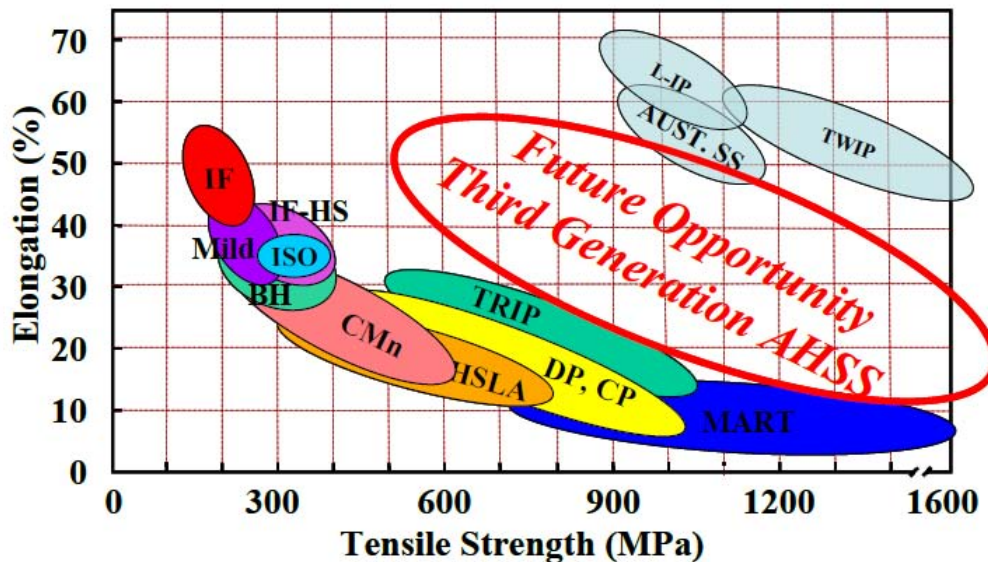
Figure 2 – Schematic representation of tensile strength/total elongation balance for different already developed and future steels [MAT'06].

There are different metallurgical concepts that can offer a steel product with the satisfactory strength-ductility balance: carbide free bainite (CFB), annealed martensite matrix (AMM), quenching and partitioning (Q&P) and, finally, so-called "Medium Mn" steel (MMS). This research is focused on the last concept.

Medium Mn TRIP steel is a promising solution to get high strength steels with good formability. Recently, a lot of studies on MMS concept were done and published. The results of some of these studies [MIL'72], [FUR'89], [HUA'94], [FUR'94], [MER'07], [SUH'09], [SHI'10], [COO'10], [GIB'11], [JUN'11], [CAO'11], [ARL'11] are shown in Figure 3. This graph presents the Ultimate Tensile Stress (UTS) as a function of Total Elongation (TE) and the targeted domain of the 3rd Generation AHSS. It can be seen that MMS has a great potential since some combinations already satisfy the target of third generation high strength steels.
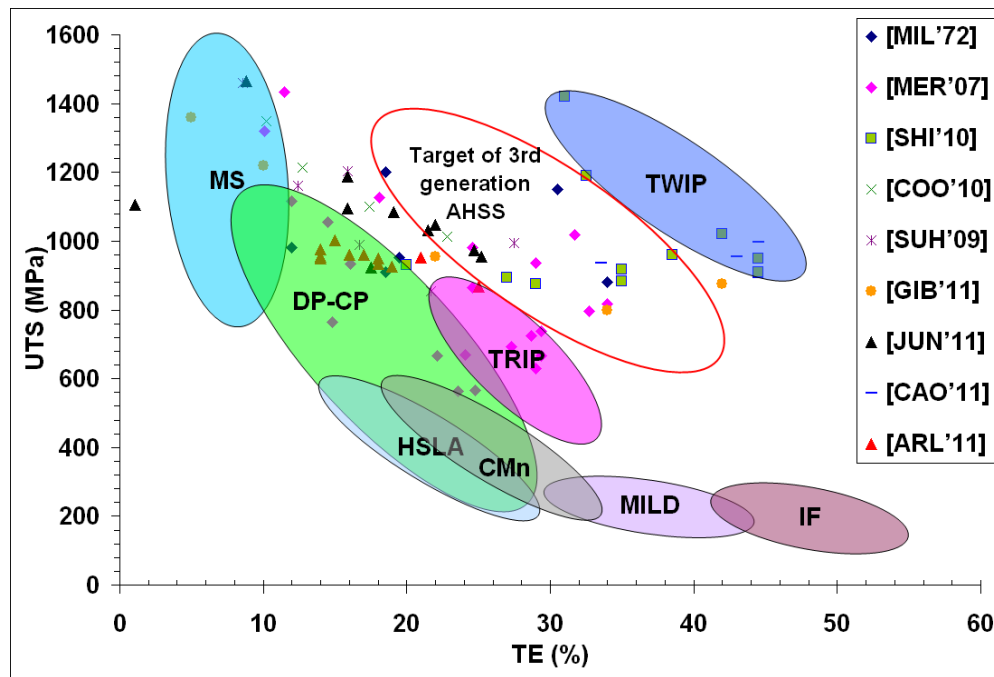
Figure 3 – Published results of mechanical properties of Medium Mn steels – ultimate tensile strength (UTS) as a function of total elongation (TE); target of third generation high strength steels is marked with red ellipse.

Aim of this study

The mechanical response of MMS is very attractive. However the studies of these steels started not so long time ago. Hence, there are a certain amount of unanswered questions about microstructure formation, mechanical behavior and the link between these two properties. Therefore, it was proposed to investigate the following topics:

1. Understand the mechanisms of microstructure formation during intercritical annealing of MMS:
   - **C and Mn distribution between phases;**
   - **Mechanisms of austenite formation and stabilization ;**
2. Explain the relation between microstructure and mechanical properties obtained after thermal treatments:
   - **Influence of Mn and ultra-fine size on work hardening;**
   - **Austenite strain induced transformation - TRIP effect;**
3. Develop a model for prediction of mechanical behavior of the steel, considered as a multi-phase evolutive material.

More global purpose of this research is to acquire all the necessary knowledge of this concept in order to build the tools (models) for the further optimization of steel compositions and thermal treatments. This objective is an essential step for the future product development of such type of steels.

Context of this study

This PhD work was done in a specific context. Before starting the PhD, the author of this work was working for 4 years and continued to work during the PhD in ArcelorMittal Maizieres Research centre, in the Automotive department and more precisely in the Metallurgy Prospects and Manufacturing (MPM) team. Therefore, this PhD work was accomplished in particular

11

conditions with somehow following time partitioning: 50% of the authors' time was allocated to its engineer work in ArcelorMittal Maizieres Research centre and other 50% was dedicated to the PhD study.

This work was done within the collaboration between ArcelorMittal Maizieres Research centre and the University of Lorraine, in particular LEM3 laboratory. It was supervised by three persons:

> Director – Alain HAZOTTE (professor in LEM3 laboratory, University of Lorraine);
>
> Co-director – Mohamed GOUNÉ (former research engineer in ArcelorMittal Maizieres Research centre, now professor in ICMCB laboratory, University of Bordeaux);
>
> Co-supervisor – Olivier BOUAZIZ (former research engineer in ArcelorMittal Maizieres Research centre, now professor in LEM3 laboratory, University of Lorraine).

Finally, it should be highlighted that the major part of the experimental work was done in the ArcelorMittal Maizieres Research centre.

Presentation of the manuscript

The manuscript is divided in the following four parts.

Chapter 1 is devoted to the literature review. The analysis of the found literature relative to microstructure formation and mechanical behavior of MMS steels is presented. In the part about the microstructure, the following major topics are treated: recrystallization, standard and reverse austenite formation, and, at last, austenite thermal stability. Concerning mechanical behavior part, the following subjects in link with this study are reviewed: global analysis of mechanical properties of MMS in relation with the available microstructure characterizations (retained austenite fraction), mechanical behavior of ultra fine ferrite, fresh martensite and retained austenite (including TRIP effect) and, finally, modeling of the multiphase steel mechanical behavior.

Chapter 2 presents different experimental and numerical techniques used in this work. All the tools utilized for the elaboration of steel, for microstructure observation and analysis at different scales, for thermodynamic calculations and for final properties measurements are described. In the second part of this chapter, selection of chemical composition of steel and of the subsequent thermal treatment is given. To define temperature of the thermal treatment a combinatory approach is used. It is based on both thermodynamic simulations and particular experimental heat treatment.

In Chapter 3, the observations and analysis of microstructures obtained after different thermal treatments are presented and described. Morphology, size and chemical composition of phases are analyzed. Microstructure evolution with time and different steps of austenite formation are discussed. The results of thermodynamic simulations and their comparison with experimental values are also considered in this chapter. According to these simulations, particularities of austenite transformation in MMS are argued. This microstructure analysis permits to describe microstructure evolution and in particular to explain unambiguously the stability of austenite at room temperature. The effect of austenite size on its stability is introduced in a particular manner through the variation of M_s temperature. At last, the mechanisms of austenite size influence are debated.

Chapter 4 is dedicated to the mechanical properties of MMS. Tensile behavior of intercritically annealed medium Mn steels with different phases (two phases and three phases microstructures) is presented and analyzed. Tensile behavior of each phase constituent (as-quenched martensite, ferrite with medium Mn content and austenite with medium C and Mn content) is described.

Influence of Mn on the work hardening of the different phases and on the mechanical stability of austenite is discussed. Finally, a global mechanical model capable to predict the whole tensile curve of the intercritically annealed medium Mn steels with different phases is proposed. This model is based on the analysis of the mechanical behavior of each constituent and on the detailed experimental description of the microstructures. The performance of the model is also discussed.

References

[ARL'11] A. Arlazarov, M. Gouné, O. Bouaziz, A. Hazotte, F. Kegel, Effect of intercritical annealing time on microstructure and mechanical behavior of advanced medium Mn steels, Proceedings of THERMEC 2011 Conference, Materials Science Forum, 706-709, 2012, 2693-2698.

[CAO'11] W.Q. Cao, J. Shi, Ch. Wang, C. Wang, L. Xu, M. Wang, H. Dong, Work hardening behavior of ultrafine grained duplex medium-Mn steels annealed by ART, Proceedings of HMnS 2011 Conference, Korea, 2011.

[COO'10] B.C. De Cooman, S. Lee, S.S. Kumar, Ultra-fine grained manganese TRIP steels, Proceedings of 2nd International Conference "Super-High Strength Steels", Italy, 2010, 1-11.

[EC] http://ec.europa.eu/clima/policies/transport/vehicles/cars/index_en.htm

[FUR'89] T. Furukawa, Dependence of strength-ductility characteristics on thermal history in low carbon 5wt.% Mn steels, Materials Science and Technology, 5, 1989, 465-470.

[FUR'94] T. Furukawa, H. Huang, O. Matsumura, Effects of carbon content on mechanical properties of 5wt.% Mn steels exhibiting transformation induced plasticity, Materials Science and Technology, 10(11), 1994, 964-969.

[GIB'11] P.J. Gibbs, E. De Moor, M.J. Merwin, B. Clausen, J.G. Speer, D.K. Matlock, Austenite stability effects on tensile behavior of Manganese-enriched-austenite Transformation-Induced Plasticity Steel, Metallurgical and Materials Transactions A, 42, 2011, 3691-3702.

[HUA'94] H. Huang, O. Matsumura, T. Furukawa, Retained austenite in low carbon, manganese steel after intercritical heat treatment, Materials Science and Technology, 10(7), 1994, 621-626.

[JUN'11] H.J. Jun, O. Yakubovsky, N. Fonstein, On Stability of Retained Austenite in Medium Mn TRIP Steels, Proceedings of HMnS 2011 Conference, Korea, 2011.

[MAT'06] D. K. Matlock, J.G. Speer, "Design considerations for the next generation of Advanced High Strength Sheet Steels," Proc. of the 3rd International Conference on Structural Steels, ed. by H.C. Lee, the Korean Institute of Metals and Materials, Korea, 2006, 774-781.

[MER'07] M.J. Merwin, Microstructure and Properties of Cold Rolled and Annealed Low-Carbon Manganese TRIP Steels, Proceedings of AIST Steel Properties & Applications Conference, Detroit, 2007, 67-84.

[MIL'72] R.L. Miller, Ultrafine-grained microstructures and mechanical properties of Alloy Steels, Metallurgical Transactions, 3, 1972, 905-912.

[MON'12] Monitoring CO_2 emissions from new passenger cars in the EU: summary of data for 2012.

[SHI'10] J. Shi, X. Sun, M. Wang, W. Hui, H. Dong, W. Cao, Enhanced work-hardening behavior and mechanical properties in ultrafine-grained steels with large-fractioned metastable austenite, Scripta Materialia, 63, 2010, 815-818.

[SUH'09] D.W. Suh, S.J. Park, T.H. Lee, C.S. Oh, S.J. Kim, Influence of Al on the microstructural evolution and mechanical behavior of low-carbon, manganese Transformation-Induced-Plasticity Steel, Metallurgical and Materials Transactions A, 41, 2009, 397-408.

CHAPTER 1: LITERATURE REVIEW

1.1 General Description

More than 200 years ago (in 1774) manganese was elaborated in metallic state and from the end of nineteenth century manganese is widely applied as an alloying element for the steel elaboration. One of the most remarkable and important discovery in the field of steels was done by Sir Robert Abbott Hadfield. He searched for a hard and in the same time tough steel and developed a steel containing around 12% Mn and having outstanding combination of hardness and toughness. His invention was called in his honor Hadfield steel and since that time was produced in significant quantities [DES'76] [MAN'56].

Gradually, manganese became a common alloying element for the steel production. Its influence on different properties (hardenability, grain size, phase transformations, mechanical behavior and etc…) was widely studied. However, manganese content was often limited to ~2% because of its important hardenability [DES'76].

In the end of 60's and beginning of 70's of the twentieth century, Medium Mn steels (up to 6% Mn) were first proposed by Grange and Hribal [GRA'68] as an air-hardenable material. Fully martensitic structure was obtained for a 0.1 wt.% C – 6 wt.% Mn steel with the cooling rate of 1.7°C/min. But this structure had poor toughness properties. Thus, a tempering treatment was applied and resulted in a good balance between strength and ductility. Miller and Grange [MIL'70], [MIL'72] continued to work on this material and found that this good mechanical behavior can be explained by rather high fraction of austenite retained after tempering and ultra-fine size of the microstructure features. In the beginning of 90's, Furukawa et al. [FUR'89], [HUA'94], [FUR'94] also found a good balance of strength and ductility after annealing martensitic hot rolled steels with 5 wt.% Mn in their intercritical domain. One more time it was shown that ultra-fine microstructure and retained austenite have an important role in these steels. These studies also claimed that there are optimum temperature and time to get the maximum of retained austenite.

Nowadays, due to the increasing demand for the development of "3rd generation high strength steels" the interest to MMS attained its maximum and the number of research and development studies is exponentially growing.

Final properties of the steel product depend on its chemical composition and final structure: grain size, phase's fractions, precipitates and dislocation content. Further, the final microstructure in most of the cases is directly linked to all the steps of elaboration (thermo-mechanical treatments). Generally, one of the most important steps, that will condition the final properties, is annealing.

Heat treatment necessary for the production of MMS is conventional annealing: heating to soaking temperature, holding and final cooling. Thus, most of the phenomena happening during annealing are already well described. However, there are some particularities in these steels. Due to the high manganese content which increases drastically the steel hardenability, in majority of the cases, the initial (before annealing) microstructure will be fully martensitic or a mixture of bainite and martensite. Also, thanks to high manganese content which decreases grain boundaries mobility, a very fine size of microstructural features is expected. These two particularities will impact the phase transformations during annealing and will result in different mechanical properties. The available in the literature information necessary for understanding of phase transformations, microstructure formation and mechanical properties of MMS will be given in this chapter.

1.2 Mechanisms of phase transformations

Generally, in the simple Fe-C-Mn system during heating the following phenomena can happen: recrystallization, carbide dissolution and austenite nucleation and growth. The microstructure in the end of heating depends strongly on the initial state of the material: initial microstructure and/or the deformation level.

In the case of important deformation level without any dependence on initial microstructure the steel will progressively evolve through recrystallization, carbide dissolution and austenite nucleation and growth.

When initial structure is not-deformed (case of double annealing for example) the recrystallization step after deformation is suppressed and carbide dissolution and austenite nucleation and growth will depend on the initial microstructure of steel.

The case of intermediate deformation rate combines all the difficulties: recrystallization and dependence of carbide dissolution and of austenite nucleation and growth on the initial microstructure of steel.

In the work of Arlazarov et al. [ARL'12] it was shown that after intercritical annealing of MMS a complex ultrafine mixture of ferrite, retained austenite and/or martensite can be obtained. Examples of such microstructures are presented in Figure 4. Complexity in the phase constituents and their morphology results from the interference of different phenomena happening during annealing. The increase of Mn content is known to decrease the temperature range of intercritical domain. Thus, to obtain a certain fraction of austenite the annealing temperature should be lower. On the other hand, at lower annealing temperature recrystallization and cementite dissolution have a more sluggish kinetics. Therefore, increase of Mn creates an overlap between recrystallization, cementite dissolution and austenite transformation. In addition, development and interaction of these phenomena depend on the initial (before annealing) microstructure. At last, austenite stabilization or its transformation to martensite during final cooling step will be significantly influenced by the processes occurring during heating and holding.
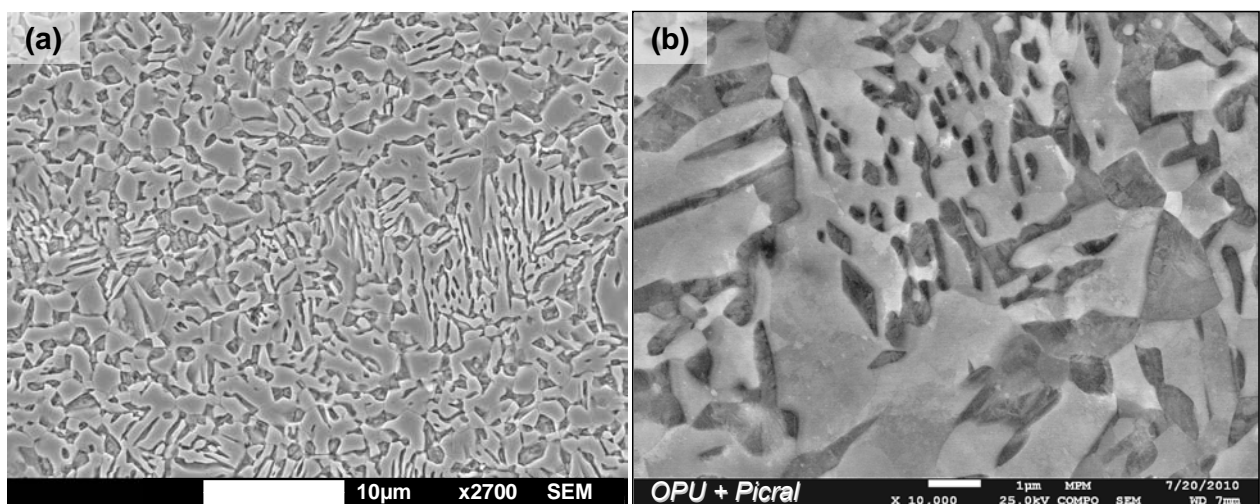
Figure 4 – Observed in the SEM-FEG microstructures of the medium Mn steel annealed at 670°C for 6h (a), revealed with Marshall reagent, and 7h (b), revealed with OPU polishing and picral etching. In both cases uniform light grey colour corresponds to ferrite and rough dark grey areas are martensite and/or retained austenite [ARL'12].

Taking into account the complexity of microstructure formation in the annealed MMS, it is necessary to introduce the descriptions of each phenomenon. Therefore, further in this sub-chapter will be presented the following topics:

  1.2.1 Recrystallization;

  1.2.2 Austenite formation during intercritical annealing;

  1.2.3 Particular case of Austenite Reverse Transformation (ART);

  1.2.4 Austenite stabilization during annealing.

1.2.1 Recrystallization

Deformation of steel like rolling, forging or other introduces in the material a certain number of defects (in particular dislocations) that will depend on the strain rate. Deformed metal has a certain amount of stored energy, hence during reheating and soaking it tends to suppress the defects and to recover its structure and properties. Depending on the heating rate, reheating temperature and quantity of stored energy, the following processes can happen: rearrangement and annihilation of dislocations, formation of new dislocation-free grains and their growth. Hence, recrystallization process can be divided in 3 steps:

 o recovery - rearrangement and annihilation of dislocations, formation of sub-structure;

 o recrystallization – nucleation of new dislocation-free grains;

 o grain growth – the larger grains grow consuming the smaller ones in order to obtain the lower energy configuration of grain boundaries [HUM'04].

Schematic representation of different states of recrystallization is presented in Figure 5.
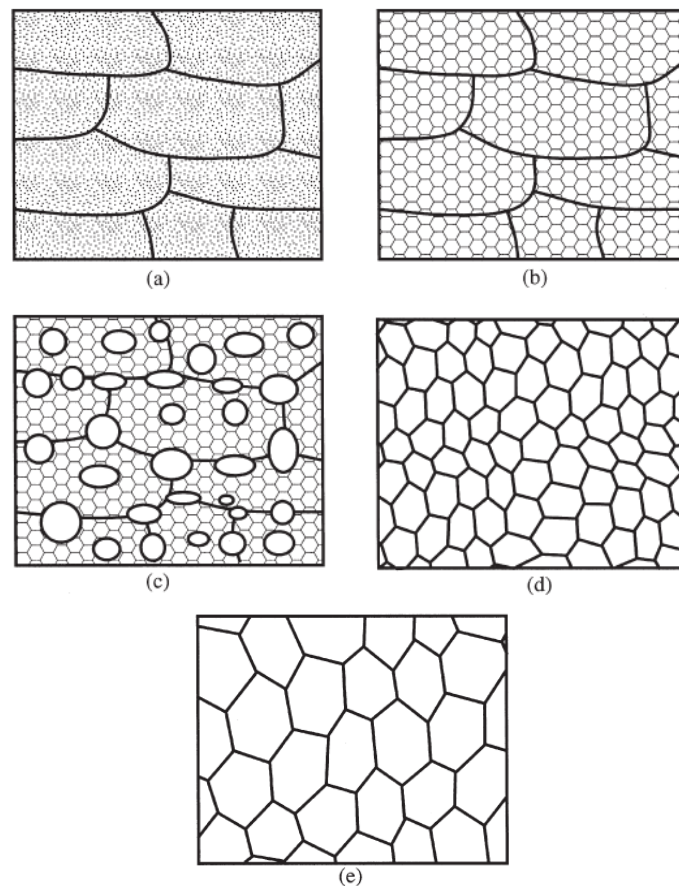
Figure 5 - Schematic description of different steps of recrystallization: (a) Deformed state, (b) Recovered, (c) Partially recrystallized, (d) Fully recrystallized and (e) Grain growth [HUM'04].

As it was mentioned previously, in the case of not-deformed initial microstructure there is no recrystallization in the majority of the cases. However, when initial structure is fully martensitic, the dislocation density is high enough to provoke martensite recrystallization (nucleation of new ferrite grains). Some studies about martensite recovery and recrystallyzation were already done in the past. First of all in late 60's and in the beginning of 70's G. R. Speich [SPE'69], [SPE'72] investigated the effect of tempering in low carbon martensite. Early stages of carbon segregation and carbide precipitation were observed and temperature ranges of martensite recovery and recrystallization were established. Recovered martensite was characterized by the lath structure with a certain dislocation density, issued from the as-quenched lath martensite, and after recrystallization strain-free equiaxed grains were observed. Then, in the beginning of 70's, R. Caron and G. Krauss [CAR'72] made an exhaustive study of the microstructure evolution during tempering of 0.2 wt.% C steel. They found that coarsening of fine lath martensite structure with the elongated packet-lath morphology is the major microstructure transformation and only at late stages of tempering an equiaxed structure gradually appears. Figure 6 shows their microstructure observations with optical microscope (OM) and electron micrograph extraction replica of the sample tempered at 700°C for 12h.
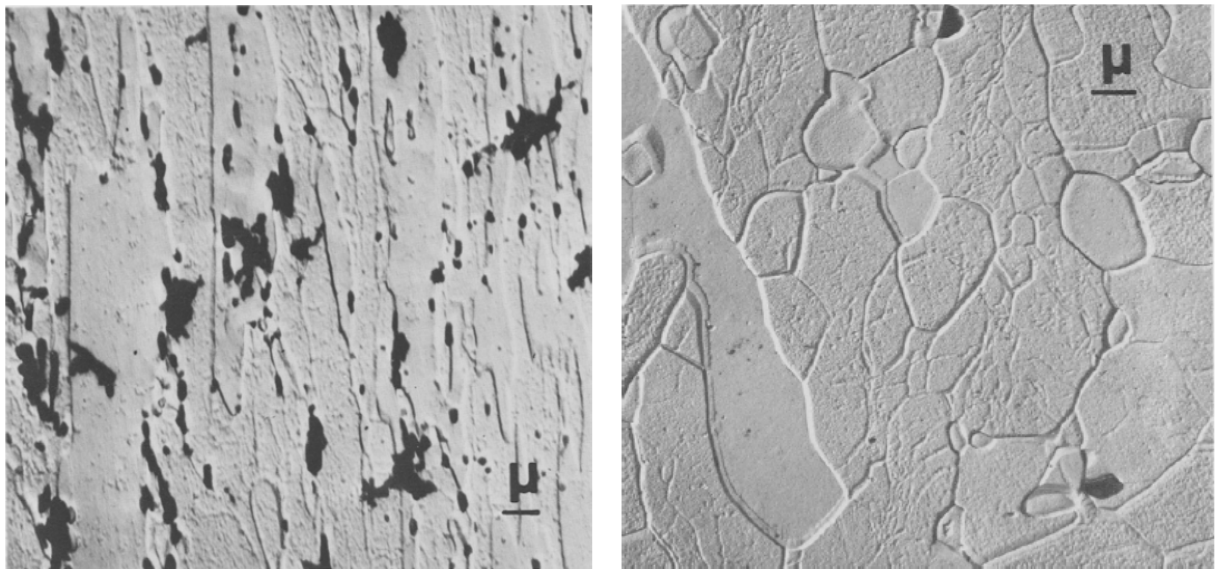
Figure 6 – Extraction replica TEM electron micrographs of lath martensite tempered at 500°C for 5h (at left) and at 700°C for 12h (at right) [CAR'72].

In spite of the equiaxed form of grains the increase in high angle boundaries expected from the formation of strain-free grains was not observed. Hence, R. Caron and G. Krauss proposed the following scenario of as-quenched martensite tempering:
- ⇨ first recovery takes place and significantly decreases the low angle boundaries content. At this stage the morphology of the tempered martensite is lath-like coming from the initial lath morphology of the as-quenched martensite. In the same time carbon segregation and carbide precipitation occurs at very early stages of tempering;
- ⇨ then recovery continues by polygonization or low angle boundary formation because the recrystallization is delayed due to the pinning of grain boundaries by carbide particles. As well process of carbide spheroidization, or Ostwald ripening, can occur;
- ⇨ finally the aligned coarsened lath morphology, left from the earlier stages, transforms to an equiaxed ferritic grains through the grain growth mechanism [CAR'72].

These results were supported by the work of S. Takaki et al. [TAK'92] on the commercial 0.2%C steel. No proofs of the as-quenched martensite recrystallization were found. However,

recrystallization of the deformed lath martensite was observed and the influence of deformation rate on the recovery and recrystallization was studied.

More recent research works of T. Tsuchiyama et al. [TSU'01], [NAT'05] and [TSU'10] showed that recrystallization of ultra-low carbon steel at high tempering temperatures and long times is possible through the specific bulge nucleation and growth (BNG) mechanism (Figure 7). Bulging of packet boundaries and prior austenite grain boundaries results in the recrystallized grains nucleus that grow afterwards by consuming martensitic structure with high dislocation density.
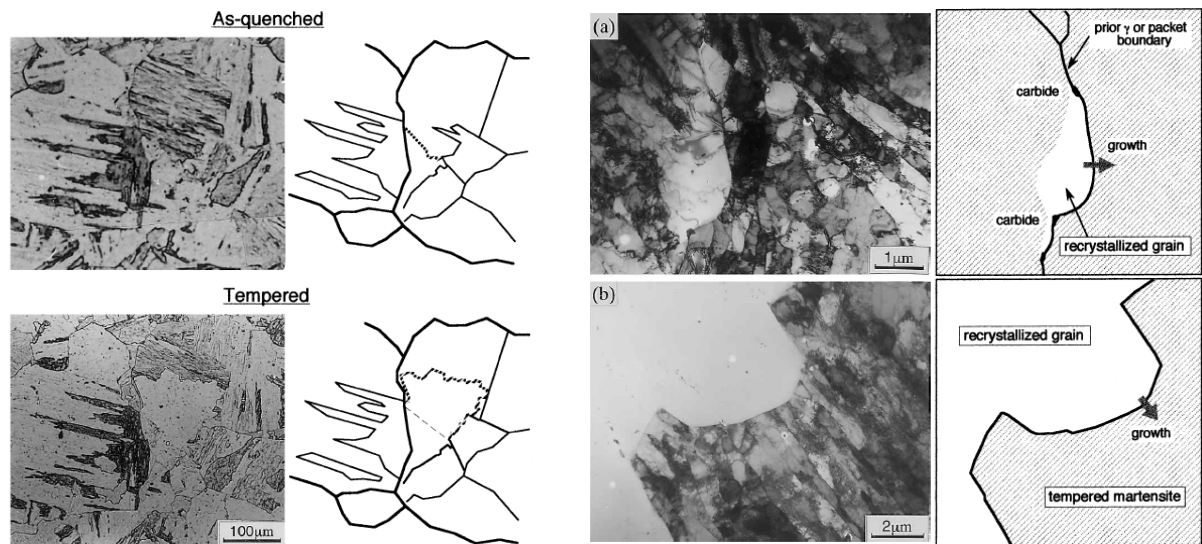
Figure 7 – Left part - Optical micrographs and traces of grain boundaries obtained by the in-situ observation of the as-quenched specimen (upper pictures) and tempered at 1 023 K for 3.6 ks (lower ones). A bulging packet boundary is shown by the hatched line. Right part - Transmission electron micrographs and traces showing nucleation (tempered at 973 K for 2.1 ks) (a) and growth (tempered at 973 K for 2.7 ks) (b) of recrystallized grains in the ULC steel [TSU'01].

ArcelorMittal internal experience also shows the possibility of the as-quenched martensite recrystallization in 0.4C-0.7Mn steel [TAU'13]. Martensite, obtained after austenitization at 900°C for 5min followed by water quench, was then tempered at 690°C for 60h and resulted in microstructure consisting of strain-free equiaxed ferrite grains and cementite (Figure 8).
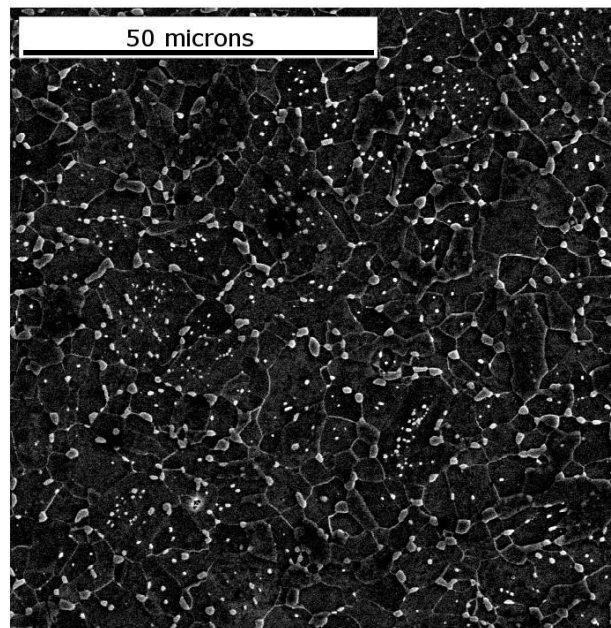
Figure 8 – SEM image of the ferrite-Fe₃C carbides microstructure, obtained after as-quenched martensite tempering at 690°C for 60h [TAU'13].

1.2.2 Austenite formation during intercritical annealing

Austenite formation in steels and alloys was broadly studied for more than 100 years. One of the first works on austenite was done by Arnold and McWilliams in 1905 [ARN'05]. They found that austenite forms during heating through the nucleation and growth mechanisms. The same conclusion was done by Roberts and Mehl [ROB'43], but they also have done the exhaustive analysis of the austenite formation kinetics starting from the ferrite-cementite microstructure. Development of dual-phase and TRIP steel grades from the early 80's pushed the researchers to perform numerous works on the austenite formation. A detailed study of austenite formation in steels with various carbon content and 1.5wt.% Mn was done by Garcia and DeArdo [GAR'81]. Different initial microstructures were used: spheroidized cementite in a recrystallized ferrite matrix; spheroidized cementite in a cold rolled ferrite matrix and ferrite plus pearlite. It was found that austenite nucleates at cementite particles located on the ferrite grain boundaries in the case of spheroidized cementite and on either pearlite colony boundaries or boundaries separating colonies and ferrite grains in the case of pearlite.

The kinetics of austenite formation at 725°C was also studied. It appears that austenite forms slightly more rapidly from cold rolled ferrite than from recrystallized ferrite or ferrite-pearlite structures (Figure 9). However the final amount of formed austenite is very similar for different cases.
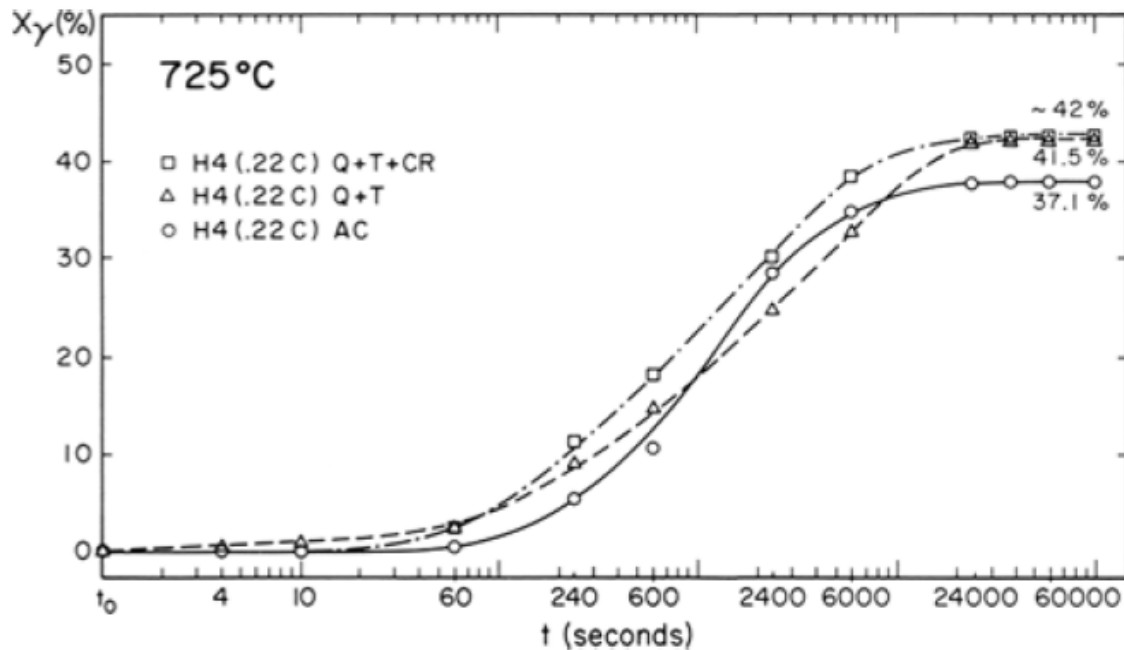
Figure 9 – Comparison of austenite formation kinetics at 725°C from various starting microstructures [GAR'81].

Another interesting thing observed by Garcia and DeArdo [GAR'81] was the effect of Mn segregation (banding) on the pearlite microstructure: pearlite in the zones with higher Mn content had a more fine interlamellar spacing in comparison with the pearlite outside of this Mn bands.

Similar but very important study was done by Speich et al. [SPE'81]. Series of 1.5 pct manganese steels containing different carbon amounts and with a ferrite-pearlite starting microstructure were investigated in the range of 740 to 900°C. According to the obtained experimental results, the kinetics of austenite formation was separated into three steps:

1) prompt nucleation of austenite at the ferrite-pearlite interface and very rapid growth of austenite into pearlite until the full dissolution of cementite (Figure 10(1));

2) after dissolution of cementite, further growth of austenite into ferrite occurs with slower rate that is controlled by carbon diffusion in austenite at high temperatures (850 to 900°C) and by manganese diffusion in ferrite at low intercritical temperatures (740 to 780°C) (Figure 10(2a) and (2b));

3) very sluggish final equilibration of the manganese contents of the austenite and ferrite phases controlled by manganese diffusion in austenite (Figure 10(3)).

With the help of diffusion models and experimental results, austenite formation diagram which graphically illustrate the amount of produced austenite and processes controlling kinetics at different times and temperatures was constructed for one of the steels (Figure 11).
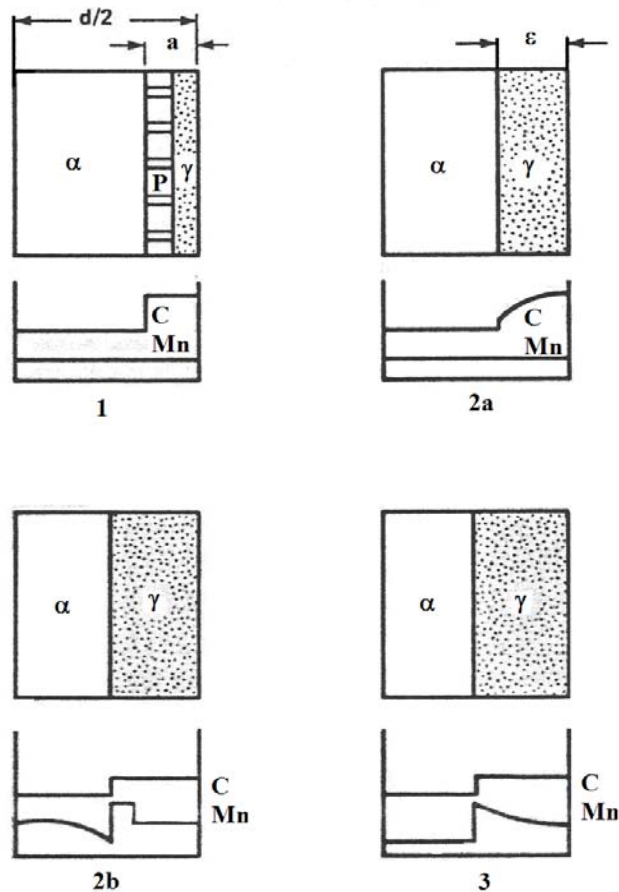
Figure 10 – Schematic representation of austenite formation and growth during intercritical annealing of ferrite-pearlite steels: 1 - dissolution of pearlite, 2a - austenite growth with carbon diffusion in austenite, 2b - austenite growth with manganese diffusion in ferrite, 3 - final equilibration with manganese diffusion in austenite [SPE'81].
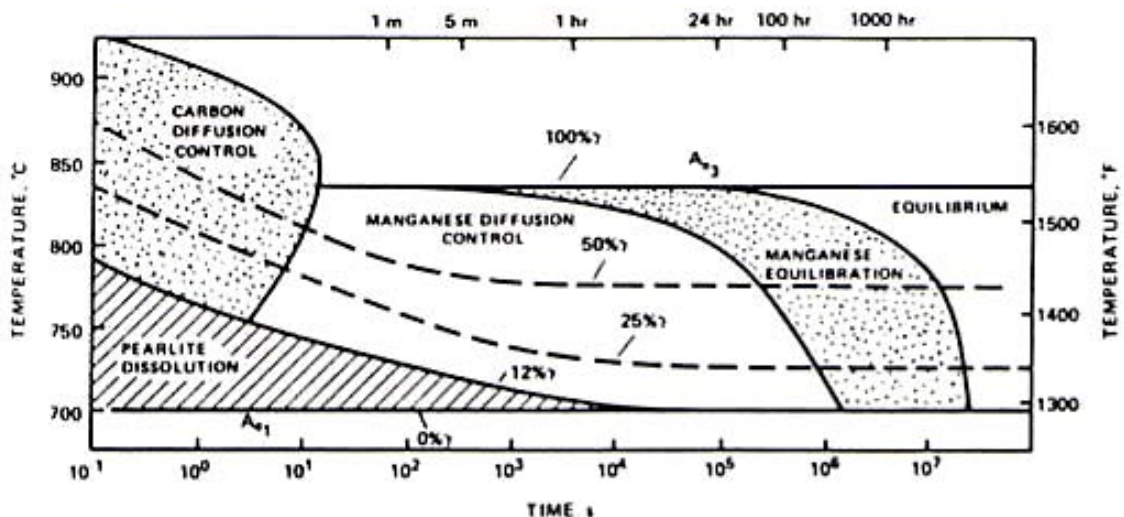
Figure 11 – Diagram for austenite formation and growth in 0.12C-1.5Mn (wt.%) steel [SPE'81].

On the other hand, Pussegoda et al. [PUS'84] studied 0.06C, 2.83Mn, 0.33Si (wt.%) steel and demonstrated significant partitioning of Mn between ferrite and austenite during intercritical annealing. It was shown that Mn can diffuse to the center of austenite grains within a reasonable

time at 695°C of the order of hours rather than centuries (Figure 12). This result was partly attributed to the obtained very fine-grained microstructure with ferrite grain size of ~5µm and austenite grain size of ~ 1µm. Also diffusion rate of Mn in austenite at 695°C was estimated at ~10-14 cm^2/s which is considerably higher than that obtained by extrapolation of diffusion measurements from higher temperatures.

Effect of cold deformation on the austenite formation kinetics in 0.11C-1.58Mn-0.4Si (wt.%) steel was studied by El-Sesy et al. [ELS'90]. Figure 13 shows the austenite fraction evolution with the time at 735°C for the samples with different initial states: hot-rolled, 25% and 50% cold deformed states. It appears that the kinetics of austenite formation (at least till the complete cementite dissolution) increases with the enhancement of cold rolling from 0% to 50%. Two possible reasons of the cold-deformation influence were proposed:

 ➢ Higher deformation rate decreases the size of recrystallized ferrite grains hence increasing the number of austenite nucleation sites at the intersections of ferrite grains with pearlite. Higher density of ferrite grain boundaries also promotes easier diffusion of substitutional alloying elements (for example, Mn) during the second step of austenite growth;
 ➢ Increase of cold rolling accelerates austenite formation due to the higher driving force or lower activation energy [ELS'90].
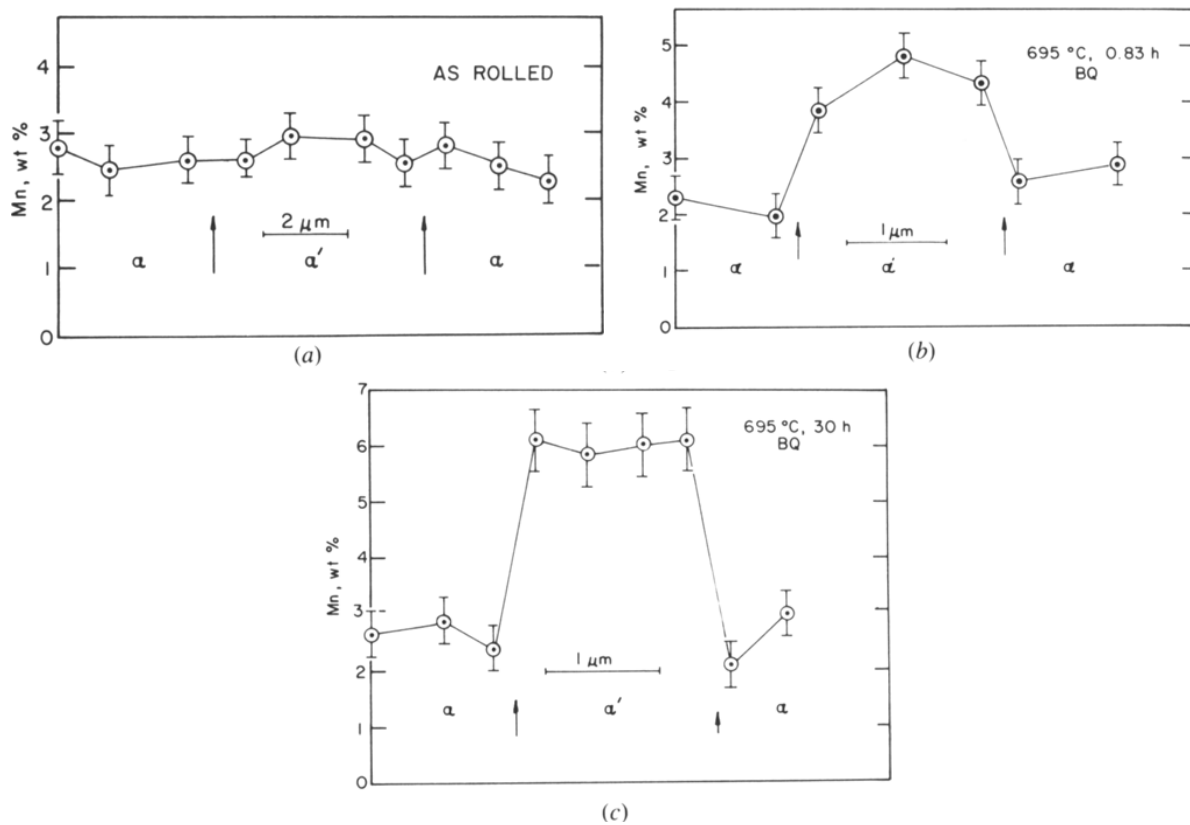
Figure 12 – Mn distribution in ferrite and martensite: (a) as-rolled (before heat treatment), and after 695°C intercritical annealing for (b) 0.83 h and (c) 30 h followed by brine quenching. Positions of the a/a' boundaries are indicated [PUS'84].
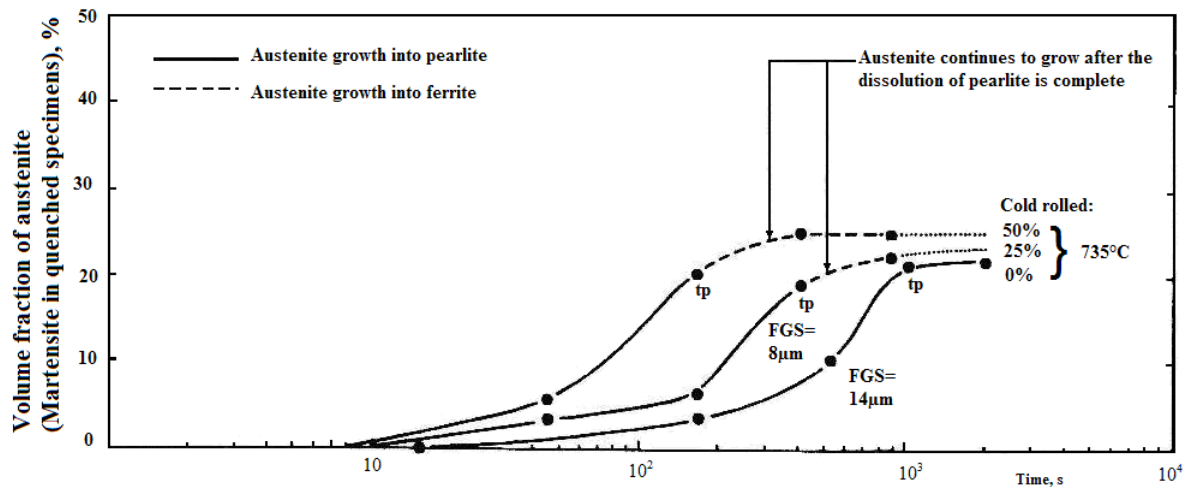
Figure 13 – Effect of cold deformation on the austenite formation kinetics in 0.11C-1.58Mn-0.4Si steel at 735°C. FGS is the ferrite grain size and tp is the time of complete pearlite dissolution [ELS'90]

Finally, manganese influence on austenite formation was also investigated in the past [BAI'69], [WEL'48]. Fe-C equilibrium diagram and the effect of manganese on the form and position of austenitic region are shown in Figure 14. It can be noted that Mn extends austenitic domain to lower temperatures and diminish the intercritical domain (austenite+ ferrite). In the same time, Mn lowers the eutectoid point "E" in both temperature and carbon content.

Manganese also enhances stability of austenite and, hence, enlarges the region of metastable austenite. The delay of austenite decomposition into ferrite plus pearlite at 525°C and into bainite at 310°C is clearly illustrated on the isothermal transformation diagrams in Figure 15 [BAI'69].

All these Mn effects are quite important for the appropriate choice of annealing temperature.
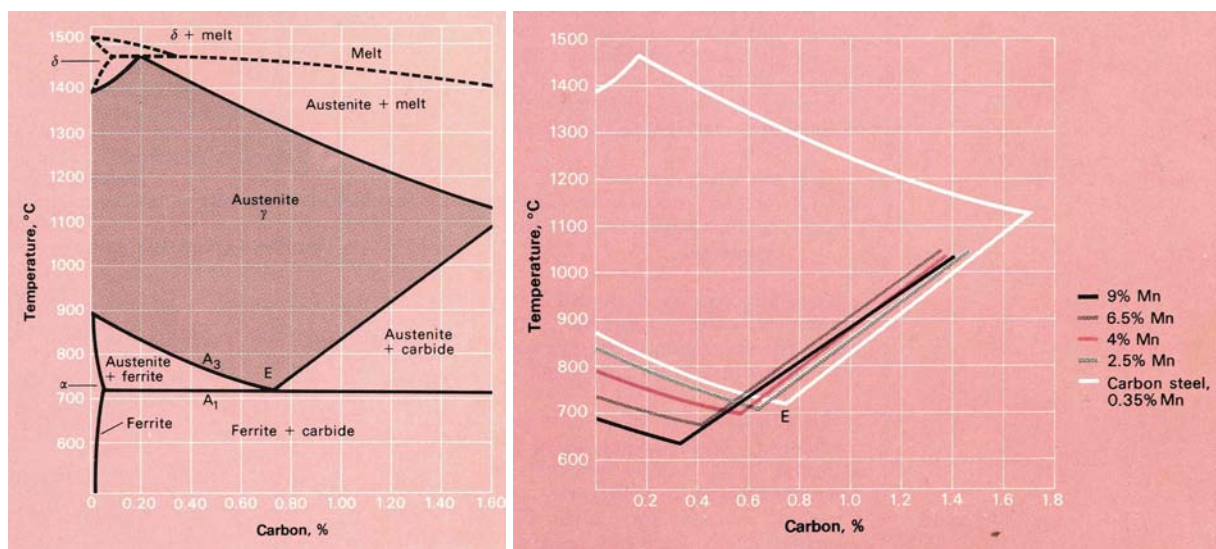
Figure 14 – Fe-C equilibrium diagram and the effect of manganese on the form and position of austenitic region (taken from [DES'76]).

24
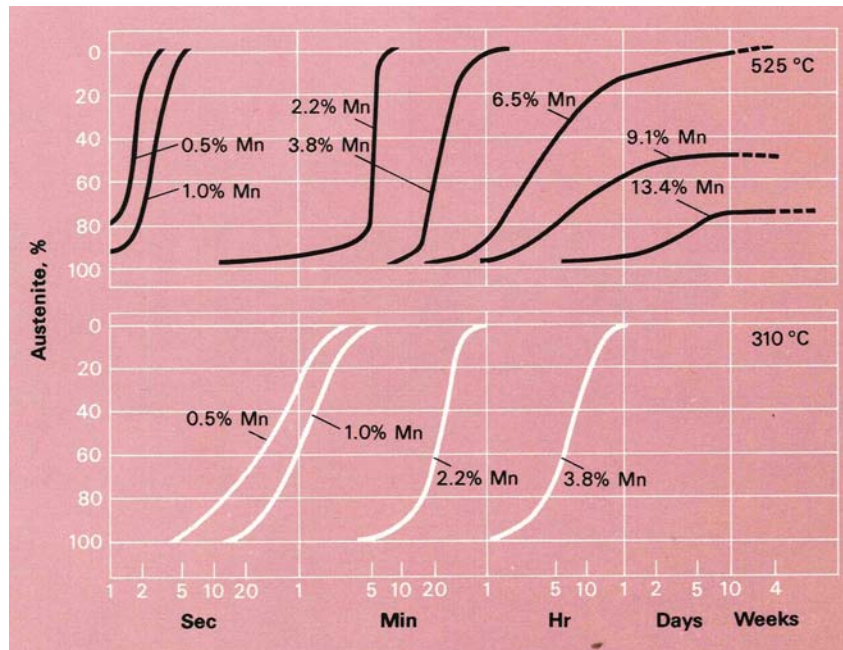
Figure 15 – Isothermal transformation diagram – effect of manganese on the austenite decomposition of 0.55 wt.% C steel at two different temperatures (taken from [DES'76]).

1.2.3 Particular case of Austenite Reverse Transformation (ART)

Austenite formation from initial martensite structure has some particularities, thus a special name is attributed to this transformation. The name differs according to different authors and studied alloys: reverse martensitic transformation [KRA'62], [KRA'63], reverse transformation [MAT'74-1], [MAT'74-2], reverse austenite transformation, austenite reverse transformation, annealed martensite [SUG'02-1], [SUG'02-2], [SUG'05] … All these names describe the transformation upon heating of martensite to the austenite. However, depending on the alloy composition, the mechanisms of such transformation can differ. In this work the major attention will be paid to the description of such transformation in Fe-C-Mn steels and only some results in Fe-C-Ni system will be discussed.

The pioneer study in this field was done by Nehrenberg in the late 40's on different C-Mn commercial steels [NEH'50]. He investigated the dependence of austenite formation on the initial microstructure: pearlite, spheroidite (spheroidal carbides and ferrite), martensite, tempered martensite and bainite. It was found that from pearlite and spheroidite austenite grows more or less freely and equiaxed ferrite-austenite structure is obtained. On the other hand, martensite, tempered martensite or bainite result in acicular shape of final autenite and ferrite and a lamellar microstructure consisting of these alternate acicular phases is obtained.

Plichta and Arronson [PLI'74] looked on the effectiveness of different alloying elements for the production of acicular morphology. It was found that Mn, Ni and Cu stimulate the formation of fine, complex, acicular network of boundaries in which the influence of initial martensite structure is clearly reflected. The proposed explanation was that the rates of austenite nucleation are sufficiently high to restrict significantly the migration of martensite needle boundaries.

Interesting discoveries were also done by Matsuda and Okamura [MAT'74-1], [MAT'74-2] when they studied Fe-C-Ni steels. The final microstructure after reverse transformation consisted of two types of austenite grains: globular and acicular. Then, they examined the effect of heating rate on the formed microstructures and found that the number of globular grains decreases with

25

the decrease of heating rate. Figure 16 shows two examples of microstructure and the evolution of globular austenite grains quantity as a function of heating rate. It was also observed that cementite is more enriched in Mn with lower heating rate. Hence, it was supposed that the decrease in the number of globular austenite grains is due to the inhibited by the Mn segregation growth. Similar type of observations was also done by Kinoshita and Ueda [KIN'74] for Fe-0.21C-1Cr (wt.%) steel and by Law and Edmonds [LAW'80] for the Fe-0.2C-1V (wt.%) steel.
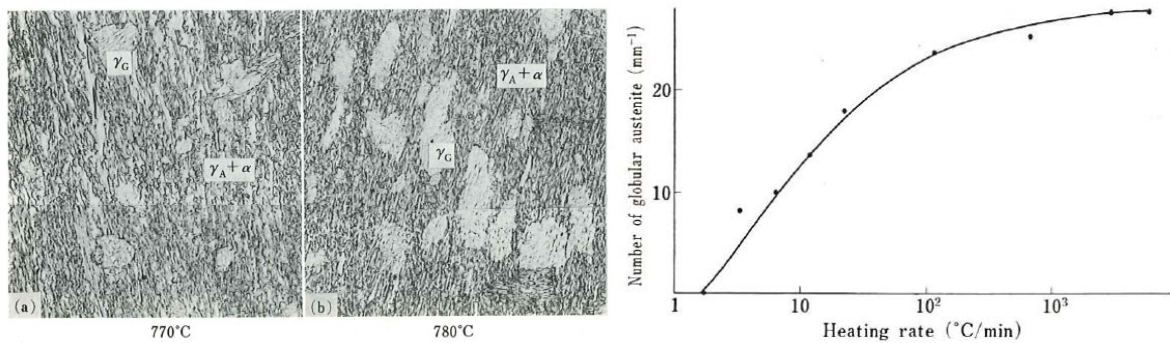
Figure 16 – At left - microstructure of specimens quenched from 770 and 780°C: γ_G – globular austenite and $\gamma_A + \alpha$ – acicular austenite + ferrite. At right – number of globular austenite grains as a function of heating rate [MAT'74-1], [MAT'74-2].

Another researcher who contributed a lot to the development of ART annealing was Gareth Thomas [KOO'76], [KOO'77], [KIM'81], [NAK'85]. He was one of the persons who clearly showed an interest of ART annealing for industrial use: grain refinement, lath morphology and improvement of mechanical behavior. He also obviously demonstrated the difference between ART, intercritical annealing and formation of ferrite from high temperature austenite. That is why some researchers call the fibrous microstructure obtained with ART as "Thomas fibers". Figure 17 shows the scheme of thermal cycles which were compared and the relative resulting microstructures [KIM'81]. Using transmission electron microscopy (TEM) it was also observed that ferrite regions have some subgrain structure after ART and intercritical annealing, while the step quenched coarse ferrite was free of such subgrains.

Different studies [TOK'82], [MAT'84], [YI'85], [CAI'85] also showed that the prior to annealing martensite structure will condition austenite nucleation and, hence, the morphology of final microstructure. These investigations point out the importance of the following parameters for the control of austenite shape and distribution:
- prior austenite grain size;
- presence of non-dissolved carbides;
- presence of defects (deformation state);
- recrystallization state of martensite.

In particular, Yi et al. [YI'85] observed an unambiguous difference in the morphology of austenite obtained from two different martensitic states. Succinct representation of their results is given in Figure 18. It appears that very rapid austenitization prevents the full dissolution of carbides in austenite and limits the austenite grain growth, hence in the following intercritical annealing new austenite nucleates mostly on the prior austenite grain boundaries and its shape is more globular. In contrary, austenite nucleates at lath and packet boundaries and has a lath-like morphology in the case of initial martensite with fully dissolved carbides and bigger grains.
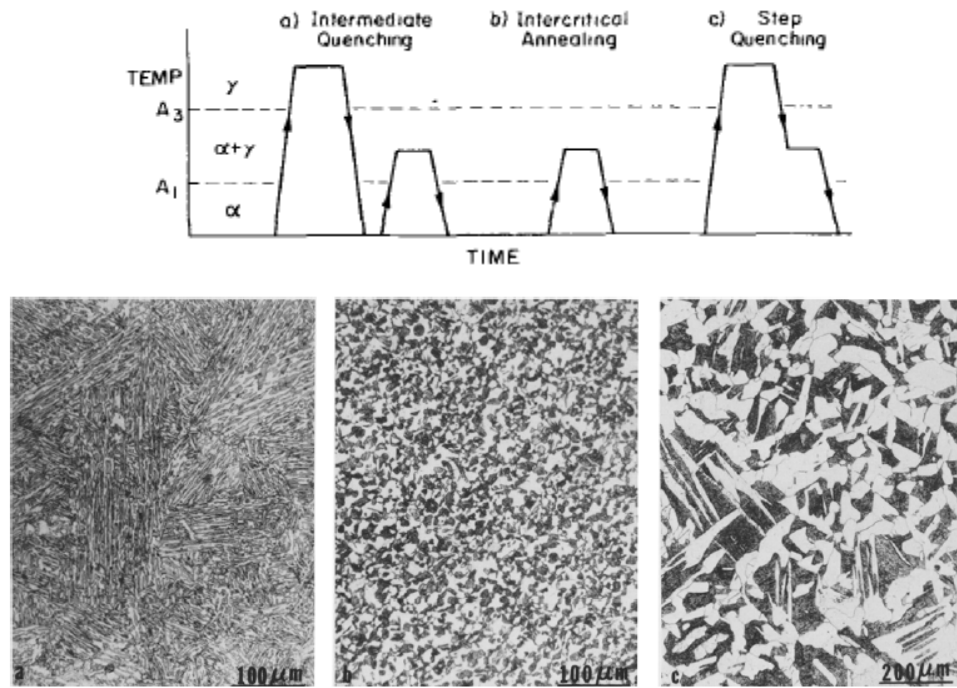
Figure 17 – Scheme of applied heat treatments and corresponding final microstructures after: (a) Intermediate Quenching (ART); (b) Intercritical Annealing and (c) Step Quenching.

MT-1 : Austenitized at 1150°C for 3 hours, water-quenched

MT-2: - Heating to 1000°C at 10°C/s, then hold for 10s, water-quenched

a)

b)
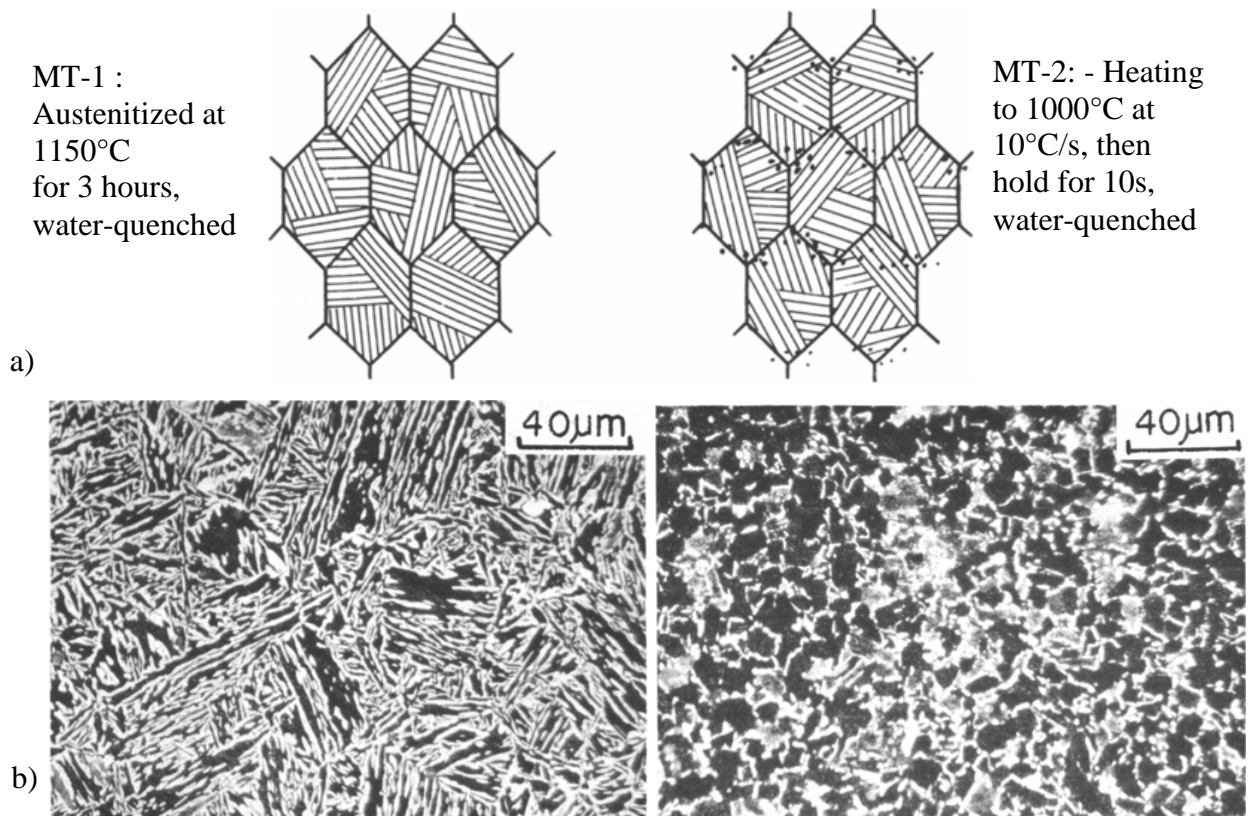
Figure 18 – a) Schematic illustrations of the starting microstructures: MT-1 and MT-2. b) Austenite particles (martensite at room temperature) revealed with LePera's etchant: MT-1 sample annealed at 840°C for 2 min and water-quenched and MT-2 sample annealed at 780°C for 10 sec and water-quenched.

Cai et al. [CAI'85] also observed sluggish austenite kinetics and an extensive partitioning of Mn between annealed martensite (ferrite) and austenite. This indicates that driving force for the austenite growth is rather small and the kinetics is controlled by the manganese diffusion.

Two very recent studies of ART mechanisms [WEI'13] and [NAK'13] investigated formation and growth of austenite from as quenched martensite and came to almost the same conclusions. Wei et al. [WEI'13] studied 0.1C–3Mn–1.5Si (wt.%) steel and found that during intercritical annealing of as-quenched martensitic structure, austenite will grow from thin austenite films between laths retained upon quenching, but also austenite will nucleate at lath boundaries and packet boundaries of martensite and within laths.

As found by Speich et al. [SPE'81] the growth of austenite can be divided on three stages:

1. initial no-partitioned growth of austenite, controlled by rapid carbon diffusion in ferrite, which is gradually replaced by carbon diffusion in austenite;
2. intermediate slow growth, controlled by diffusion of Mn and/or Si in ferrite;
3. very slow growth, controlled by diffusion of Mn and/or Si in austenite for final equilibration, which accompanies the shrinkage of austenite [WEI'13].

These three stages are clearly depicted in Figure 19.
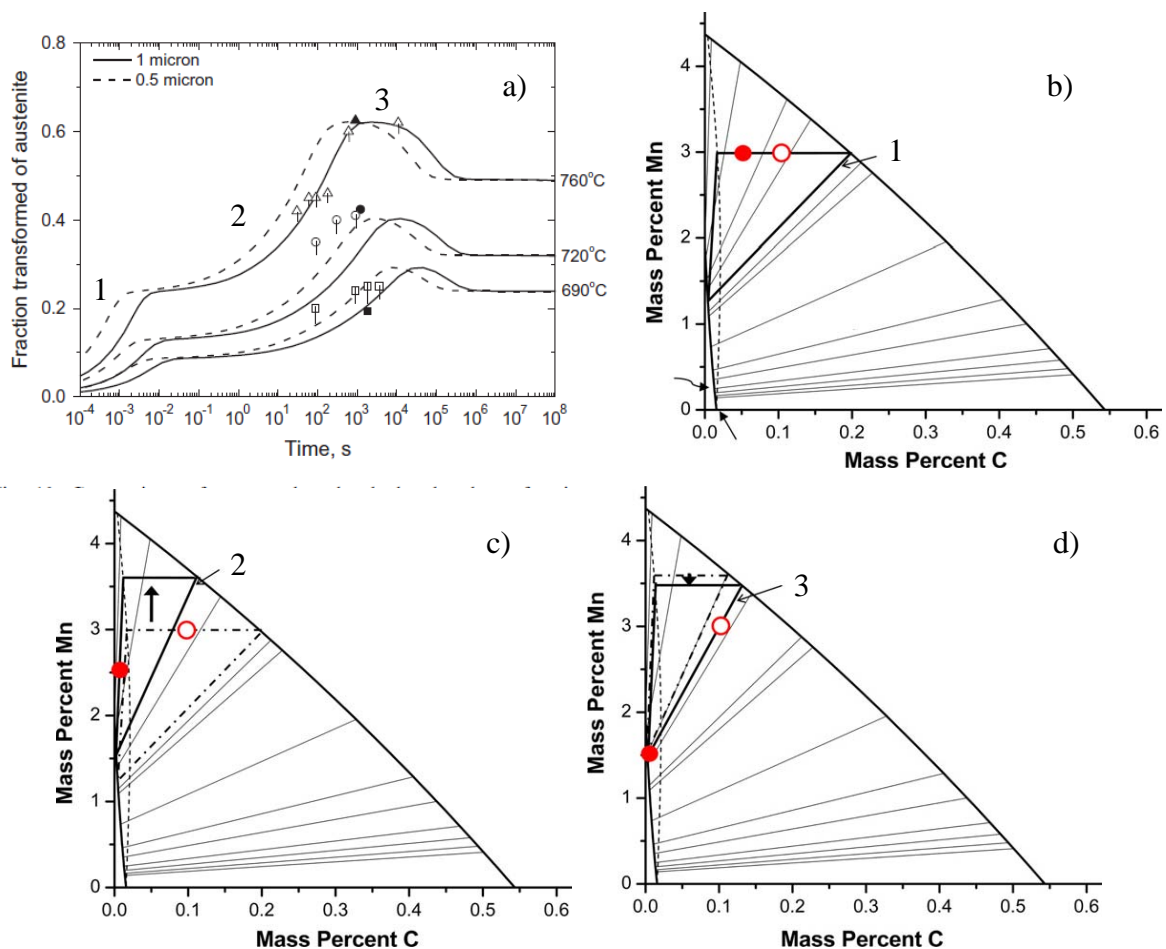
Figure 19 – a) Comparison of measured and calculated volume fractions of austenite (open symbols are measured by point counting and solid ones are from dilatometry). b), c), d) - Isothermal sections of a ternary Fe–C–Mn phase diagram illustrating different steps of austenite growth during annealing (open circles indicate the bulk alloy composition; solid circles represent the mean composition of the ferrite matrix changing with time) [WEI'13].

28

Internal ArcelorMittal results [MOU'03] confirmed the observations of fine fibrous microstructure obtained after intercritical annealing of martensite and their interest for improvement of mechanical behavior.

1.2.4 Austenite stabilization during annealing

It is known that during cooling from the austenitic or intercritical region, austenite will undergo a transformation according to the cooling rate: ferrite, pearlite, bainite or martensite. But in the case of high stability of austenite, these transformations can be avoided and austenite will be retained at the room temperature. Concerning medium Mn steels, ferrite, pearlite and bainite transformations are strongly delayed due to the high Mn content. Hence, in the majority of cases the only transformation that takes place during cooling is the martensitic one. Numerous studies were done on the observation and comprehension of martensitic transformation and many reviews were edited. The reviews or books used in this work as the base for the understanding of martensite and its transformation are the following: [KUR'60], [KUR'77], [OLS'92], [KRA'99]. These authors have done a considerable contribution to the knowledge building about martensite.

Martensite transformation is characterized by two temperatures: M_s – temperature at which martensite starts to form and M_f – temperature when martensite transformation is finished. Accordingly, during cooling austenite does not transform at temperatures higher than M_s. Therefore, it is very important to know M_s temperature since it can be used as an indicator of austenite thermal stability.

A lot of studies were done about the influence of different parameters on the M_s temperature. It is commonly agreed that M_s temperature depends on chemical composition, prior austenite grain size, hydrostatic pressure and applied stress. It is also known that the effect of chemical composition and fine prior austenite grain size (less than 10µm) are of major importance. A number of different relations linking chemical composition and M_s temperature exist in the literature. Probably the most common relations are those proposed by Steven and Haynes [STE'56] and Andrews [AND'65]. However, more recent work of Van Bohemen [BOH'12] proposed a better correlation of M_s temperature and carbon content, using an exponential carbon dependence. Also a clear review of the past investigations and an extension of M_s relation to higher and broader alloying elements contents was done by Barbier [BAR'14]. Van Bohemen's and Barbier's formulas are presented hereafter. Both give very satisfactory results, but Barbier's formula has a wider application field. Hence, in this work it will be taken as a reference.

$$M_s = 565 - 600 \cdot (1 - \exp(-0.96 \cdot w_C)) - 31 \cdot w_{Mn} - 13 \cdot w_{Si} - 10 \cdot w_{Cr} - 8 \cdot w_{Ni} - 12 \cdot w_{Mo} \quad ^{[BOH12]} \tag{1}$$

$$M_s = 545 - 601.2 \cdot (1 - \exp(-0.868 \cdot w_C)) - 34.4 \cdot w_{Mn} - 13.7 \cdot w_{Si} - 9.2 \cdot w_{Cr} - 17.3 \cdot w_{Ni} - 15.4 \cdot w_{Mo}$$
$$+ 10.8 \cdot w_V + 4.7 \cdot w_{Co} - 1.4 \cdot w_{Al} - 16.3 \cdot w_{Cu} - 361 \cdot w_{Nb} - 2.44 \cdot w_{Ti} - 3448 \cdot w_B \quad ^{[BAR14]} \tag{2}$$

where w_i is the alloying element content in austenite expressed in weight percents.

Studies about the effect of prior austenite grain size on the austenite stability and M_s temperature are more rare. This is probably related to the experimental difficulties as the observation of prior austenite grains is quite complex. Therefore, the first studies were done in more theoretical ways. One of the most common work is that of Fisher et al. [FIS'49] where a nucleation and growth model to predict the kinetics of martensite transformation was proposed. Effect of prior austenite grain size was introduced in the model by the authors, based on the geometrical constraints: the volume fraction of forming martensite is proportional to the volume of the prior austenite grain size.

Modern studies [WAN'01], [DRI'04], [JIM'07-1], [JIM'07-2], [YAN'09] confirmed the fact that small austenite grain size decreases considerably the M_s temperature. Two last works as well proposed their ways to take into account the influence of austenite grain size.

Jimenez-Melero et al. [JIM'07-2] suggested the following equation:

$$M_s^{'} = M_s - BV_\gamma^{-\frac{1}{3}} \tag{3}$$

where M_s is taken from the Andrews equation [AND'65], V_γ is the volume of austenite grain, and B is a parameter that can be obtained from thermodynamic calculations. For spherical grains, the factor B was fitted to the value of 475 µm.K.

Yang et al. [YAN'09] had the same global idea, but a different formula was given in their study of Fe-C-Ni-Mn alloys:

$$M_s = M_s^0 - \frac{1}{b} \ln \left[\frac{1}{aV_\gamma} \left\{ \exp\left(-\frac{\ln(1-f)}{m} \right) - 1 \right\} + 1 \right] \tag{4}$$

where V_γ is the volume of austenite grain, f is martensite fraction (for M_s calculation $f = 0.01$), m is the plate aspect ratio (m = 0.05 from [CHR'79]) and a = $1 mm^{-3}$, b = 0.2689 and M_s^0 = 363.5°C are three fitting parameters.

Figure 20 presents the comparison of both models ([JIM'07-2] and [YAN'09]) in terms of the decrease of M_s temperature:
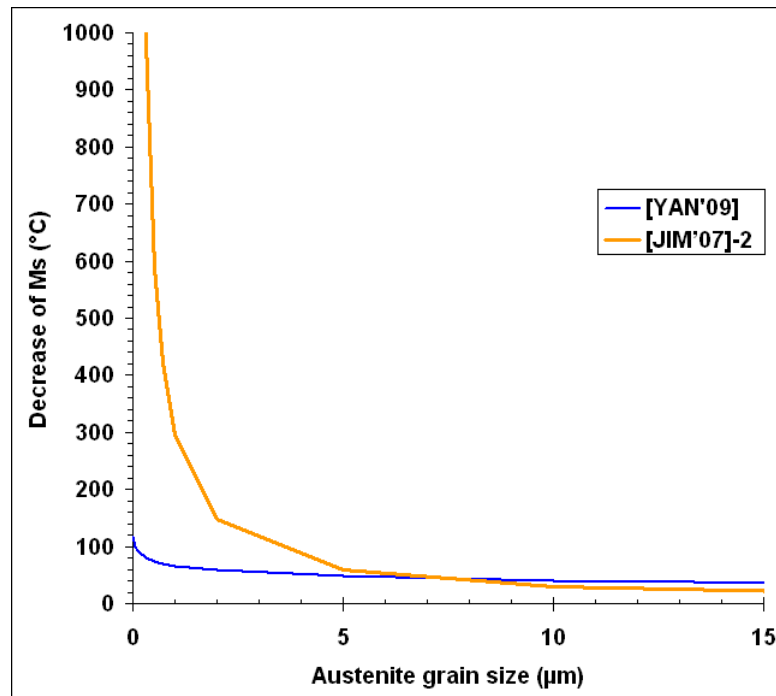
Figure 20 - Decrease of M_s temperature as a function of austenite grain size according to both studies: [JIM'07-2] and [YAN'09].

As it can be seen there are some key limitations in both solutions:
- Jimenez-Melero et al. model gives too high impact of very small grains (less than 2µm);
- Yang et al. equation, in contrary, predicts too low impact of fine grains (less than 2µm).

Such restrictions leave the possibility for the future investigations and new solutions.

Another important topic that was also largely studied is the kinetics of martensite transformation. In Fe-C-Mn steels austenite to martensite transformation is athermal. This means that kinetics of martensite transformation only depends on the decrease of temperature, thus driving force for the transformation increases with higher supercooling below the M_s temperature. The most widespread model to predict the kinetics of athermal martensite transformation is the Koistinen and Marburger empirical equation [KOI'59]:

$$f_{RA} = \exp\left(-\alpha \cdot \left(M_s - T_q\right)\right)$$ (5)

where f_{RA} is the volume fraction of retained austenite, T_q is the temperature reached during quenching and $\alpha=0.011$ is a fitting parameter.

Recent works of Van Bohemen et al. [BOH'09] and of Lee et al. [LEE'13-1] proposed some modifications to this equation. In the former one, it was first found that the curvature of martensite transformation kinetics curve depends on chemical composition of austenite. The curvature is controlled by the parameter α, hence the following empirical dependence of α on the chemical composition was established, based on numerous dilatometer data:

$$\alpha_m = 0.0224 - 0.0107 \cdot w_C - 0.0007 \cdot w_{Mn} - 0.00012 \cdot w_{Cr} - 0.00005 \cdot w_{Ni} - 0.0001 \cdot w_{Mo}$$ (6)

Similar modifications were proposed by Lee et al, but as the work was done on different steel compositions (medium Mn steels), other coefficients were used for the alloying elements. Also Lee et al. introduced supplementary fitting parameter (β) to improve the curvature prediction:

$$f_{\alpha'} = 1 - \exp\left[-\alpha\left(M_s - T_q\right)^{\beta}\right]$$
$$\alpha = 0.0076 - 0.0182 \cdot w_C - 0.00014 \cdot w_{Mn}$$ (7)
$$\beta = 1.4609 - 0.4483 \cdot w_C - 0.0545 \cdot w_{Mn}$$

From the previously mentioned works, it appears that two factors have the major influence on the M_s temperature, and thus on austenite stability:

1. chemical enrichment of austenite with alloying elements (C, Mn, Si and others);
2. austenite grain size that can give an important increase of austenite stability when its value is very small.

Considering these factors, one can imagine an intercritical annealing that allows considerable partitioning of C and Mn (as major austenite stabilizers) and in the same time low austenite grain size. Hence, using such intercritical annealing an important fraction of austenite can be retained at the room temperature.

One of the first works that showed experimental confirmation of important Mn partitioning in medium Mn steels was the study of Kim et al. [KIM'05]. It was shown that high amounts of retained austenite can be stabilized after intercritical annealing and that the stability of retained austenite was due to both C and Mn partitioning (Figure 21).
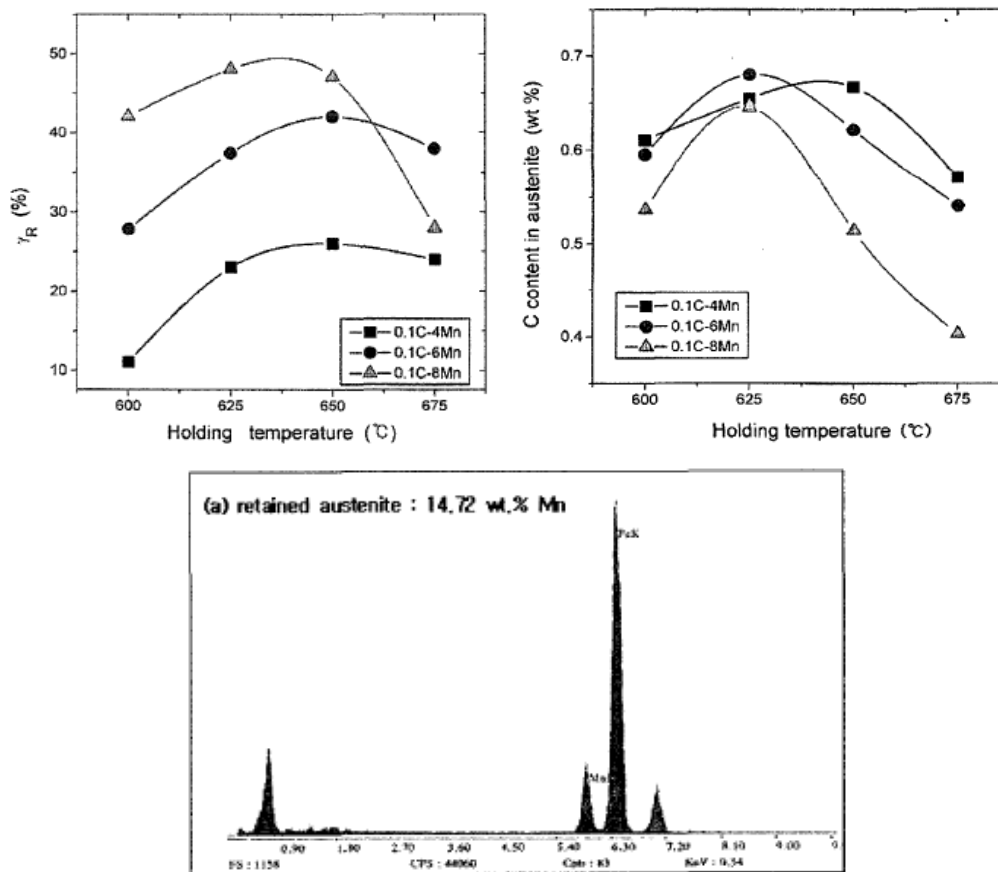
Figure 21 – Two upper figures: effect of holding temperature on the amount of retained austenite and of its carbon content after 6h annealing at different temperatures. Lower figure: EDS-TEM analysis of retained austenite in 8 wt.% Mn steel after 6h annealing at 625°C [KIM'05].

Recent studies of different authors [COO'10], [WAN'11], [LUO'11], [JUN'11], [LUO'13] confirmed the partitioning of Mn during intercritical annealing and high Mn enrichment of austenite. Examples of TEM observations and EDX profiles across austenite grains taken from the work of [COO'10] are presented in Figure 22.
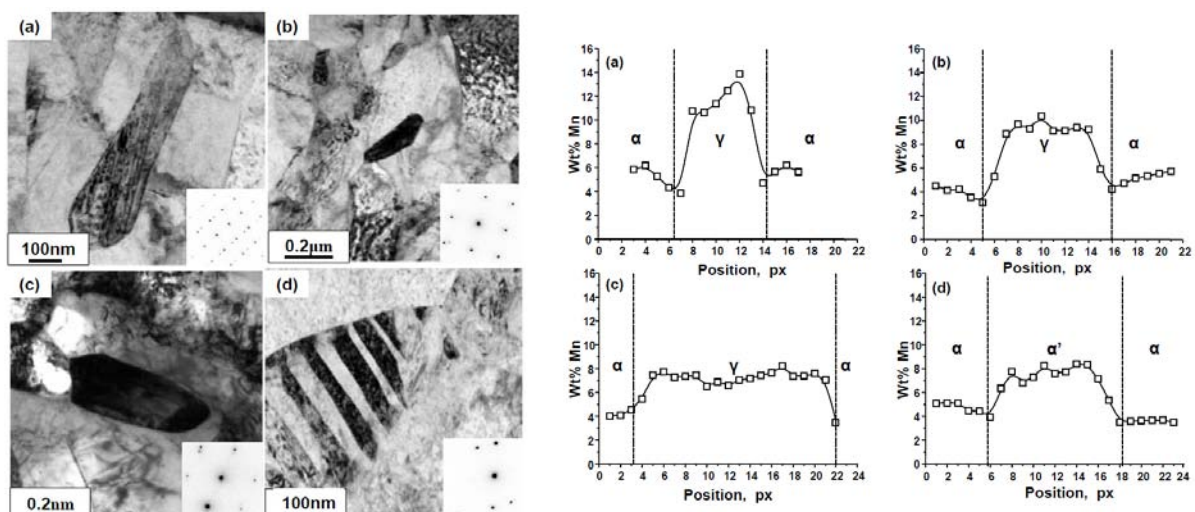
Figure 22 –TEM images (at left) and EDX profiles (at right) of the samples after intercritical annealing at different temperatures: (a) – 640, (b) – 660, (c) – 680, (d) – 700.

32

As it can be seen from Figure 22, the obtained austenite grain size is ultra fine (less than 1μm). This means that an important contribution of grain size effect on the stability of austenite is expected. Already in the early works on medium Mn steels of Huang et al. [HUA'94] the ultra fine grain size was reported and its influence on austenite stability was anticipated. Current works [WAN'11], [LUO'11], [JUN'11] confirmed the ultra fine grain size of austenite with the quantitative results. An example of such quantification taken from the work of Luo et al. [LUO'11] is shown in Figure 23. Also, Lee et al. [LEE'13-2] based on their previous work [LEE'13-1] proposed a way to consider the influence of austenite grain size on the optimal selection of annealing temperature to obtain maximum fraction of retained austenite.

Time	Thickness of α lath (μm)	Thickness of γ lath (μm)	Wt.% Mn in γ	Wt.% C in γ	Volume fraction of γ, %
0				0.68(0.02)	1.46(1)
1 min	0.4(0.17)	0.1(0.07)	7.4(1.4)	0.59(0.06)	4.54(1.5)
5 min	0.3(0.1)	0.15(0.09)	7.8(1.3)	0.53(0.06)	8.4(1.8)
10 min					12.6(3)
30 min					17.4(3)
1 h	0.3(0.1)	0.2(0.1)	7.7(1.3)	0.64(0.06)	22.5(3)
3 h					24.0(2)
6 h	0.3(0.1)	0.25(0.1)	8.6(0.8)	0.65(0.04)	30.9(2.5)
12 h	0.3(0.1)	0.3(0.1)	7.9(0.6)	0.69(0.03)	35.8(3)
48 h	0.4(0.1)	0.3(0.1)	9.1(0.4)	0.62(0.02)	31.9(2)
144 h	0.4(0.1)	0.33(0.15	9(0.7)	0.64(0.03)	32.7(2)
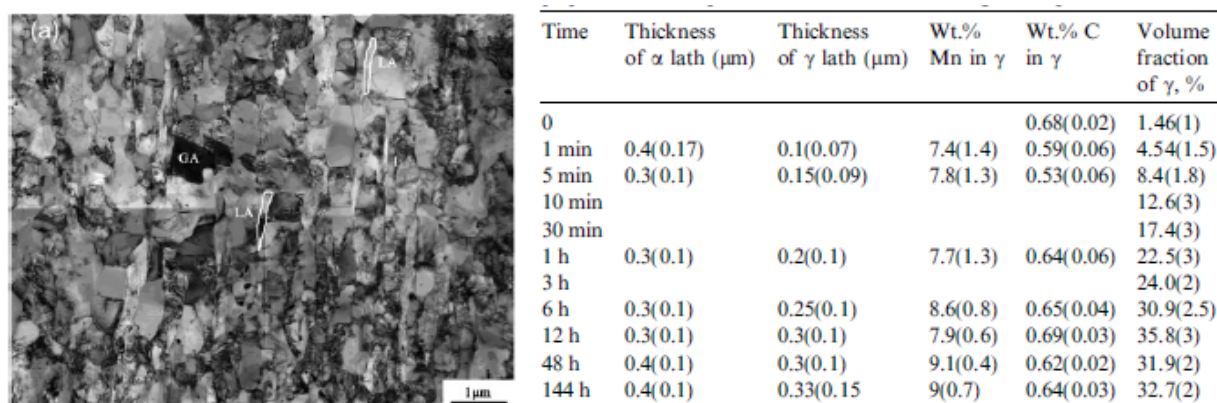
Figure 23 – At left microstructure observation using TEM and at right apparent thickness of austenite and ferrite laths, Mn content and austenite volume fraction as measured by TEM, STEM-EDX and XRD respectively [LUO'11].

1.3 Mechanical Properties of Medium Mn steels

In general, MMS are the steels with an enhanced TRIP effect due to the high volume fraction of retained austenite. The matrix of these steels is an ultra fine ferrite (in certain cases the mean size is less than 1μm). The hard phase in such matrix is represented by retained austenite (RA) and, if its stability is not sufficient, fresh martensite. Recently, a lot of studies describing mechanical behavior of MMS were performed and published. In order to analyze the existing data and to have a clear vision on the trends of mechanical behavior of MMS, a data base was built in the beginning of this work. It was updated during the whole period of this work. The entire data base can be found in Annex 1.1. Further will be presented only some extracted data, considered to be the most relevant for the standard intercritically annealed MMS (no Q&P).

1.3.1 Overview of the mechanical properties

First of all, Figure 24 presents the classical Ultimate Tensile Strength versus Total Elongation (UTS-TE) as well as more specific Yield Strength versus Uniform Elongation (YS-Uel) charts. As it can be seen and was already stated, these two graphs show the clear potential of MMS to fulfill the requirement of 3rd generation AHSS steels. Looking on the UTS-TE graph, it can be stated that UTS ranging from 1000 to 1200MPa can be obtained with TE ranging from 12 to 37. This means that it is possible to create a variety of strength-ductility combinations using MMS. Even though there are some points with higher UTS (up to 1400MPa), the general trend is that with the increase of UTS the ductility slightly goes down. For the YS-Uel the tendency is less clear, but in the same time the quantity of available data is also lower. Nevertheless, in certain

cases very attractive combinations of YS and Uel can be obtained (~1000MPa with more than 20% of Uel).

Using the available data set, it was decided to investigate relationships between some mechanical characteristics and microstructure parameters. Generally, ductility is correlated with the RA fraction. Thus, Figure 25 presents two dependencies: TE and Uel as a function of RA fraction. It can be seen that the correlations are much dispersed. Of course, there is a trend that with increasing austenite fraction elongation increases, but there are probably also other parameters, like austenite stability for example, that also have an important influence. In all the cases, it is clear that tensile elongation cannot be attributed to RA fraction only.
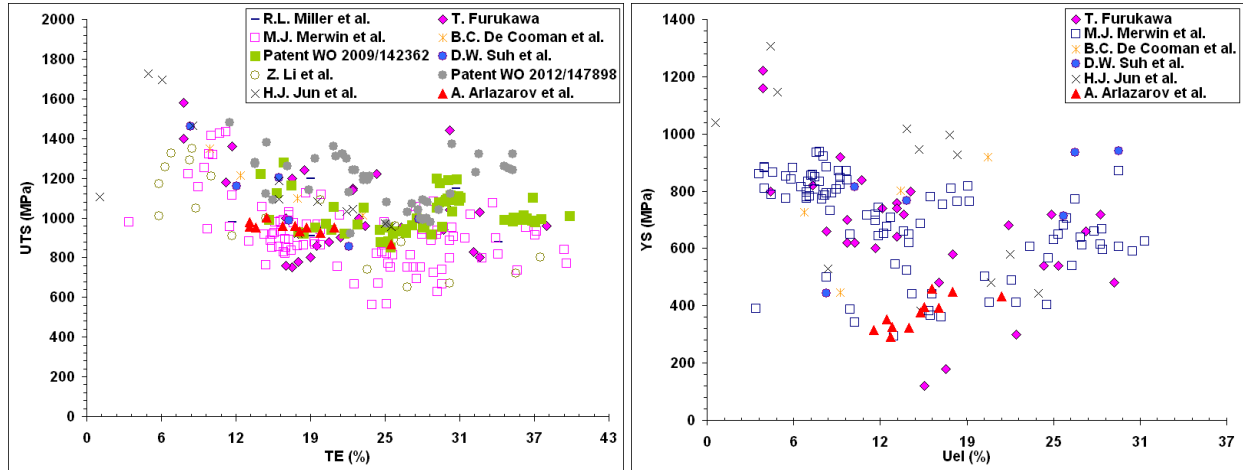
Figure 24 – UTS-TE and YS-Uel (when the data were available) charts using the most relevant data found in the literature and patents.
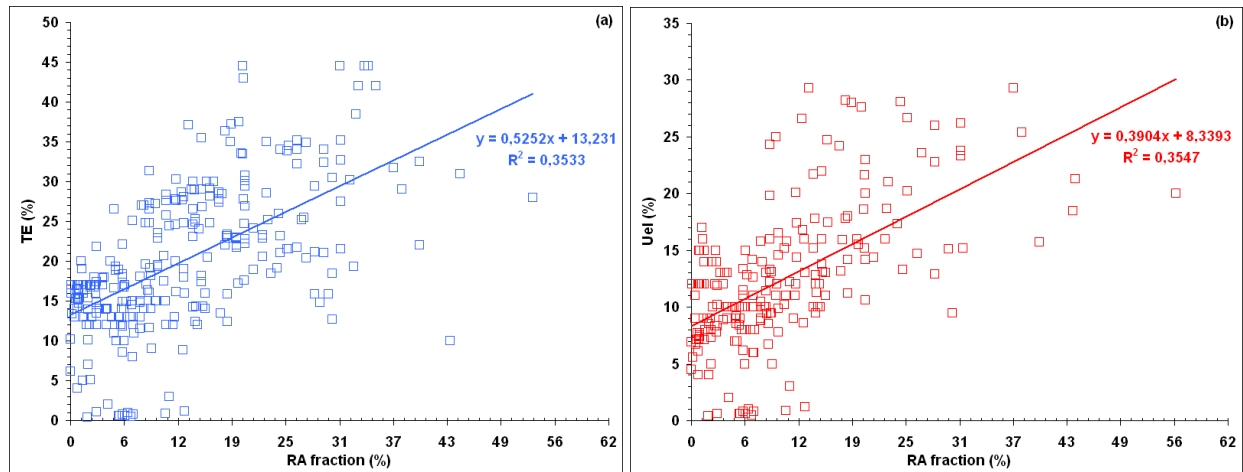
Figure 25 – Influence of retained austenite fraction on: (a) – TE; (b) – Uel; plotted with the available literature data.

Relation between maximum true stress and RA fraction is plotted in Figure 26. It can be observed that there is no correlation between these two parameters. It was then supposed that maximum true stress should depend not directly on the RA, but rather on the global fraction of hard constituents: fresh martensite and RA. Unfortunately, in the majority of the articles only fraction of RA was given. Hence, further investigations of the links between microstructure and mechanical properties were not possible.

At last, it is known that mechanical behavior of a multi-phase material depends on the behavior of each phase under mechanical loading. Taking into account that the studied steels can contain 3 different phases (ultra-fine ferrite, retained austenite and fresh martensite), further text will provide the knowledge about mechanical behavior of each phase. In addition, the information concerning the TRIP effect (induced martensite transformation) will be given. Finally, the possibilities of global modeling of multi-phase steel will be discussed.
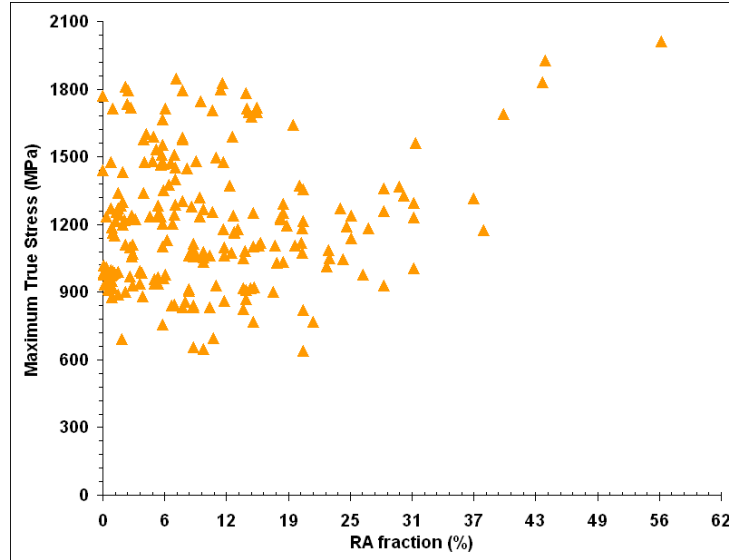
Figure 26 – Relation between ultimate true stress and retained austenite fraction; plotted with the available literature data.

1.3.2 Mechanical behavior of ultra fine ferrite

Classically, the yield and flow stresses in polycrystalline materials can be described using the following Hall-Petch equation:

$$\sigma = \sigma_0 + \frac{k}{\sqrt{D}} \tag{8}$$

where σ is the yield or flow stress, D is the mean grain size and σ_0 and k are constants.

This equation shows a direct relation between the stress and inverse square root of the mean grain size. Physical origin of this relationship is that the grain boundaries are obstacles for dislocation motion. Further, the works about the dislocations movement and storage of Bergström [BER'70], Mecking and Kocks [MEC'81], and Estrin [EST'96] allowed a more sophisticated description of ferrite behavior law and of its dependence on the mean grain size. For example, in the work of Allain and Bouaziz [ALL'08] it was proposed to use the following expression for the evolution of ferrite flow stress (σ_F) as a function of its deformation (ε_F):

$$\sigma_F = \sigma_0 + \frac{\alpha \cdot M \cdot \mu \cdot \sqrt{b}}{\sqrt{D}} \cdot \sqrt{\frac{1 - \exp(-f \cdot M \cdot \varepsilon_F)}{f}} \tag{9}$$

where α is a constant of the order of unity ($\alpha = 0.4$), M is the mean Taylor factor (M= 3), μ is the shear modulus of the ferrite (μ =80GPa), b is the Burgers' vector (b $\approx$ 2.5×10⁻¹⁰ m), D is the ferrite mean grain size, σ_0 is the lattice friction stress which depends on the chemical composition (elements in solid solution) and on the temperature, and *f* is a fitting parameter related to the intensity of dynamic recovery processes, and adjusted on the experimental results.

Both laws (8) and (9) were derived and fitted from data with the average grain size mostly higher than 2 µm. In this range of grain sizes (more than 2 µm) these laws show quite good performance and the predictions are in good agreement with the experimental data. However, when the grain size is ultra low (below 2 or even 1 µm) such approaches appear to be inappropriate. Several works pointed out this point and proposed some new considerations and/or theories [CHO'89], [EMB'94], [BOU'09], [BOU'10]. However, for the moment there is no clear vision in the literature about the strengthening mechanism of the steels with ultra-fine (or nanoscale) grain size. The difficulty also exists in the production of such fine scale structures and measurements of their mechanical properties. Only a few recent works proposed some valuable data [OHM'04], [TSU'08]. An example of stress-strain curves obtained on a given steel with different ferrite grain sizes is shown in Figure 27. Looking on these results, it can be seen that for the grain sizes lower than 1µm the work hardening is close to zero. As well, the strength increase with decreasing grain size appears more pronounced for the ultra-fine structures. But even in these works the obtained ferrite grains co-existed with cementite particles, which can also have an influence on the mechanical behavior. Thus, their presence should be considered carefully.

The important dependence on the grain size of YS, UTS and Uel for the ferritic steels with ultra-fine grains was also shown in the more recent work of Bouaziz [BOU'09] (Figure 28). The variation of YS, UTS and Uel as a function of grain size appears to be almost linear in the domain of grain sizes between 0.1 and 1 µm. This clearly shows that for the ultra-fine ferrite grains, the classical Hall-Petch relation between the stress and inverse square root of the mean grain size is not effective. Therefore, for the ultra-fine grains it seems to be more appropriate to take into account grain size influence on the stress in form of 1/D.
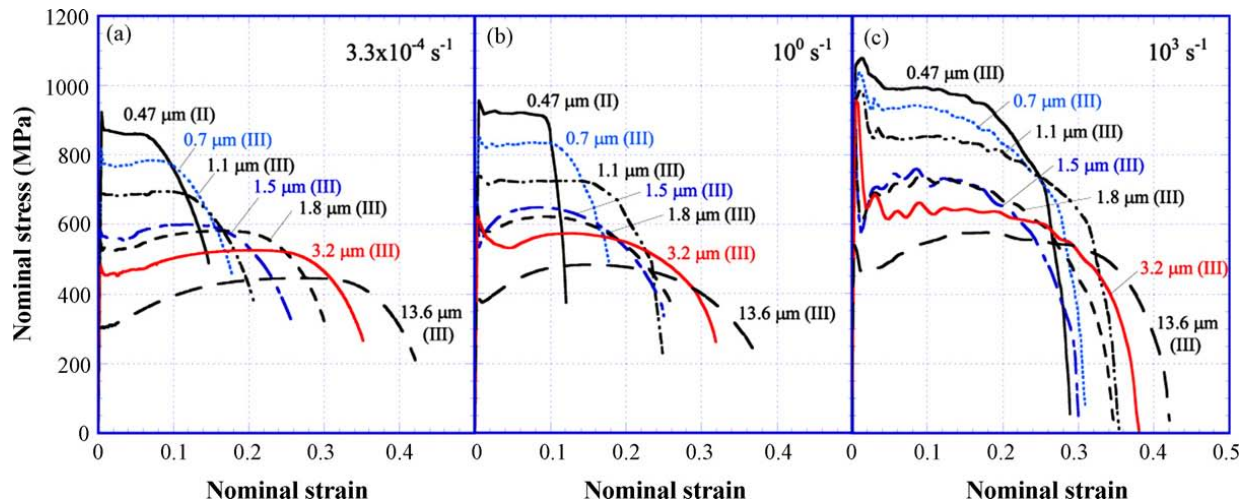
Figure 27 - Nominal stress–nominal strain curves of the ferrite-cementite steels obtained by tensile tests with strain rates of 3.3×10^{-4} s^{-1} (a), 100 s^{-1} (b), and 10^3 s^{-1} (c) at 296K [TSU'08].

Till now, only the behavior of ultra-fine ferrite with polygonal morphology was discussed. Concerning the lath-like ultra fine ferrite structures, the literature is rather poor. Naturally, lath structure of ferrite can be found in tempered martensite and pearlite. In the first case (tempered martensite) the resulting ferrite, depending on the tempering temperature, contains a certain density of dislocations and in the same time some carbides are generally present. Thus, the understanding of mechanical behavior of such mixture is rather complex. In addition, data about stress-strain behavior of tempered martensite are really rare, especially for high tempering temperatures.
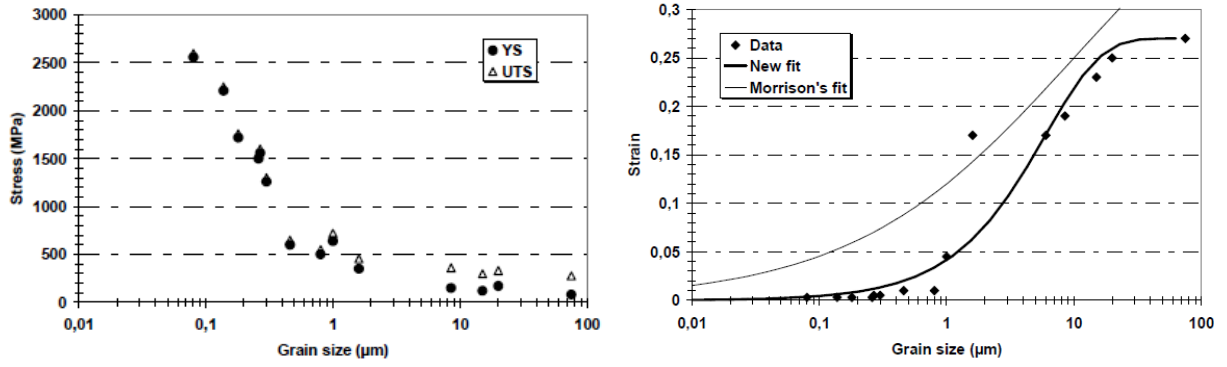
Figure 28 - Variation of the YS, UTS (at left) and Uel (at right) as a function of the grain size for pure iron and IF steels [BOU'09].

In most of the works, only hardness and/or 0.2% offset yield stress are considered. In the case of pearlite, the stress-strain data are more abundant and the ferrite contains much lower number of defects. However, the problem is how to dissociate the separate contribution of ultra-fine lath ferrite and lamellar cementite. It is commonly admitted that mechanical properties of pearlitic steel strongly depends on the interlamellar spacing. Based on experimental results, Bouaziz and Buessler [BOU'02] proposed a semi-empirical behavior law for pearlite. It was assumed that only ferrite in between the cementite lamellae deforms plastically. Thus, the yield stress was considered to be dependent on solid solution hardening and on interlamellar spacing with the form inspired from the Orowan's [ORO'54] theory. Finally, plastic strain hardening was supposed to be isotropic and to follow a Voce type law. Consequently, the general form of the pearlite law was as follows:

$$\sigma_p = \sigma_0 + \frac{\mu \cdot M \cdot b}{\lambda} + \frac{K}{g} \cdot \left(1 - \exp\left(-\frac{g \cdot \varepsilon_p}{2} \right) \right) \tag{10}$$

where λ is the interlamellar spacing, and K and g are fitting parameters adjusted on the experimental tensile curves of fully pearlitic steels with different interlamellar spacing.

1.3.3 Mechanical behavior of fresh martensite

Martensite is one of the hardest phase in the steel and also one of the most complex due to its ultra-fine, acicular and multi-variant structure. Martensite is a metastable phase obtained in the steels during cooling with sufficient rate from austenite to room temperature. As it was already stated, martensitic transformation is athermal and displacive. This means a lot of things. First of all, there is no diffusion of atoms at long distance during transformation. As a result, the produced martensite inherits the composition of prior austenite. Secondary, during transformation the face centered cubic (FCC) lattice structure is changed to the body centered tetragonal (BCT) one and this involves two things: volume change and large shear. Finally, the transformed fraction of martensite depends only on the temperature below M_s and is independent of time. Of course, such complicated transformation produces a very complex structure. According to the study of Krauss and Marder [KRA'71], low M_s twinned martensite is called "plate martensite", whereas high M_s needle-like martensite is called "lath martensite". In this work only lath-martensite is considered. An example of complicated lath-martensite structure taken from Morito et al. [MOR'05] is given in Figure 29.
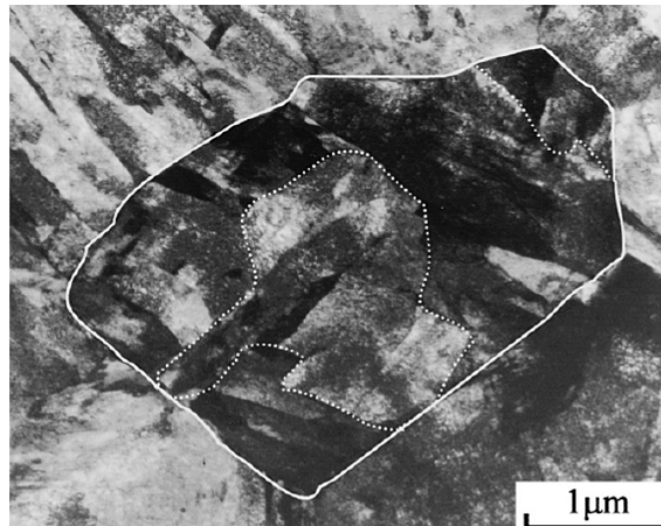
Figure 29 – TEM image of lath martensite in the 0.2C-1.5Mn-0.15V (wt.%) steel formed from fine-grained austenite with a 2.3 µm mean grain size. The plain and dotted white lines show prior austenite grain and packet boundaries, respectively [MOR'05].

It is evident that such complex nano-scale structure will result in specific mechanical behavior. An example of true stress-true strain curves of martensitic steels with different carbon content is given in Figure 30. As it can be seen, very high levels of strength can be obtained, but in counterpart the ductility is rather low. However, ductility can be improved with tempering treatments, which will not be discussed here. Different sources of strengthening are discussed in the literature: grain and substructure (packets, laths), solid solution, precipitation, internal stresses and others. But the most generally acknowledged correlation between a mechanical and a metallurgical parameter is the evolution of martensite hardness related to its carbon content. Such dependence is very well demonstrated in the review of Krauss [KRA'99], where hardness measurements from a number of authors were plotted as a function of martensite carbon content for the variety of carbon concentrations (Figure 31).
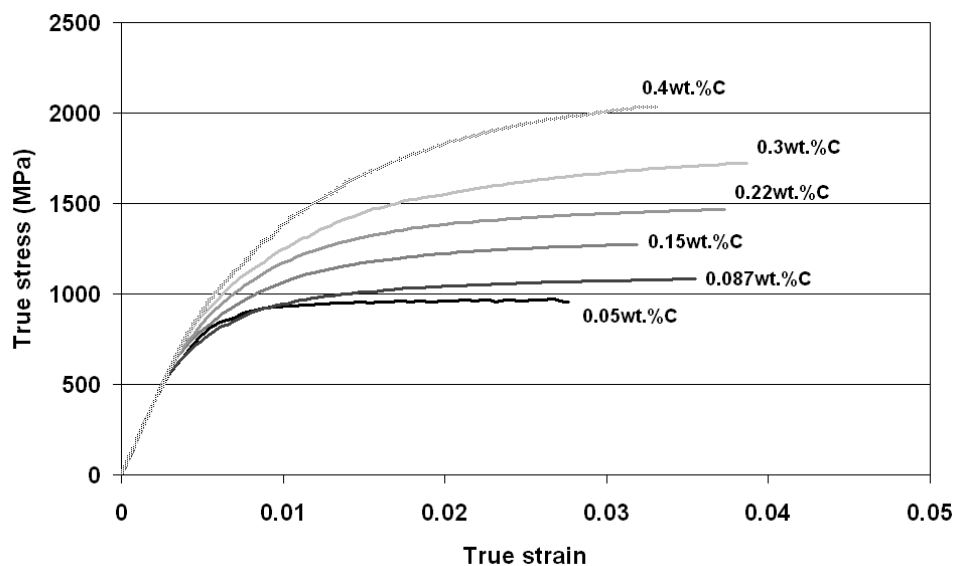
Figure 30 – Normalized true stress – true strain tensile curves of martensitic steels with different carbon contents [ALL'12].

38
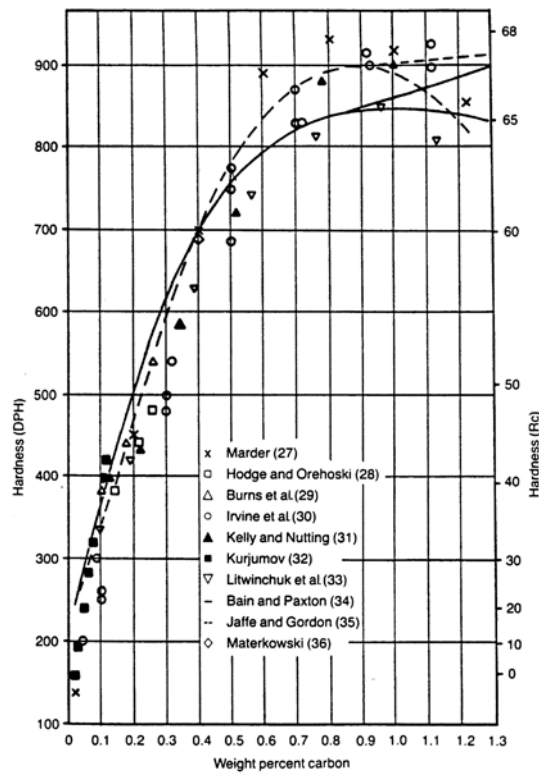
Figure 31 – Hardness of martensitic microstructures in steels as a function of their carbon content [KRA'99].

As well, there is an important quantity of data about the influence of different alloying elements on the martensite hardness [GRA'77], [YUR'87]. Such effect of alloying elements is naturally included in the prediction of yield stress. For example, the effect of Mn on the martensite yield strength was shown in the review of Krauss [KRA'99] by combining the data from the studies of Speich et al. [SPE'68] and Norstrom [NOR'76] (Figure 32). However, very few studies discuss the influence of Mn and other substitution elements on the strength of martensite.
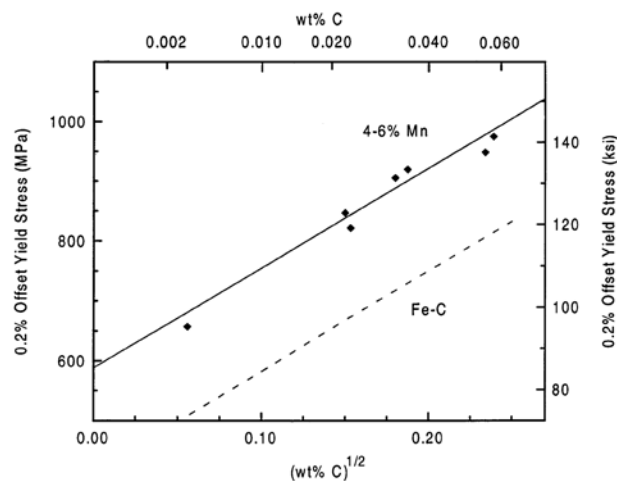
Figure 32 – 0.2% offset yield stress as a function of carbon content for Fe–C [SPE'68] and for Fe–C –Mn alloys [NOR'76].

In addition, there is a lack of data about the influence of substitution elements on the strain hardening of martensitic steels. Only one study concerning the effect of Cr on the work hardening of martensite was found [VAS'74]. Thus, it appears that the Mn effect on the strength and strain hardening of martensitic carbon steels is not clear and needs more studies.

The amount of considerations in the literature about strain-hardening mechanisms of martensitic steels is quite low, probably related to their poor uniform elongation (i.e. necking strain). Principally, the mechanical behavior of martensite is either described with phenomenological polynomial law [CHO'09] or it is reduced to an elastic or an elastic-perfectly plastic law [DEL'07]. However, recently a Continuum Composite Approach (CCA) was proposed to predict the complete tensile curves of as-quenched martensitic steels [ALL'12]. The general idea of this approach is to consider martensite as a composite of elastic-perfectly plastic phases in interaction. All the phases have the same Young modulus, and the density of probability $f(\sigma)$ to find a phase with a given yield strength defines the so-called "stress spectrum". Consequently, the behavior of any martensitic steel can be described using its distinctive stress spectrum. An example of such spectrum $f(\sigma)$ and of its associated cumulated function $F(\sigma)$ are given in Figure 33. The principal equation of the model relates the macroscopic stress Σ to a given macroscopic strain E in the following way:

$$\Sigma = \int_{\sigma_{min}}^{\sigma_L} f(\sigma)\sigma d\sigma + \sigma_L \int_{\sigma_L}^{+\infty} f(\sigma)d\sigma \tag{11}$$

where σ_{min} is the threshold stress at which the softest phases of the composite plasticize and $\sigma_L(E)$ is the highest yield stress among the plasticized phases for a given macroscopic strain E. The first integral is the contribution of already plasticized zones of the composite and the second one is the contribution of the zones that remains elastic under σ_L loading. In majority of the cases, these integrals cannot be solved explicitly. However, it is possible to calculate the derivative as a function of the macroscopic strain (i.e. the macroscopic strain-hardening rate):

$$\frac{d\Sigma}{dE} = \frac{1}{\frac{1}{Y} + \frac{F(\sigma_L)}{\beta}} (1 - F(\sigma_L)) \tag{12}$$

where Y is the young modulus and β is a constant parameter that allows describing the interactions between the zones in the composite after any plasticization:

$$\beta = -\frac{\Sigma - \sigma}{E - \varepsilon} \tag{13}$$

where σ and ε are respectively the local stress and the local strain in each element of the composite.

This model was fitted on the mixed database: mechanical behavior of certain martensitic steels was taken from the literature and others were determined experimentally. The adjustements of the mechanical spectrums was done using the KJMA type law with three fitting parameters: σ_{min}, σ_0 and n. The last two parameters control the shape and the width stress spectrum. Comparison between the results from the model and experimental data is shown in Figure 34. As it can be seen, not only very good agreement between the model and experimental true stress-true strain curves was obtained, but also very good prediction of strain hardening was achieved (Figure 34(b)). As well, the simulation of elastic-plastic transitions was very accurate and exact. Finally, using such sophisticated model permits to describe the tensile behavior of martensite in a univocal way and to explain low microplasticity yield stress, very high strain hardening rate and large Bauschinger effect.

However, as in the previous studies, only the effect of C content on the strength and strain hardening was taken into account (Figure 34(c)).
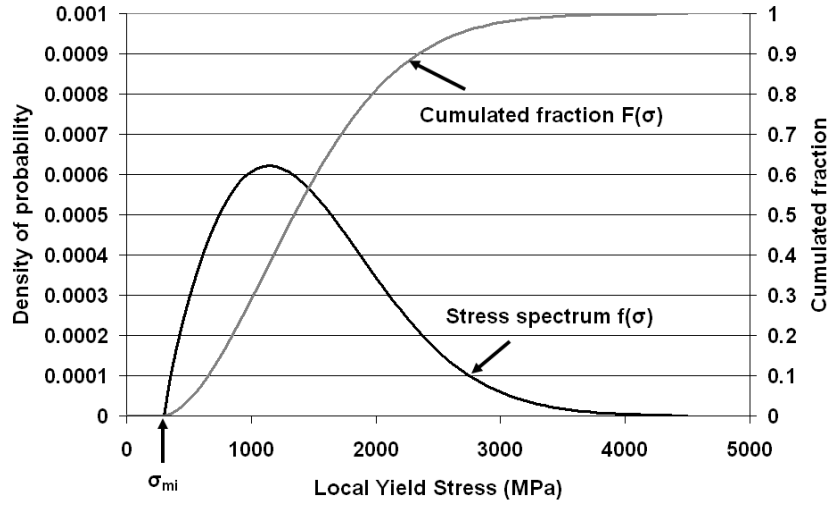
Figure 33 – Typical stress spectrum f(σ) with associated cumulated function F(σ) and the definition of σ$_{min}$ [ALL'12].
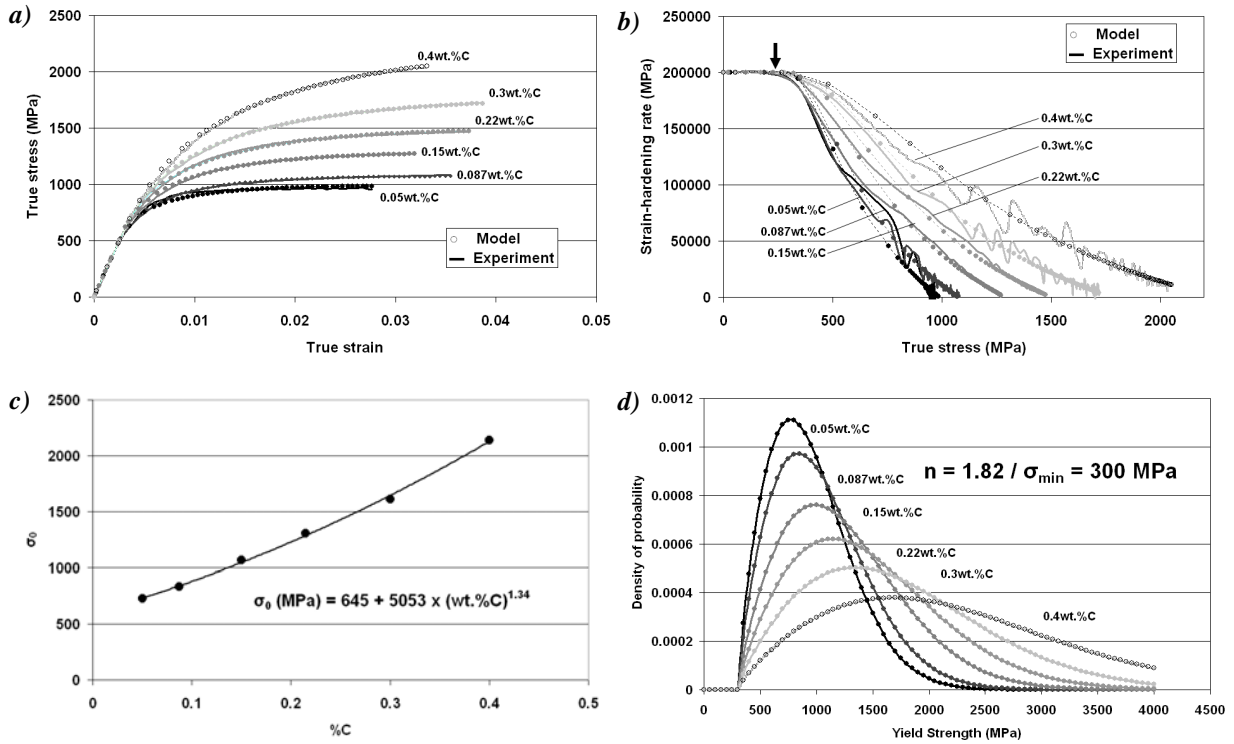
Figure 34 – (a) Comparison between the results of the model and experimental tensile curves of the studied steels; (b) Comparison between the results of the model and experimental evolution of the slopes of the tensile curves as a function of true stress; (c) Evolution of the adjusted σ$_0$ parameters with C content of steels; (d) Adjusted stress spectrums for different martensitic steels [ALL'12].

The present description of martensite structure and mechanical behavior is clearly not exhaustive. Only very rapid overview of the main results was presented here. More information about martensite is available in the books of Kurdjumov [KUR'60], [KUR'77] and Olson and Owen [OLS'92], but also in the review of Krauss [KRA'99] and in the more recent PhD work of Badinier [BAD'13].

1.3.4 Mechanical behavior of retained austenite

Austenite present at room temperature, also called retained austenite (RA), is a metastable phase. Usually, RA is obtained at room temperature due to the chemical enrichment with C and Mn and in some cases due to the ultra fine size of austenite. The stacking fault energy (SFE) of C-Mn steels is low. Consequently, multiple simultaneous and/or sequential deformation mechanisms are possible:

> ➢ dislocation slip;
> ➢ mechanical twinning;
> ➢ transformation to α'- or ε- martensite.

One more time, chemical composition (mostly C and Mn), deformation temperature and in a less extend austenite grain size have major influence on the deformation mechanisms that will govern austenite behavior. According to Schumann's phase stability diagram (left part of Figure 35) [SCH'72], only transformation to α'-martensite occurs till 10 wt.% of Mn. In the same time, from the right part of Figure 35 showing the modified diagram with experimentally determined domain of mechanical twinning (shaded area), it can also be stated that no twinning occurs for the compositions with Mn content lower than 10 wt.% and C lower than 1.2 wt.%. As this work concerns mostly the steels in this composition range, only dislocation slip and transformation to α'- martensite will be considered further as possible deformation mechanisms.
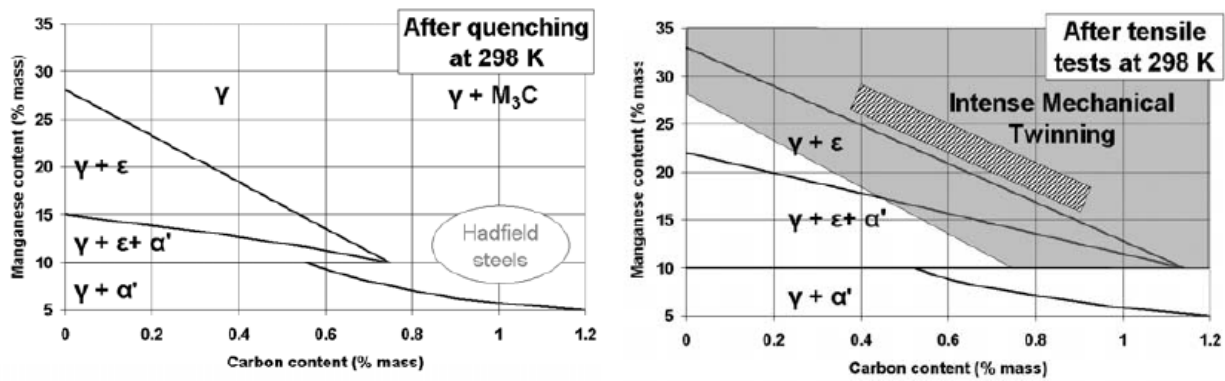
Figure 35 – At left is presented Schumann's Fe-Mn-C phase stability diagram at 298K and at right – modified Schumann's Fe-Mn-C phase stability diagram after tensile tests at 298K [SCO'05].

It is very difficult or even impossible to obtain experimentally the mechanical behavior (with dislocation slip mechanism) of austenite with low C and Mn levels. Firstly, because it is complicated to produce fully austenitic steel with low C-Mn levels at room temperature and, secondly, due to the occurrence of the martensite induced transformation. However, inspired from the works concerning ferrite and highly alloyed austenitic steels, at least two behavior laws of austenite were proposed. Hereafter these two models will be briefly described and compared.

The first one, proposed by Perlade et al. [PER'03], assumes that austenite follows the classical relation for polycrystals between flow stress (σ_A) and the total dislocation density (ρ):

$$\sigma_A = \sigma_{0_A} + \alpha M \mu b \sqrt{\rho} \qquad (14)$$

where α = 0.4 is a constant, M = 3 is the average Taylor factor, m = 72 GPa is the shear modulus, b = 2.5*10^{-10} m is the Burgers vector and σ_{0A} is the friction stress of austenite.

According to [PIC'78], this friction stress can be expressed as:

$$\sigma_{0_A} = 68 + 354 \cdot w_C + 20 \cdot w_{Si} + 3.7 \cdot w_{Cr} \tag{15}$$

where w_C, w_{Si} and w_{Cr} are taken in weight percents.

In this approach it was also considered that induced during deformation martensite, which is much harder, results in a strong hardening of the retained austenite islands. In fact, induced martensite laths will reduce the mean free path of dislocations, thus increasing dislocation density and strengthening of austenite. Finally, taking into account the works of Mecking and Kocks [MEC'81] concerning the dislocation accumulation and annihilation due to the dynamic recovery, it was proposed to consider the evolution of the dislocation density with shear strain for dislocation glide with the following equation:

$$\frac{d\sigma}{M \cdot d\varepsilon} = \frac{1}{b \cdot \Lambda} - f \cdot \rho \tag{16}$$

where Λ is the dislocation mean free path and f is a constant. In this equation, the dislocation storage rate is described by the first term $(1/b\Lambda)$ and dynamic recovery by the second one $(-f\rho)$.

Another behavior law was proposed by Bouaziz et al. [BOU'11]. The modeling approach was quite similar, but it was extended to the TWIP steels, thus permitting an experimental validation. A semi-phenomenological model was proposed to predict the stress–strain behavior of C-Mn TWIP steels as a function of Mn and C content. The flow stress was expressed as:

$$\sigma_A = \sigma_{0_A} + \sigma_{1_A} + \sigma_{2_A} \tag{17}$$

where σ_{0A} is the yield stress of austenite that increases with C content and decreases with Mn content in the following manner:

$$\sigma_{0_A} = 228 + 187 \cdot w_C - 2 \cdot w_{Mn} \tag{18}$$

with w_C and w_{Mn} in weight percents.

The flow stress of austenite without any TWIP effect (σ_{1A}) was taken in the form of well known Voce law:

$$\sigma_{1_A} = K \cdot \left[\frac{1 - \exp(-f \cdot \varepsilon_A)}{f} \right] \tag{19}$$

where K and f are material related constants and ε_A is the strain of the austenite.

Finally, σ_{2A}, which represented the contribution of the dynamic composite effect related to the development of backstresses (i.e. TWIP effects), was expressed as:

$$\sigma_{2_A} = m \cdot \varepsilon^p \tag{20}$$

where m and p are dimensionless material-related parameters.

Using this modeling approach, Bouaziz et al. obtained rather accurate predictions of the true stress-true strain curves of different C-Mn TWIP steels. Comparison between model and experimental true stress-true strain curves is presented in Figure 36. The negative effect of Mn on the yield stress is obvious from this data. For example, Figure 36(b) presents the true stress-true strain curves for two steels with almost the same C level but different Mn contents. It can be seen that higher Mn content steel has lower yield strength.

Comparison between the models proposed by Perlade and Bouaziz led to the following remarks. Bouaziz approach appears to be better for the prediction of the yield stress of austenite in medium and high-Mn steels. For example, for the 1.2C-12Mn steel Bouaziz model gives the YS = 428MPa, which is close to the experimental value (~430MPa). Perlade's model is not so far (YS = 493MPa), but for higher Mn this difference increases significantly. Moreover, Bouaziz model proposes the combined contributions of dislocation slip and twining, which is a clear advantage. However, for our work this is of minor interest because, as it was stated previously, the studied compositions are out of twining domain. Finally, the evident advantage of Perlade's model is the fact that it takes into account the strengthening of austenite due to the martensite induced transformation.
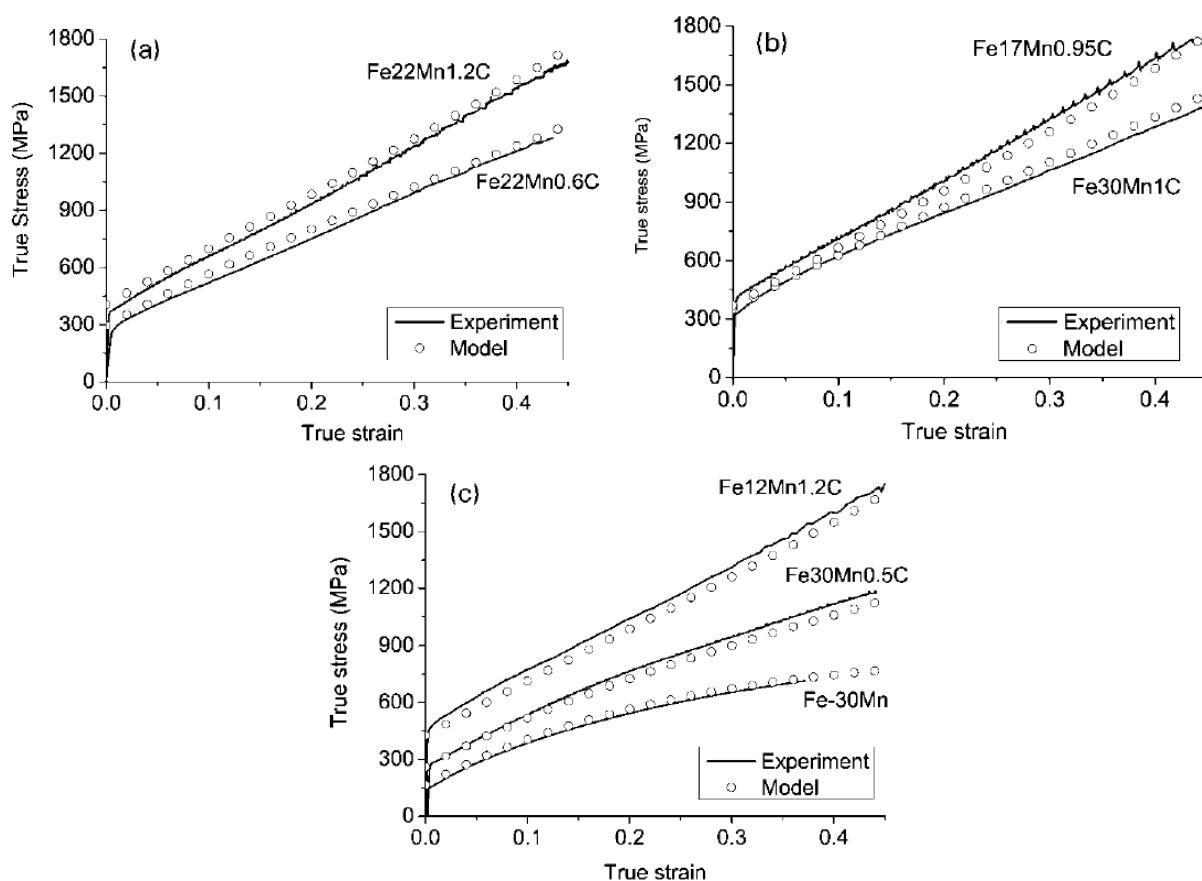
Figure 36 – Comparison between experimental and model predicted true stress-true strain curves [BOU'11].

1.3.5 Mechanical stability of retained austenite and induced transformation

As it was said beforehand, retained austenite is a metastable phase. Consequently, during mechanical loading it will transform to α'- or ε- martensite. Such transformation is very beneficial for the global mechanical behavior of the steel. Indeed, it considerably increases strain hardening rate and delays necking. This phenomenon is called TRansformation Induced Plasticity (TRIP) effect. A lot of works were done on the characterization, understanding and modeling of austenite mechanical stability and TRIP effect in the low Mn steels and alloys [ZAC'67], [GER'70], [BHA'72], [ZAC'74], [OLS'75], [OLS'78], [TAM'82], [RAG'92], [SUG'92], [JAC'01], [JAC'07]. Nowadays using new machines for fine in-situ characterizations like neutron diffraction or high energy synchrotron X-ray diffraction, the studies of TRIP effect continues [TOM'04], [MUR'08], [JUN'10], [BLO'14]. In the same time, the investigations of the huge TRIP effect in the MMS, its understanding and modeling are also multiplying [SHI'10], [CAO'11-1], [WAN'13], [CAI'13], [SUH'13], [GIB'11], [COO'13], [RYU'13]. Of course this topic is of prime interest for us, as it has a direct link with our work. Further, a short summary of the observations found in the literature is given. It is divided in two parts: characterization of austenite stability and TRIP effect in MMS steels and modeling of austenite induced transformation.

1.3.5.1 Austenite stability and TRIP effect in medium Mn steels

Two of the first experimental results concerning the retained austenite evolution under mechanical loading of MMS were published by Shi et al. [SHI'10] and Cao et al. [CAO'11-1]. The evolution of microstructure and mechanical properties as a function of holding time at intercritical temperature was studied for hot forged steels with 0.2 wt.% C and 4.7 wt.% Mn. Figure 37 shows the evolution of retained austenite fraction as a function of strain for 4 different holding times at 650°C and as a function of deformation temperature for 6h holding time. An optimum holding time (in this case 6h) was found where the best TRIP effect can be achieved, meaning the optimum stability of retained austenite. And, as expected, austenite transformation was accelerated at lower deformation temperatures.
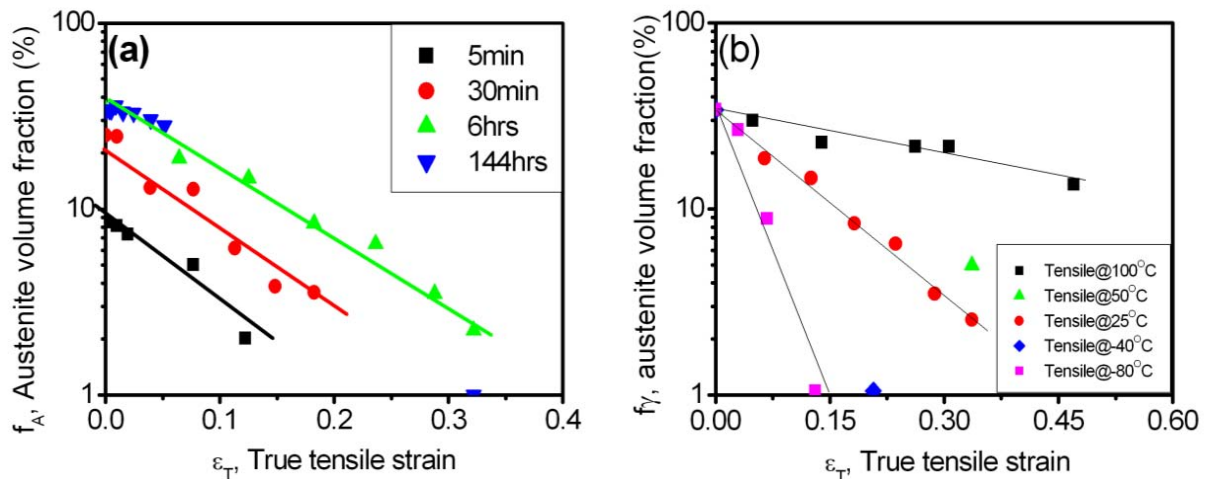
Figure 37 – Retained austenite volume fraction versus true tensile strain: (a) samples with 5min, 30min, 6h and 144h holding time at 650°C and deformed at 25°C; (b) 6h annealed samples deformed at different temperatures: 100°C, 50°C, 25°C, -40°C, -80°C [CAO'11-1].

Microstructure observations of specimens annealed for 6h then deformed were published later by Wang et al. [WAN'13]. It was concluded that retained austenite was transformed in majority of cases to α'- martensite through strain induced transformation, due to the high density of micro-twins and stacking faults in austenite grains. Presence of ε-martensite was also detected, but its fraction was so low that it was considered as negligible.

Suh et al. [SUH'13] studied steels with different C and Mn levels and 2 wt.% Al. These steels were cold rolled and annealed at different intercritical temperatures. Evolution of retained austenite fraction during tensile test was measured. The evolution of normalized fraction versus engineering strain is presented in Figure 38. It can be seen that the rate of strain-induced transformation increases with increasing annealing temperature. In this work, it was also found that there is an optimum annealing temperature in the intercritical domain that can provide optimum stability of retained austenite and consequently best TRIP effect. In particular, for 0.11C-4.5Mn-0.45Si-2.2Al steel this temperature was 720°C, while it was 700°C for 0.055C-5.6Mn-0.49Si-2.1Al steel.
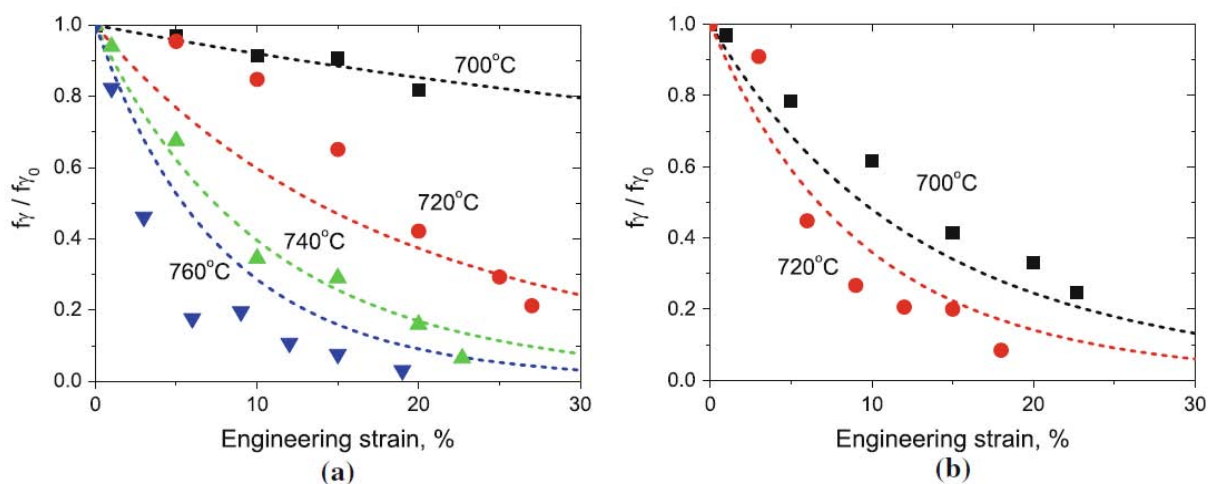
Figure 38 – Normalized austenite fraction as a function of engineering strain for (a) 0.11C-4.5Mn-0.45Si-2.2Al and (b) 0.055C-5.6Mn-0.49Si-2.1Al steels. Symbols are measured values and lines are calculated ones.

Gibbs et al. [GIB'11], [COO'13] performed less statistical, but more rigorous study about the deformation behavior of retained austenite during tensile loading. Cold rolled 0.1C-7.1Mn-0.13Si (wt.%) steel was intercritically annealed at 575, 600, 625 and 650°C for 168h. Then in-situ neutron diffraction experiments were carried out during tensile tests. This permitted to plot the evolution of retained austenite as a function of strain (Figure 39). The observed tendency is the same than in the case of Suh et al. [SUH'13]: the induced transformation rate increases with the increase of holding temperature. However, further analysis of samples annealed at 600°C and 650°C [COO'13] showed two things:
- in the sample with the high austenite stability (600°C), the latter was deformed by the glide of partial dislocations trailing stacking faults. Strain induced transformation of the austenite took place only after the yield point elongation;
- on the other hand, austenite islands of the sample annealed at 650°C contained some stacking faults and thin ε-martensite laths, which promoted the stress induced transformation of austenite at lower stress levels.
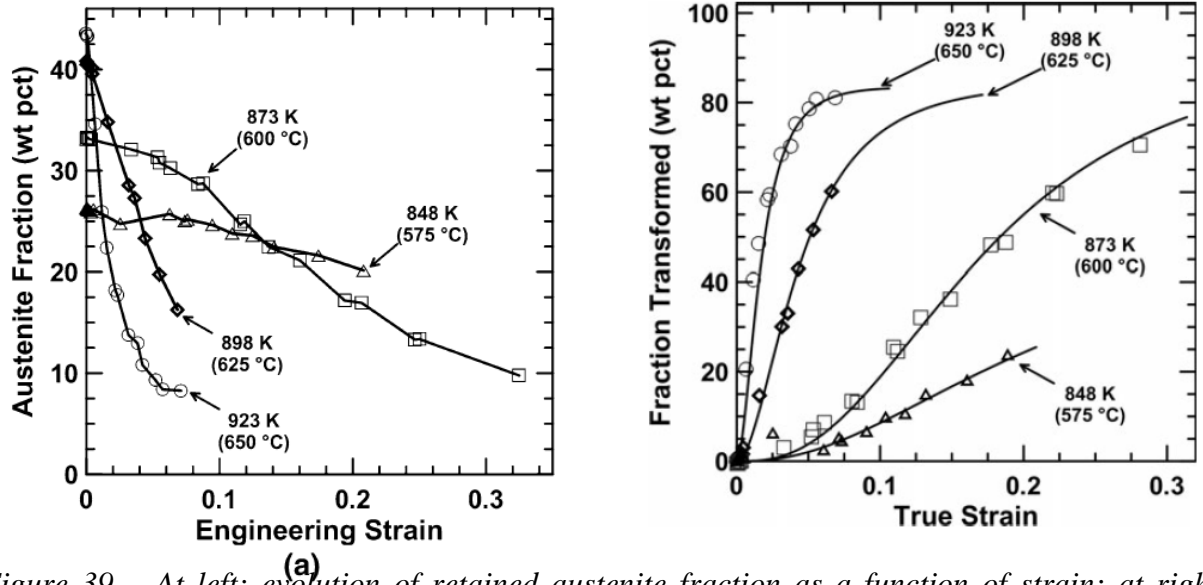
Figure 39 – At left: evolution of retained austenite fraction as a function of strain; at right: evolution of transformed austenite fraction as a function of true strain (points) and fitted Olson-Cohen model (lines) [GIB'11].

1.3.5.2 Models for austenite induced transformation

Generally, for the modeling of the induced austenite transformation a modified Kolmogorov-Johnson-Mehl-Avrami approach [KOL'37], [JOH'39], [AVR'39] is used. One of the most commonly applied formulation of such approach is the equation proposed by Olson and Cohen [OLS'75]:

$$F_{ind}^M = 1 - \exp\left[- \beta \cdot \left(1 - \exp(- \alpha \varepsilon)\right)^n\right] \qquad (21)$$

where n is a constant parameter, α is dependent on the stacking fault energy and defines the rate of shear band formation, and β is related to the probability that a shear band intersection forms a martensite nucleus. This probability depends on the temperature through its link with the chemical driving force.

Another equation proposed even earlier by Guimaraes [GUI'72] for 0.06C-31Ni (wt.%) steel was closer to the standard Kolmogorov equation:

$$F_{ind}^M = 1 - \exp\left(- k \varepsilon_p^z\right) \qquad (22)$$

where k and z are constant fitting parameters and ε_p is the true plastic strain.

Most of the induced transformation models use one of these two equations with adapted fitting parameters. However, some works [ANG'54], [LUD'69], [GER'70] rather proposed a direct power law of the following type:

$$F_{ind}^M = A \cdot \varepsilon^B \cdot F_{RA} \qquad (23)$$

where A and B are fitting parameters and F_{RA} is the volume fraction of retained austenite.

Finally, Perlade et al. [PER'03] proposed a model for the induced martensite transformation based on the Raghavan's physical approach for the isothermal martensite transformation in Fe-

Ni alloys [RAG'92]. Brief description of Raghavan's approach is as follows. Usually, the rate of first-order transformation at a given temperature depends on the nucleation and growth rates of the new phase. In the case of martensite transformation the growth of plates or laths is stopped by the prior austenite grain boundaries or/and by the neighboring units. Hence, in comparison with classical nucleation-and-growth processes (mutual impingement) there are additional obstacles for the growth. The global martensite transformation rate (dF_M/dt) is then controlled by the nucleation rate per unit volume of parent phase at any instant (dN_V/dt) and by the transformed volume fraction per nucleation event (dF_M/dN_V):

$$\frac{d\mathrm{F}_\mathrm{M}}{dt} = \frac{dN_V}{dt} \cdot \frac{d\mathrm{F}_\mathrm{M}}{dN_V} \tag{24}$$

Raghavan also observed that nucleation accelerates very rapidly even at earliest stages, indicating a strong autocatalytic effect. Therefore, he suggested that the number of new nucleation sites generated by autocatalysis is proportional to the volume fraction of formed martensite:

$$n_f = n_i + p \cdot F_M - N_V \tag{25}$$

where n_f is the number of sites at martensite fraction F_M, p is the so-called "autocatalytic factor" and N_V is the number of martensite plates up to F_M.

Based on the work of Pati and Cohen [PAT'69], Raghavan used the following equation for the nucleation rate:

$$\frac{dN}{dt} = \left[n_i + \mathrm{F}_\mathrm{M} \cdot \left(p - \frac{1}{\overline{V}} \right) \right] \cdot \nu \cdot \exp\left(-\frac{\Delta W_a}{kT} \right) \tag{26}$$

where $\overline{V} = \mathrm{F}_\mathrm{M} / N_V$ is the mean plates volume at martensite fraction F_M, ν is a vibration frequency term and ΔW_a is the activation energy for nucleation.

In the model of Perlade et al. [PER'03], it was considered that at the temperatures above M_s the austenite to martensite transformation can take place when the applied stress level is high enough – "stress assisted transformation" (Figure 40(a)). Such transformation can be modeled by incorporating the thermodynamic effect of the applied stress in the theory developed for the transformation upon cooling (Figure 40(b)). When the stress exceeds the yield stress of austenite the martensite nucleation will be strain-induced on potent sites induced by the plastic strain. This domain is characterized by the M_s^σ temperature.

Effect of plastic strain on the nucleation rate was then introduced in the activation energy (ΔW) through the driving force (ΔG) in the following manner:

$$\Delta W_a = A + B \cdot \Delta G \tag{27}$$

where A and B are two positive constants and ΔG is taken as a sum of chemical and mechanical contributions:

$$\Delta G = \Delta G^{\sigma=0} + \frac{\partial \Delta G}{\partial \sigma} \cdot \sigma_\gamma \tag{28}$$
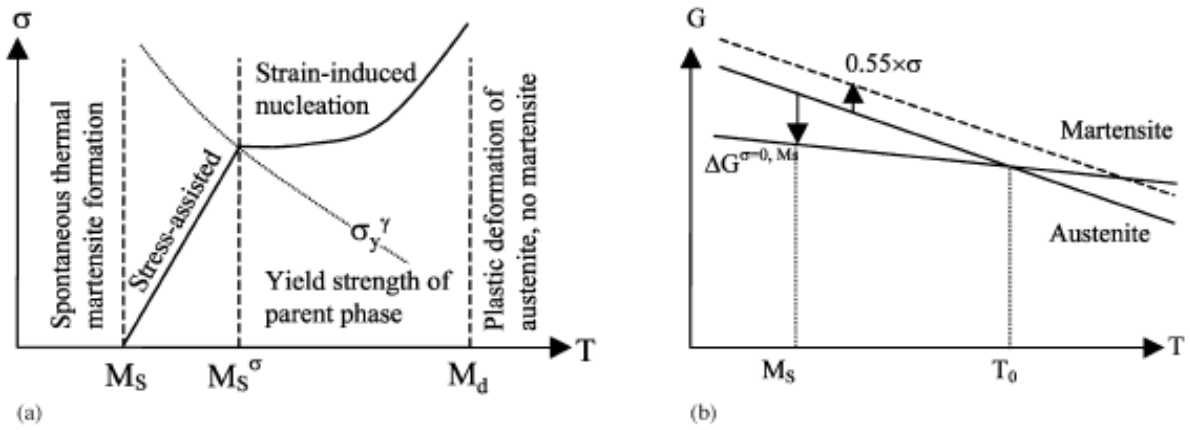
Figure 40 – (a) Evolution of the martensite nucleation stress with temperature, (b) Gibbs free energy curves versus temperature and effect of an applied stress σ [PER'03].

Using such a physically based approach is advantageous as it directly takes into account the effects of chemical composition, austenite size and plastic strain on the induced martensite transformation. As it can be seen in Figure 41, good predictions in comparison with the experimental volume fractions of induced martensite were obtained. However, in the work of Moulin et al. [MOU'02] it was shown that the modeled induced martensite transformation is very sensitive to the grain size of retained austenite (Figure 42). This means that for the majority of cases the retained austenite size should be fitted in order to obtain good description of experimental data.
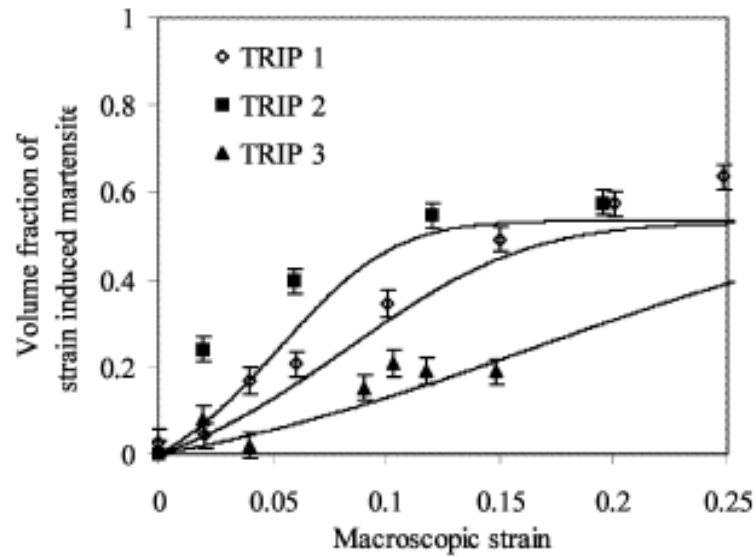
Figure 41 – Volume fraction of strain induced martensite as a function of the macroscopic strain for the different TRIP steels. Symbols are the obtained experimental results and curves are the predictions of the model [PER'03].
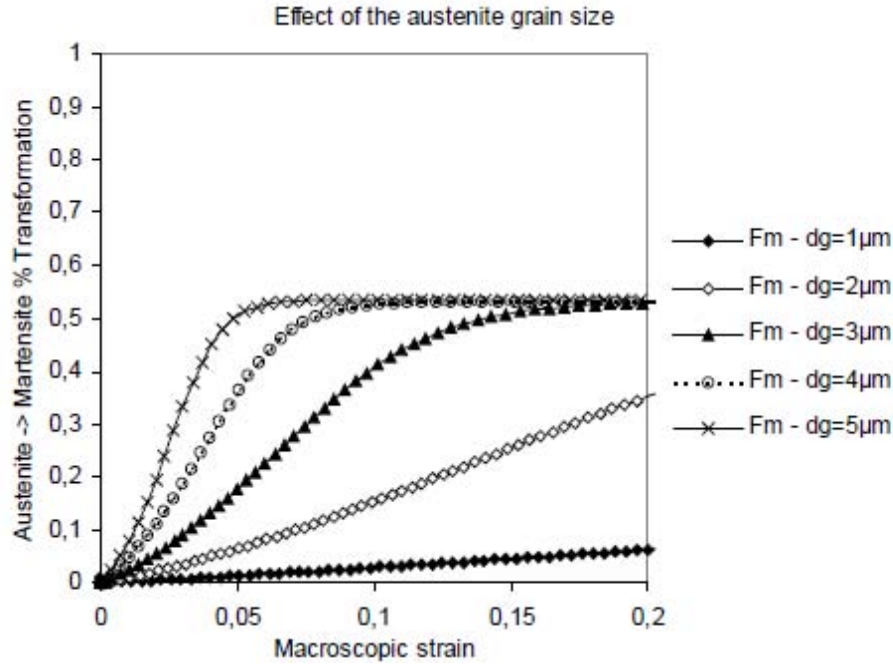
Figure 42 – Influence of the retained austenite size on the martensite induced transformation according to the Perlade's model [MOU'02].

1.3.6 Modeling of the multiphase steel mechanical behavior

For the multiphase structures the stress and strain levels of the global material depends on the stress and strain values of each phase. The behavior laws that consider the behavior of each constituent are so-called "mixture rules". One of the first works that proposed the additivity of the stress and strain tensors for a multicomponent system was the article of Hill [HIL'63]:

$$\overline{\sigma} = f_1 \cdot \overline{\sigma}_1 + f_2 \cdot \overline{\sigma}_2 \tag{29}$$

$$\overline{\varepsilon} = f_1 \cdot \overline{\varepsilon}_1 + f_2 \cdot \overline{\varepsilon}_2 \tag{30}$$

where f_1 and f_2 are the phase volume fractions ($f_1 + f_2 = 1$); σ_i and ε_i are the stress and the strain of each component.

This approach means that there is stress and strain partitioning between the multiple constituents of the system. These two equations were very frequently used separately (with the iso-strain or iso-stress hypothesis) or together [FIS'77], [KAR'75], [TAM'73]. Utilization of both equations is more adapted as it results in less pronounced stress partitioning than the iso-strain model.

Another way to improve the predictions of iso-strain model was proposed by Gladman et al. [GLA'72]. Actually the authors suggested to use a power law for the volume fraction of constituents in the equation (29):

$$\overline{\sigma} = f_1^n \cdot \overline{\sigma}_1 + (1 - f_1^n) \cdot \overline{\sigma}_2 \tag{31}$$

Nevertheless this approach is still less precise than the general modeling with both equations (29) and (30), especially in the case of multicomponent system with more than 2 constituents.

Even though the combined mixture law for stress and strain gives rather good results, its disadvantage is the need of a fitting parameter in order to solve the system of two equations. Actually, equations (29) and (30) do not describe the transfer of stress and strain between phases.

Commonly to take into account this stress and strain transfer, a parameter β, that describes the slope of line AB in Figure 43, is determined in the following way [FIS'77], [GOE'85]:

$$\beta = \frac{\sigma_2 - \sigma_1}{\varepsilon_2 - \varepsilon_1} \tag{32}$$

where β is a fitting parameter that is fixed in the range between 0 and ∞, depending on the studied case.
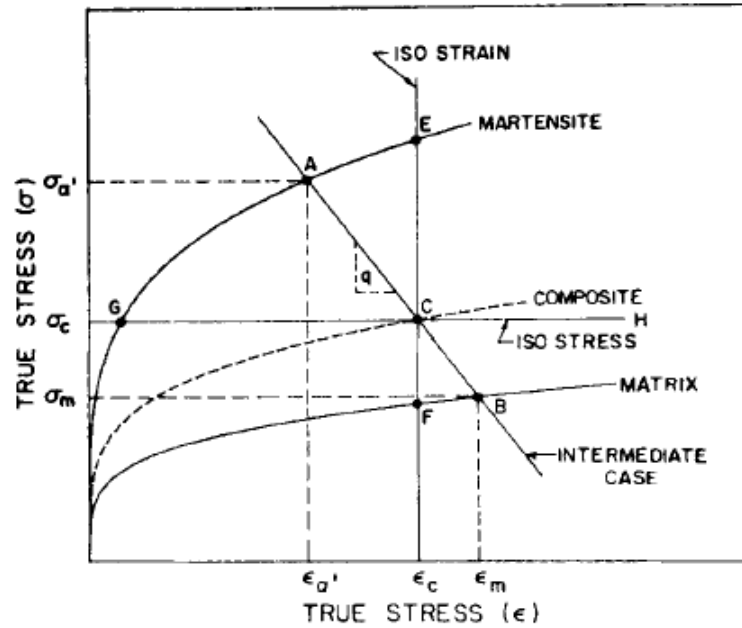
Figure 43 – Schematic representation of the three different conditions of the mixture law (iso-stress, iso-strain, and intermediate one) with the lines EF, GH, and AB, respectively, and the true stress-true strain curves of a soft phase matrix (m), hard phase α'-martensite, and the composite [GOE'85].

In order to avoid this arbitrary fitting parameter, Bouaziz and Buessler [BOU'02] proposed another approach. For a disordered microstructure in whatever material state, mechanical work increment was suggested to be equal in each constituent. As well, the global increment of strain was considered to be the sum of strain increments in each constituent multiplied by their volume fractions. In terms of expressions this means a system of two equations:

$$\sigma_1 d\varepsilon_1 = \sigma_2 d\varepsilon_2 \tag{33}$$
$$d\varepsilon = f_1 d\varepsilon_1 + f_2 d\varepsilon_2 \tag{34}$$

where σ_i and ε_i are the stress and the strain of each constituent and f_i their respective volume fractions.

This approach was called Iso-W and was used further for the modeling of different multiphase materials. It was successfully applied for ferrite-pearlite [BOU'02] and low-Mn (standard) TRIP [PER'03] steels. Furthermore, it was recently utilized by Lee et al. [LEE'13-3] for the modeling of the mechanical behavior of a medium Mn steel containing 0.08 wt.% C, 6.15 wt.% Mn, 1.5 wt.% Si, 2.0 wt.% Al, 0.08 wt.% V and with bimodal grain size distribution.

51

1.3.7 Yield Point Elongation

In addition, one particularity of the mechanical behavior of MMS should be stated. There are a lot of examples where a yield point elongation (YPE) is observed. A yield point elongation phenomenon is a localized, heterogeneous transition from elastic to plastic deformation. An example of stress-strain curve presenting YPE is shown in Figure 44. Generally, YPE elongation occurs in low carbon steels due to the pinning of dislocations by interstitial atoms (typically carbon and nitrogen). In order to liberate the dislocations and make them available for the further motion, an additional energy (stress) is required. This stress corresponds to the Upper Yield Stress (in this work it will be abbreviated as YS_H). After the YS_H the dislocations are free and the needed stress for their motion becomes abruptly lower. This leads to lower macroscopic stress of the specimen: Lower Yield Stress (in this work it will be abbreviated as YS_L). The plastic deformation of material is then localized and heterogeneous. At this moment Lüders band between plastically deformed and undeformed material appears and moves with a constant cross head velocity. During the propagation of the band from one end of the specimen to the other, the nominal stress–strain curve is flat or fluctuates around a constant stress value due to the interaction of moving dislocations with the interstitial atoms. Once the band has gone through the entire specimen, the deformation became homogeneous and a positive strain hardening is observed. There are two major factors affecting Lüders bands formation: microstructure (grain size, ageing state and crystallographic structure) and macroscopic geometry of the sample.
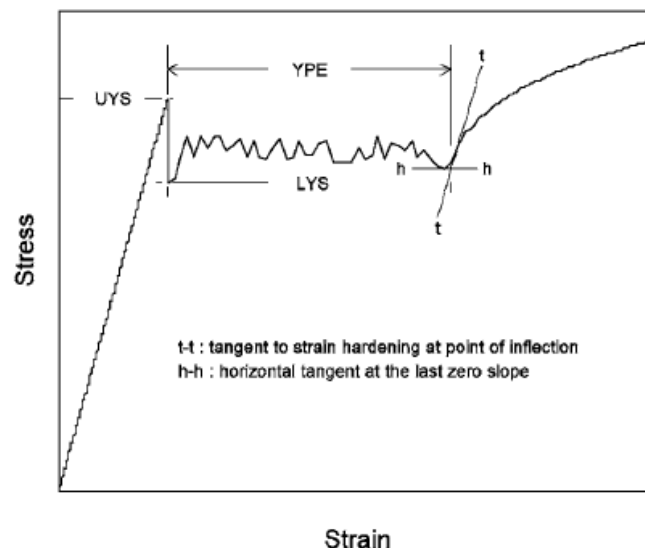
Figure 44 – Stress-strain diagram showing Yield Point Elongation (YPE) and Upper (UYS) and Lower (LYS) Yield Strengths [AST'09].

These stress localization and Lüders band propagation in MMS were studied in details by De Cooman et al. [COO'13] and Gibbs et al. [GIB'14]. The outputs from both works were similar. It was found that yielding behavior of a 7 wt.% Mn steel was controlled by the intercritical annealing temperature, which in its turn has a great influence on the final microstructure and stability of retained austenite. Two possible scenarios were detected and described.
1) Yielding of the duplex ferrite-austenite microstructure, obtained after low temperature intercritical annealing, proceeded through a localized plastic deformation of ferrite (Lüders band nucleation and propagation at a constant stress). In the range of yield point elongation, the retained austenite deformed by the glide of partial dislocations trailing stacking faults and only about 6% from the whole austenite fraction was transformed into martensite. The major part of the strain-induced retained austenite transformation took place after the yield point elongation.

2) On the other hand, complex microstructure consisting of ferrite, α'-martensite, ε-martensite, and a low stability retained austenite, obtained after high temperature intercritical annealing, yielded in another manner. In fact, stress-induced retained austenite transformation was quite rapid, thus providing high work hardening rate and avoiding localized deformation.

These results one more time underline the complexity of mechanical behavior of MMS steels and the importance of their microstructure control, in particular stability of retained austenite.

References

[ALL'08] S. Allain, O. Bouaziz, Microstructure based modeling for the mechanical behavior of ferrite–pearlite steels suitable to capture isotropic and kinematic hardening, Materials Science and Engineering: A, 496, 2008, 329-336.

[ALL'12] S. Allain, O. Bouaziz, M. Takahashi, Toward a New Interpretation of the Mechanical Behaviour of As-quenched Low Alloyed Martensitic Steels, ISIJ International, 52 (4), 2012, 717-722.

[AND'65] K.W. Andrews, Empirical formulae for the calculation of some transformation temperatures, Journal of the Iron and Steel Institute, 203(7), 1965, 721-727.

[ANG'54] T. Angel, Formation of martensite in austenitic stainless steels-effects of deformation, temperature, and composition, Journal of the Iron and Steel Institute, 177(1), 1954, 165.

[ARL'11] A. Arlazarov, M. Gouné, O. Bouaziz, A. Hazotte, F. Kegel, Effect of intercritical annealing time on microstructure and mechanical behavior of advanced medium Mn steels, Proceedings of THERMEC 2011 Conference, Materials Science Forum, 706-709, 2012, 2693-2698.

[ARL'12] A. Arlazarov, M. Gouné, O. Bouaziz, A. Hazotte, G. Petitgand, P. Barges, Evolution of microstructure and mechanical properties of medium Mn steels during double annealing, Materials Science and Engineering A, 542, 2012, 31-39.

[ARN'05] J.O. Arnold, A. McWilliam, The Thermal Transformations of Carbon Steels, Journal of Iron and Steel Institute, 2, 1905, 27-55.

[ASM'95] ASM Handbook, Volume 1, Properties and Selection: Irons, Steels, and High-Performance Alloys, ASM International, 1995.

[AST'09] E28 Committee, Test Methods for Tension Testing of Metallic Materials, ASTM International, 2009.

[AVR'39] M. Avrami, Kinetics of phase change. I General theory. The Journal of Chemical Physics, 7(12), 1939, 1103-1112.

[AYD'13] H. Aydin, E. Essadiqi, I.H. Jung, S. Yue, Development of 3rd generation AHSS with medium Mn content alloying compositions, Materials Science and Engineering A, 564, 2013, 501-508.

[BAD'13] G. Badinier, PhD work, Effect of Carbon Segregation and Carbide Precipitation on the Mechanical Response of Martensite, The University Of British Columbia (Vancouver), 2013.

[BAI'69] E.C. Bain, H.W. Paxton, Alloying Elements in Steel, American Society for Metals, Metals Park, Ohio, 1966.

[BAR'14] D. Barbier, Extension of the Martensite Transformation Temperature Relation to Larger Alloying Elements and Contents, Advanced Engineering Materials, 16, 2014, 122-127.

[BER'70] Y. Bergström, A dislocation model for the stress-strain behaviour of polycrystalline α-Fe with special emphasis on the variation of the densities of mobile and immobile dislocations, Materials Science and Engineering, 5(4), 1970, 193-200.

[BHA'72] D. Bhandarkar, V. F. Zackay, E.R. Parker, Stability and mechanical properties of some metastable austenitic steels, Metallurgical Transactions, 3(10), 1972, 2619-2631.

[BHO'11] N. Bhowmika, S.K. Ghosha, P.P. Chattopadhyaya, A. Haldar, Microstructure evolution and mechanical properties in hot rolled DELTA-TRIP steel, Proceedings of HMnS 2011 Conference, Korea, 2011.

[BLO'14] R. Blondé, E. Jimenez-Melero, L. Zhao, N. Schell, E. Brück, S. van der Zwaag, N.H. van Dijk, The mechanical stability of retained austenite in low-alloyed TRIP steel under shear loading, Materials Science and Engineering A, 594, 2014, 125-134.

[BOH'09] S.M.C. van Bohemen, J. Sietsma, Martensite Formation in Partially and Fully Austenitic Plain Carbon Steels, Metallurgical and Materials Transactions A, 40, 2009, 1059-1068.

[BOH'12] S.M.C. van Bohemen, Bainite and martensite start temperature calculated with exponential carbon dependence, Materials Science and Technology, 28, 2012, 487-495.

[BOU'02] O. Bouaziz, P. Buessler, Mechanical behaviour of multiphase materials: an intermediate mixture law without fitting parameter, Revue de Métallurgie, 99(01), 2002, 71-77.

[BOU'09] O. Bouaziz, The "Ductilities" in Single Phase Steels from Usual to Nano-Scale Microstructures, Materials Science Forum, 633-634, 2009, 205-210.

[BOU'10] O. Bouaziz, Y. Estrin, Y. Bréchet, J.D. Embury, Critical grain size for dislocation storage and consequences for strain hardening of nanocrystalline materials, Scripta Materialia, 63, 2010, 477-479.

[BOU'11] O. Bouaziz, H. Zurob, B. Chehab, J.D. Embury, S. Allain, M. Huang, Effect of chemical composition on work hardening of Fe–Mn–C TWIP steels, Materials Science and Technology, 27(3), 2011, 707-709.

[CAI'85] X.L. Cai, A.J. Garratt-Reed, W.S. Owen, The development of some dual-phase steel structures from different starting microstructures, Metallurgical Transactions A, 16, 1985, 543-557.

[CAI'13] Z.H. Cai, H. Ding, X. Xue, J. Jiang, Q.B. Xin, R.D.K. Misra, Significance of control of austenite stability and three-stage work-hardening behavior of an ultrahigh strength–high ductility combination transformation-induced plasticity steel, Scripta Materialia, 68, 2013, 865-868.

[CAO'11-1] W.Q. Cao, J. Shi, Ch. Wang, C. Wang, L. Xu, M. Wang and H. Dong, Work hardening behavior of ultrafine grained duplex medium-Mn steels annealed by ART, Proceedings of HMnS 2011 Conference, Korea, 2011.

[CAO'11-2] W.Q. Cao, C. Wang, J. Shi, M.Q. Wang, W.J. Hui, H. Dong, Microstructure and mechanical properties of Fe–0.2C–5Mn steel processed by ART-annealing, Materials Science and Engineering A, 528, 2011, 6661-6666.

[CAR'72] R. Caron, G. Krauss, The tempering of Fe-C lath martensite, Metallurgical and Materials Transactions B, 3, 1972, 2381-2389.

[CHO'89] A.H. Chokshi, A. Rosen, J. Karch, H. Gleiter, On the validity of the Hall-Petch relationship in nanocrystalline materials, Scripta Metallurgica, 23, 1989, 1679-1683.

[CHO'09] K.S. Choi, W.N. Liu, X. Sun, M.A. Khaleel, Influence of martensite mechanical properties on failure mode and ductility of dual-phase steels, Metallurgical and Materials Transactions A, 40(4), 2009, 796-809.

[CHR'79] J.W. Christian, Thermodynamics and kinetics of martensite, in: G.B. Olson, M. Cohen (Eds.), International Conference on Martensitic Transformations ICOMAT'79, 1979, 220-234.

[COO'10] B.C. De Cooman, S. Lee, S.S. Kumar, Ultra-fine grained manganese TRIP steels, Proceedings of 2nd International Conference "Super-High Strength Steels", Italy, 2010, 1-11.

[COO'13] B.C. De Cooman, P. Gibbs, S. Lee, D.K. Matlock, Transmission Electron Microscopy Analysis of Yielding in Ultrafine-Grained Medium Mn Transformation-Induced Plasticity Steel, Metallurgical and Materials Transactions A, 44, 2013, 2563-2572.

[DEL'07] M. Delincé, Y. Bréchet, J.D. Embury, M.G.D. Geers, P.J. Jacques, T. Pardoen, Structure–property optimization of ultrafine-grained dual-phase steels using a microstructure-based strain hardening model, Acta materialia, 55(7), 2007, 2337-2350.

[DES'76] C.D. Desforges, W.E. Duckworth, T.F.J.N. Ryan, Manganese in ferrous metallurgy, Page Bros Ltd., Norwich, 1976.

[DON'11] H. Dong, W. Cao, J. Shi, C. Wang, M. Wang, The medium Manganese steels: phenomena and industry potentials, Proceedings of HMnS 2011 Conference, Korea, 2011.

[DRI'04] J. Drillet, P. Barges, V. Robert, Effect of carbon content and island size on mechanical stability of the austenite, Internal Arcelor Research report, 2004.

[ELS'90] I. A. El-Sesy, H.J. Klaar, A.H. Hussein, Effect of intercritical temperature and cold deformation on the kinetics of austenite formation during the intercritical annealing of dual-phase steels, Materials Technology – Steel research 61, 3, 1990, 131-135

[EMB'94] J.D. Embury, J.P. Hirth, On dislocation storage and the mechanical response of fine scale microstructures, Acta Metallurgica et Materialia, 42, 1994, 2051-2056.

[EST'96] Y. Estrin, Dislocation-density-related constitutive modeling, in the book "Unified constitutive laws of plastic deformation", (Eds. AS Krausz and K. Krausz), Academic Press, 1996, 69-106

[FIS'49] J.C. Fisher, J.H. Hollomon, D. Turnbull, Kinetics of the austenite → martensite transformation, Transactions of the American Institute of Mining and Metallurgical Engineers, 185(10), 1949, 691-700.

[FIS'77] H. Fischmeister, B. Karlsson, Plasticity of two-phase materials with a coarse microstructure, Zeitschrift für Metallkunde, 68, 1977, 311.

[FUR'89] T. Furukawa, Dependence of strength-ductility characteristics on thermal history in low carbon 5wt.% Mn steels, Materials Science and Technology, 5, 1989, 465- 470.

[FUR'94] T. Furukawa, H. Huang, O. Matsumura, Effects of carbon content on mechanical properties of 5wt.% Mn steels exhibiting transformation induced plasticity, Materials Science and Technology, 10(11), 1994, 964-969.

[GAR'81] C.I. Garcia, A.J. DeArdo, Formation of Austenite in 1.5 Pct Mn Steels, Metallurgical Transactions A, 12, 1981, 521-530.

[GER'70] W.W. Gerberich, G. Thomas, E.R. Parker, V.F. Zackay, Metastable austenites: decomposition and strength, California University, Berkeley, Lawrence Radiation Laboratory, 1970.

[GIB'11] P.J. Gibbs, E. De Moor, M.J. Merwin, B. Clausen, J.G. Speer, D.K. Matlock, Austenite stability effects on tensile behavior of Manganese-enriched-austenite Transformation-Induced Plasticity Steel, Metallurgical and Materials Transactions A, 42, 2011, 3691-3702.

[GIB'14] P.J. Gibbs, B.C. De Cooman, D.W. Brown, B. Clausen, J.G. Schroth, M.J. Merwin, D.K. Matlock, Strain partitioning in ultra-fine grained medium-manganese transformation induced plasticity steel, Materials Science and Engineering A, 609, 2014, 323-333.

[GLA'72] T. Gladman, I.D. McIvor, F.B. Pickering, Some Aspects of the Structure-Property Relationships in High-C Ferrite-Pearlite Steels, Journal of Iron Steel Institute, 210(12), 1972, 916-930.

[GOE'85] N.C. Goel, S. Sangal, K. Tangri, A theoretical model for the flow behavior of commercial dual-phase steels containing metastable retained austenite: Part I. derivation of flow curve equations, Metallurgical Transactions A, 16, 1985, 2013-2021.

[GRA'68] R.A. Grange, C.R. Hribal, Low-Carbon 6% Manganese Martensitic Steels, Edgar C. Bain Laboratory for Fundamental Research Report No. 1453, USS, November 1968.

[GRA'77] R.A. Grange, C. R. Hribal, L. F. Porter, Hardness of tempered martensite in carbon and low-alloy steels, Metallurgical Transactions A, 8(11), 1977, 1775-1785.

[HAN'11] T.K. Han, H.G. Seong, D.J. Kim, H.J. Kang, Mechanical properties of duplex phase X-AHSS for automotive, Proceedings of HMnS 2011 Conference, Korea, 2011.

[HANA'11] T. Hanamura, S. Torizuka, A. Sunahara, M. Imagumbai, H. Takechi, Excellent total mechanical-properties-balance of 5% Mn, 30000 MPa% Steel, ISIJ International, 51, 2011, 685- 687.

[HIL'63] R. Hill, Elastic properties of reinforced solids: some theoretical principles, Journal of the Mechanics and Physics of Solids, 11, 1963, 357-372.

[HUA'94] H. Huang, O. Matsumura, T. Furukawa, Retained austenite in low carbon, manganese steel after intercritical heat treatment, Materials Science and Technology, 10(7), 1994, 621-626.

[HUM'04] F.J. Humphreys, M. Hatherly, Recrystallization and related annealing phenomena, Second edition, 2004

[JAC'01] P.J. Jacques, F. Delannay, J. Ladrière, On the influence of interactions between phases on the mechanical stability of retained austenite in transformation-induced plasticity multiphase steels, Metallurgical and Materials Transactions A, 32, 2001, 2759-2768.

[JAC'07] P.J. Jacques, Q. Furnémont, F. Lani, T. Pardoen, F. Delannay, Multiscale mechanics of TRIP-assisted multiphase steels: I. Characterization and mechanical testing, Acta Materialia, 55, 2007, 3681-3693.

[JIM'07-1] E. Jimenez-Melero, N. Van Dijk, L. Zhao, J. Sietsma, S. Offerman, J. Wright, S. van der Zwaag, Characterization of individual retained austenite grains and their stability in low-alloyed TRIP steels, Acta Materialia, 55, 2007, 6713-6723.

[JIM'07-2] E. Jimenez-Melero, N. Van Dijk, L. Zhao, J. Sietsma, S. Offerman, J. Wright, S. van der Zwaag, Martensitic transformation of individual grains in low-alloyed TRIP steels, Scripta Materialia, 56, 2007, 421-424.

[JIN'09] Y.H. Jin, K.G. Chin, S.B. Lee, J.H. Kwak, High strength steel sheet and hot dip galvanized steel sheet having high ductility and excellent delayed fracture resistance and method for manufacturing the same, International Patent No.: WO 2009/142362 A1.

[JOH'39] W.A. Johnson, R.F. Mehl, Reaction kinetics in processes of nucleation and growth, Transactions of AIME, 135(8), 1939, 396-415.

[JUN'10] J. Jung, H. Kim, B.C. De Cooman, Yielding behavior of Nb micro-alloyed C-Mn-Si TRIP steel studied by In-situ synchrotron X-ray diffraction, ISIJ International, 50, 2010, 620-629.

[JUN'11] H.J. Jun, O. Yakubovsky, N. Fonstein, On Stability of Retained Austenite in Medium Mn TRIP Steels, Proceedings of HMnS 2011 Conference, Korea, 2011.

[KAR'75] B. Karlsson, G. Linden, Plastic deformation of ferrite-pearlite structures in steel, Materials Science and Engineering, 17, 1975, 209-219.

[KAW'12] Y. Kawasaki, H. Hasegawa, S. Kaneko, Y. Nagataki, High-strength steel plate with excellent formability and stability of material properties, and method for manufacturing same, International Patent No.: WO 2012/147898 A1.

[KIM'81] N.J. Kim, G. Thomas, Effects of morphology on the mechanical behavior of a dual phase Fe/2Si/0.1 C steel, Metallurgical Transactions A, 12, 1981, 483-489.

[KIM'05] D.E. Kim, Y.K. Park, O.Y. Lee, K.G. Jin, S.J. Kim, Formation of retained austenite and mechanical properties of 4~8%Mn hot rolled TRIP steels, Korean Journal of Materials Research, 15(2), 2005, 115-120.

[KIN'74] S. Kinoshita, T. Ueda, Some observations on formation of austenite grains, Transactions ISIJ, 14(6), 1974, 411-418.

[KOB'84] T. Kobayashi, W. Yagi, T. Kazino, Y. Ueda, Effect of heat treatment on toughness of high manganese cast steel, The Iron and Steel Institute of Japan (ISIJ), 70, 1984, 861-868.

[KOI'59] D.P. Koistinen, R.E. Marburger, A general equation prescribing the extent of the austenite-martensite transformation in pure iron-carbon alloys and plain carbon steels, Acta Metallurgica, 7, 1959, 59-60.

[KOL'37] А.Н. Колмогоров, К статистической теории кристаллизации металлов. Известия Российской академии наук. Серия математическая, 1(3), 1937, 355-359 (A.N. Kolmogorov, Toward Statistical Theory of Metal Crystallization, News of Russian Science Academy, Mathematical Volume, 1(3), 1937, 355-359).

[KOO'76] J.Y. Koo, G. Thomas, Thermal cycling treatments and microstructures for improved properties of Fe-0.12% C-0.5% Mn steels, Materials Science and Engineering, 24, 1976, 187-198.

[KOO'77] J.Y. Koo, G. Thomas, Design of duplex Fe/X/0.1C steels for improved mechanical properties, Metallurgical Transactions, A, 8, 1977, 525-528.

[KRA'62] G. Krauss, M. Cohen, Strengthening and annealing of austenite formed by the reverse martensitic transformation, TMS-AIME, 224, 1962, 1212-1221.

[KRA'63] G. Krauss, Fine structure of austenite produced by the reverse martensitic transformation, Acta Metallurgica, 11, 1963, 499-509.

[KRA'71] G. Krauss, A. Marder, The morphology of martensite in iron alloys, Metallurgical and Materials Transactions B, 2 (9), 1971, 2343-2357.

[KRA'99] G. Krauss, Martensite in steel: strength and structure, Materials Science and Engineering A, 1999, 273, 40-57.

[KUR'60] Г.В. Курдюмов, Явления закалки и отпуска стали, Металлургиздат, 1960 (G.V. Kurdjumov, Quench and Tempering Phenomena in Steel, Metallurgizdat, 1960).

[KUR'77] Г.В. Курдюмов, Л.М. Утевский, Р.И. Энтин, Превращения в железе и стали, Наука, 1977 (G.V. Kurdjumov, L.M. Utevskiy, R.I. Entin, Phase Transformations in Iron and Steel, Science, 1977).

[LAW'80] N.C. Law, D.V. Edmonds, The Formation of Austenite in a Low-Alloy Steel, Metallurgical Transactions A, 11, 1980, 33-46.

[LEE'13-1] S.J. Lee, S. Lee, B.C. De Cooman, Martensite transformation of sub-micron retained austenite in ultra-fine grained manganese transformation-induced plasticity steel, International Journal of Materials Research, 104(5), 2013, 423-429.

[LEE'13-2] S. Lee, B.C. Cooman, On the Selection of the Optimal Intercritical Annealing Temperature for Medium Mn TRIP Steel, Metallurgical and Materials Transactions A, 44, 2013, 5018-5024.

[LEE'13-3] S. Lee, Y. Estrin, B.C. De Cooman, Constitutive Modeling of the Mechanical Properties of V-added Medium Manganese TRIP Steel, Metallurgical and Materials Transactions A, 44, 2013, 3136-3146.

[LI'11] Z. Li, A. Zhao, D. Tang, G. Zhu, Cold-Rolled Low-Carbon Medium-Manganese TRIP Steels, Proceedings of HMnS 2011 Conference, Korea, 2011.

[LUD'69] D.C. Ludwigson, J.A. Berger, Plastic behaviour of metastable austenitic stainless steels, Journal of the Iron and Steel Institute, 207(1), 1969, 63-69.

[LUO'11] H. Luo, J. Shi, C. Wang, W. Cao, X. Sun, H. Dong, Experimental and numerical analysis on formation of stable austenite during the intercritical annealing of 5Mn steel, Acta Materialia, 59, 2011, 4002-4014.

[LUO'13] H.W. Luo, C.H. Qiu, H. Dong, J. Shi, Experimental and numerical analysis of influence of carbide on austenitisation kinetics in 5Mn TRIP steel, Materials Science and Technology, 30(11), 2013, 1367-1377.

[MAA'71] H. Maartensson, The effect of the transformation substructure on the mechanical properties of a low-carbon manganese martensitic steel, Metallurgical and Materials Transactions B, 2, 1971, 3490-3492.

[MAN'56] Manganese Steel, Printed by Robert Cunningham and Sons Ltd. for Olivier and Boyd Ltd., 1956.

[MAT'74-1] S. Matsuda, Y. Okamura, Microstructural and Kinetic Studies of Reverse Transformation in a Low-C Low-Alloy Steel, Transactions ISIJ, 14(5), 1974, 363-368.

[MAT'74-2] S. Matsuda, Y. Okamura, The Later Stage of Reverse Transformation in Low-C Low-Alloy Steel, Transactions ISIJ, 14(6), 1974, 444-449.

[MAT'84] N. Matsumura, M. Tokizane, Microstructure and Mechanical Properties of Dual-phase Steel Produced by Intercritical Annealing of Lath Martensite, ISIJ, 70, 1984, 246-253.

[MEC'81] H. Mecking, U. F. Kocks, Kinetics of flow and strain-hardening, Acta Metallurgica, 29(11), 1981, 1865-1875.

[MER'06] M.J. Merwin, Method for producing high strength, high ductility steel strip, US Patent No.: US 2006/0162824A1.

[MER'07] M.J. Merwin, Microstructure and Properties of Cold Rolled and Annealed Low-Carbon Manganese TRIP Steels, Proceedings of AIST Steel Properties & Applications Conference, Detroit, 2007, 67-84.

[MIL'70] R.L. Miller, R.A. Grange, Mechanical Properties of Ultrafine-Grained Ferrite-Austenite Mixtures in Fe-6Mn-0.1C Steel, Edgar C. Bain Laboratory for Fundamental Research Report No. 1546, USS, 1970.

[MIL'72] R.L. Miller, Ultrafine-grained microstructures and mechanical properties of Alloy Steels, Metallurgical Transactions, 3, 1972, 905-912.

[MOO'11] E.D. Moor, J.G. Speer, D.K. Matlock, J.H. Kwak, S.B. Lee, Effect of Carbon and Manganese on the Quenching and Partitioning response of CMnSi steels, ISIJ International, 51, 2011, 137-144.

[MOR'05] S. Morito, H. Saito, T. Ogawa, T. Furuhara, T. Maki, Effect of austenite grain size on the morphology and crystallography of lath martensite in low carbon steels, ISIJ International, 45 (1), 2005, 91-94.

[MOU'02] A. Moulin, A. Perlade, O. Bouaziz, Study of some microstructure-properties relationships in TRIP steels, Internal ArcelorMittal report ref. 20083, 2002.

[MOU'03] A. Moulin, A. Blazejewski, Y. Robert, M. Gouné, Elaboration of a TRIP steel after continuous annealing of a martensitic microstructure: evidence of inheritance effects, Internal Arcelor Research report, 2003.

[MUR'08] O. Muránsky, P. Šittner, J. Zrnik, E.C. Oliver, The Structure Dependence of Deformation Behavior of Transformation-Induced Plasticity–Assisted Steel Monitoring by In-Situ Neutron Diffraction, Metallurgical and Materials Transactions A, 39, 2008, 3097-3104.

[NAK'85] A.H. Nakagawa, G. Thomas, Microstructure-mechanical property relationships of dual-phase steel wire, Metallurgical Transactions A, 16, 1985, 831-840.

[NAK'13] N. Nakada, K. Mizutani, T. Tsuchiyama, S. Takaki, Difference in transformation behavior between ferrite and austenite formations in medium manganese steel, Acta Materialia, 65, 2014, 251-258.

[NAT'05] M. Natori, Y. Futamura, T. Tsuchiyama, S. Takaki, Difference in recrystallization behavior between lath martensite and deformed ferrite in ultralow carbon steel, Scripta Materialia, 53, 2005, 603-608.

[NEH'50] A.E. Nehrenberg, The Growth of Austenite as Related to Prior Structure, Transactions AIME, 188, 1950, 162-174.

[NOR'76] L. Norstrom, Yield Strength of Quenched Low-C Lath Martensite, Scandinavian Journal of Metallurgy, 5(4), 1976, 159-165.

[OHM'04] A. Ohmori, S. Torizuka, K. Nagai, Strain-hardening due to Dispersed Cementite for Low Carbon Ultrafine-grained Steels, ISIJ International, 44 (6), 2004, 1063-1071.

[OLS'75] G.B. Olson, M. Cohen, Kinetics of strain-induced martensitic nucleation, Metallurgical transactions A, 6(4), 1975, 791-795.

[OLS'78] G.B. Olson, M. Azrin, Transformation behavior of TRIP steels, Metallurgical Transactions A, 9, 1978, 713-721.

[OLS'92] G. B. Olson, W. S. Owen, Martensite, A tribute to Morris Cohen, ASM International, 1992

[ORO'54] E. Orowan, Dislocations and mechanical properties, chapter 3 of the book "Dislocations in metals", Ed. M. Cohen, AIME, 1954, 69-195.

[PAT'69] S.R. Pati, M. Cohen, Nucleation of the isothermal martensitic transformation, Acta Metallurgica, 17(3), 1969, 189-199.

[PER'03] A. Perlade, O. Bouaziz, Q. Furnémont, A physically based model for TRIP-aided carbon steels behaviour, Materials Science and Engineering A, 356, 2003, 145-152.

[PIC'78] F.B. Pickering, Physical metallurgy and the design of steels, London: Applied Science Publishers, 63, 1978.

[PLI'74] M.R. Plichta, H.I. Arronson, Influence of alloying elements upon morphology of austenite formed from martensite in Fe-C-X alloys, Metallurgical Transactions, 5, 1974, 2611-2613

[PUS'84] N. Pussegoda, W.R. Tyson, P. Wycliffe, G.R. Purdy, Segregation of manganese during intercritical annealing of dual phase steels, Metallurgical and Materials Transactions A, 15, 1984, 1499-1502.

[RAG'92] V. Raghavan, Kinetics of martensitic transformations, ASM International, Martensite (USA), 1992, 197-225.

[ROB'43] G.A. Roberts, R.F. Mehl, The mechanism and the rate of formation of austenite from ferrite-cementite aggregates, Transactions of the ASM, 31, 1943, 613-650.

[RYU'13] J.H. Ryu, J.I. Kim, H.S. Kim, C.S. Oh, H.K.D.H. Bhadeshia, D.W. Suh, Austenite stability and heterogeneous deformation in fine-grained transformation-induced plasticity-assisted steel, Scripta Materialia, 68, 2013, 933-936.

[SAN'10] M.J. Santofimia, T. Nguyen-Minh, L. Zhao, R. Petrov, I. Sabirov, J. Sietsma, New low carbon Q&P steels containing film-like intercritical ferrite, Materials Science and Engineering A, 527, 2010, 6429-6439.

[SCH'72] V.H. Schumann, Martensitische Umwandlung in austenitischen Mangan-Kohlenstoff-Stählen, Neue Hütte, 17(10), 1972, 605-609.

[SCO'06] C. Scott, S. Allain, M. Faral, N. Guelton, The development of a new Fe-Mn-C austenitic steel for automotive applications, Revue de Métallurgie, 103, 2006, 293-302.

[SHI'10] J. Shi, X. Sun, M. Wang, W. Hui, H. Dong, W. Cao, Enhanced work-hardening behavior and mechanical properties in ultrafine-grained steels with large-fractioned metastable austenite, Sripta Materialia, 63, 2010, 815-818.

[SPE'68] G.R. Speich, H. Warlimont, Yield strength and transformation substructure of low-carbon martensite, Journal of the Iron and Steel Institute, 206, 1968, 385-392.

[SPE'69] G.R. Speich, Tempering of low-carbon martensite, Transactions of the Metallurgical Society AIME, 245(12), 1969, 2553-2564.

[SPE'72] G.R. Speich, W.C. Leslie, Tempering of steel, Metallurgical Transactions, 3(5), 1972, 1043-1054.

[SPE'81] G.R. Speich, V.A. Demarest, R.L. Miller, Formation of austenite during intercritical annealing of dual-phase steels. Metallurgical Transactions A, 12A, 1981, 1419-1428.

[STE'56] W. Steven, A.G. Haynes, The temperature of formation of martensite and bainite in low-alloy steels, Journal of the Iron and Steel Institute, 183(8), 1956, 349-359.

[SUG'92] K.I. Sugimoto, M. Kobayashi, S.I. Hashimoto, Ductility and strain-induced transformation in a high-strength transformation-induced plasticity-aided dual-phase steel, Metallurgical Transactions A, 23, 1992, 3085-3091.

[SUG'02-1] K.I. Sugimoto, R. Kikuchi, S.I. Hashimoto, Development of high strength low alloy TRIP-aided steels with annealed martensite matrix, Steel research, 73(6-7), 2002, 253-258.

[SUG'02-2] K.I. Sugimoto, A. Kanda, R. Kikuchi, S.I. Hashimoto, T. Kashima, S. Ikeda, Ductility and formability of newly developed high strength low alloy TRIP-aided sheet steels with annealed martensite matrix. ISIJ International, 42(8), 2002, 910-915.

[SUG'05] K.I. Sugimoto, B. Yu, Y.I. Mukai, S. Ikeda, Microstructure and formability of aluminum bearing TRIP-aided steels with annealed martensite matrix, ISIJ International, 45(8), 2005, 1194-1200.

[SUH'09] D.W. Suh, S.J. Park, T.H. Lee, C.S. Oh, S.J. Kim, Influence of Al on the microstructural evolution and mechanical behavior of low-carbon, manganese Transformation-Induced-Plasticity Steel, Metallurgical and Materials Transactions A, 41, 2009, 397-408.

[SUH'13] D.W. Suh, J.H. Ryu, M.S. Joo, H.S. Yang, K. Lee, H.K.D.H. Bhadeshia, Medium-Alloy Manganese-Rich Transformation-Induced Plasticity Steels, Metallurgical and Materials Transactions A, 44, 2013, 286-293.

[TAK'92] S. Takaki, S. Iizuka, K. Tomimura, Y. Tokunaga, Influence of Cold Working on Recovery and Recrystallization of Lath Martensite in 0.2%C Steel, Materials Transactions, JIM, 33(6), 1992, 577-584.

[TAM'73] I. Tamura, Y. Tomota, H. Ozawa, Strength and ductility of Fe-Ni-C alloys composed of austenite and martensite with various strength, Proceedings of 3rd International Conference "Strength of Metals and Alloys", Institute of Metal and Iron, London, 1973, 611-615.

[TAM'82] I. Tamura, Deformation-induced martensitic transformation and transformation-induced plasticity in steels, Metal Science, 16, 1982, 245-253.

[TAU'13] V. Taupin, R. Pesci, S. Berbenni, S. Berveiller, R. Ouahab, O. Bouaziz, Lattice strain measurements using synchrotron diffraction to calibrate a micromechanical modeling in a ferrite–cementite steel, Materials Science and Engineering: A, 561, 2013, 67-77.

[TOK'82] M. Tokizane, N. Matsumura, K. Tsuzaki, T. Maki, I. Tamura, Recrystallization and Formation of Austenite in Deformed Lath Martensitic Structure of Low Carbon Steels, Metallurgical Transactions A, 13, 1982, 1379-1388.

[TOM'04] Y. Tomota, H. Tokuda, Y. Adachi, M. Wakita, N. Minakawa, A. Moriai, Y. Morii, Tensile behavior of TRIP-aided multi-phase steels studied by in situ neutron diffraction, Acta Materialia, 52, 2004, 5737-5745.

[TSU'01] T. Tsuchiyama, Y. Miyamoto, S. Takaki, Recrystallization of Lath Martensite with Bulge Nucleation and Growth Mechanism, ISIJ International, 41(9), 2001, 1047–1052.

[TSU'08] N. Tsuchida, H. Masuda, Y. Harada, K. Fukaura, Y. Tomota, K. Nagai, Effect of ferrite grain size on tensile deformation behavior of a ferrite-cementite low carbon steel, Materials Science and Engineering: A, 488, 2008, 446-452.

[TSU'10] T. Tsuchiyama, M. Natori, N. Nakada, S. Takaki, Conditions for Grain Boundary Bulging during Tempering of Lath Martensite in Ultra-low Carbon Steel, ISIJ International, 50, 2010, 771-773.

[VAS'74] A.G. Vasil'eva, D.A. Prokoshkin, V.V. Goryushin, Effect of chromium on strain hardening of martensite, Metal Science and Heat Treatment, 16(6), 1974, 507-510.

[WAN'01] J. Wang, S. Van Der Zwaag, Stabilization mechanisms of retained austenite in transformation-induced plasticity steel, Metallurgical and Materials Transactions A, 32, 2001, 1527-1539.

[WAN'11] C. Wang, J. Shi, Y.W. CUN, W.J. Hui, M.Q. Wang, H. Dong, W.Q. Cao, Development of ultrafine lamellar ferrite and austenite duplex structure in 0.2C 5Mn steel during ART-annealing, ISIJ International, 51(4), 2011, 651-656.

[WAN'13] C. Wang, W. Cao, J. Shi, C. Huang, H. Dong, Deformation microstructures and strengthening mechanisms of an ultrafine grained duplex medium-Mn steel, Materials Science and Engineering A, 562, 2013, 89-95.

[WEI'13] R. Wei, M. Enomoto, R. Hadian, H.S. Zurob, G.R. Purdy, Growth of austenite from as-quenched martensite during intercritical annealing in an Fe–0.1C–3Mn–1.5Si alloy, Acta Materialia, 61, 2013, 697-707.

[WEL'48] C. Wells, Metals Handbook, American Society for Metals, Metals Park, Ohio, 1948.

[XU'12] H.F. Xu, J. Zhao, W.Q. Cao, J. Shi, C.Y. Wang, C. Wang, J. Li, H. Dong, Heat treatment effects on the microstructure and mechanical properties of a medium manganese steel (0.2C–5Mn), Materials Science and Engineering A, 532, 2012, 435-442.

[YAN'09] H. Yang, H. Bhadeshia, Austenite grain size and the martensite-start temperature, Scripta Materialia, 60, 2009, 493-495.

[YI'85] J.J. Yi, I.S. Kim, H.S. Choi, Austenitization during intercritical annealing of an Fe-C-Si-Mn dual-phase steel, Metallurgical Transactions A, 16, 1985, 1237-1245.

[YUR'87] N. Yurioka, M. Okumura, T. Kasuya, H.J.U. Cotton, Prediction of HAZ hardness of transformable steels, Metal Construction, 19(4), 1987, 217.

[ZAC'67] V.F. Zackay, E.R. Parker, D. Fahr, R. Busch, The enhancement of ductility in high-strength steels, ASM Trans Quart, 60(2), 1967, 252-259.

[ZAC'74] V.F. Zackay, E.R. Parker, J.W. Morris, G. Thomas, The application of materials science to the design of engineering alloys. A Review, Materials Science and Engineering, 16(3), 1974, 201-221.

CHAPTER 2: METHODS AND SELECTION OF MATERIALS AND TREATMENTS

In the first part of this chapter a brief description of machines, techniques and methods used in this work will be given. The second part will present the results of a primary study that aims the selection of steel composition and adapted heat treatment. This part can be called "alloy design".

2.1 Machines, techniques and methods

In this section are presented the tools and methods used for the elaboration of samples and their characterization. In majority of the cases, the following strategy was adopted for the experiments and analysis:
1. heat treatments;
2. tensile tests;
3. microstructure observation and quantification;
4. fine characterization;
5. model simulations.

Therefore, the presentation of different tools in this section will follow this plan.

2.1.1 Heat treatments

Different heat treatments, aiming production of samples for different analyses, were performed with one dilatometer and two furnaces:
1) Dilatometer Bähr DIL 805 was used for the study of cementite precipitation during heating and characterization of phase transformations;
2) AET Gradient Batch Annealing furnace that produces a gradient of temperature on one sheet sample was used for the rapid evaluation of mechanical properties as a function of holding temperature;
3) NABERTHERM furnace that allows simple homogeneous heat treatments was used as a major tool for the elaboration of big size samples (tensile tests and microstructure analysis).

The main characteristics of these three tools are presented hereafter.

Dilatometer Bähr DIL 805

Dilatometry is most often used to characterize the phase transformations (transition points and kinetics) in steels. In this work, a Bähr DIL 805 dilatometer was used to follow the cementite precipitation during heating and to study the phase transformations (austenite, ferrite and martensite) during annealing.

A picture of Bähr DIL 805 dilatometer and a schematic representation of the experimental cell are presented in Figure 45. The dilatometer follows the length variations of the sample occurring during the imposed heat treatment. The sample is heated and maintained at temperature by a high-frequency induction coil. Temperature control is done by one or several thermocouples. Usually, Pt-Rt/Rh 10% (type S) thermocouples are used. The sample is maintained by the quartz rods and one of them is mobile. Hence, when the length variations occur, one rod is moving and the linear displacement is captured by an LVDT (Linear Variable Differential Transformer) sensor.
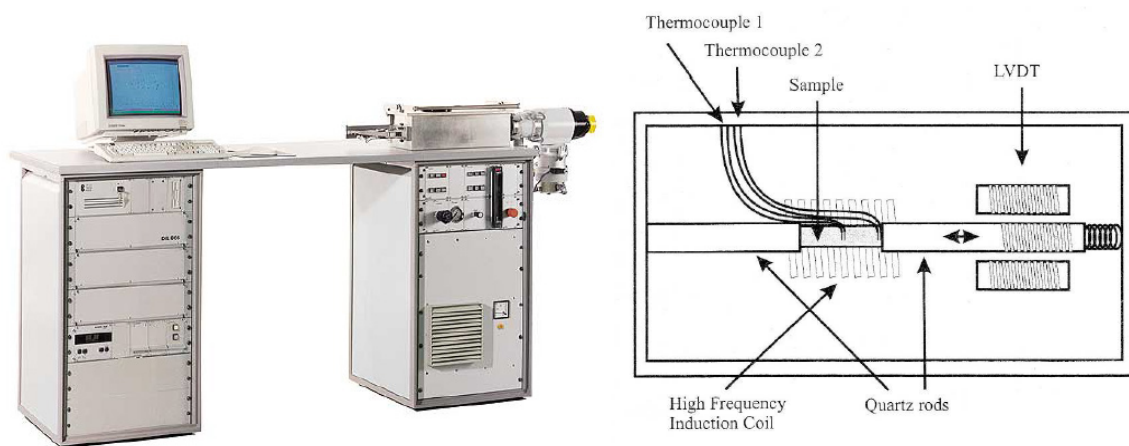
Figure 45 – Global view on Bähr DIL 805 dilatometer (at left) and schematic representation of the experimental cell (at right).

To avoid oxidation during treatment vacuum is done in the experimental chamber, then a small amount of helium (He) is injected. Cooling rate can be controlled and high cooling rates can be obtained using He gas injection. Three types of samples were used:

- Ø4 mm × 10 mm cylindrical rod – hot rolled steel;
- 4 mm × 4 mm × 10 mm parallelepiped – hot rolled steel;
- 1.2 mm × 4 mm × 10 mm parallelepiped – cold rolled steel.

AET Gradient Batch Annealing furnace

The AET batch annealing (BA) furnace is presented in Figure 46. It consists of 4 zones that can be controlled independently in terms of heating and holding. This allows producing a gradient of temperature on one sheet sample. Therefore, this furnace is named Gradient Batch Annealing (GBA) furnace. The precise control of the temperatures in the different zones is assured by 12 thermocouples located in different axial and transversal positions. A linear temperature gradient between 400°C and 800°C can be obtained on a sample with the length of 700 mm. It can be supposed that each 15 mm segment of the annealed sheet has a constant global mean temperature. Thus, for each temperature segment it is possible to prepare two so-called mini tensile samples, which will be described later in the text. Usually, the heating rate is quite low and it takes hours (in between 10 and 40h) to reach the target temperature, which is comparable with industrial batch annealing process. Fast cooling is not possible, only natural cooling or controlled slow cooling can be produced. Annealing is performed under vacuum in the entire furnace chamber in order to avoid oxidation and decarburization during treatment.

NABERTHERM furnace

The NABERTHERM furnace is shown in Figure 47. This is a 700 × 500 × 250 mm isolated chamber, which temperature is regulated by resistance heating. The furnace is first heated and stabilized at the target temperature. Maximum holding temperature is 1280°C. Then, Argon or Nitrogen gas is introduced in the chamber in order to protect the sample from the possible oxidation and decarburization. Next, the sample is put in the deep part of the chamber, which is characterized by more homogeneous temperature, and held for a desired time. The heating rate depends on the sample thickness and geometry, and it cannot be controlled or varied in-situ. However, for the same sample thickness and geometry, the heating rate will be the same or quite similar. Finally, after holding for a certain time, the sample is cooled down with three possible ways: water quench, oil quench or air cooling. As it was said previously, in the deep part of the chamber the sample has a completely homogeneous temperature (less than 5°C difference between different points of the sample).

Figure 46 – AET Gradient Batch Annealing (GBA) furnace.

Figure 47 – NABERTHERM furnace.

2.1.2 Tensile tests

After thermal treatments using gradient batch annealing furnace, small tensile specimens were prepared with gauge length 20 mm and section 5×1 mm^2 (Figure 48). Specimens were cut along the transverse direction of the steel sheet. For each temperature two tensile tests were done at room temperature with a constant strain rate of 0.13 s^{-1}.
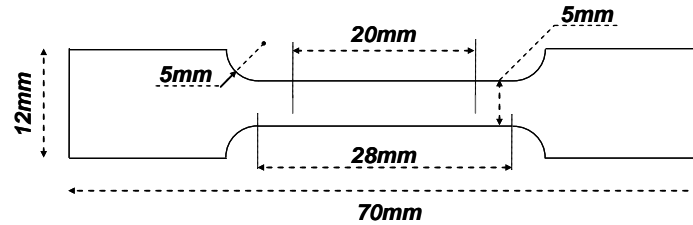
Figure 48 – Scheme of the small (so-called "mini") specimens used for tensile tests after gradient batch annealing.

In the case of heat treatments with Nabertherm furnace, two specimens with gauge length 50 mm and section 12.5×1 mm^2 (ASTM E8 geometry, Figure 49) were machined and tensile tests were performed at room temperature with a constant strain rate of 0.008 s^{-1}. Specimens were cut along the longitudinal direction of the steel sheet.
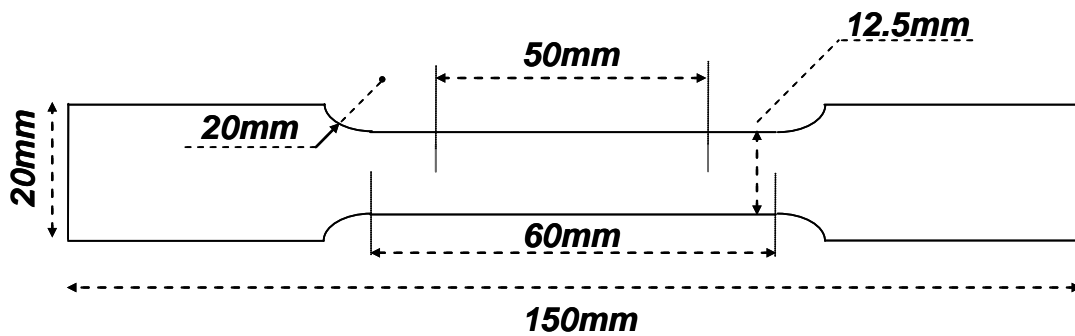
Figure 49 – Scheme of the so-called ISO 12.5x50 specimens used for tensile test after annealing in the Nabertherm furnace.

Tensile tests were realized on a Zwick 1474 machine with macroXtens SE50 extensometer (*Figure 50*). This machine has a capacity of 50 kN. The cross head rate can be varied between 0.0005 and 600 mm/min with the precision of 0.002 % of the used value. The acquisition frequency in the system is 500 Hz. The electronic device for the force measurement corresponds to the type I, according to the ISO 7500/1 standard:
- rank 0 in the range from 200 N to 50000 N;
- rank 1 in the range lower than 200 N.

The displacement was measured using a macroXtens SE50 extensometer, which is a high resolution extensometer (Figure 51). According to standard EN ISO 9513, this extensometer has a precision rank of 0.5. The maximal error in the measurements of cross head displacement between two points in the range between 20 and 200 µm is ±1µm.

Figure 50 – Zwick 1474 machine.

Figure 51 – MacroXtens SE50 extensometer: at left – global view; at right – zoom on the part which is in contact with tensile specimen.

2.1.3 Quantification of retained austenite

Two methods were used to quantify the volume fraction of retained austenite: X-Ray Diffraction (XRD) and saturation magnetization measurements (Sigmametry). The results from both techniques were compared and discussed. Finally, the most pertinent ones were retained for the global microstructure analysis in this work. Further, both techniques will be briefly presented and the comparison of results will be discussed.

X-Ray Diffraction (XRD)

X-ray diffraction is a powerful tool for the analysis of crystalline phase structures. This technique is widely used for the characterization of different phases in steels. In particular, austenite fraction and carbon content can be evaluated using X-ray diffraction patterns. Diffraction phenomenon in crystals is effective because the wavelength λ of X-rays is typically of the same order of magnitude (1–100 angstroms) as the spacing between the crystal planes.

In this work, steel samples of 15×15 mm^2 were mechanically grinded to their quarter thickness and polished down to 1 µm to obtain a mirror surface. Then, the X-ray diffraction measurements were done using a Siemens D5000 diffractometer with a cobalt tube, under 30 kV and 30 mA (Co K$_\alpha$ radiation with $\lambda = 1.8$ Å). The scans were done in the configuration θ-2θ. In order to avoid texture effect, the angle variations were the following: 2θ from 55° to 129° with 0.026° step, ψ from 0° to 60° with a step of 5° and φ from 0° to 360° in continuous rotation. Siemens D5000 diffractometer and scheme of goniometric configuration are shown in Figure 52.
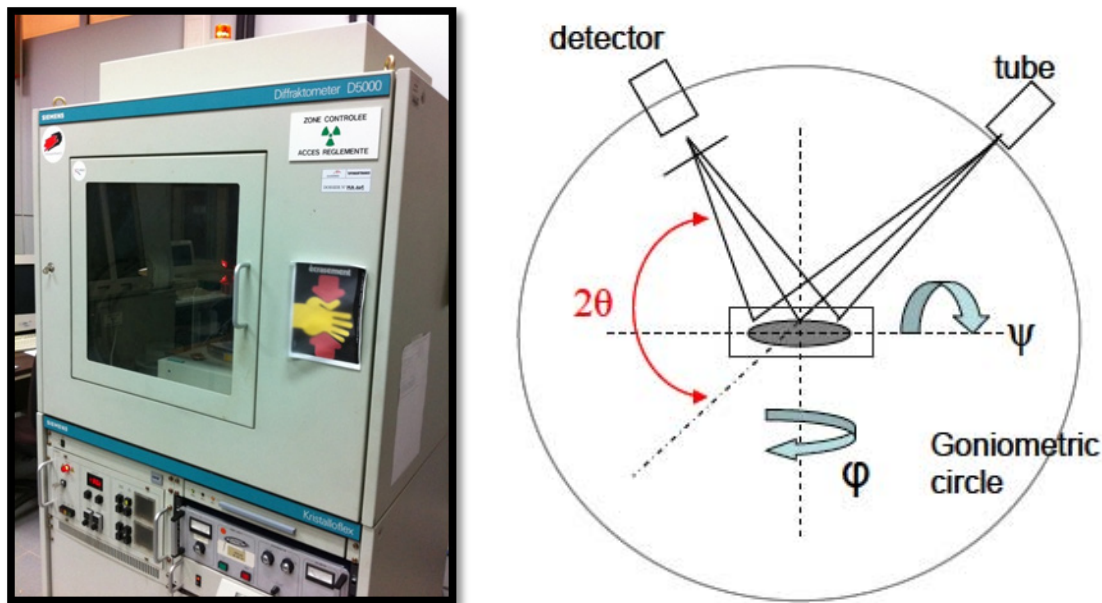
Figure 52 – Siemens D5000 diffractometer (at left) and scheme of goniometric circle with tube, detector and sample positions and the rotation angles 2θ, ψ and φ.

The retained austenite fraction was calculated using the integrated intensities of $(220)_\alpha$, $(211)_\alpha$, $(200)_\alpha$ and $(200)_\gamma$, $(220)_\gamma$, $(311)_\gamma$ reflections. An example of XRD spectra with identified α and γ peaks is shown in Figure 53. It was obtained for the sample annealed at 650°C for 1h and water quenched.
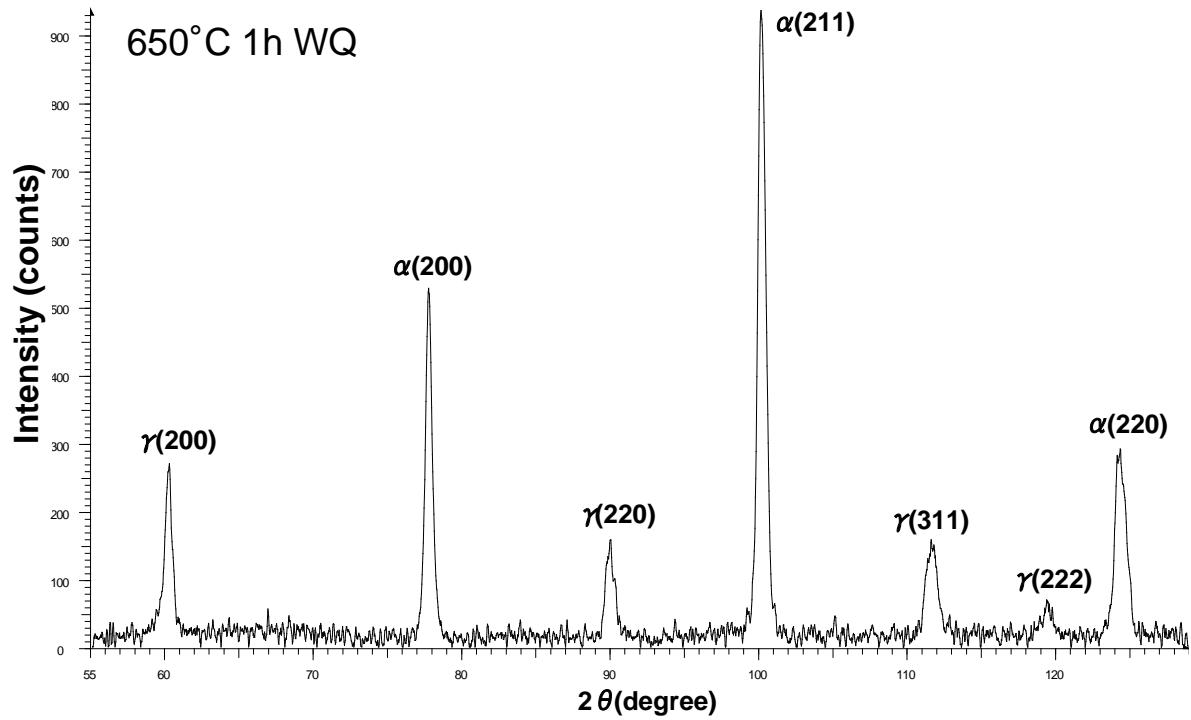
Figure 53 – XRD spectra of the sample annealed at 650°C for 1h and water quenched.

The Averbach-Cohen [AVE'48] method was used to calculate the volume fraction of retained austenite, through the following equation:

$$\frac{f_\gamma}{f_\alpha} = \frac{I_\gamma^{hkl}}{I_\alpha^{hkl}} \cdot \frac{R_\alpha^{hkl}}{R_\gamma^{hkl}} \tag{35}$$

$$f_\gamma = \frac{1}{1 + \dfrac{R_\gamma^{hkl}}{R_\alpha^{hkl}} \cdot \dfrac{I_\alpha^{hkl}}{I_\gamma^{hkl}}} \tag{36}$$

where f_γ and f_α are the volume fractions of austenite and ferrite, I_α^{hkl} and I_γ^{hkl} are the average integrated intensities of $(220)_\alpha$, $(211)_\alpha$, $(200)_\alpha$ and $(200)_\gamma$, $(220)_\gamma$, $(311)_\gamma$ diffraction peaks and R_α^{hkl} and R_γ^{hkl} are constant parameters related to the α and γ phases and studied hkl plans.

R_α^{hkl} and R_γ^{hkl} parameters were determined internally using a reference sample with known retained austenite volume fraction. The average integrated intensities of $(220)_\alpha$, $(211)_\alpha$, $(200)_\alpha$ and $(200)_\gamma$, $(220)_\gamma$, $(311)_\gamma$ diffraction peaks are measured from the obtained XRD spectra. Then, 9 ratios between the average integrated intensities of the 3 peaks of austenite and the 3 peaks of ferrite are calculated. Next, using the ratio $R_\gamma^{hkl} / R_\alpha^{hkl}$ obtained on the reference sample, 9 values of austenite fraction are determined. Finally, the average over these 9 values is considered to be the volume fraction of retained austenite in the sample.

Saturation magnetization measurements

There are two major disadvantages of XRD measurements:
- the depth of analysis is only about 10-20 microns, just below the prepared sample surface;
- the sample preparation is time consuming and mechanical grinding can affect the stability of retained austenite.

Therefore, the amount of retained austenite was also evaluated using magnetic saturation measurements (Sigmametry). The advantages of this technique are that the measurement is done in the whole volume of the sample and that the sample preparation is quite simple. A small carefully cut sample of about 5 mm wide and from 5.5 to 6 mm long (the ratio of length to width has to be superior to 1) is used. This sample is put in the device generating a magnetic field sufficient for complete magnetization and the level of saturation magnetization is measured. Most of the phases in classical steels are ferromagnetic at room temperature, except the austenite and epsilon martensite that are paramagnetic. Consequently, using magnetic saturation method it is possible to determine retained austenite fraction.

Saturation magnetization of a multiphase sample depends on the saturation magnetization of each phase (σ_s^i):

$$\sigma_s = \sum_i \frac{\sigma_s^i \cdot m^i}{m} \tag{37}$$

where m is the global mass of the sample and m^i is the mass of each phase, thus $m = \sum_i m^i$.

Thus, when the mass of the sample contain m^a amount of austenite and m^f of ferrite, the equation becomes as follows:

$$\sigma_s = \frac{\sigma_s^a \cdot m^a}{m} + \frac{\sigma_s^f \cdot m^f}{m} \tag{38}$$

As it was stated previously austenite is a paramagnetic phase, hence its saturation magnetization can be considered as negligible (approximately 0.3 to 0.7 $\mu Tm^3/kg$). Therefore, the saturation magnetization of the sample takes the following form:

$$\sigma_s = \frac{\sigma_s^f \cdot m^f}{m} \tag{39}$$

Finally, to obtain the fraction of retained austenite it is necessary to perform two measurements:
1) the saturation magnetization of the studied sample containing retained austenite (σ_s);
2) the saturation magnetization of the specimen without retained austenite (σ_s^f reference sample).

Then the fraction of retained austenite is calculated:

$$f_{RA} = \frac{\sigma_s^f - \sigma_s}{\sigma_s^f} \tag{40}$$

Usually, the specimen without retained austenite is obtained by applying a heat treatment on the initial sample for austenite destabilization. The standard TRIP steels are annealed at 500°C for 1h in order to get the reference samples.

In this work, due to the high Mn content (low temperature domain of austenite existence), the destabilization of austenite was not so trivial. Therefore, three different samples were chosen for the reference:

➢ one after austenitization at 750°C for 30min and quenching – expected to have fully martensitic structure;
➢ one after annealing of initial martensite structure (850°C - 1min WQ) at 500°C for 1h;
➢ one after annealing of initial martensite structure (750°C - 30min WQ) at 500°C for 30h.

The microstructures after these 3 different treatments were observed using FEG SEM (Figure 54). All the microstructures were considered to be free of retained austenite.

For each thermal treatment at least 2 samples were prepared for saturation magnetization measurements. Further, only the average values of the saturation magnetization or retained austenite fraction will be presented.
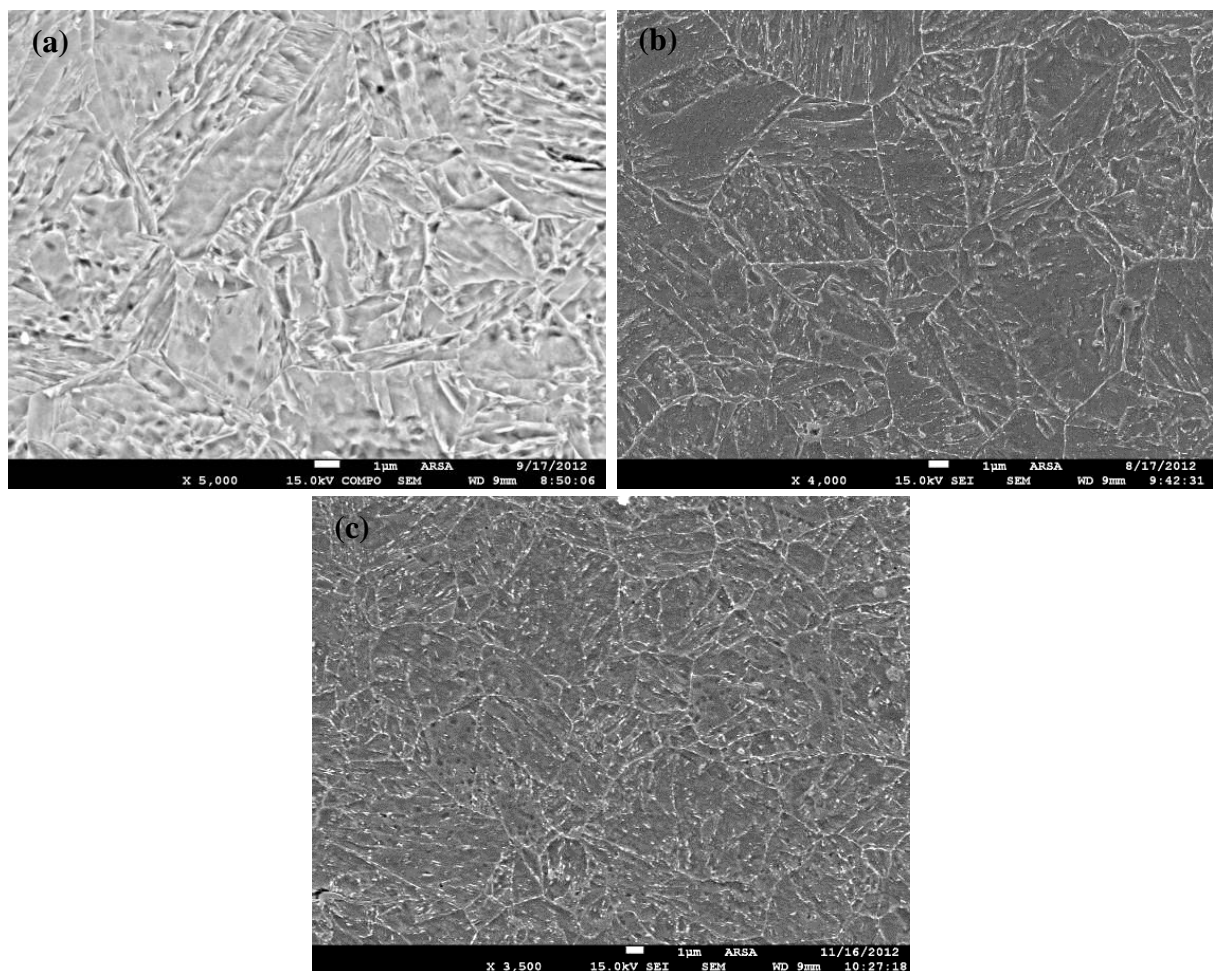
Figure 54 – Microstructure observations (FEG SEM images) of the different reference samples for saturation magnetization measurements: (a) martensitic structure obtained by austenitization at 750°C for 30min and quenching; (b) sample after double annealing: 850°C - 1min WQ followed by 500°C for 1h WQ; (c) sample after double annealing: 750°C - 30min WQ followed by 500°C for 30h WQ.

Table 1 presents the mean values of σ_s^f obtained for different reference samples. As it can be seen, these values are quite close. This means that any reference sample can be used for the evaluation of retained austenite fraction. However, in order to obtain some vision on the possible dispersion of the calculated retained austenite fraction, all possible combinations between σ_s and σ_s^f were used, then the average value was taken. The mean standard deviation of the retained austenite fraction estimation was calculated to be 1.4 % and the mean confidence interval was about 5 %. These rather low values are evidence for the robustness of the saturation magnetization method.

Table 1 – Mean values of σ_s^f measured for different reference samples.

	Reference samples		
Treatment	750°C-30minWQ	500°C-1hWQ	500°C-30hWQ
Mean σ_s^f value, µTm³/kg	259	257	259

Comparison between XRD and Sigmametry results

The values of retained austenite fractions measured on different samples using XRD and Sigmametry techniques are plotted in Figure 55 as a function of holding time at 650°C.
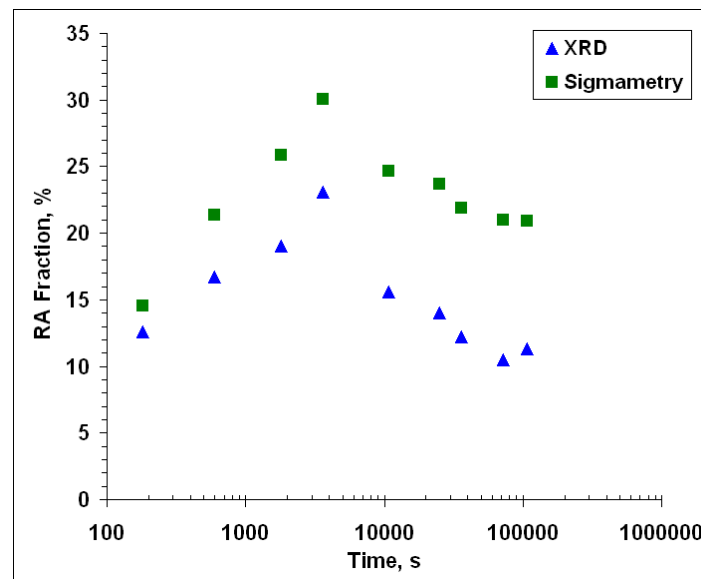
Figure 55 – Retained austenite (RA) fraction as a function of holding time at 650°C. Comparison of two techniques: XRD (blue triangles) and Sigmametry (green squares).

It can be seen that the shape of the RA fraction evolution with holding time is almost the same for both techniques. However, there is a significant difference between the two curves. The values obtained with XRD are much lower than those from Sigmametry, except the first point at 3min which is rather close. For the standard TRIP steels, it is known that mechanical polishing preceding XRD analysis can affect the results of the measurement. Therefore, based on the works of Zaefferer et al. [ZAE'08], it was decided to perform XRD analysis using different preparation methods on two samples with different stability of retained austenite (30min WQ and 30h WQ). For the comparison, two samples (TRIP 800 and Q&P steels) from other studies were also included in the test procedure. All the obtained results are presented in Table 2.

Table 2 – Retained austenite (RA) fraction measured using XRD technique with different polishing methods and using Sigmametry. Results were obtained on two samples from this study (30min WQ and 30h WQ) and on two samples from other studies (TRIP 800 and Q&P steels).

Technique	Preparation	This study		Samples from other studies	
		30min WQ	30h WQ	TRIP800	Q&P
XRD	Mechanical polishing (down to 1 µm)	17.7	11.3	13.4	20.8
	Chemical polishing	17.7	12.4	-	-
	Electrochemical polishing	24.2	19.0	14.5	22.1
Sigmametry	Standard	25.9	20.9	15.2	20.7

The results in Table 2 clearly show that the effect of mechanical polishing is very important in the case of the MMS studied in this work. This effect is significantly less pronounced in the case of TRIP 800 and Q&P steels. It can also be observed that, even though electrochemical polishing permits to suppress the major part of hardened layer from mechanical polishing, the values obtained by XRD are still slightly below those from Sigmametry analysis. Such an important effect of mechanical polishing is probably due to the lower mechanical stability of RA. Further in the work it will be shown that a part of RA stability is controlled by the size of the austenite and not only by carbon content as in the case of TRIP and Q&P steels. Hence, it is supposed that mechanical stability of RA stabilized by the size effect is lower than that coming from carbon enrichment. Nevertheless, more studies are still needed to confirm this hypothesis.

It is interesting to highlight that, very lately, Matsuoka et al. [MAT'13] reported that grain refinement of austenite is ineffective for suppression of deformation-induced martensite transformation. In fact, in the case of deformation-induced martensite transformation, the multi-variant transformation is no longer necessary and single-variant transformation is favored. Thus the mechanical stability of austenite is claimed to be independent of the austenite size. Such approach is in good agreement with the results obtained in this work. Finally, based on the obtained results, sigmametry technique was considered to be more adapted for this study and almost all the RA fractions presented in this work were obtained by this method.

2.1.4 Samples preparation for observations

Small samples with about 20 mm length and 5 mm width were cut in the longitudinal direction from the heads of tensile specimens. Then, they were mounted in a conductive resin under heat and high pressure. The effect of mounting cycle was shown to have no or very limited influence on the microstructure. Next, the samples were mechanically grinded and polished to obtain a mirror surface.
To reveal the microstructure, different etchants were used:
Dino or Marshall etching – for the global microstructure observations in the optical microscope (OM) and/or scanning electron microscope (SEM);
light Metabisulfite + Dino etchings – for the observations of microstructure in the SEM, and following quantifications of fresh martensite + retained austenite fractions;
Picral etching – for the observations of carbides in the SEM.

Chemical compositions of these different etchants are as follows:

Dino
- 100ml of hydrogen peroxide (H_2O_2 30%);
- 4g of ethane diacid ($C_2H_2O_4$-$2H_2O$);
- 2ml of sulphuric acid (H_2SO_4);
- 1.5ml fluohydric acid (HF);
- 140ml of distilled water;

Marshall
- 50ml of hydrogen peroxide (H_2O_2 30%);
- 4g of ethane diacid ($C_2H_2O_4$-$2H_2O$);
- 2-3ml of sulphuric acid (H_2SO_4 65%);
- 55ml of distilled water;

Metabisulfite
- 7g sodium disulfite;
- 100 ml distilled water;

Picral
- 4g picric acid;
- 10ml ethanol.

2.1.5 Microstructure characterization

Optical Microscope (OM)

First, characterization using optical microscopy (OM) was systematically performed. Such type of observation provides initial information about the microstructure and permits the qualitative analysis of phase components. As well, macroscopic vision of the steel structure is obtained, which is necessary for the analysis of global homogeneity of the sample and possible decarburization of the edges. Microstructure observations were done using the Zeiss Axiovert 200 MAT microscope (Figure 56).

Figure 56 – Zeiss Axiovert 200 MAT optical microscope.

Scanning Electron Microscope (SEM)

FEG SEM JEOL 7001F was used for finer observation of the microstructures after different etchings. This equipment is presented in Figure 57. Most often, the following operating conditions were used:

➢ Work distance – 10 mm;
➢ Accelerating voltage – 15 kV;
➢ Aperture – 8 or 9.

Figure 57 – Field Emission Gun Scanning Electron Microscope (FEG SEM) JEOL 7001F.

In order to perform precise quantification of fresh martensite + retained austenite fractions, Back Scattered Electrons (BSE) imaging mode was utilized. BSE images allow higher contrast between phases while smoothing variations inside the martensite islands, which make easier the image analysis (Figure 58).

Quantitative analysis – Aphelion and Image J

Microstructural quantifications were performed on the SEM images. As said beforehand, fresh martensite + retained austenite fractions were estimated using Aphelion® semi-automatic image analyzer software [ADC'15] with internally developed routines. BSE images of the samples etched with light Metabisulfite + Dino etchings were acquired at magnification of 3000. The fractions were determined using a simple threshold method (Figure 58). Preliminary comparison with the standard point counting showed that this method was more effective with small amount of available images. For each sample, 10 images were analyzed, which represents a surface of about 400 000 μm^2. The confidence range on the mean fractions was estimated to be about 10 % of the resulted value.
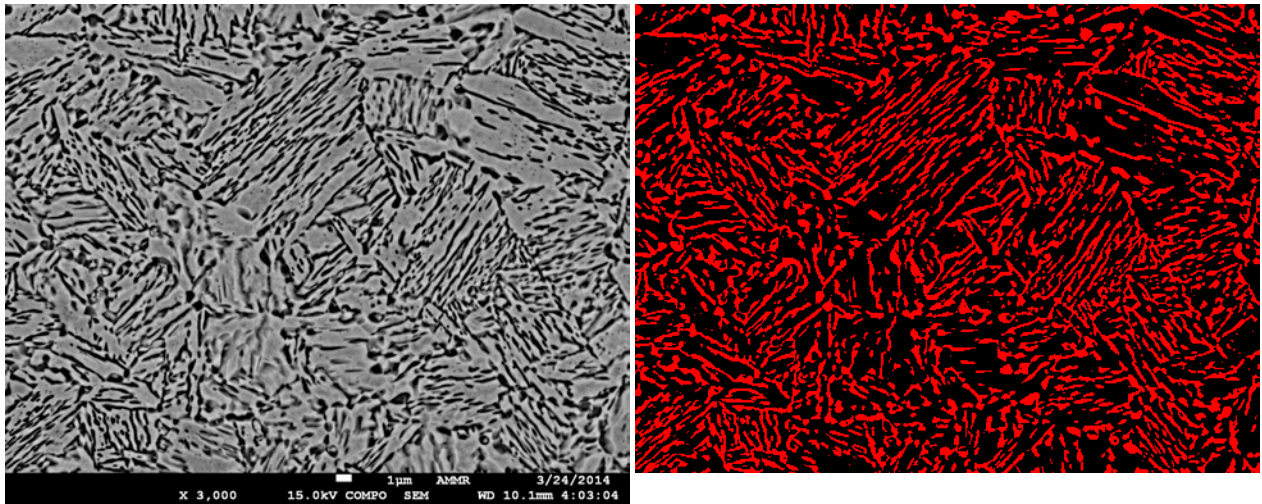
Figure 58 – Example of BSE image (at left) and of binary image obtained after threshold (at right). 1h WQ sample after Metabisulfite + Dino etchings.

Austenite size was evaluated using Image J® software [SCH'12], [COL'07], [GIR'04] and a manual selection procedure. In that case, standard Secondary Electrons images obtained by SEM FEG at a higher magnification (×5000 and ×10000) were preferred. As it will be explained in Chapter 3, two morphologies of austenite were observed. Thus, to estimate the size of austenite two types of measurements were considered:

1) width of the laths: the distance between the two interfaces of a given lath in the normal direction was considered;
2) equivalent diameter of polygons: distance between the two interfaces of polygon in random direction.

An example of the performed measurements is shown in Figure 59. 100 measurements were performed for each type of morphology: laths and polygons.
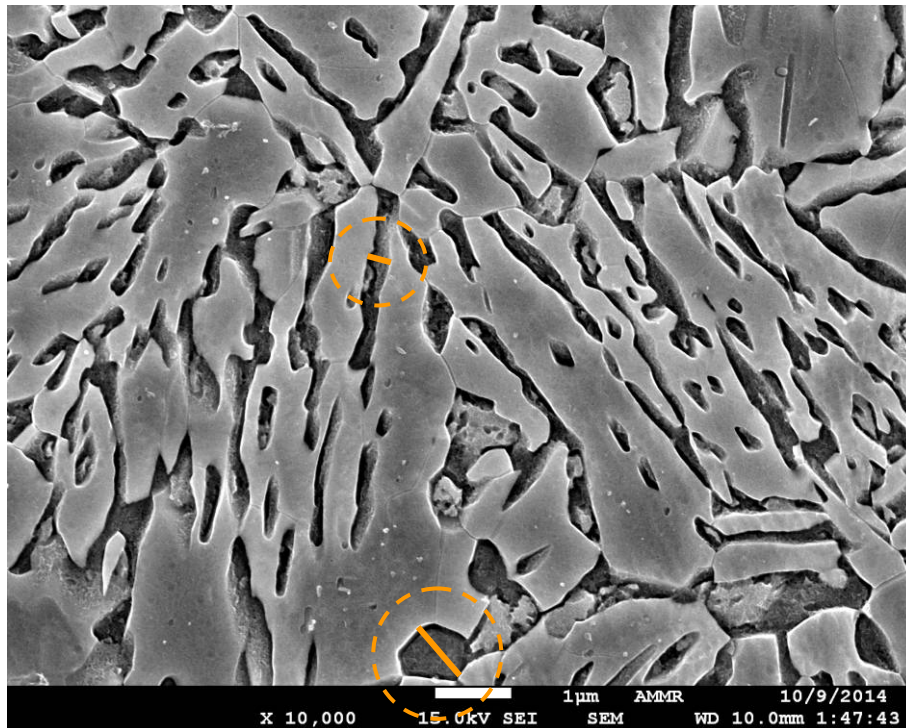
Figure 59 – Example of the performed measurements of lath width and equivalent diameter of polygon. 2h WQ sample after Metabisulfite + Dino etchings.

2.1.6 Fine characterization tools

Transmission Electron Microscope (TEM)

High magnification observations of microstructure, as well as Mn content measurements in different phases, were performed using a JEOL 2100F TEM (Figure 60) with Brüker Energy Dispersive X-ray Spectrometer (EDX). Two kinds of samples were used for TEM observations: replicas and thin foils.

Replicas were prepared using the following procedure:
- standard mechanical polishing till 1 µm;
- etching first with 2 % Nital, then Picral;
- deposition of a cellulose acetate (Biodène) film;
- 20min drying, then peeling-off (detachment) of the film from the sample;
- carbon vapor deposition (~30-50 nm) on the film;
- cutting the film in squares of 4 mm^2 and putting them on the copper grid;
- dissolution of cellulose acetate film in a mixture of solvents.

Figure 60 – View on JEOL 2100F TEM.

In order to prepare a thin disk shaped foil the steel sheet was ground mechanically to about 80 µm thickness, then twin-jet electropolished in a solution of 5% perchloric and 95% acetic acids at about 15°C.

Convergent Beam Electron Diffraction (CBED) in STEM mode (Scanning TEM) was used to make difference between the phases present in the microstructure. Obtained Kikuchi patterns were indexed using "Euclid's Phantasies V1.1" software developed in LEM3 laboratory (University of Lorraine) [FUN'03]. Such methodology is very similar to the Electron Back Scattered Diffraction (EBSD) mapping used in SEM. However, the accuracy of orientation determination on the patterns generated by TEM can be better than 0.1°, thus making this tool opportune for ultra fine scale studies. In certain cases, when indexing was not possible or doubtful, the standard Selected Area Diffraction (SAD) in mode TEM was used.

Electron probe microanalyzer (EPMA)

Manganese distribution and segregations were characterized using the CAMECA SX100 electron probe microanalyzer (EPMA). An example of CAMECA SX100 EPMA is presented in Figure 61.

Figure 61 – CAMECA SX100 Electron probe microanalyzer.

The function of EPMA can be explained in the following manner. The generated electron beam strikes the analyzed sample and the interaction between prime electrons and the sample atoms provokes the emission of characteristic X-rays. This emitted X-rays are analyzed in a Wavelength-Dispersive Spectrometer (WDS), owing to single-crystal monochromators which diffract a precise wavelength onto a detector where the photons are counted. Then, using a reference sample, the elemental concentrations can be determined. The qualitative and quantitative distribution (mapping) of chemical elements can be obtained by scanning a small area of the sample [BEN'87]. Generally, with an electron beam of about 1 μm diameter, the analyzed volume of material at each measuring point is approximately 1 $μm^3$.

In this work the following test conditions were used for acquiring manganese maps:
- Accelerating voltage – 15 keV;
- Current – 2 μA;
- Step size – 0.5 μm;
- Time step – 0.1 s/pixel.

Mn quantitative maps were built by combining the intensity in the distribution map and the intensity given by the quantitative analysis.

NanoSIMS analyzer

Recently, in the studies of Valle et al. [VAL'06] and Drillet et al. [DRI'12], it was shown that the NanoSIMS (SIMS for Secondary Ion Mass Spectrometry) technique is a powerful tool for the characterization of carbon distribution in steels. For this reason, Cameca NanoSIMS 50 (Figure 62) was used in this work to confirm the C level of retained austenite and martensite (prior austenite) in certain samples. The specimen preparation for NanoSIMS analysis is rather simple. Moreover, the advantages of Cameca NanoSIMS 50 are its high lateral resolution (about 50 nm) and its high sensitivity (detection limit for carbon is 0.0063 wt.%).

Secondary ion mass spectroscopy is based on the analysis of secondary ions, induced by an initial ion bombardment, with a mass spectrometer. In fact, the surface of a solid sample is sputtered by primary heavy ions of a few keV energy. At a contact with the surface of target

sample, this primary beam generates a sequence of atom collisions, followed by the ejection of atoms and atom clusters. A fraction of the emitted particles is spontaneously ionized – "secondary ions". Such a secondary ion emission supplies the information about the chemical composition of the emitting area. The ions of interest are isolated using the mass analyzer. Finally, ion detection system permits to record the magnitude of the secondary ions signal and to present this data in forms of quantitative maps for a chosen element. Schematic representation of the SIMS technique is shown in Figure 63.

Figure 62 – Photo of Cameca NanoSIMS 50.

High vacuum is necessary inside the machine for two reasons:
- to avoid the interactions of secondary ions with the background gases on their way to the SIMS detector;
- to decrease the contamination by adsorption of background gas particles during measurement.

Detection and counting systems

Separating the ions of interest using mass spectrometer

Primary heavy ions beam

Collecting of emitted secondary ions

Sputtering of the sample surface
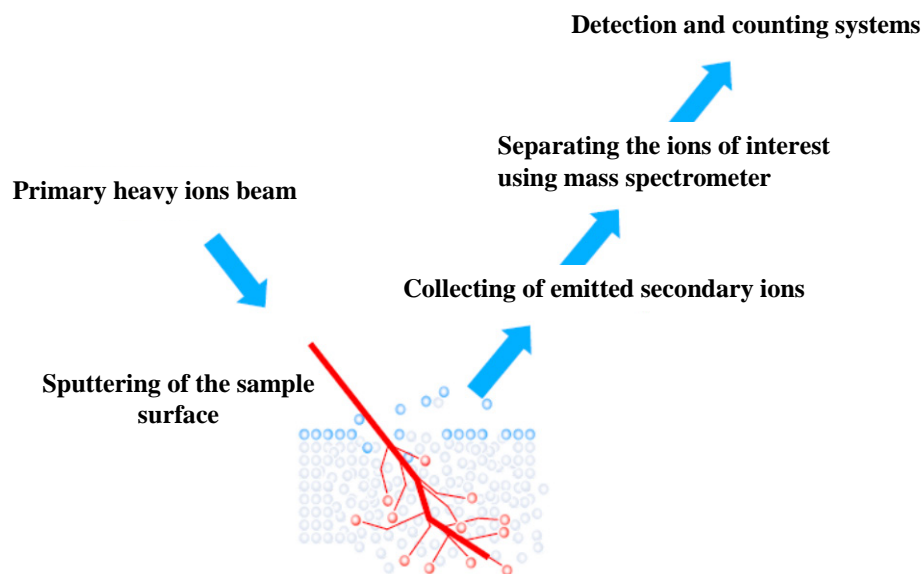
Figure 63 – Scheme of the SIMS technique (modified from [PUS'09]).

The major difference between static SIMS and dynamic SIMS (nanoSIMS) modes is the resolution depth. The first one analyses only the surface of the sample, which is mostly limited to the first top monolayer. The second one has a depth resolution ranging from sub-nm to tens of nm, therefore giving the possibility to investigate bulk composition and depth distribution of trace elements.

In this work NanoSIMS 50 machine was used to obtain ^{12}C ion maps of studied samples in order to estimate carbon content of austenite. The samples were mounted in an aluminum ring using Wood's alloy and disposed in a sample holder (Figure 64). $10 \times 10 \ \mu m^2$ areas were scanned using a focused Cs^+ primary ion beam (<1 pA) and the SIMS intensities were measured. Before the measurements, surface of the samples was pre-sputtered in order to eliminate any carbon contamination.
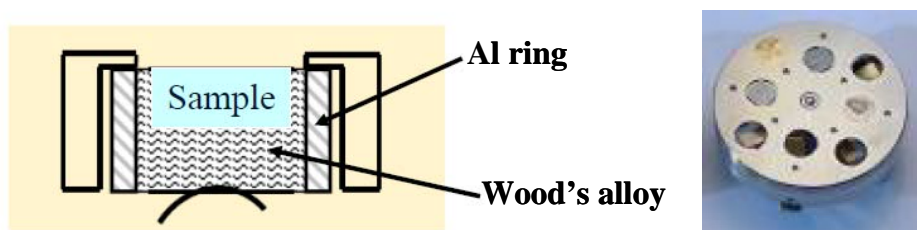
Figure 64 – Scheme of a sample mounted in Al ring sample (at left) and nanoSIMS sample holder (at right) (modified from [PUS'09]).

To evaluate the carbon content of studied samples, a reference sample with known carbon content in martensite (prior austenite) was scanned. The C content of austenite was estimated by comparison of the obtained SIMS intensities between the analyzed samples and the reference one. Image analysis using Image J® software was done on the obtained ^{12}C ion maps to extract the mean intensity level in austenite islands. Examples of a ^{12}C ion map and of the selection of martensite zones for the averaging of SIMS intensities are shown in Figure 65. Then, the austenite C content of studied samples was estimated, taking into account the C level of reference sample and the determined mean intensities. This methodology was employed for the first time and was considered to be adapted for such type of studies.
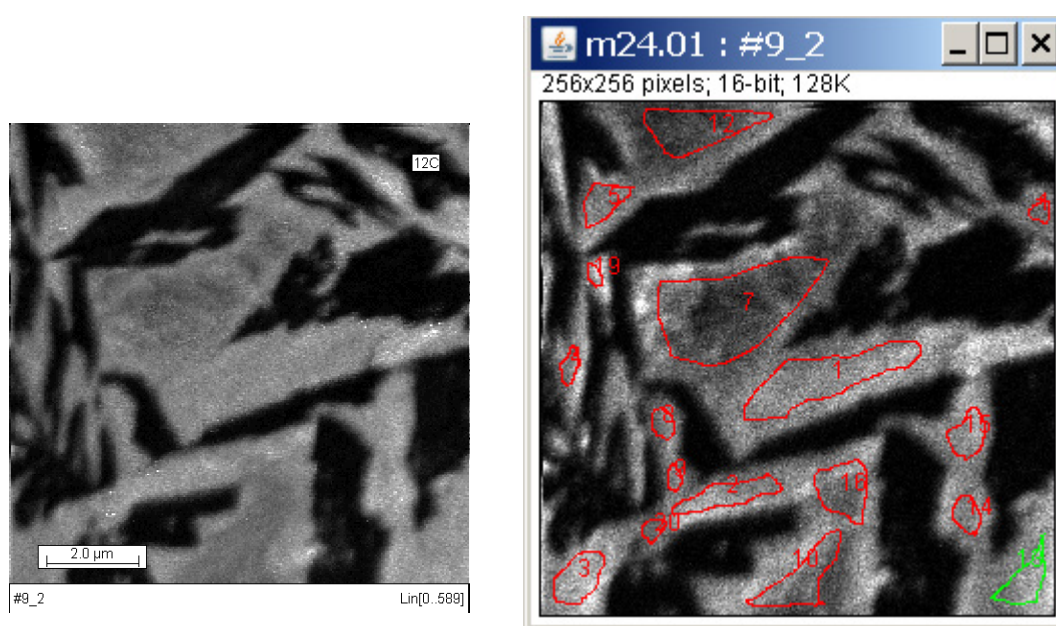
Figure 65 – ^{12}C ion map of the reference sample and the selection of martensite zones for the averaging of SIMS intensities.

2.1.7 Thermo-Calc and DICTRA softwares

Thermodynamic simulations were performed using Thermo-Calc® and DICTRA®™ softwares for deeper study of phase transformations.
Thermo-Calc® software was used for two major objectives:
1. to visualize the effect of Mn on phase transformations using pseudo-binary diagrams;
2. to obtain expected phase fractions and compositions in ortho-equilibrium condition; this information was used for:
   a. selection of annealing temperature;
   b. comparison with experimental results.

DICTRA®™ software coupled with Thermo-Calc® was used for thermo-kinetics simulation of phase transformations during annealing. The aims of these simulations were to assist the analysis of the experimental data and to propose a way for the prediction of the final microstructure.

Starting from the 1980 [HIL'80], [SUN'85], researchers continuously develop the "CALPHAD" (CALculation of PHAse Diagrams) approach in order to have complete thermodynamic data bases for different alloys systems. These data bases allow different kinds of calculations of thermodynamic properties as functions of temperature, composition, pressure, etc., construction of phase diagrams and evaluation of other thermodynamic factors and parameters. To use these data bases, different softwares were created. For instance, Thermo-Calc company developed two softwares: Thermo-Calc® (TCC™ and TCW™) for thermochemical equilibrium calculations based on the minimization of Gibbs energy and DICTRA®™ for kinetic simulations based on the diffusion theory [AND'02]. Both softwares were considered to be adapted for this study and were used with TCFE5 and MOB2 databases [THE'15].

Thermo-Calc simulations were performed in Chapter 2.2 (so-called "Alloy design") in order to evaluate the effect of Mn on the phase transformations in steel and to predict different phase fractions at equilibrium conditions. DICTRA was used to simulate the dissolution of cementite and the formation of austenite under local equilibrium conditions. The initial conditions and the results of simulations are reported in Chapter 3.

2.2 Selection of composition and treatment

2.2.1 Selection of composition and elaboration/characterization of obtained steel

The precursor works of Matlock [MAT'06] show that a certain level of retained austenite is necessary (from 20% to 30%) to achieve the mechanical properties, especially the balance between strength and ductility, in order to fulfill the requirements of 3rd generation AHSS steels. It is well known that an increase in the concentration of both carbon and manganese, which are strong austenite stabilizers, results in an improved stability of austenite at room temperature. Furthermore, a reduction in the austenite grain size is well known to increase the austenite stability by suppressing the martensite transformation. These two aspects, austenite composition and size, were considered for the development of steels with large volume fraction of retained austenite. In particular, such high fraction of retained austenite can be achieved in ultrafine-grained steels with 5-7 wt.% Mn content and relatively low carbon content. This type of microstructure provides an excellent combination of strength and ductility thanks to the enhanced TRIP effect. The composition used in this work (see Table 3) follows the aforesaid philosophy. It is worth noting that both carbon and manganese contents were limited respectively to 0.1 wt.% and 5 wt.% in order to prevent the problems linked to the welding properties and to

the resistance of spot welds. At this point, it is also important to mention that theoretically, considering only the chemical contribution to M_s temperature, the selected composition does not allow stabilizing 30% of retained austenite at room temperature. As it will be discussed and demonstrated later in this thesis, the size effect plays a key role on the austenite stability.

Vacuum induction melting was used to prepare the steel. Chemical composition of the obtained steel is shown in Table 3. The level of C and Mn was slightly lower than the targeted ones. The ingot was then reheated to 1200°C and hot rolled with the finishing temperature around 930°C. Coiling was simulated by a slow cooling in the furnace from 625°C. Microstructure of hot rolled steel consists of bainite and martensite (Figure 66) and its microhardness was evaluated to be around 340 HV. Afterward, 70% of reduction was done to get the final thickness of cold rolled steel at about 1.2 mm.

Table 3 – Chemical composition of studied steel (10^{-3} wt. %).

Ref.	C	Mn	P	S	Si	Al	Cr	N	B(ppm)
2260B	98	4740	5	1	6	3	3	7.2	6
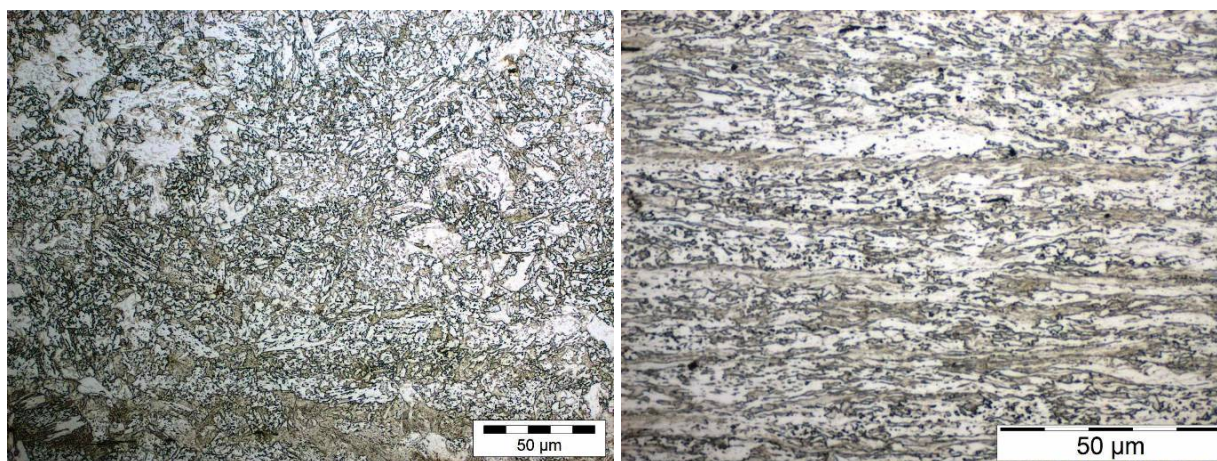
Figure 66 – Observed microstructures after hot rolling with coiling at 625°C (at left – Nital etching) and after cold rolling (at right – Dino etching).

2.2.2 Thermal treatment selection

As it was discussed in Chapter 1.1, globally, there are two ways to anneal a MMS: direct annealing of cold rolled metal or double annealing, i.e. austenitization followed by quench then second annealing with corresponding ART phenomena. As shown previously [KIM'81], one of the main advantages of double annealing, when the initial microstructure before second annealing is martensite and/or bainite, is the very fine resulting microstructure and a particular morphology of its constituents: lath-like and/or fibers. From a mechanical point of view, this provides better balance between strength and ductility and better damage properties [SUG'02], [SUG'00], [HEL'11], [KRE'11]. From a phase transformation point of view, finer grain size is supposed to enhance both the kinetics of austenite formation and the stability of austenite. Finally, it should be stated that double annealing with the first annealing in fully austenitic domain permits to decrease the so-called "heritage effects". Indeed, direct annealing is very dependent on the prior steps of steel processing like coiling and cold rolling rate. Normally, in the case of double annealing, due to the full austenitization at the first step, these "heritage effects" have lower impact.

For all the above reasons, it was decided to investigate this type of thermal treatment. However, the choice of annealing temperature is of major importance since it determines both the fractions of microstructure constituents and the stability of austenite via its composition and size. In order to better assess the annealing temperature, it was decided to proceed in two steps:
- thermodynamic calculations using Thermo-Calc software. This step is necessary to determine the temperature and the composition ranges for the existence of different phases;
- combinatory experiments using gradient batch annealing in order to determine the effects of temperature on mechanical properties.

Batch annealing was selected as a type of second intercritical treatment based on the works of Furukawa et al. [FUR'89], [FUR'94] and Huang et al. [HUA'94], which shown that optimal retained austenite fraction and mechanical properties were obtained after 3h annealing.

2.2.2.1 Thermodynamic calculations

Four pseudo-binary diagrams with 1.7 wt.%, 2.7 wt.%, 3.7 wt.% and 4.7 wt.% Mn content were calculated (Figure 67) to visualize the global effect of Mn on the possible phase transformations. The analysis of these pseudo-binary diagrams brings the following outcomes:
- ✓ increasing Mn expands austenite domain to lower temperatures;
- ✓ two phase domain α+γ is moved to the lower temperatures and slightly expanded at low C concentrations;
- ✓ three phase region (α+γ+θ) is also expanded, meaning higher stability of cementite;
- ✓ slope of the solvus between intercritical and austenitic domains (red line) decreases, leading to the rapid change of austenite volume fraction with temperature variation.

Then, some ortho-equilibrium simulations were done to obtain the temperature evolution of phase fractions and their respective compositions for the studied steel (Fe-0.098 wt.% C-4.7 wt.% Mn). A part of the results is shown in Figure 68. Figure 68(a) shows that complete dissolution of cementite happens at 610°C (blue line) and fully austenite structure is obtained at 740°C (red line). This means that the intercritical domain exists in a rather narrow temperature range: from 610 to 740°C. In Figure 68(b) it can be seen that the evolution of C content in austenite is in form of peak with the highest amount achieved at temperature when complete dissolution of cementite happens. In the same time, Mn content in austenite is continuously decreasing till the value of steel composition (4.7 wt.%) in fully austenite structure. Such evolution of chemical composition of austenite supposes that there is a similar peak evolution of retained austenite fraction if only chemical stability of retained austenite (no size effect) is taken into account. This means that there is an optimum annealing temperature to get the highest amount of retained austenite which was observed in the previous studies [FUR'89].

In order to assess this optimum temperature and to obtain the evolution of retained austenite fraction at room temperature as a function of annealing temperature the following calculations were performed. The M_s temperature was evaluated using Andrews relation [AND'65]. In the case of simple C-Mn steels without other alloying elements, it takes the following form:

$$M_s^0(°C) = 539 - 423 \cdot w_C^A - 30.4 \cdot w_{Mn}^A \tag{41}$$

where w_C^A and w_{Mn}^A are C and Mn contents in austenite taken in weight percents.

Then, Koistinen and Marburger empirical equation [KOI'59] was taken for the estimation of retained austenite fraction at room temperature (20°C):

$$f_{RA} = f_A \cdot \exp\left(-\alpha \cdot \left(M_s - T_q\right)\right) \tag{42}$$

where f_{RA} is the volume fraction of retained austenite, f_A is the volume fraction of austenite before martensite transformation (austenite fraction at the end of holding before quenching), T_q is temperature reached during quenching (in this study it is equal to 20°C – room temperature) and $\alpha=0.011$ is a fitting parameter.

Finally, using the data from Figure 68 (austenite fraction and its composition) the calculations were done and the results are presented in Figure 69.
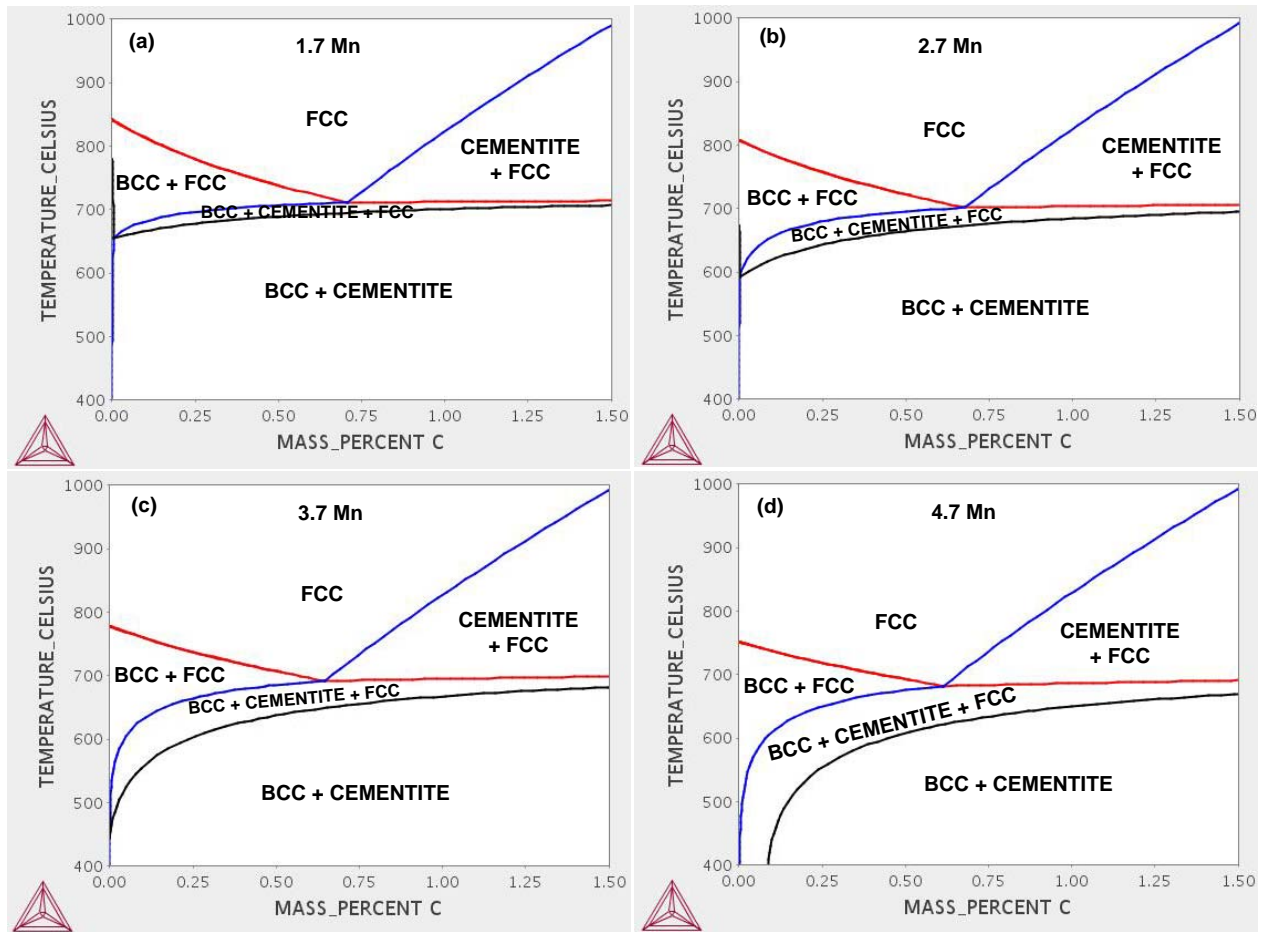
Figure 67 – Pseudo-binary diagrams calculated with Thermo-Calc software for the steels with four different Mn contents: (a) 1.7 wt.%; (b) 2.7 wt.%; (c) 3.7 wt.%; (d) 4.7 wt.%.
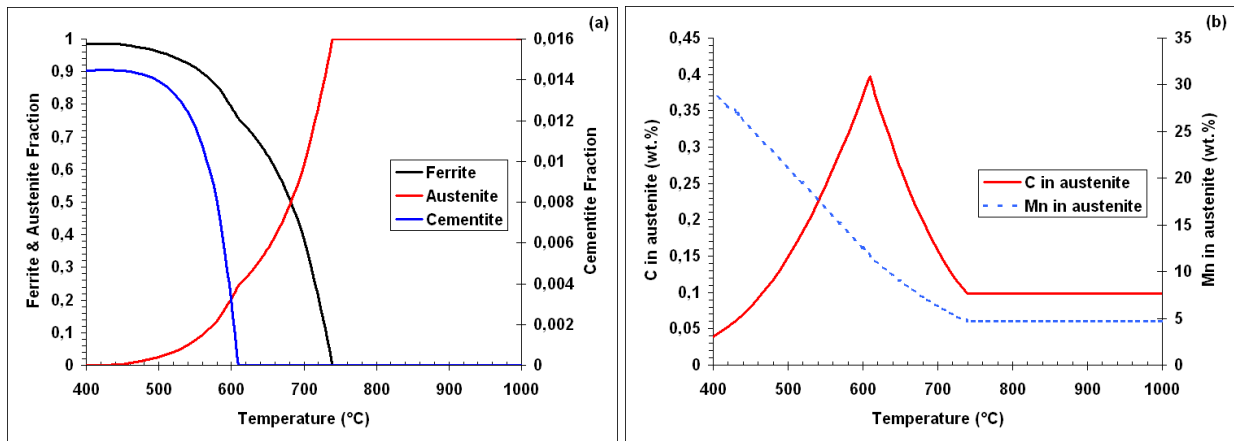
Figure 68 – Evolution of phase fractions and austenite C and Mn contents with temperature according to the Thermo-Calc simulations: steel with 0.098 wt.% C and 4.7 wt.% Mn.
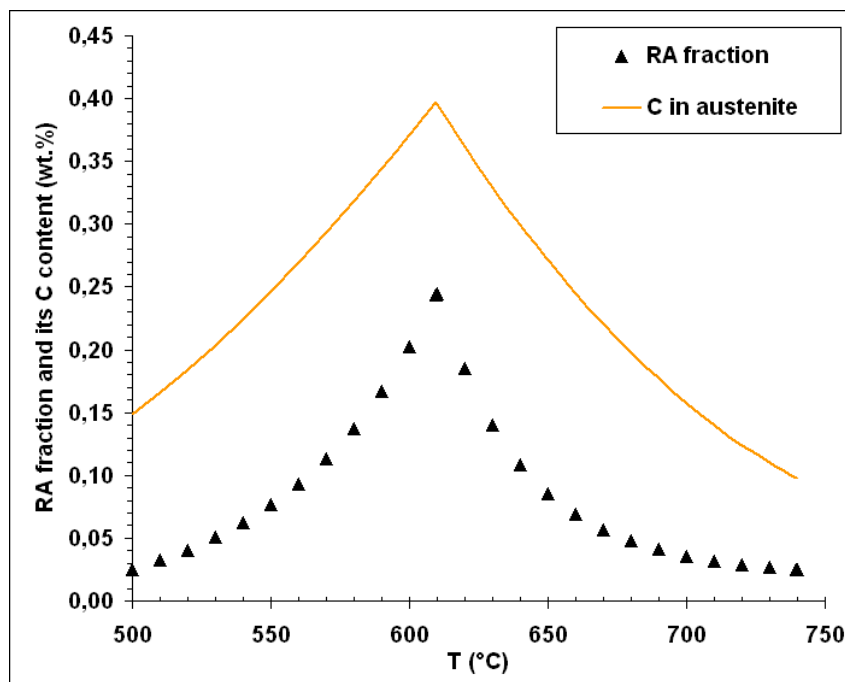
Figure 69 – Evolution of retained austenite fraction and its C content as a function of annealing temperature (using the data from Thermo-Calc simulations).

It can be seen that the peak of retained austenite corresponds exactly to the peak of C content in austenite, which in its turn is related to the temperature of cementite dissolution. From a thermodynamic point of view, the optimum temperature is calculated around 610°C. However, it should be noted that kinetics effects, such as cementite dissolution and austenite growth, are not taken into account in this type of calculations. As it was seen in pseudo-binary diagrams (Figure 67), stability of formed cementite increases with the increase of Mn, thus cementite dissolution in MMS can be sluggish. Knowing that the carbon peak is directly related to the cementite dissolution, one can expect that the peak of retained austenite fraction will be also controlled by both cementite dissolution and austenite growth. Therefore, the temperature of 610°C determined by thermodynamic calculations can be clearly considered as a lower value. In a more pragmatic way, it is possible to approach the optimum annealing temperature by using a combinatory experiment.

2.2.2.2 Combinatory experiments

As explained previously, it was decided to perform a specific thermal treatment (batch annealing) in the furnace in which it is possible to control the gradient of temperature. The principle of gradient batch annealing furnace was explained in the previous section. The furnace was programmed to obtain a linear gradient of soaking temperature between 600 and 700°C (range defined from aforementioned thermodynamic calculations). The scheme of annealing cycle is presented in the left part of Figure 70. Based on the literature and preliminary dilatometry trials, it can be reasonably supposed that the slow cooling does not affect significantly the microstructure. Indeed, it was found that ferrite formation does not occur at very low cooling rates and, even during holding in the domain with high driving force for ferrite formation, the transformation was very sluggish. This is probably due to the high Mn content in austenite before cooling.

A steel sheet 230 mm long and 150 mm wide was heat treated. The obtained gradient of temperature depending on the position in the sheet is shown in the right part of Figure 70. For each temperature two "mini" tensile samples with the gauge length of 20 mm and section of 5 mm × 1.2 mm were prepared. Then, tensile tests were performed. The evolution of mechanical properties as a function of holding temperature is presented in Figure 71. Table of all results and all tensile curves can be found in Annex 2.
These results clearly show that there is an optimum domain of temperatures where a good balance between strength and ductility can be achieved. For the studied composition, it appears that the optimum range of temperatures is between 640 and 660°C. As it was anticipated in the previous part of the work, these temperatures are higher than those predicted by ortho-equilibrium calculations, due to the kinetics effects.
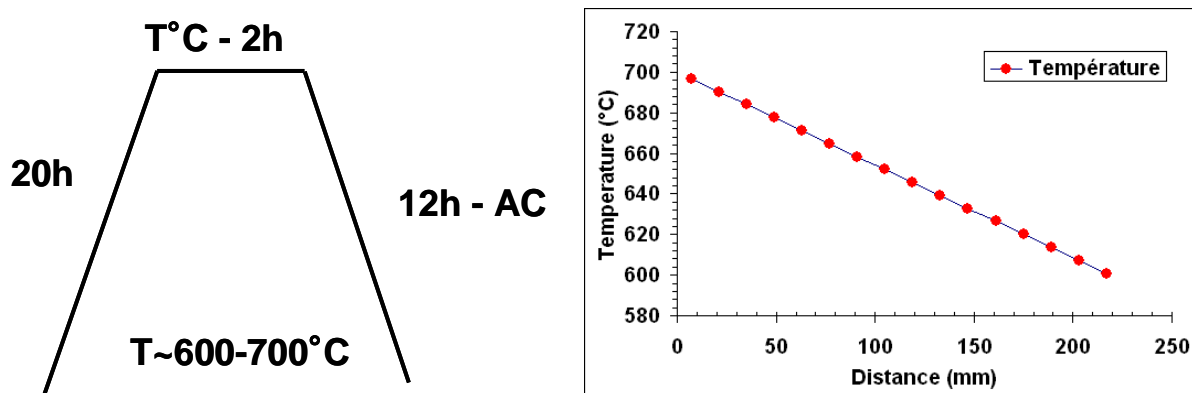
Figure 70 – Scheme of gradient batch annealing cycle (in the left part of the figure) and the obtained gradient of temperature depending on the position in the sheet (in the right part).

XRD analysis was performed on all samples to study the evolution of retained austenite fraction. Results are presented in Figure 72. Taking into account only the evolution of retained austenite fraction, one can conclude that the optimal temperature is ~690°C, but this will be an erroneous outcome. In fact, the optimum ductility (elongation) was obtained at temperature range of 640-660°C, as already stated. This is due to one more parameter that introduces another level of complexity in the choice of optimal treatment: the mechanical stability of retained austenite. As it can be seen in Figure 72, different retained austenite fractions can provide the same level of strength-ductility balance and, alternatively, the same retained austenite fraction can result in different strength-ductility. This indicates directly that strength-ductility balance is related to both parameters: fraction and stability of retained austenite. At this stage of the work, it was not possible to get better understanding about the mechanical stability of retained austenite.
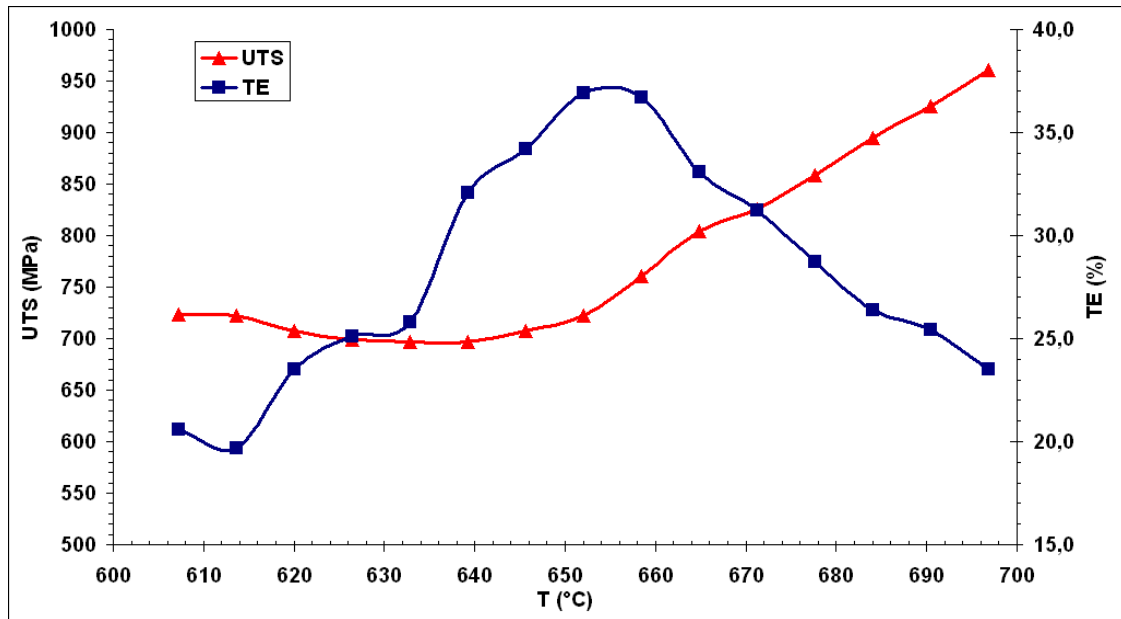
Figure 71 – Evolution of ultimate tensile strength (UTS) and total elongation (TE) as a function of holding temperature.

Based on the obtained results, it was decided to select the soaking temperature of 650°C and to investigate the impact of soaking time on the microstructure and mechanical properties evolution.
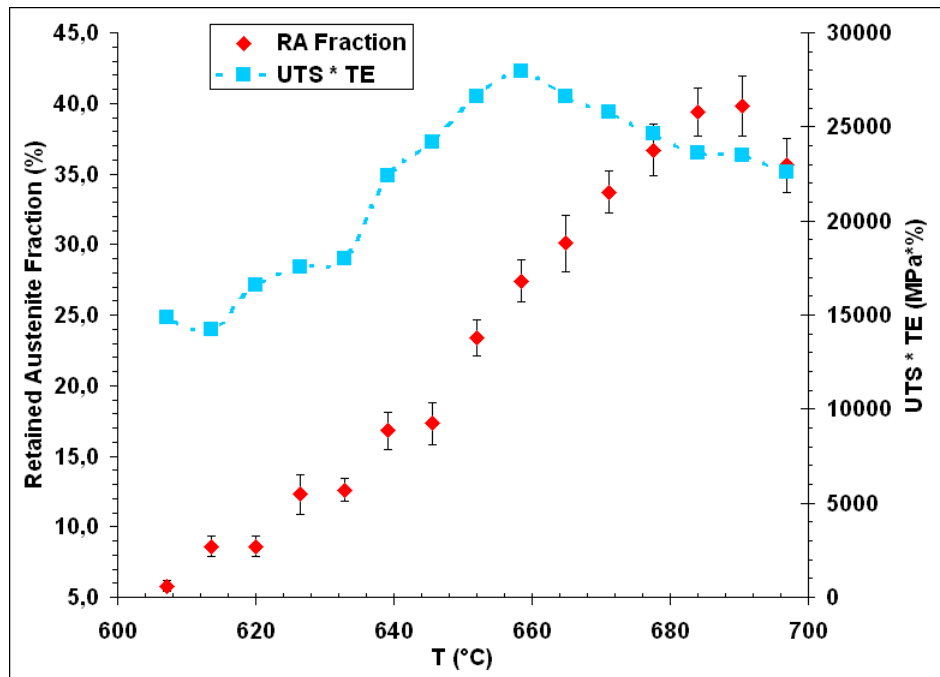
Figure 72 – Evolution of retained austenite fraction and balance between strength and ductility expressed by UTS*TE as a function of annealing temperature.

The decisions taken in part 2.2 can be summarized in the following manner:
1. selected composition: 0.1 wt.% C and 5 wt.% Mn;
2. selected heat treatment: double annealing with first austenitization above Ae$_3$ followed by intercritical batch annealing at 650°C.

References

[ADC'15] http://www.adcis.net/

[AND'65] K.W. Andrews, Empirical formulae for the calculation of some transformation temperatures, Journal of the Iron and Steel Institute, 203(7), 1965, 721-727.

[AND'02] J.O. Andersson, T. Helander, L. Höglund, P.F. Shi and B. Sundman, Thermo-Calc and DICTRA, Computational tools for materials science, Calphad, 26, 2002, 273-312.

[AST'09] E28 Committee, Test Methods for Tension Testing of Metallic Materials, ASTM International, 2009.

[AVE'48] B. L. Averbach and M. Cohen, X ray determination of retained austenite by integrated intensities, Transactions AIME, 176, 1948, 401-415.

[BEN'87] D. Benoit, F. Grillon, F. Maurice, N. Roinel, J. Ruste, R. Tixier, Microanalyse par sonde électronique: spectrométrie de rayons X, ANRT, 1987.

[COL'07] T.J. Collins, ImageJ for microscopy, BioTechniques, 43 (1), 2007, 25-30.

[DES'76] C.D. Desforges, W.E. Duckworth and T.F.J.N. Ryan, Manganese in ferrous metallurgy, Page Bros Ltd., Norwich, 1976.

[DRI'12] J. Drillet, N. Valle, T. Iung, Nanometric Scale Investigation of Phase Transformations in Advanced Steels for Automotive Application, Metallurgical and Materials Transactions A, 43, 2012, 4947-4956.

[FUN'03] J.J. Fundenberger, A. Morawiec, E. Bouzy, J.S. Lecomte, Polycrystal orientation maps from TEM, Ultramicroscopy, 96, 2003, 127-137.

[FUR'89] T. Furukawa, Dependence of strength-ductility characteristics on thermal history in low carbon 5wt.% Mn steels, Materials Science and Technology, 5, 1989, 465-470.

[FUR'94] T. Furukawa, H. Huang, O. Matsumura, Effects of carbon content on mechanical properties of 5wt.% Mn steels exhibiting transformation induced plasticity, Materials Science and Technology, 10 (11), 1994, 964-969.

[GIR'04] V. Girish, A. Vijayalakshmi, Affordable image analysis using NIH Image/ImageJ, Indian Journal of Cancer, 41 (1), 2004, 47.

[HEL'11] J.C. Hell, M. Dehmas, S. Allain, J.M. Prado, A. Hazotte, J.P. Chateau, Microstructure–properties relationships in carbide-free bainitic steels, ISIJ International, 51, 2011, 1724-1732.

[HIL'80] M. Hillert, Empirical methods of predicting and representing thermodynamic properties of ternary solution phases, Calphad, 4(1), 1980, 1-12.

[HUA'94] H. Huang, O. Matsumura, T. Furukawa, Retained austenite in low carbon, manganese steel after intercritical heat treatment, Materials Science and Technology, 10 (7), 1994, 621-626.

[KIM'81] N.J. Kim, G. Thomas, Effects of morphology on the mechanical behavior of a dual phase Fe/2Si/0.1 C steel, Metallurgical Transactions A, 12, 1981, 483-489.

[KOI'59] D.P. Koistinen, R.E. Marburger, A general equation prescribing the extent of the austenite-martensite transformation in pure iron-carbon alloys and plain carbon steels, Acta Metallurgica, 1959, 7 59-60.

[KRE'11] B. Krebs, L. Germain, A. Hazotte, M. Gouné, Banded structure in Dual Phase steels in relation with the austenite-to-ferrite transformation mechanisms, Journal of Materials Science, 46, 2011, 7026-7038.

[MAT'06] D.K. Matlock, J.G. Speer, Design considerations for the next generation of advanced high strength sheet steels, Proceedings of 3rd International Conference on Advanced Structural Steels, Korea, 2006, 774-781.

[MAT'13] Y. Matsuoka, T. Iwasaki, N. Nakada, T. Tsuchiyama, S. Takaki, Effect of Grain Size on Thermal and Mechanical Stability of Austenite in Metastable Austenitic Stainless Steel, ISIJ International, 53, 2013, 1224-1230.

[PUS'09] I. Pushkareva, PhD report, Evolution microstructurale d'un acier Dual Phase. Optimisation de la résistance à l'endommagement, Institut National Polytechnique de Lorraine (INPL), 2009, http://pegase.scd.inpl-nancy.fr/theses/2009_PUSHKAREVA_I.pdf.

[SCH'12] C.A. Schneider, W.S. Rasband, K.W. Eliceiri, NIH Image to ImageJ: 25 years of image analysis, Nature Methods, 9 (7), 2012, 671-675.

[SUN'85] B. Sundman, B. Jansson, J.O. Andersson, The Thermo-Calc databank system, Calphad, 9, 1985, 153-190

[SUG'00] K.I. Sugimoto, J. Sakaguchi, T. Iida, T. Kashima, Stretch-flangeability of a high-strength TRIP type bainitic sheet steel, ISIJ International, 40(9), 2000, 920-926.

[SUG'02] K.I. Sugimoto, A. Kanda, R. Kikuchi, S.I. Hashimoto, T. Kashima and S. Ikeda, Ductility and formability of newly developed high strength low alloy TRIP-aided sheet steels with annealed martensite matrix, ISIJ international, 42(8), 2002, 910-915.

[THE'15] http://www.thermocalc.com/products-services/databases/

[VAL'06] N. Valle, J. Drillet, O. Bouaziz, H.N. Migeon, Study of the carbon distribution in multi-phase steels using the NanoSIMS 50, Applied Surface Science, 252, 2006, 7051-7053.

[ZAE'08] S. Zaefferer, P. Romano, F. Friedel, EBSD as a tool to identify and quantify bainite and ferrite in low-alloyed Al-TRIP steels, Journal of Microscopy, 230, 2008, 499-508.

CHAPTER 3: MICROSTRUCTURE EVOLUTION DURING INTERCRITICAL ANNEALING

As it was already stated, final mechanical properties of steels are closely related to the microstructure parameters: nature, composition, volume fraction, size and morphology of the microstructure constituents. In its turn, microstructure depends on the applied thermo-mechanical treatments. In this chapter, the microstructure evolutions resulting from the double annealing treatment will be presented and discussed.

According to the considerations described in chapter 2.2, the heat treatment schematically presented in Figure 73 was chosen for the further investigations. It consists of two thermal cycles. First, a complete austenitization at 750°C for 30 minutes followed by water quench. Second, an intercritical annealing at 650°C with different holding times (3min, 10min, 30min, 1h, 2h, 3h, 7h, 10h, 20h and 30h) followed by water quench in the end. All double annealing treatments were performed in Nabertherm furnace under Ar atmosphere to avoid any decarburization. The mean heating rate in the furnace was about 5°C/s. However, in the end of heating section the heating rate was much lower. Finally, the holding temperature ±5°C was achieved after ~200s.
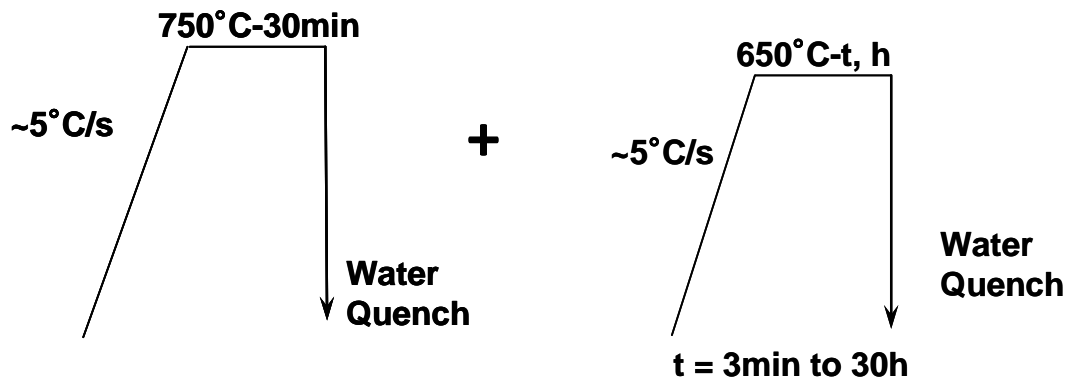
Figure 73 – Schematic representation of performed double annealing cycles.

3.1 Characterisation of the microstructure after austenitization

The microstructure after first annealing cycle (austenitization followed by quench) was characterized using different techniques: optical microscope (OM), scanning electron microscope (SEM), transmission electron microscope (TEM) and X-ray diffraction (XRD). Figure 74 presents the observations (OM, SEM, TEM) of the obtained microstructure. It can be seen that the resulting microstructure is composed of lath martensite. Applying image analysis on OM images after Dino etching, prior austenite grain size was estimated to be around 4µm. Furthermore, optical observation after Klemm etching revealed the presence of a small quantity of retained austenite in the martensite matrix as highlighted in Figure 75(b). Finer characterization of retained austenite done with TEM (Figure 75(d)) confirms this observation. The evaluation of retained austenite volume fraction from the XRD spectrum (Figure 75(c)) was not possible due to its very low value. Thus, it was considered that there was less than 3% of retained austenite. A mean Mn content in retained austenite islands of 9 wt.% was measured by EDX. This value was considered as relatively high. As a consequence, the microstructure at the beginning of the second cycle consists of a fully martensitic structure in which some small quantities of retained austenite are present.
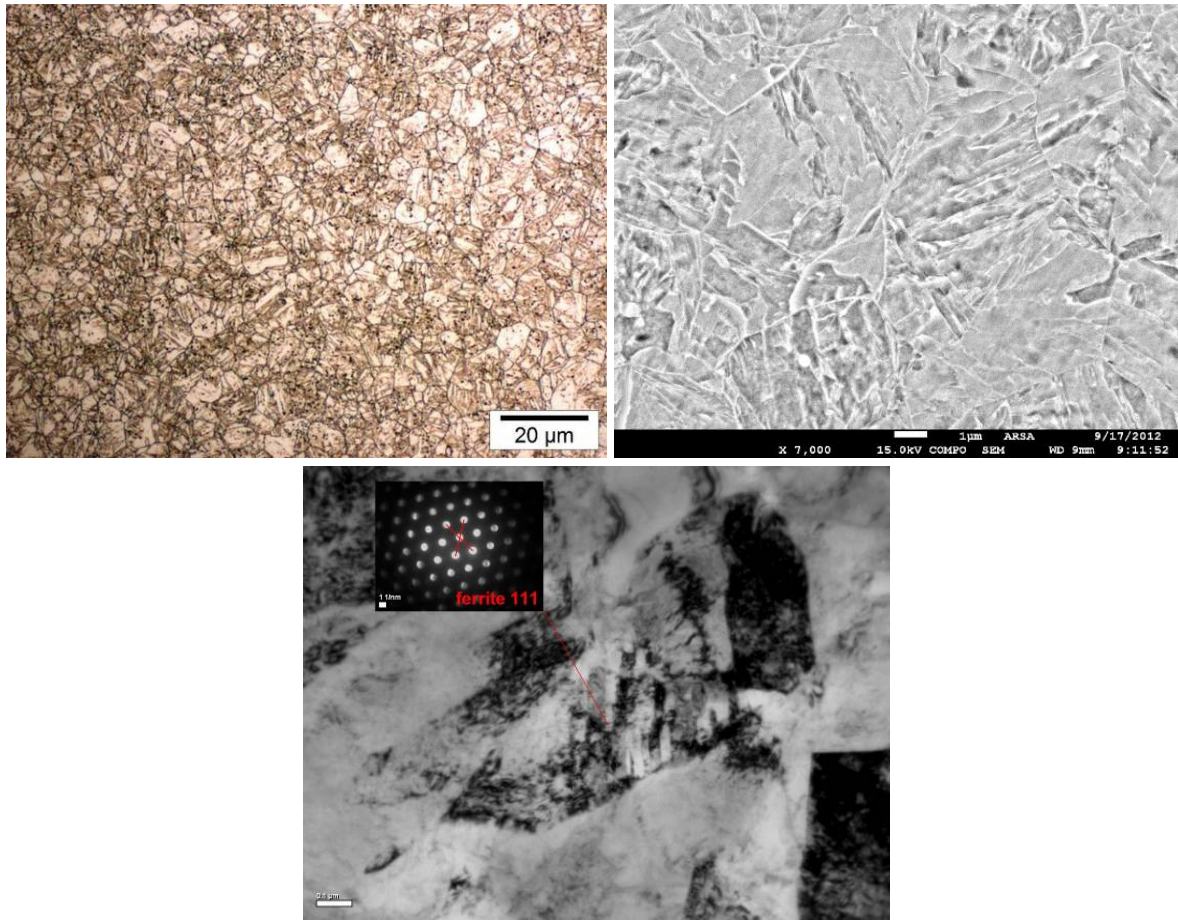
Figure 74 – Characterization of the martensite present in the microstructure after first annealing cycle: a) OM image after Dino etching [ARL'13]; b) SEM image after Metabisulfite etching; c) TEM image obtained on thin foil.
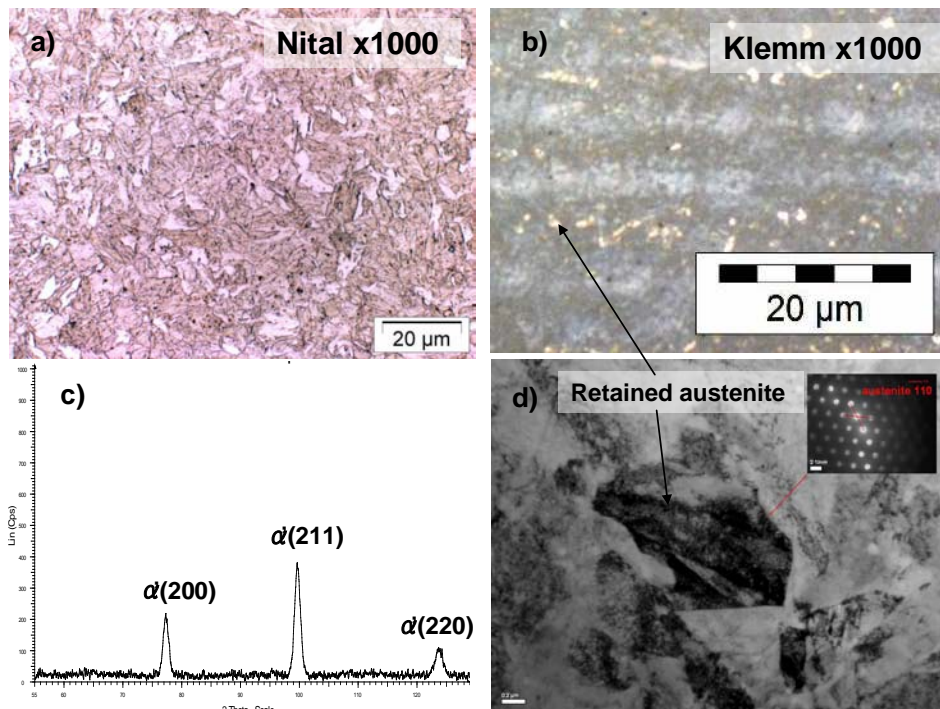
Figure 75 – Observation of retained austenite in the microstructure after first annealing cycle: a) OM image after Nital etching; b) OM image after Klemm etching; c) XRD spectrum; d) TEM image of retained austenite.

The presence of retained austenite after quenching can be due to the existence of Mn microsegregations. Therefore, Mn distribution was analyzed using EPMA and the results are presented in Figure 76. As expected, microsegregation of Mn can be observed. Nevertheless, the mean segregation level is only about 5.5 wt.% which is a rather low value in comparison with the measured Mn content in retained austenite islands by TEM-EDX (~9 wt.%). Locally, Mn composition can reach a value as high as 15 wt.% (red zones on the Mn map) which is more consistent with the level of Mn necessary for austenite stabilization. Finally, the obtained mean segregation level corresponds to a partition coefficient of about 1.2.

Quantitative X Image of Mn (wt.%)
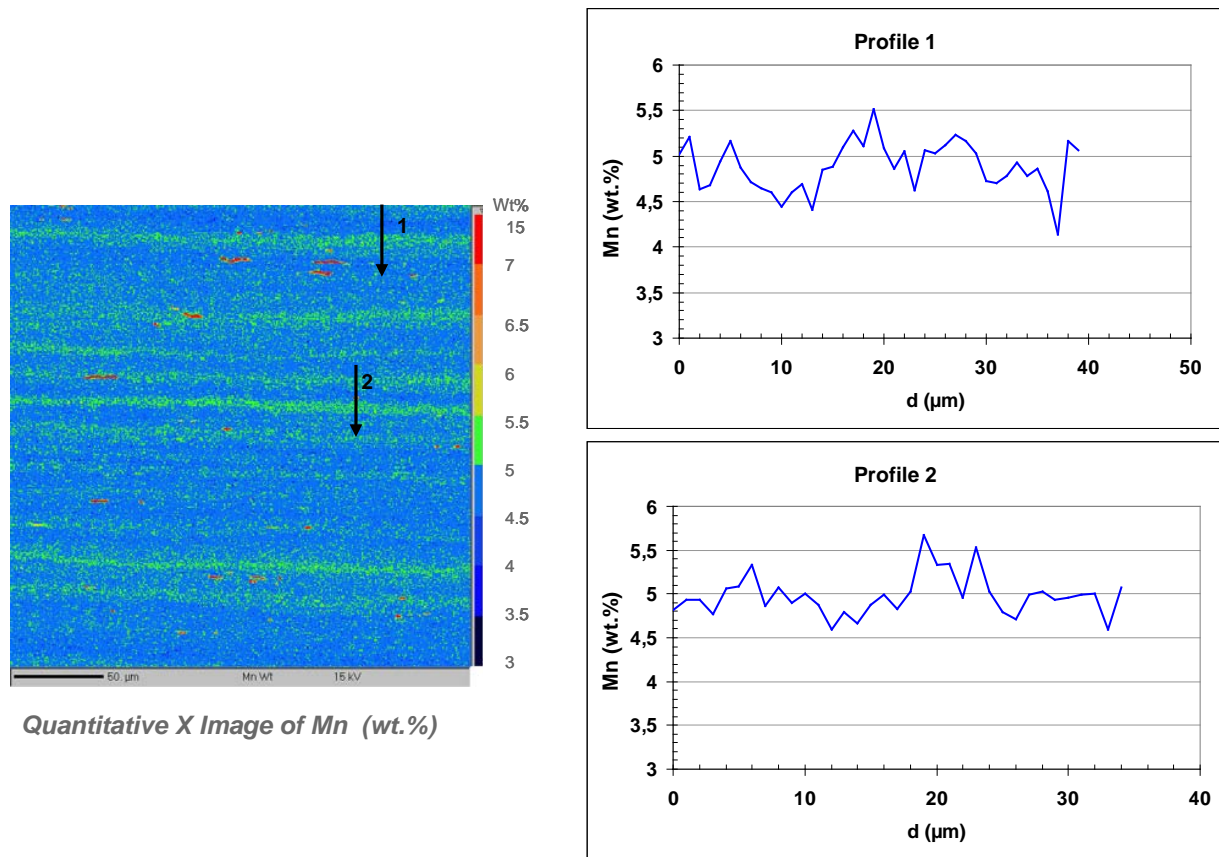
Figure 76 – EPMA quantitative analysis of Mn distribution in the microstructure after first annealing: a) quantitative Mn map (rolling direction is parallel to abscisse); b) Mn profiles along the lines 1 and 2.

3.2 Microstructure evolution during annealing at 650°C

Before going into the core of this section (microstructure characterization), a short recall of the previously obtained results is given hereafter.

First of all, the initial microstructure before intercritical annealing is fully martensitic without any prior deformation. Next, based on the thermodynamic calculations (Chapter 2.2), the expected stable phases are ferrite + austenite at 650°C and a ferrite + cementite mixture at low temperature. The austenite formation can thus result from different phase transformations including the formation of cementite at lower temperature and its dissolution at higher temperature. It is worth noting that cementite particles would act as preferential nucleation sites for austenite. Therefore, the objective of this section is to characterise and to analyse the microstructural evolution during annealing at 650°C and its role on the stabilization of retained austenite at room temperature.

3.2.1 Microsegregation evolution

Generally, the cold rolled high strength steels are subjected to microsegregations (especially Mn) due to the former processing conditions. These microsegregations result from the solidification process and introduce dispersions in the microstructure, which can have a significant impact on phase transformations, microstructure evolution and both mechanical and damage properties. Therefore, it is important to characterize the states of dispersions and microsegregations at different steps of heat treatment.

Beforehand, it was shown that the initial (before intercritical annealing) microstructure has Mn microsegregations. Hence, it was of interest to follow the evolution of Mn microsegregation during intercritical annealing. For that purpose, four samples (3min, 1h, 10h and 30h) were subjected to EPMA analysis. The obtained quantitative images of Mn distribution are shown in Figure 77. The complete data from EPMA analysis are presented in Annex 3.1.
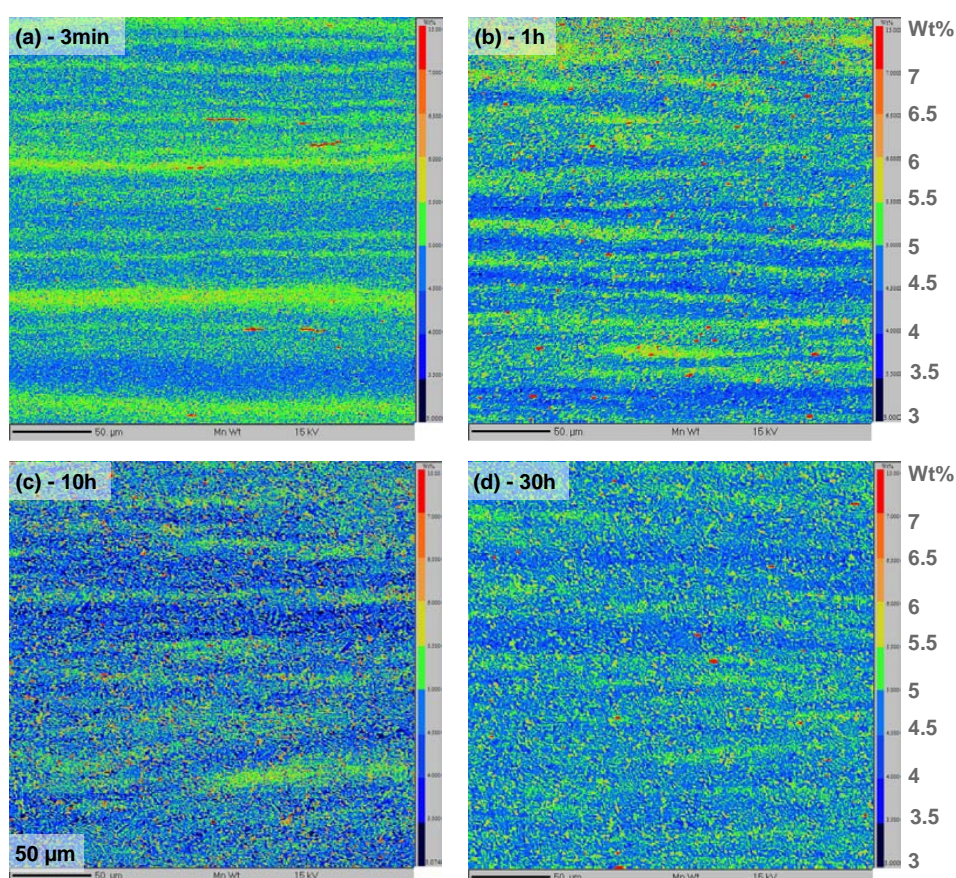
Figure 77 – Quantitative Mn maps obtained with EPMA for samples after annealing at 650°C for 3min, 1h, 10h and 30h.

Figure 77(a) and (b) show that Mn microsegregation is still evident after short time annealing (3min or 1h). For the samples with longer annealing time (10h and 30h) the situation is different (Figure 77(c) and (d)). An important redistribution of Mn happens during such a long intercritical annealing. These analyses suggest that there is a progressive homogenization of Mn in segregated bands during annealing, as observed in [LAV'49], [KRE'11]. In that case, the Mn diffusion length is expected to be of the order of the initial mean distance between bands, i.e. order of 10 µm. The long-range diffusion of Mn supposes that Mn should diffuse in a two-phase matrix of ferrite and austenite. This means that the effective diffusivity of Mn may be different from that in pure ferrite and in pure austenite. This phenomenon was already discussed in the work of Arlazarov et al. [ARL'12-1]. It was shown that such long-range Mn homogenization

was controlled by an apparent diffusivity similar to the one in ferrite. Both the small segregated band spacing and the ultra-fine size of microstructure constituents are supposed to enhance this phenomenon in the particular case of MMS.

It is worth noting that another type of Mn partitioning may occur at smaller scale. It is mainly linked to the interactions between Mn and migrating α/γ interface during austenite growth. This partition is driven by short-range diffusion and depends on temperature and microstructural parameters. This topic will be discussed more deeply later using more precise data of TEM hypermaps.

3.2.2 Evolution of cementite precipitation state

Carbides were first analyzed during heating process using interrupted cycles (heating to the temperature followed by He quench). Three different temperatures were considered 550°C, 600°C and 650°C. The observations were done on TEM replicas. The Mn content of carbides was measured by EDX. All the obtained results can be found in Annex 3.2. Figure 78 highlights only the most significant ones.
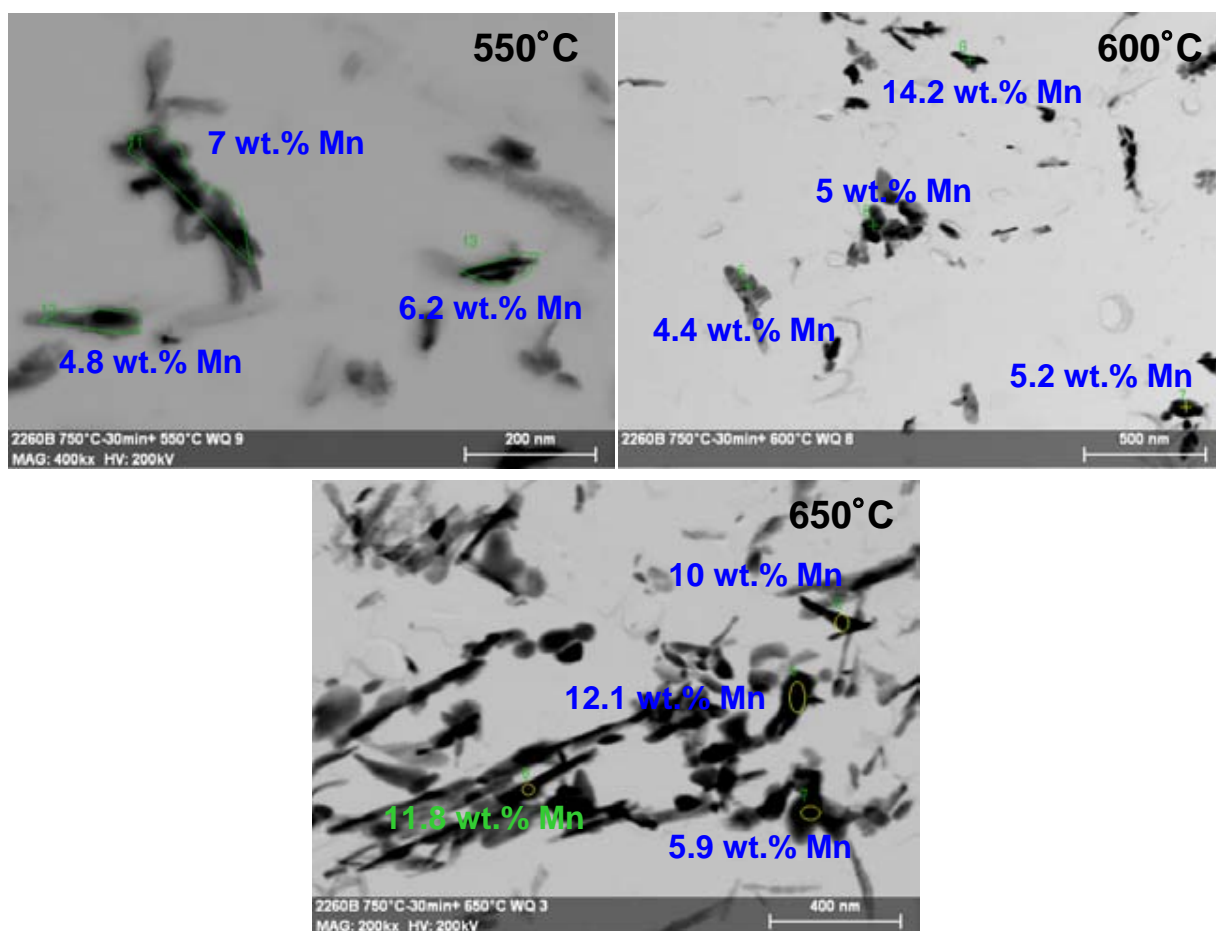
Figure 78 – TEM images on replicas of the samples obtained with different reheating temperatures: 550, 600 and 650°C. Mn content of carbides measured with EDX is shown directly on the images.

The mean Mn content of carbides at 650°C was determined from EDX measurements. Its value was estimated to be about 10 wt.%. Then, the time evolution of carbides during holding at 650°C (3min, 1h, 2h and 3h) was analyzed using TEM thin foils. The main results are presented in Figure 79.
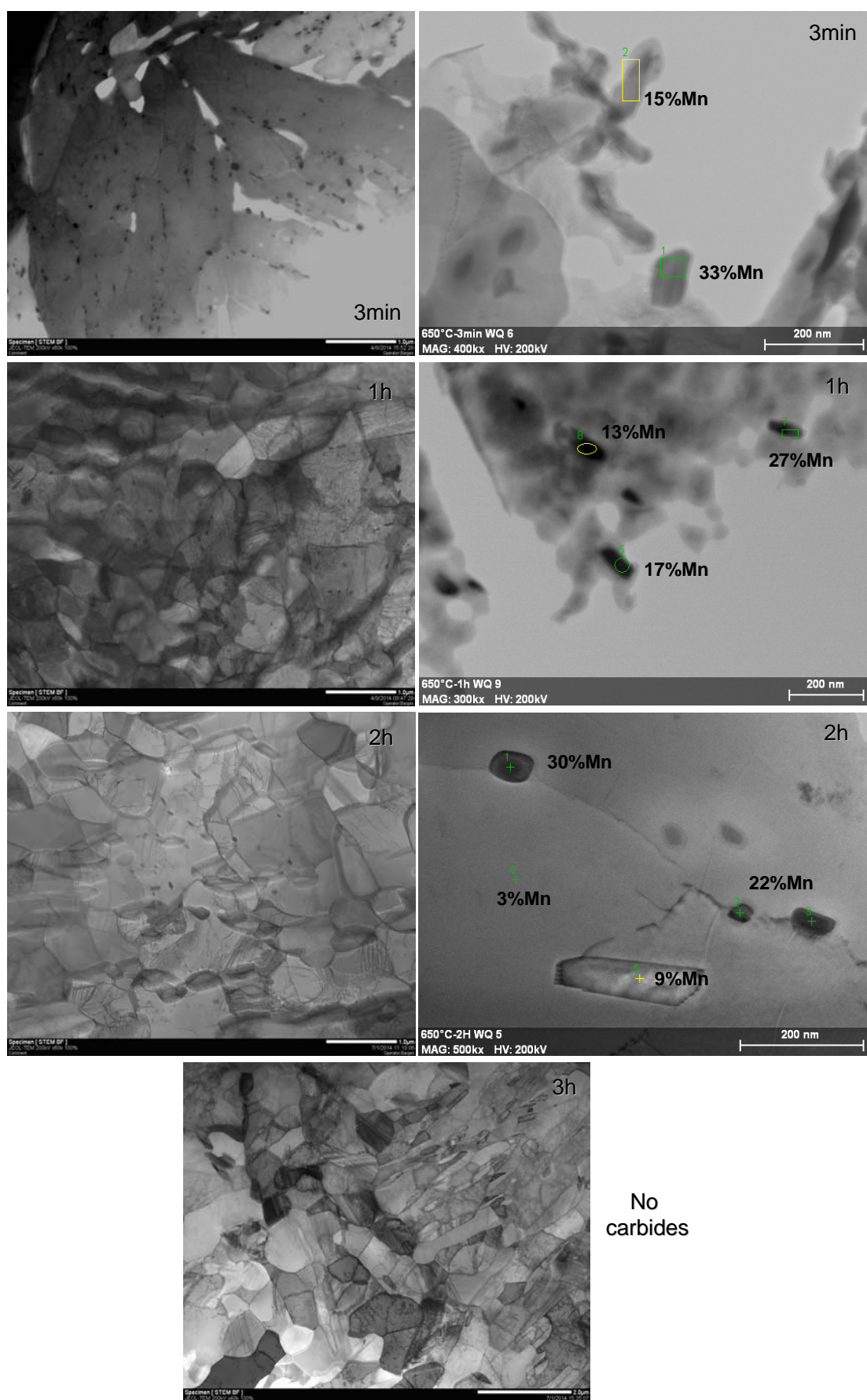
Figure 79 – TEM images obtained on thin foils of samples with 3min, 1h, 2h and 3h holding time. Carbides observation was particularly targeted. Mn EDX measurements are directly presented on the images.

In a general manner, the carbides precipitation state depends on time at 650°C. For short holding time (3min), high volume fraction was observed. In terms of Mn content, there were two populations of carbides: one with high Mn content around 30 wt.% and another one with lower one about 15wt.%. Also, two types of morphology were detected: rod one and polygonal one (more or less rectangular). After 1h holding time, the volume fraction of carbides decreases, but there are still a certain amount of carbides with bimodal Mn content and shape. After 2h holding time, the sample can be considered as almost carbide free: only a few carbides with high Mn amount (~25 wt.%) remains in some areas. Finally, carbides are completely dissolved after 3h holding. It is also important to note that it was not possible to establish any link between carbides morphology and their Mn content from the analyzed data.

Using Convergent Beam Electron Diffraction (CBED) and Selected Area Electron Diffraction (SAD) it was determined that crystallographic structure of the observed carbides corresponds to cementite. This is coherent with the conclusions of Luo et al. [LUO'11], [LUO'13].

These results show the presence of cementite at 650°C for holding time as long as 2 hours. This contrasts with equilibrium thermodynamic calculations carried out in Chapter 2.2. Indeed, the temperature of complete cementite dissolution was determined to be around 610°C. This can be attributed to kinetics effects and will be clarified further by DICTRA simulations

3.2.3 Time-evolution of austenite and ferrite

The samples obtained after intercritical annealing at 650°C were firstly characterized by OM (Figure 80).
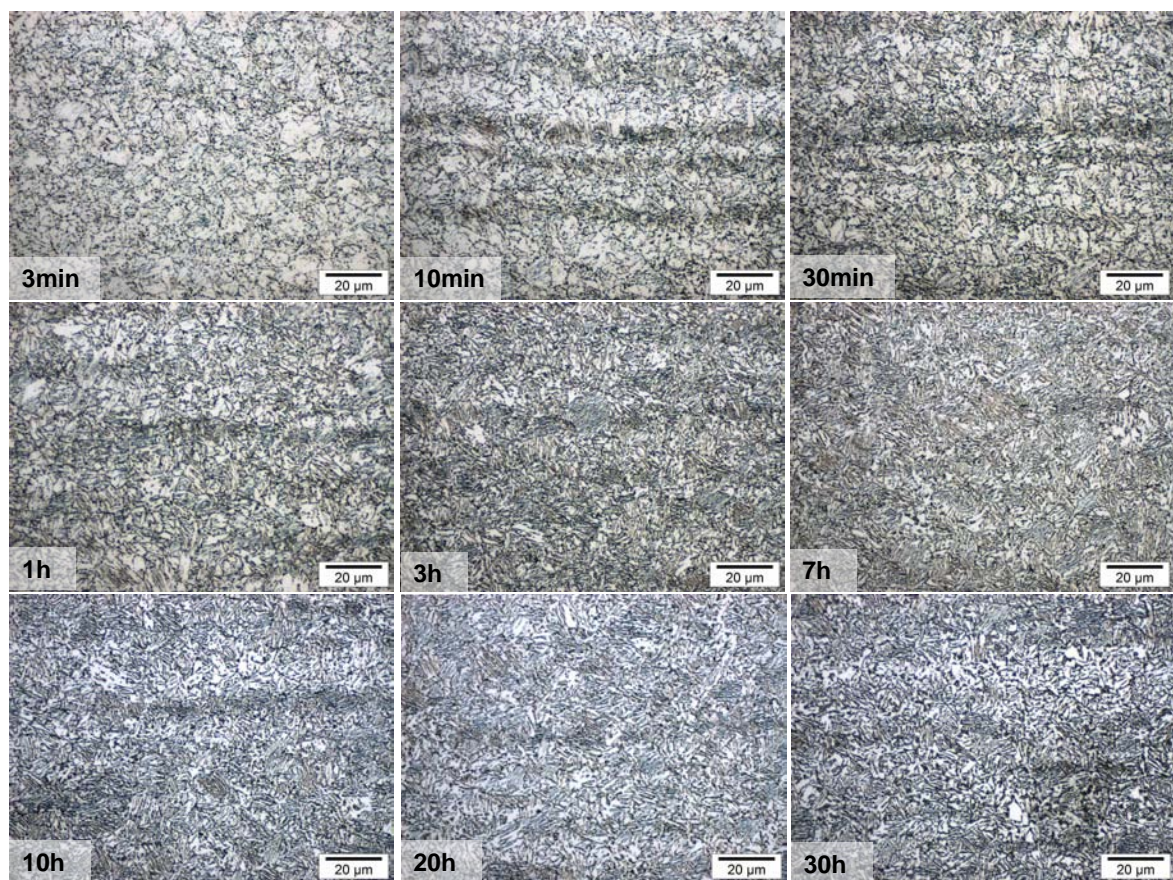
Figure 80 – Optical images of microstructures obtained with different holding time at 650°C. Dino etching [ARL'13] was used to reveal the microstructure.

Basically, a refined microstructure is evidenced by OM even after 30h holding. Thus, using OM it was only possible to get the macro vision of the microstructure. For more detailed analysis, all the microstructures were characterized using FEG SEM (Figure 81 and Figure 82). The explanation and details of the observed microstructures are given in the Figure 82. The latter shows microstructure after 10h holding at 650°C consisting of at least three phases: ferrite (F), retained austenite (RA) and fresh martensite (M). The detailed analysis of the microstructures leads to the following conclusions:

1) austenite (retained austenite and fresh martensite) and ferrite have two different morphologies: lath-like and polygonal ones;
2) at holding times longer than 3h, higher fraction of fresh martensite was observed and most of the martensite was polygonal,
3) it can be supposed that the polygonal ferrite grains results from a recrystallization process from the initial martensite structure. The first ferrite polygonal grains were observed already after 30min holding. Recrystallization of martensite is a complex subject and need a dedicated study which is not in the scope of this work.
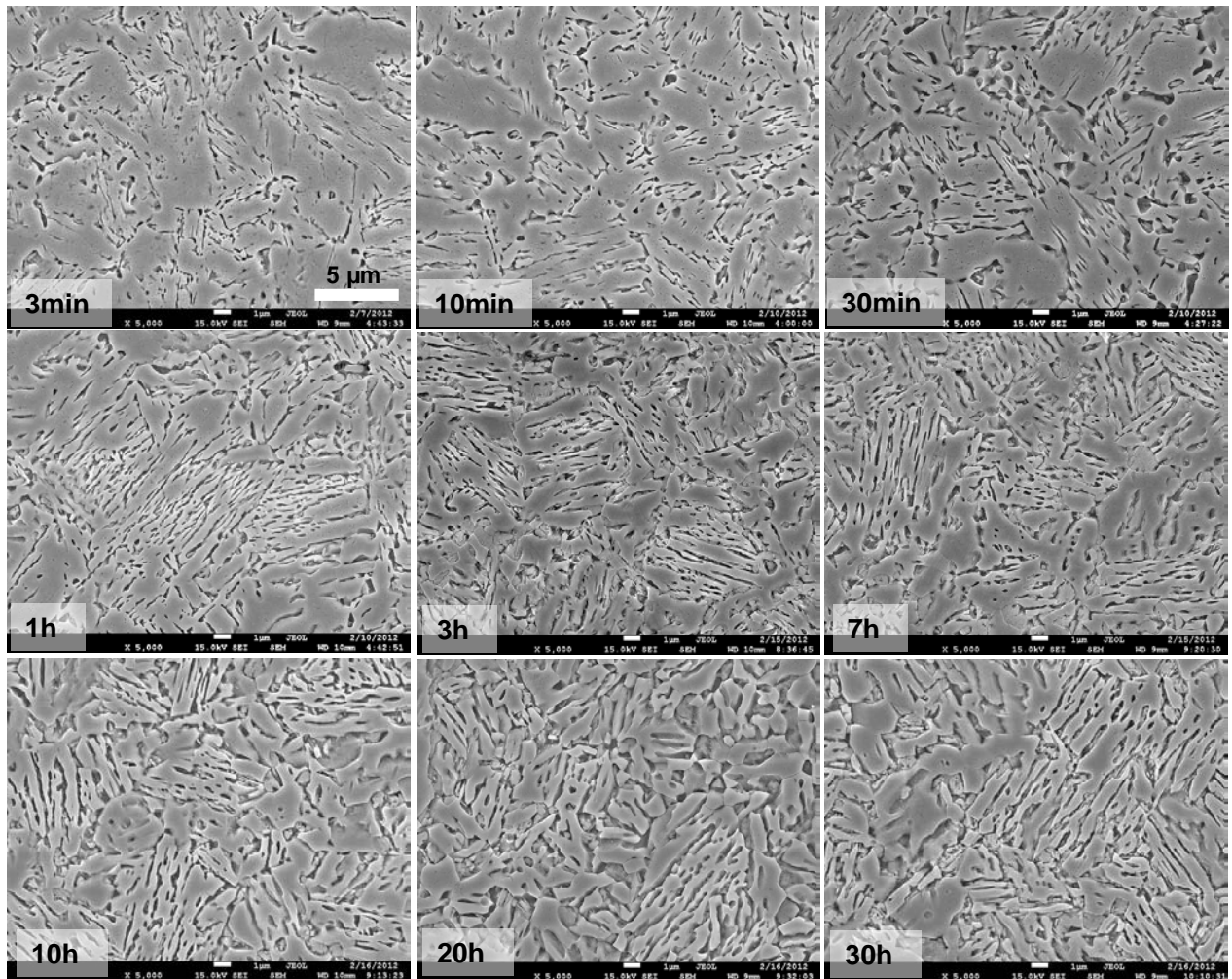
Figure 81 – SEM images of microstructures obtained with different holding time at 650°C. Dino etching was used to reveal the microstructure.
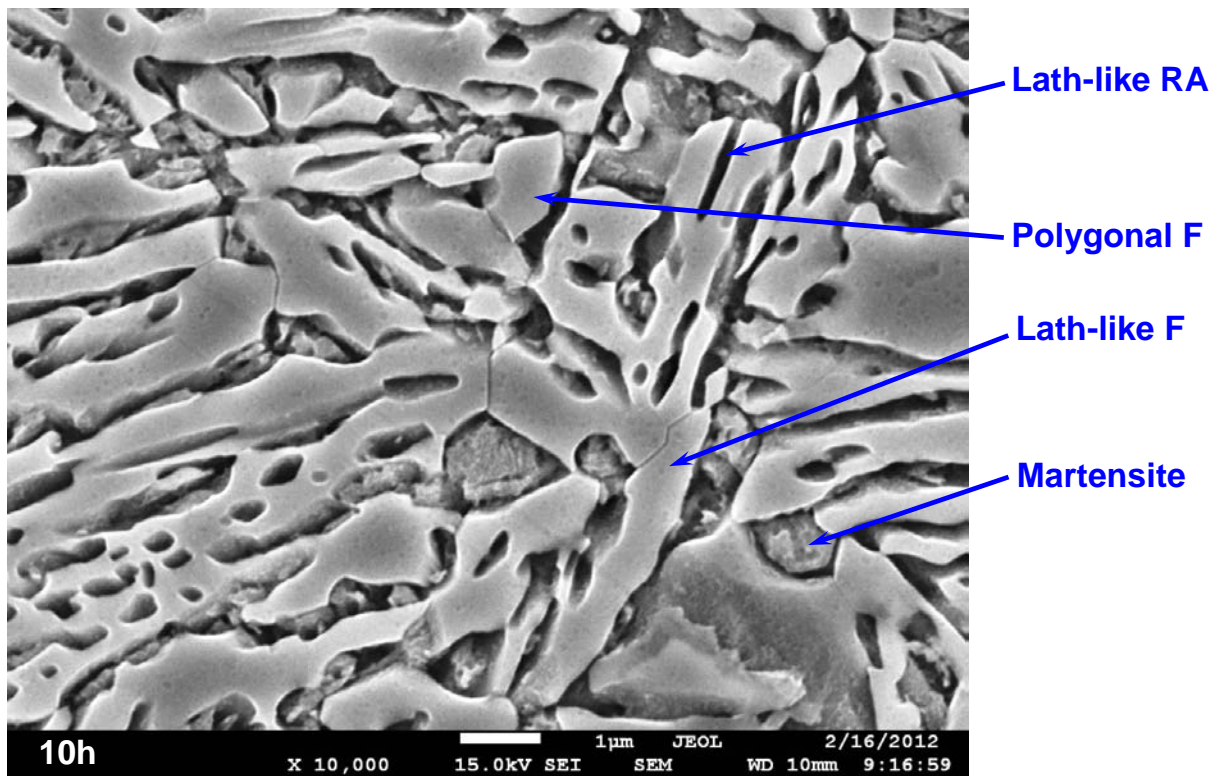
Figure 82 – SEM image of sample annealed for 10h at 650°C. Microstructure revealed with Dino etching contain at least three phases: ferrite (F), retained austenite (RA) and martensite.

The time-evolution of austenite fraction a 650°C that corresponds to retained austenite and fresh martensite (FM+RA) after quenching was evaluated by image analysis (Aphelion software) from SEM pictures. Figure 83 presents the obtained results. The corresponding kinetics is also compared with the equilibrium fraction of austenite calculated using Thermo-Calc.
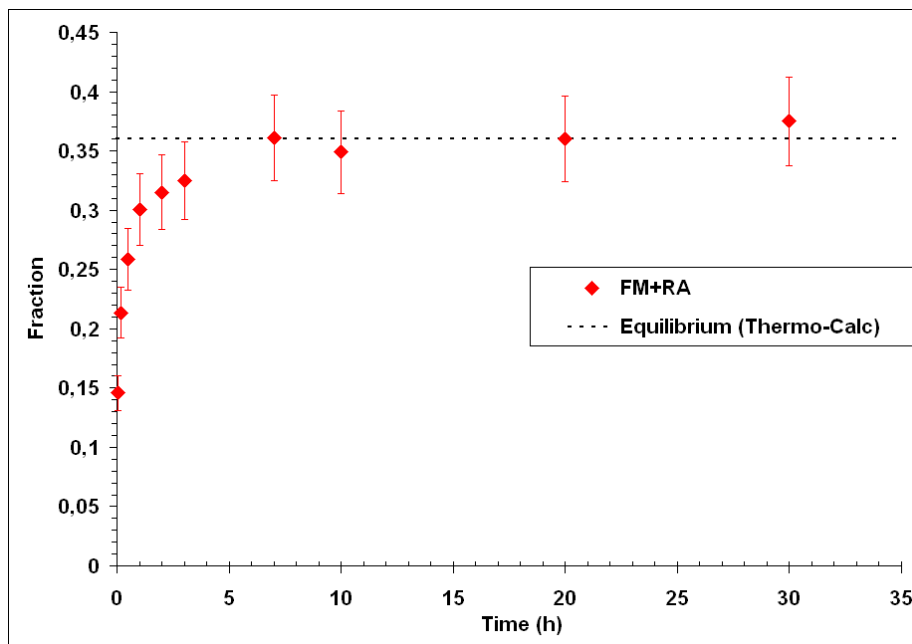
Figure 83 – Evolution of austenite fraction with holding time at 650°C. In the final structure after quench austenite is represented by retained austenite and fresh martensite (FM+RA). Equilibrium fraction of austenite at 650°C calculated using Thermo-Calc is given by the dashed line.

The rate of austenite transformation is very rapid in the beginning and then becomes more and more sluggish. The equilibrium fraction is achieved after 7h holding. The observed austenite evolution is apparently consistent with the work of Speich et al. [SPE'81], in which it was shown that there are 3 stages for austenite growth: first two rapid ones that are controlled by C and Mn diffusion in ferrite and a third sluggish stage that is controlled by Mn homogenization in austenite.

The analysis of Mn distribution between austenite and ferrite as a function of time was done using local TEM-EDX measurements and TEM-EDX hypermaps. More complete information from the overall TEM-EDX analysis can be found in Annex 3.3. Figure 84 presents the hypermaps for the samples with 1h, 2h, 3h and 10h holding time. On each hypermap the Mn-rich zones, considered to be RA or FM, and several Mn-depleted zones (F) were selected and quantified. An example of such a selection for samples after 2h and 3h holding at 650°C is shown in Figure 85. The analysis of at least 10 austenite and 5 ferrite zones of the hypermap was done for each sample. The average values of Mn content in both austenite and ferrite of different samples are reported in Table 4.

As calculated with Thermo-Calc software, the equilibrium Mn contents of ferrite and austenite at 650°C are 2.3 and 9.1 wt.%, respectively. From data in Table 4, it can be seen that Mn content of ferrite decreases with holding time and achieve the equilibrium value after 10h. In a general manner, Mn content in austenite decreases with time from 10 wt.% to 8.5 wt.%. The high Mn value at the beginning of transformation may be explained from the fact that austenite nucleates preferentially in Mn rich regions such as carbides. After longer time, the measured Mn content in austenite is close to the equilibrium one (8.5 wt.% versus 9.1 wt.%). As a consequence and surprisingly, the system reaches the equilibrium after a relatively short time of 10h; the equilibrium being defined from the calculated volume fraction of phases and from their respective compositions.

Table 4 – Mn content in austenite and ferrite zones of different samples determined from direct EDX measurements and hypermaps.

Reference	Time, s	Measured by EDX	
		Mn_F, wt.%	Mn_A, wt.%
3min WQ	180	4.3	10.0
1h WQ	3600	4.1	9.3
2h WQ	7200	3.5	8.9
3h WQ	10800	2.8	8.9
10h WQ	36000	2.3	8.7
30h WQ	108000	2.3	8.5
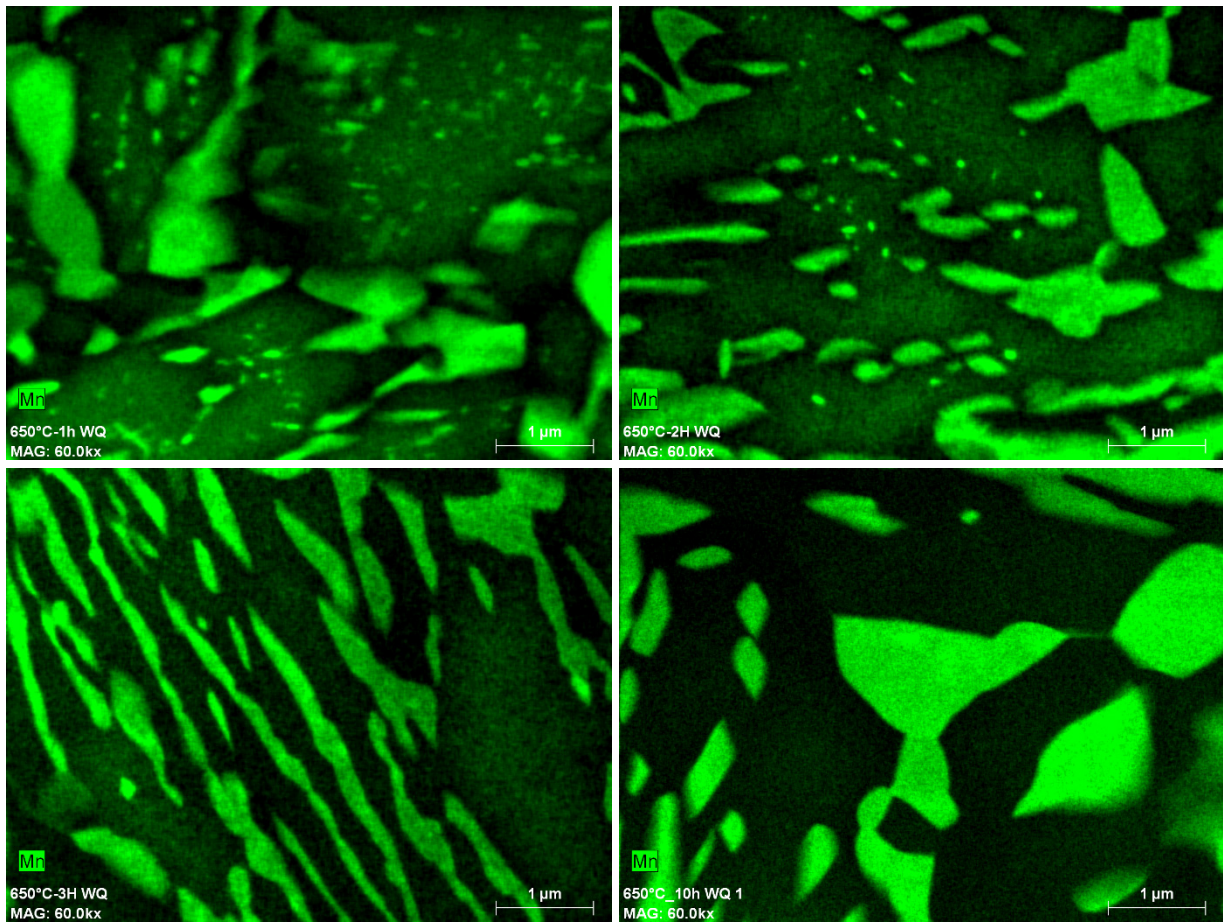
Figure 84 – EDX Mn hypermaps obtained in TEM for the 1h, 2h, 3h and 10h samples.
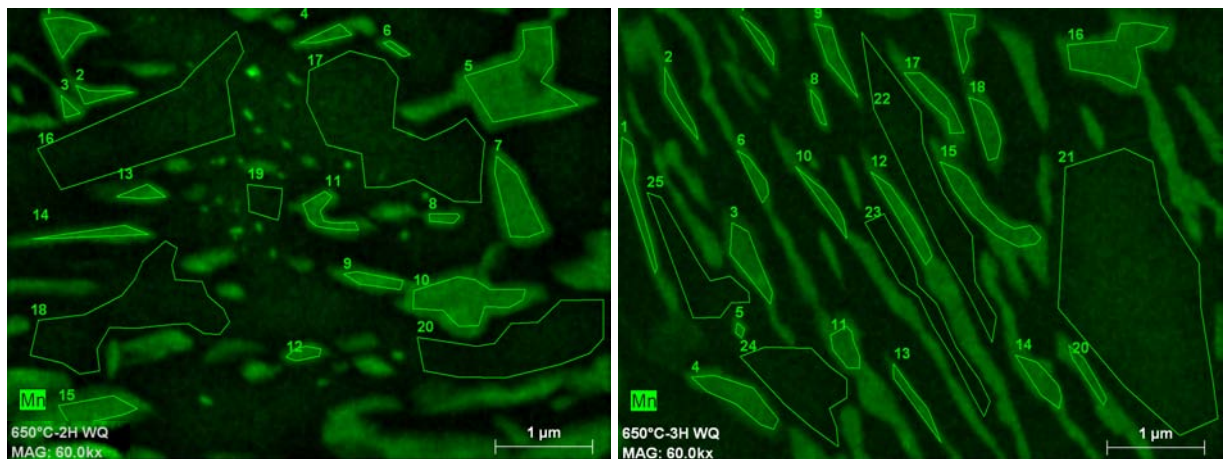
Figure 85 – Examples of selected areas for Mn analysis: at left – 2h sample, at right – 3h sample.

It was also decided to measure the level of carbon content in austenite for the samples with 1h and 30h holding time at 650°C using NanoSIMS technique. Some areas of $10 \times 10 \ \mu m^2$ were scanned using a focused Cs^+ primary ion beam (<1 pA) in the NanoSIMS 50 machine and the SIMS intensities were measured and plotted as maps (in particular ^{12}C ion maps are necessary for the estimation of carbon content). Image analysis was then performed on the obtained ^{12}C ion maps and the evaluation of carbon content was done according to the method described in chapter 2 that is mainly based on the comparison of the intensities between the analyzed sample and a reference sample with known carbon content. The carbon content was estimated for each selected zone in the ^{12}C ion maps in order to evaluate the dispersion of C content. Two ^{12}C ion

maps and the associated distribution of measurements for 1h and 30h samples are shown in Figure 86 and Figure 87.
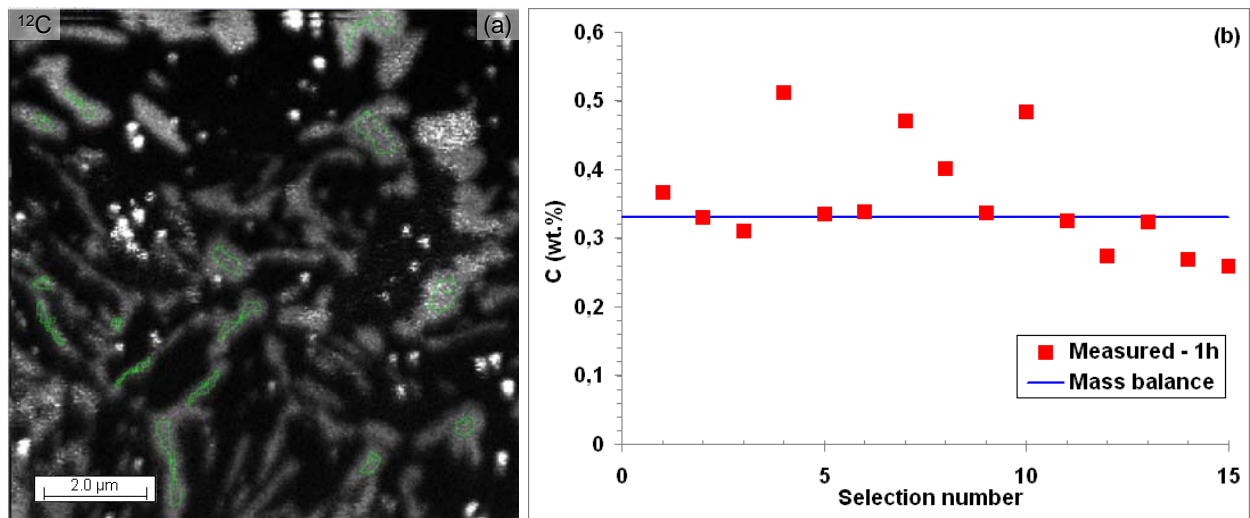
Figure 86 – NanoSIMS results for the sample with 1h holding time: (a) - ^{12}C ion map with selected zones for the intensity analysis; (b) - estimated C content of each selected area in map (a) (red square points) and calculated using mass balance (blue line).
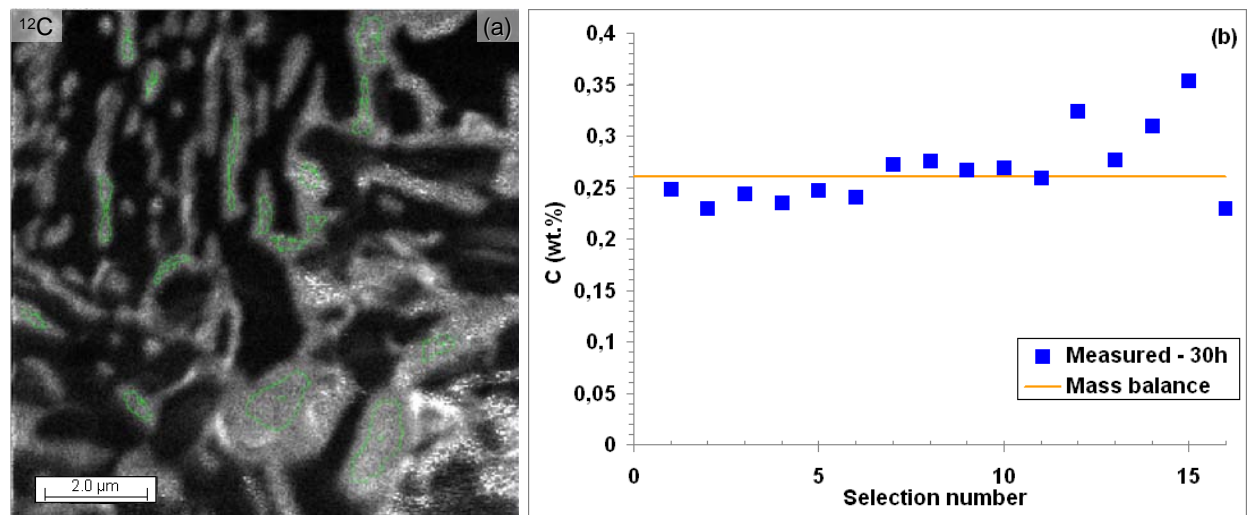
Figure 87 – NanoSIMS results for the sample with 30h holding time: (a) - ^{12}C ion map with selected zones for the intensity analysis; (b) - estimated C content of each selected area in map (a)(blue square points) and calculated using mass balance (orange line).

It is observed that the measured carbon contents show a relatively low scatter. The mean carbon content measured in both samples after 1h and 30h holding is close to 0.36 wt.% and 0.27 wt.%, respectively. These values correspond very well to the C content calculated from the mass balance that neglects carbides (Figure 86 and Figure 87) and thus suggests that a major part of carbides are completely dissolved after one hour treatment at 650°C.

3.2.4 Time-evolution of retained austenite and martensite

The volume fraction of retained austenite was evaluated by saturation magnetization measurements and that of fresh martensite was deduced from image analysis. The evolutions of retained austenite and martensite fractions with holding time at 650°C are shown in Figure 88.
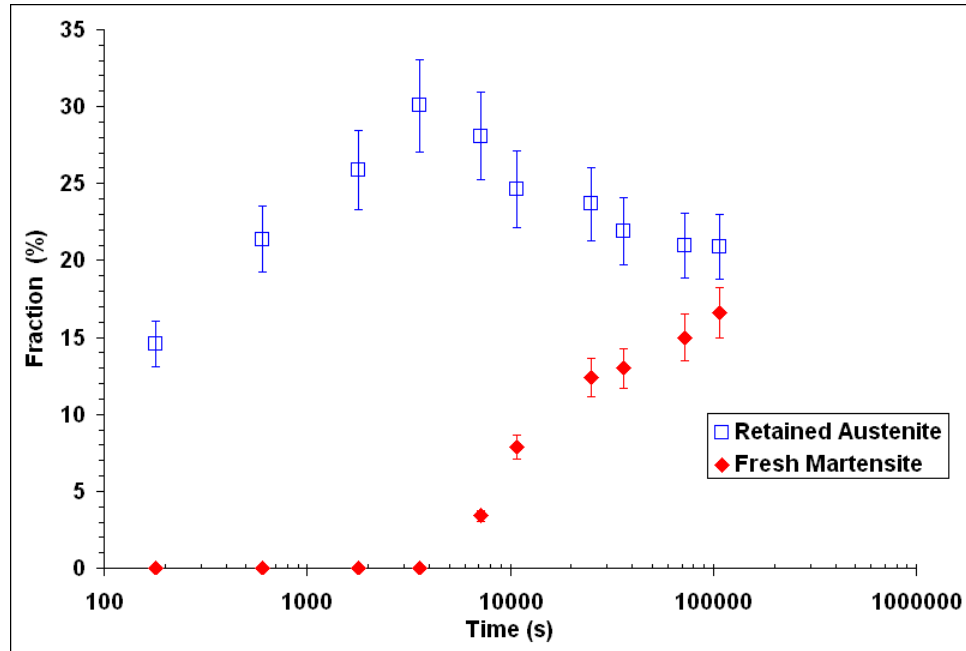
Figure 88 – RA and FM fractions as a function of holding time at 650°C.

The time-evolution of both retained austenite and fresh martensite can be divided into three successive steps:
- in the beginning of transformation, i.e. for times shorter than 1h, all the prior austenite was stabilized at room temperature,
- a decrease of RA and a concomitant increase of FM is observed for times between 1h and 10h,
- a final stage where both RA and FM seems no longer to evolve.

In addition, evolution of RA fraction with holding time has a peak-type form, which was already reported in the literature [HUA'94], [ARL'12-1] without any clear explanations. Later in this chapter, it will be shown that this temporal retained austenite evolution is a fair indicator of the mechanism of austenite stability.

Some TEM analysis of the selected samples (3min, 1h, 2h, 3h, 10h and 30h) were also performed in order to study more finely the different phases and to determine the mean Mn content in each phase. Figure 89, Figure 90 and Figure 91 present the TEM images with the indexed diffraction patterns in mode STEM (CBED) and the measured Mn content of certain phases for all the samples.
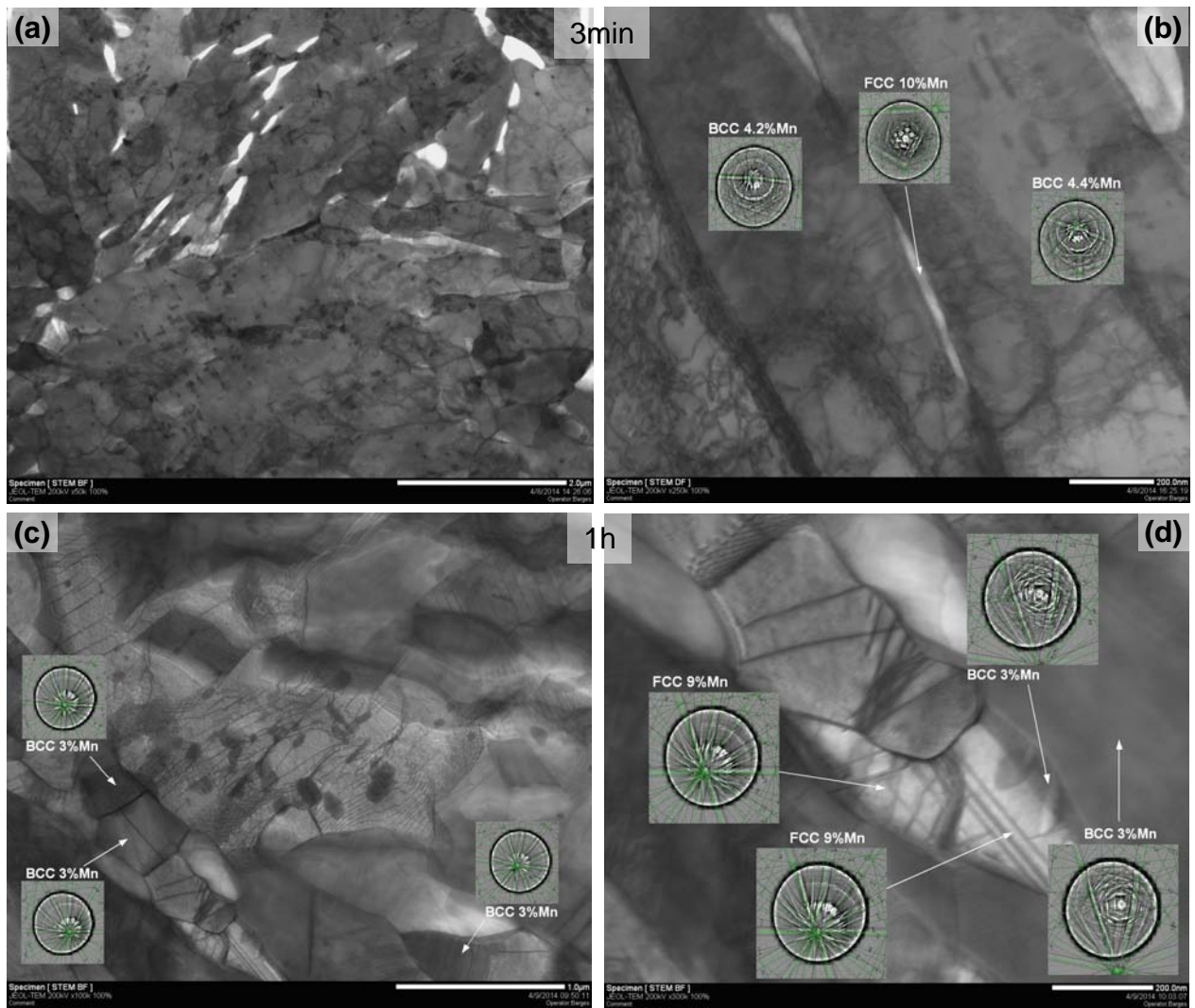
Figure 89 – TEM images of samples after 3min and 1h of holding at 650°C. The diffraction patterns in mode STEM show with arrows different phases (BCC – ferrite and FCC – retained austenite). The Mn content of different phases determined with EDX is put directly on the images.

The analysis of the sample after 3min of holding (Figure 89(a) and(b)) shows that ferrite (indexed as BCC structure) contains a high density of dislocations and some features present also a substructure. The dislocation density decreases with the increase of holding time. However, even after 30h of holding, certain grains still contain some dislocations. The presence of substructure and the decrease of dislocation density with time are certainly the indicators of martensite recovery phenomena, as already seen in the past by Speich [SPE'69] [SPE'72]. Surprisingly, it appears that recovery is delayed to longer times. The high Mn content is supposed to be the reason for such sluggish recovery kinetics. In fact, Mn effect is thought to be double. First, the increase of Mn results in lower intercritical temperature range, thus recovery of martensite happens with lower driving force. Second, Mn atoms can interact with dislocations or grain boundaries by a solute drag effect [GOR'62], [PET'00], [REI'06].

It can be seen in Figure 89(b) that ferrite of the sample with 3min holding time has a Mn content of about 4 wt.% and that the size of formed austenite is ultra fine. The sample with 1h holding (Figure 89(c) and (d)) presents coarser austenite and a lower Mn content in both ferrite and retained austenite. The retained austenite was detected further in all the samples. Its mean Mn content was estimated between 9 and 11 wt.%. In Figure 90(b) (2h sample) certain austenite

grains present some features inside the grain with lath morphology. Using CBED it was possible to distinguish some austenitic twins (FCC(Twins)) and alpha prime martensite (BCC(M)). Figure 90(b) also reveals some dislocations in the ferrite grain (outlined by the blue line) adjacent to the austenite grains. It is thought that this is due to the accommodation of transformation stress.

Figure 90(c) and (d) (3h sample) show the coexistence of ferrite (BCC) and retained austenite (FCC) as well as their double morphology (lath-like and polygonal). A high dislocation density of certain ferrite grains can be also observed. Finally, presence of lath martensite (BCC(M)) was clearly revealed in Figure 91 (10h and 30h samples).
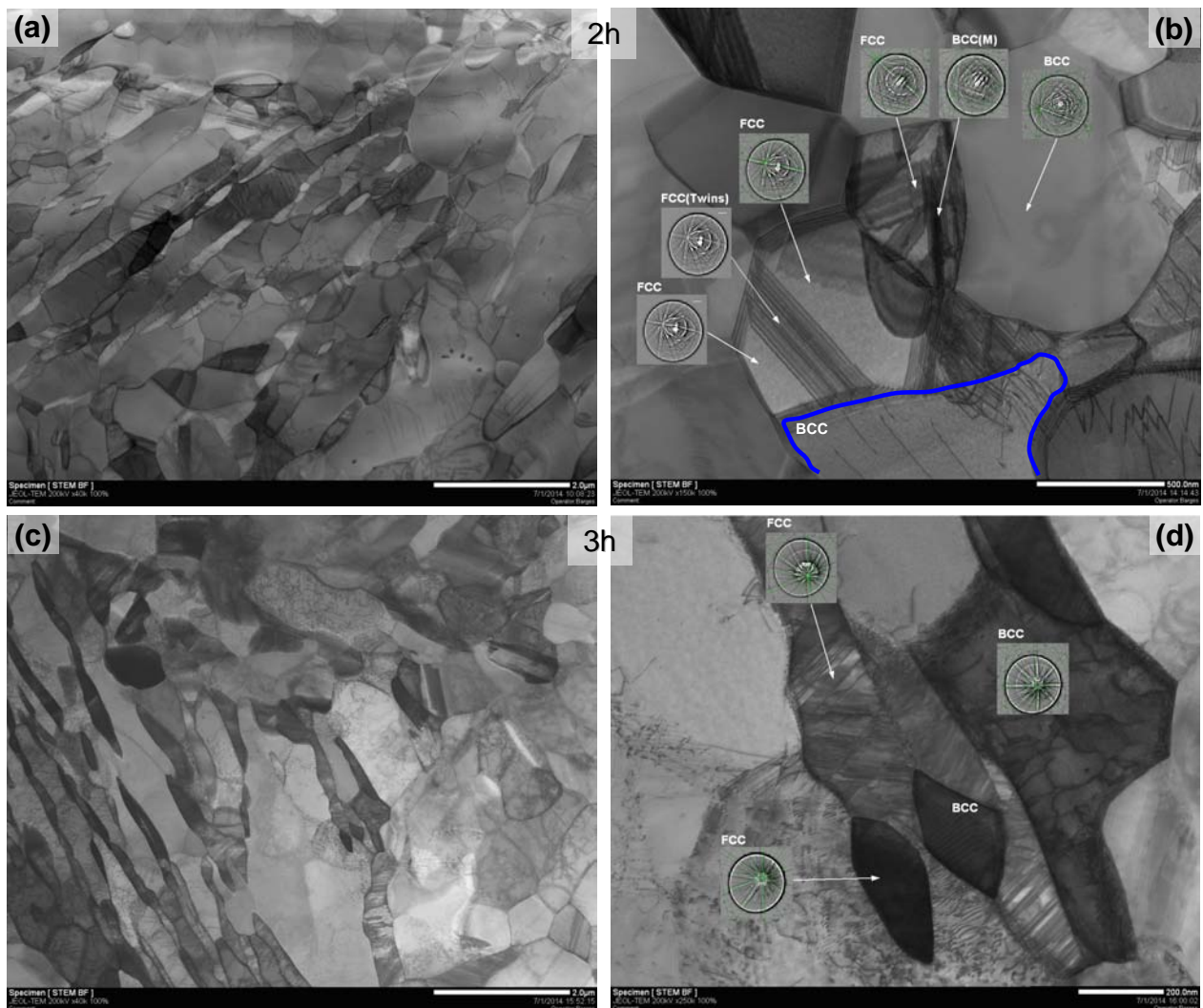
Figure 90 – TEM images of samples after 2h and 3h of holding at 650°C. The diffraction patterns in mode STEM show with arrows different phases (BCC – ferrite, BCC (M) – fresh martensite and FCC – retained austenite). The Mn content of different phases determined with EDX is put directly on the images
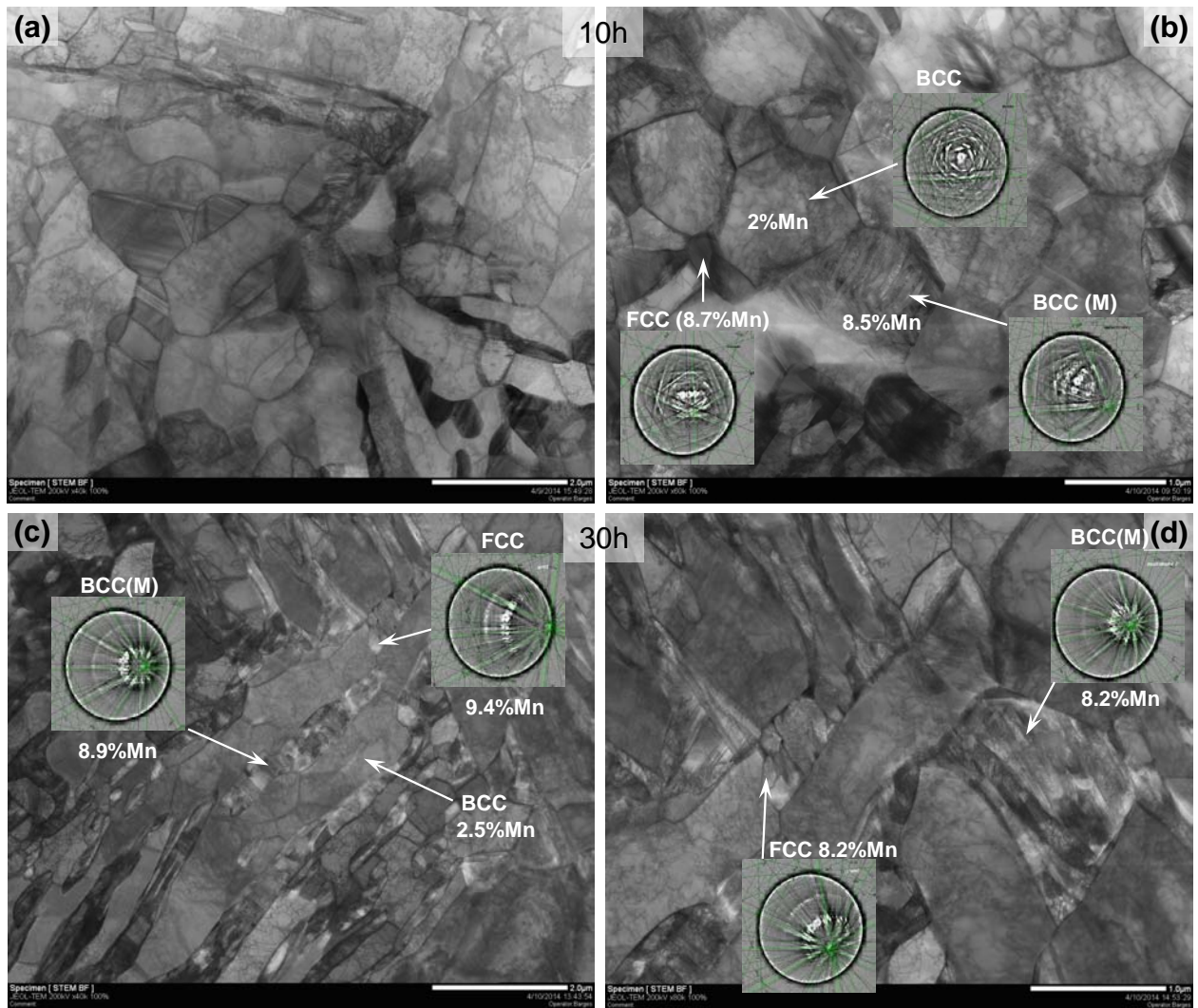
Figure 91 – TEM images of samples after 10h and 30h of holding time at 650°C. The diffraction patterns in mode STEM show with arrows different phases (BCC – ferrite, BCC (M) – fresh martensite and FCC – retained austenite). The Mn content of different phases determined with EDX is put directly on the images.

3.2.5 Geometrical and topological aspects

The analysis of both the size and morphology of phases is a key point to better understand the microstructure formation. By using SEM images at relatively high magnification (×10000 – example in Figure 59) it was possible to perform manual measurements of the size of austenite by considering martensite and retained austenite (FM+RA) in the final microstructure. For each holding time, 200 austenite features were measured by image analysis from SEM images. Both the lath and polygonal like morphologies were distinguished and their mean size was measured. Table 5 summarizes the measurements of size and includes the volume fraction of austenite at a given time for holding at 650°C.

It is clear that the low statistics and manual operations lead to uncertainties regarding the size measurements. Although, the values obtained for lath features are in rather good agreement with those found by Luo et al. [LUO'11].

Table 5 – Fraction and size measurements of FM+RA features obtained from the image analysis of FEG SEM images.

Reference	Time (s)	Fraction	Size of FM+RA features (µm)		
		FM+RA (%)	Polygonal	Lath	Global mean
3min WQ	180	15.4	0.24	0.075	0.16
10min WQ	600	20.6	0.23	0.079	0.16
30min WQ	1800	21.6	0.37	0.110	0.24
1h WQ	3600	27.3	0.37	0.110	0.24
2h WQ	7200	31.5	0.38	0.140	0.26
3h WQ	10800	32.5	0.41	0.140	0.27
7h WQ	25200	36.1	0.45	0.140	0.30
10h WQ	36000	34.9	0.46	0.170	0.31
20h WQ	72000	36.0	0.57	0.210	0.39
30h WQ	108000	37.5	0.68	0.210	0.45

Based on the microstructural investigations, it was of interest to discuss the observed double morphology (lath-like and polygonal) of ferrite and austenite. The origin of the lath like morphology of ferrite and austenite was already presented in the chapter 1.1.1.3 and is undoubtedly attributed to the initial non-deformed lath martensite structure. In previous works [NEH'50], [KOO'76], [KIM'81], [LAW'80] it was observed that austenite nucleates at lath and packet boundaries and grows preferentially along the laths, consequently producing a structure with lath-like morphology of ferrite and austenite. However, the complete vision on the sequence of carbide precipitation and austenite nucleation and growth was not completely obvious. Based on the different observations it was proposed to consider the following mechanism of austenite nucleation and growth:

- precipitation of carbides along the laths, packets boundaries and on the triple junctions of prior austenite grains;
- nucleation of austenite on the previously precipitated carbides (along the laths, packets boundaries and on the triple junctions);
- preferential growth of austenite nucleated at laths and packets boundaries along these units.

Comparison of the austenite formation mechanisms from the initial fresh martensite structure (not deformed) and from the deformed structure of MMS is schematically described in Figure 92. Figure 92(A) show the nucleation and formation of austenite from an initial non deformed martensite. In this case, as stated previously, austenite will nucleate and grow on both the laths, packets boundaries and on the triple junctions of prior austenite grains. Consequently, the final morphology of the austenite is double: lath-like and polygonal features. In the case of deformed martensite structure (Figure 92(B)) the scenario is different. Cementite precipitation is concomitant with recovery and recrystallization of ferrite. Therefore, cementite precipitates on the prior austenite grains, on the laths or packets boundaries, but also on the boundaries of new grains and/or restoration cells. The recrystallization before austenite transformation is partial. This was observed in the earlier study [ARL'12-2]. In this condition, austenite nucleates preferentially on the cementite which is located on the recrystallized ferrite boundaries. In the same time, there are also two other possible sites for austenite nucleation: prior austenite grains and laths or packets boundaries. Finally, further austenite growth and ferrite recrystallization result in the polygonal microstructure of ferrite and austenite. Comparison of the experimentally obtained microstructures from the initial martensite structure (not deformed) and from the deformed structure of MMS is shown in Figure 93. It should be stated that the both microstructures have similar fraction of austenite (martensite + retained austenite). The obtained morphologies correspond well to those described by the both mechanisms in Figure 92.

However, it should be noted that the scheme proposed in Figure 92 cannot be generalized. Cementite precipitation, recrystallization and austenite formation depend on several parameters like heating rate and path, initial structure and steel composition. Therefore, depending on these parameters the morphology of the final microstructure can be different.
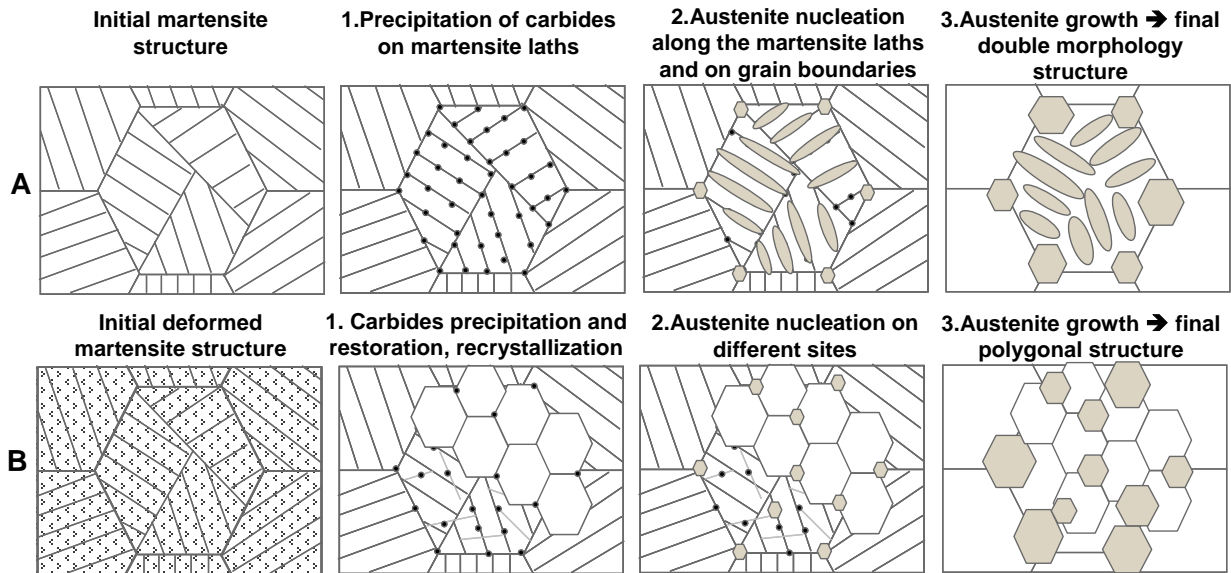
Figure 92 – Scheme of the austenite nucleation and growth in: A – non-deformed martensite structure and B – deformed structure.
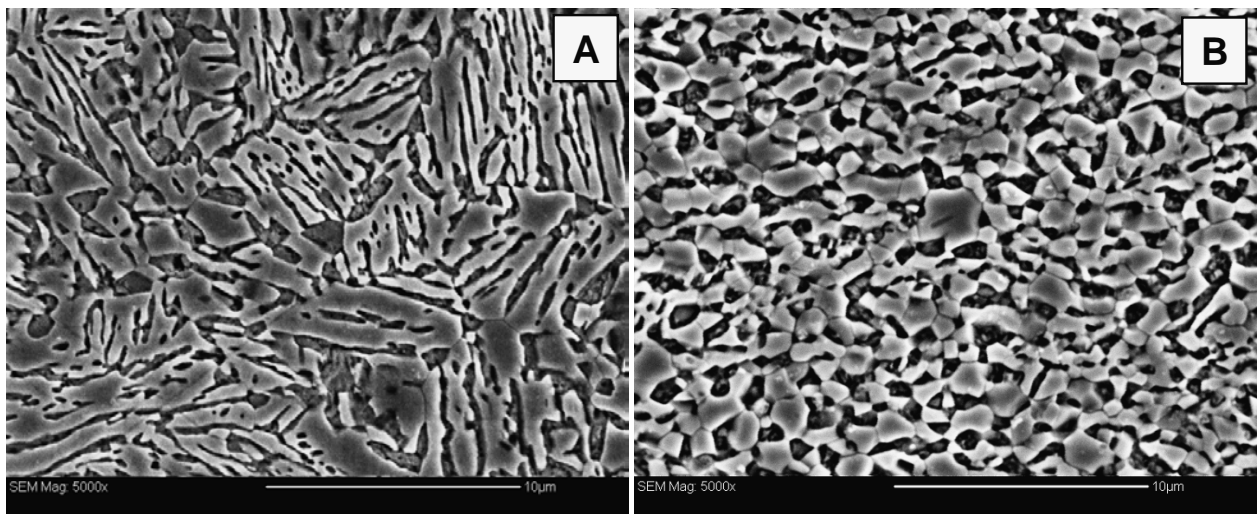
Figure 93 – Comparison of the microstructures obtained by the annealing of an initial A – non-deformed martensite structure and a B – deformed structure. Microstructure revealed with Marshall etching and observed in SEM (light grey color corresponds to ferrite and black (or deep grey) areas are martensite and/or retained austenite).

3.2.6 Overall view on the obtained experimental data

Microstructure evolution during ART annealing at 650°C was characterized using EPMA, SEM, TEM and NanoSIMS techniques. EPMA results revealed the long-range Mn homogenization controlled by the diffusivity of Mn close to those in ferrite. Small interspacing of microsegregation bands and ultra fine microstructure enhance this phenomenon. SEM characterization shown that the microstructures contained at least three phases: ferrite, retained austenite and fresh martensite. Double morphology (lath-like and polygonal) of analyzed features was revealed and a complete mechanism of such microstructure formation was proposed. From the image analysis of SEM pictures it was found that the kinetics of austenite transformation was very rapid in the beginning and then becomes smoother. Size evolution of austenite was also evaluated. Retained austenite fraction was determined by saturation magnetization method. It was found that an important amount of RA was stabilized at room temperature after final cooling. Evolution of RA fraction with holding time has a particular peak-type form. Finer TEM observations shown that carbides dissolution was sluggish: small amount of non-dissolved carbides were present even after 2h holding and contain high amount of Mn. Different phases were distinguished using CBED in STEM mode. An important dislocation density in ferrite was observed. Mn content of different phases was characterized using TEM-EDX measurements. Finally, C content of two samples, 1h and 30h, was determined by NanoSIMS technique. The obtained values were close to those, calculated from the mass balance neglecting the presence of cementite. All the obtained quantitative data is put together in the following table.

Table 6 – The values of the different parameters measured experimentally or calculated from the experimental values.

Employed tools➔		Image Analysis of SEM images		Saturation magnetization	TEM-EDX hypermaps	NanoSIMS	Calculated from mass balance
Reference	Time, s	F_A (%)	D_A (µm)	F_{RA} (%)	Mn_A (wt.%)	C_A (wt.%)	C_A (wt.%)
3min WQ	180	15.4	0.16	14.6	10.0	-	0.67
10min WQ	600	20.6	0.16	21.4	-	-	0.46
30min WQ	1800	21.6	0.24	25.9	-	-	0.38
1h WQ	3600	27.3	0.24	30.1	9.3	0.36	0.33
2h WQ	7200	31.5	0.26	26.2	8.9	-	0.31
3h WQ	10800	32.5	0.27	25.7	8.9	-	0.30
7h WQ	25200	36.1	0.30	22.6	-	-	0.27
10h WQ	36000	34.9	0.31	22.5	8.7	-	0.28
20h WQ	72000	36	0.39	21.1	-	-	0.27
30h WQ	108000	37.5	0.45	20.3	8.7	0.27	0.26

F_A - austenite fraction; D_A - austenite size; F_{RA} - retained austenite fraction; Mn_A and C_A – Mn and C contents in austenite, respectively.

3.3 Discussion of main results: experimental/modelling approach

As it was pointed out in the literature review, retained austenite fraction and its stability have significant influence on the final mechanical behavior of MMS. Under mechanical loading retained austenite transforms in martensite and thus providing additional ductility and strain hardening known as a TRIP effect. The rate of strain induced martensite transformation is linked to the fraction and stability of retained austenite. Both are directly linked with the mechanism of austenite formation during holding.

In this part, we propose to discuss more deeply the kinetics of austenite growth, the stability of austenite at room temperature and their interactions. A double experimental/modeling approach is proposed here.

3.3.1 Mechanisms of austenite formation

3.3.1.1 Effects of the representative volume

It is proposed to study the mechanisms of austenite growth using DICTRA software that is mainly based on a mean field approach. In this case, the choice of the equivalent representative volume of the microstructure is critical, all the more so when the studied microstructure is complex. The linear geometry was chosen for the main reason that the experimental observations revealed that the lath-like morphology is dominant, especially at the beginning of holding. The configuration for DICTRA calculations is given in Figure 94. Three phases were considered: θ-cementite, α-ferrite and γ-austenite, the latter one being initially set as an inactive phase at the α/θ interface. Consequently, austenite will appear when the driving force for its nucleation will be higher (absolute value) than a threshold value calculated by DICTRA under local equilibrium conditions. The simulation cycle was set to be as follows: starting at 400°C, heating to 650°C at ~1°C/s heating rate then holding at 650°C.
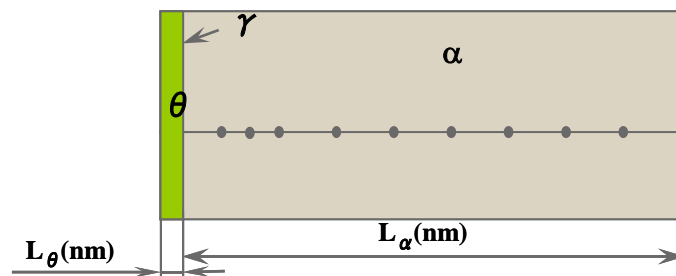
Figure 94 – Schematic representation of the linear configuration for the DICTRA simulations.

The characteristic length L_α (see Figure 94) was taken equal to the half-distance between the martensite laths. This length was approximately estimated to be 150 nm. Then the cementite region size (L_θ) was calculated from the classical mass balance considering that the volume fraction of cementite is 1.45%, value that corresponds to the equilibrium fraction at 400°C. The obtained cementite thickness was 2 nm.

The Mn content of cementite was considered to be 10 wt.% as determined in section 3.2.2 using the EDX in TEM. Both Mn and C content of ferrite were then calculated according to the mass balance: 4.53 wt.% and 2.10^{-6} wt.%, respectively.

The results in terms of kinetics of cementite dissolution and of austenite formation are presented in Figure 95.
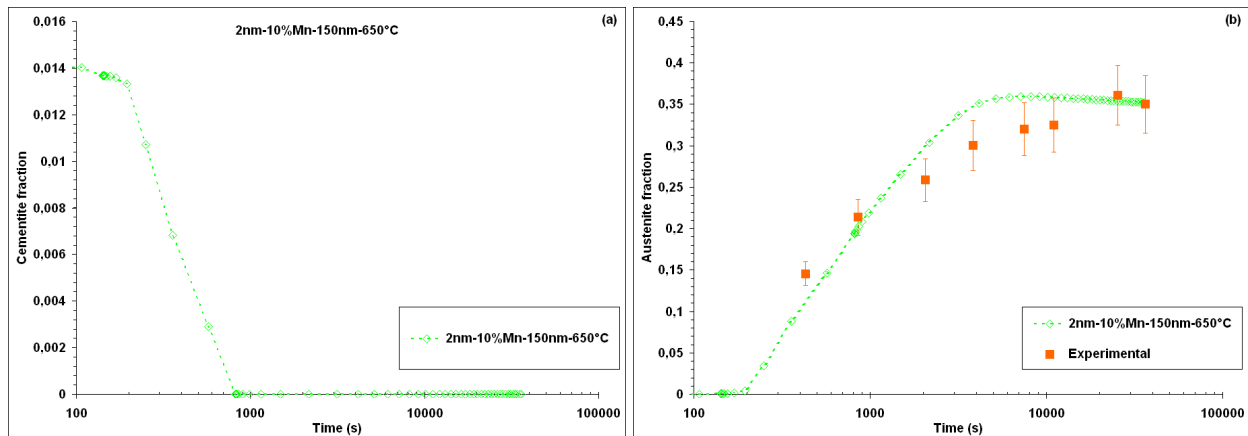
Figure 95 – Kinetics of cementite dissolution (a) and of austenite formation (b) at 650°C calculated by DICTRA. The initial state corresponds to the cementite size of 2nm and to the 10 wt.% Mn content in cementite. The experimental measurements of austenite fraction are shown with orange squares.

In a general manner, the kinetics of austenite is relatively well predicted, even if the calculated kinetics is abrupt between 30min and 3h. However, the calculated dissolution rate of cementite is rapid (complete dissolution after ~800s). This seems contradictory with the observed experimental results – carbides are still present after 2h of holding. From a theoretical point of view, there are many reasons that can explain such a result. First, the microstructure dispersions such as the size distribution and the heterogeneity of compositions are not taken into account. This can explain that some carbides may persist after rather long holding time. Second, the mean field approach used in this work imposes to choose a characteristic length (L_α), supposed to be representative of the microstructure state. This distance, very difficult to determine for the reason that the microstructure is quite complex, predetermines the size of cementite and can strongly influence the calculated kinetics. For example, the corresponding size of cementite in the initial state is of 4 nm that is far away from the measured one and would explain partially why the kinetics of cementite dissolution is faster than the observed one.

In order to better understand the influence of calculation parameters and to improve the predictions, some complementary calculations were carried out with the following considerations:
  o cementite region size was varied from 1 to 10 nm (this implies variation of ferrite region size from 75 to 750 nm);
  o Mn content of cementite was varied from 10 to 30 wt.%.

Effects of cementite size and of its Mn content on the kinetics of cementite dissolution and austenite formation are shown in Figure 96 and Figure 97. As expected, it was found that both kinetics strongly depend on the considered cementite size (and then on the ferrite region size) and on the Mn content in cementite. It is known [GOU'12-1] that an increase of Mn content in cementite decreases the driving force for cementite dissolution and influences the kinetics of the austenite growth. This effect is clearly illustrated in Figure 97. However, the effect of Mn content appears less pronounced. Furthermore, it is shown that it is not possible to describe simultaneously the experimental time for complete dissolution of cementite and the experimental kinetics for austenite growth using a given couple of cementite size and Mn content.
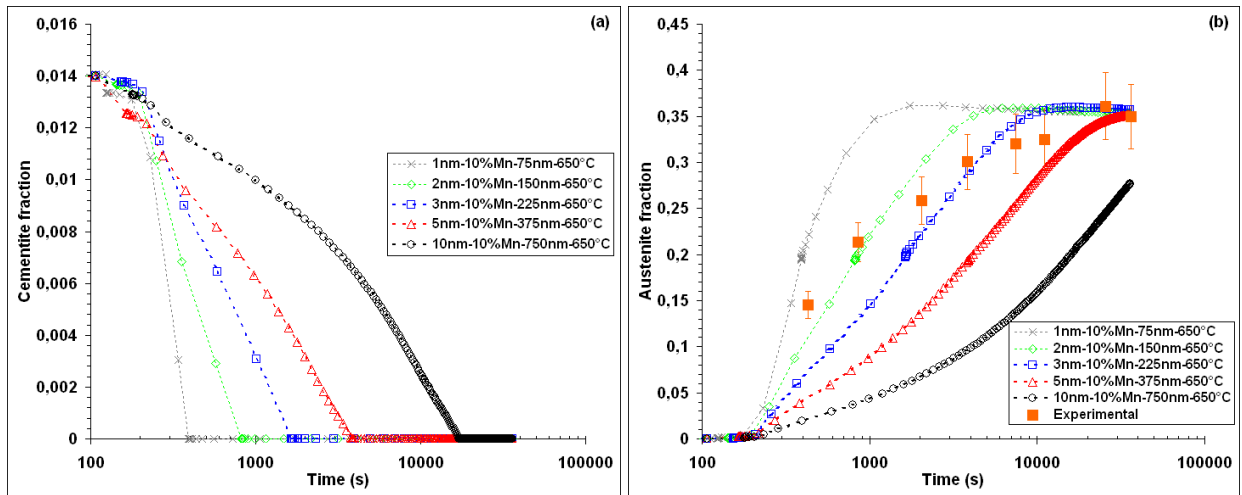
Figure 96 – Cementite and austenite fractions as a function of holding time obtained using DICTRA simulations with different size of cementite region. The experimental measurements of austenite fraction are shown with orange squares
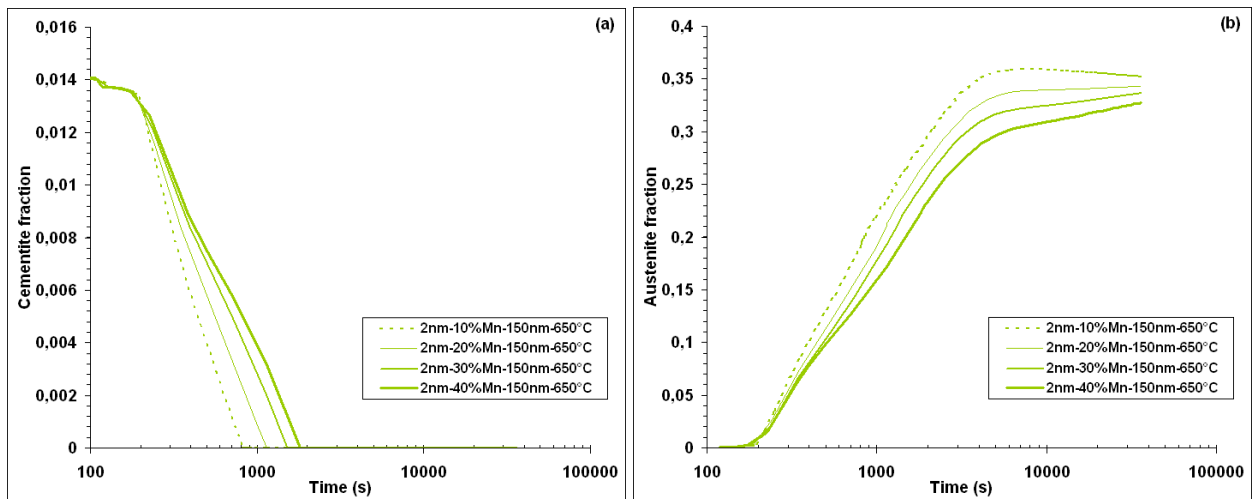
Figure 97 – Cementite and austenite fractions as a function of holding time obtained using DICTRA simulations with different Mn content of cementite region.

It is worth noting that the time for the complete dissolution of cementite is not necessary a relevant parameter in the absence of the measured kinetics of cementite dissolution. Indeed, the measurements of C content in austenite (Figure 86 and Figure 87) are in very good agreement with the C content calculated from the mass balance that neglects the presence of carbides. This is a clear evidence that a major part of carbides are completely dissolved after one hour of treatment at 650°C. The dispersion existing in the microstructure, particularly those concerning both the size and Mn content, may explain that some cementite particles persist even after longer holding time at 650°C.

In the following analysis and in view of the above, we will consider the first parameters set (L_α=150nm) as sufficiently relevant to describe the austenite growth.

111

3.3.1.2 Austenite growth controlled by Mn diffusion

The mechanism and the kinetics of austenite transformation and growth are strongly linked to the evolution of C and Mn at the transformation interfaces α/γ and γ/θ. In ternary Fe-C-Mn system the situation is more complicated in comparison with the Fe-C binary one. Indeed, both interstitial and substitutional diffusion occur during transformation and their diffusivities differ substantially. Thus, the composition of C and Mn at the α/γ that defines the tie-line for austenite growth cannot be determined by the tie-line passing through the bulk alloy composition, contrary to the Fe-C system. Furthermore, the austenite formation can be successively controlled by the C diffusion in austenite, the Mn diffusion in ferrite and, finally, by the Mn diffusion in austenite [SPE'81]. These varieties of possible growth mode for austenite have a strong influence on the kinetics of austenite formation.

The analysis of the time-evolution of both C and Mn profiles through the system at 650°C is given in Figure 98. It provides some clarifications about the mechanism of austenite growth.

The time-evolution of both C and Mn at γ/θ and α/γ define the tie-lines for cementite dissolution and austenite growth. In a first step, the focus is put only on the cementite dissolution process. It is worth noting that during this stage austenite grows into ferrite. From a theoretical point of view, the tie-line for transformation depends on both kinetics and thermodynamic properties of the studied system. However, in this specific case, it is shown that the content of both C and Mn at γ/θ and α/γ do not significantly evolve with time. The C and Mn contents are close to 0.45 wt.% and 8 wt.%, respectively, at the α/γ interface (austenite side) and are close to 0.5 wt.% and 11.5 wt.%, respectively, at the γ/θ interface (austenite side). As a consequence, the tie-lines for transformation, which are represented in Figure 99, can be considered as time-independent during cementite dissolution process.

The determination of these tie-lines is critical for the reason that they govern the austenite growth for a substantial part of austenite formation. The austenite growth is influenced by the dissolution of cementite into austenite and by the growth of austenite into ferrite (Figure 98). Obviously, these two steps are interdependent and their kinetics depends mainly on the difference between the difference of the chemical potentials of both C and Mn at γ/θ and α/γ interfaces from the austenite side (the small red and blue arrows in Figure 99). It is interesting to note that the values of carbon content at the γ/θ and α/γ interfaces are quite close (0.45 wt.% versus 0.5 wt.%). This is the reason why the carbon profile in austenite is almost flat (Figure 98). In order to go further, the C activity through the system at the beginning of transformation at 650°C (t=0s) was determined (Figure 100). The C activity is uniform through the system. As a consequence and surprisingly, the austenite growth is not controlled by C diffusion in austenite, as suggested by many authors in other steels with lower Mn content [SPE'81]. This can be explained by two concomitant effects: the high nominal Mn content and the relatively low temperature of transformation. Indeed, all this lead to a high C activity at the α/γ interface (austenite side) and to a strong decrease of the C chemical potential gradient through the system.
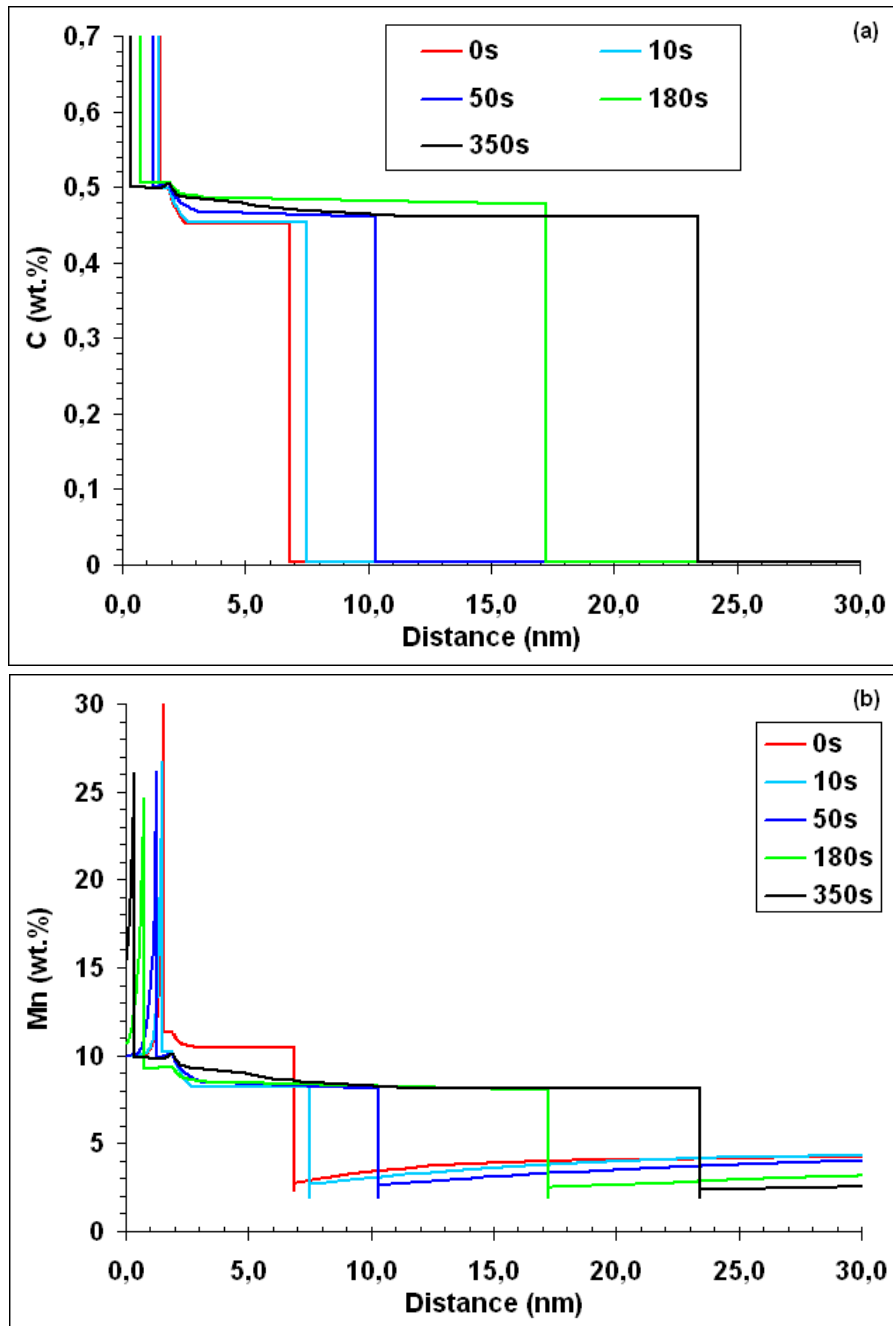
Figure 98 – DICTRA calculations of the time-evolution of both C (a) and Mn (b) profiles at 650°C during cementite dissolution. The time t=0s corresponds to the beginning of transformation at 650°C.

Figure 101 presents the profiles evolution of Mn activity. It can be seen that the Mn activity profile in austenite is relatively flat. It can thus be concluded that the driving force for cementite dissolution is weak, although the Mn content in cementite is relatively low. This explains why the kinetics of cementite dissolution is relatively slow and why the effect of Mn content in cementite on the kinetics of cementite dissolution is not significant (Figure 97). Such behavior was already observed in other Fe-C-Mn steels [GOU'12-1]. On the other hand, a gradient of Mn activity is established in ferrite and the austenite growth is thus controlled by Mn diffusion in ferrite. It is interesting to note that a substantial part of austenite is formed before the complete dissolution of cementite.
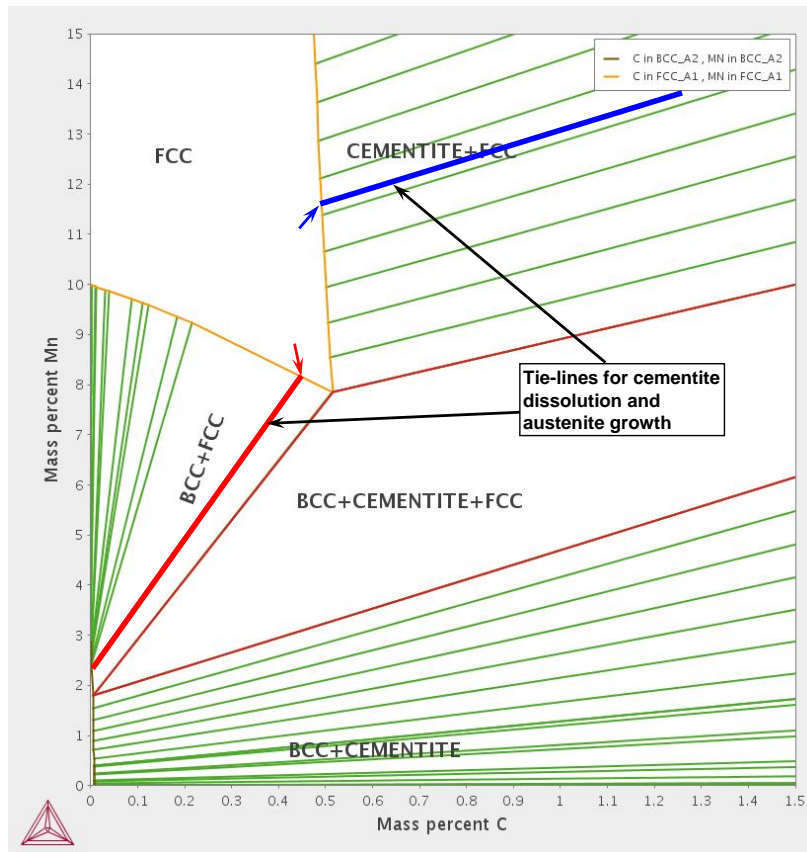
Figure 99 – Cross section of the studied Fe-C-Mn system at 650°C. The tie-lines for cementite dissolution and austenite growth are represented in blue and red lines, respectively. The contents of both C and Mn at γ/θ and α/γ ☐*interface blue arrows.*
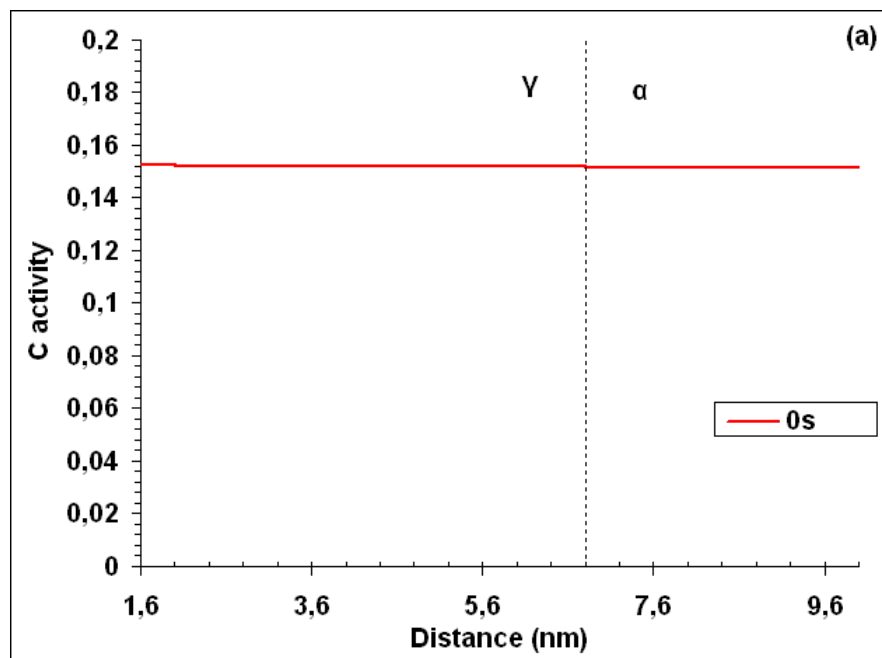
Figure 100 – DICTRA calculation of the carbon activity profile through the system at the beginning of transformation (t=0s) at 650°C.
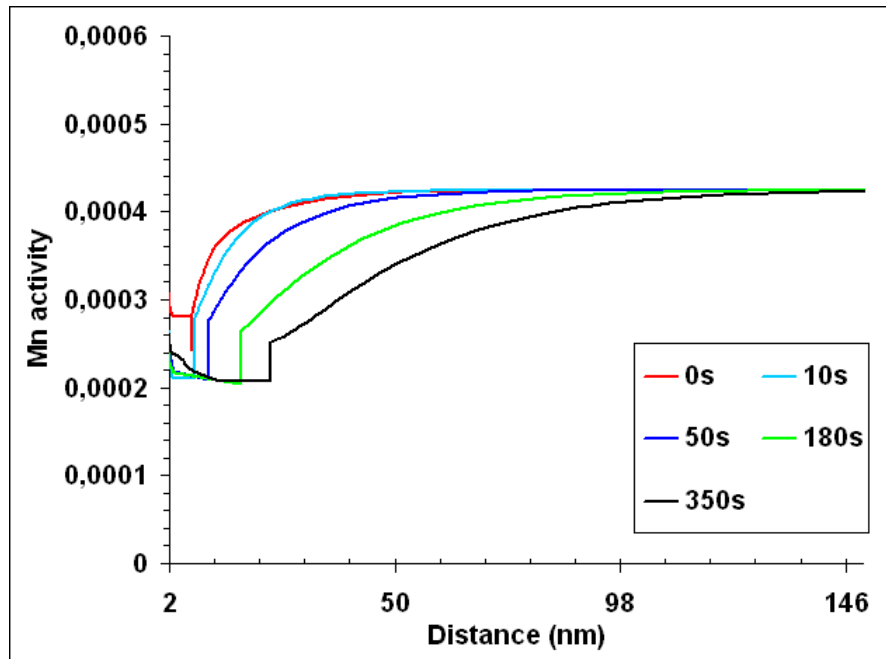
Figure 101 – DICTRA calculations of the Mn activity profile through the system at 650°C before cementite dissolution.

In a second step, when cementite is completely dissolved, an accumulation of Mn at the α/γ interface (austenite side) is highlighted (Figure 102). This is a direct consequence of Mn partitioning from ferrite to austenite. In that case, it is worth noting that the tie-line for austenite growth depends on time as shown in Figure 103. It is interesting to note that the tie-lines for transformation are located below the equilibrium tie-line for times shorter than 1800s, approximately, and above for longer times. As a consequence, it is expected to observe a decrease of Mn content at α/γ in austenite side from a certain time and shrinkage of austenite as clearly evidenced in Figure 102 and Figure 103. This retraction, also visible in Figure 95(b), is relatively slight in this case for the reason that the geometrical locus of tie-lines is relatively close to the equilibrium tie-line (see the position of tie-line at 7200s and the equilibrium tie-line in Figure 103). Surprisingly, this retraction is observed for relatively short holding time (after 2 hours). This can be partially attributed to the kinetics effect resulting from the ultra-fine structure that reduces the Mn diffusion length.

115
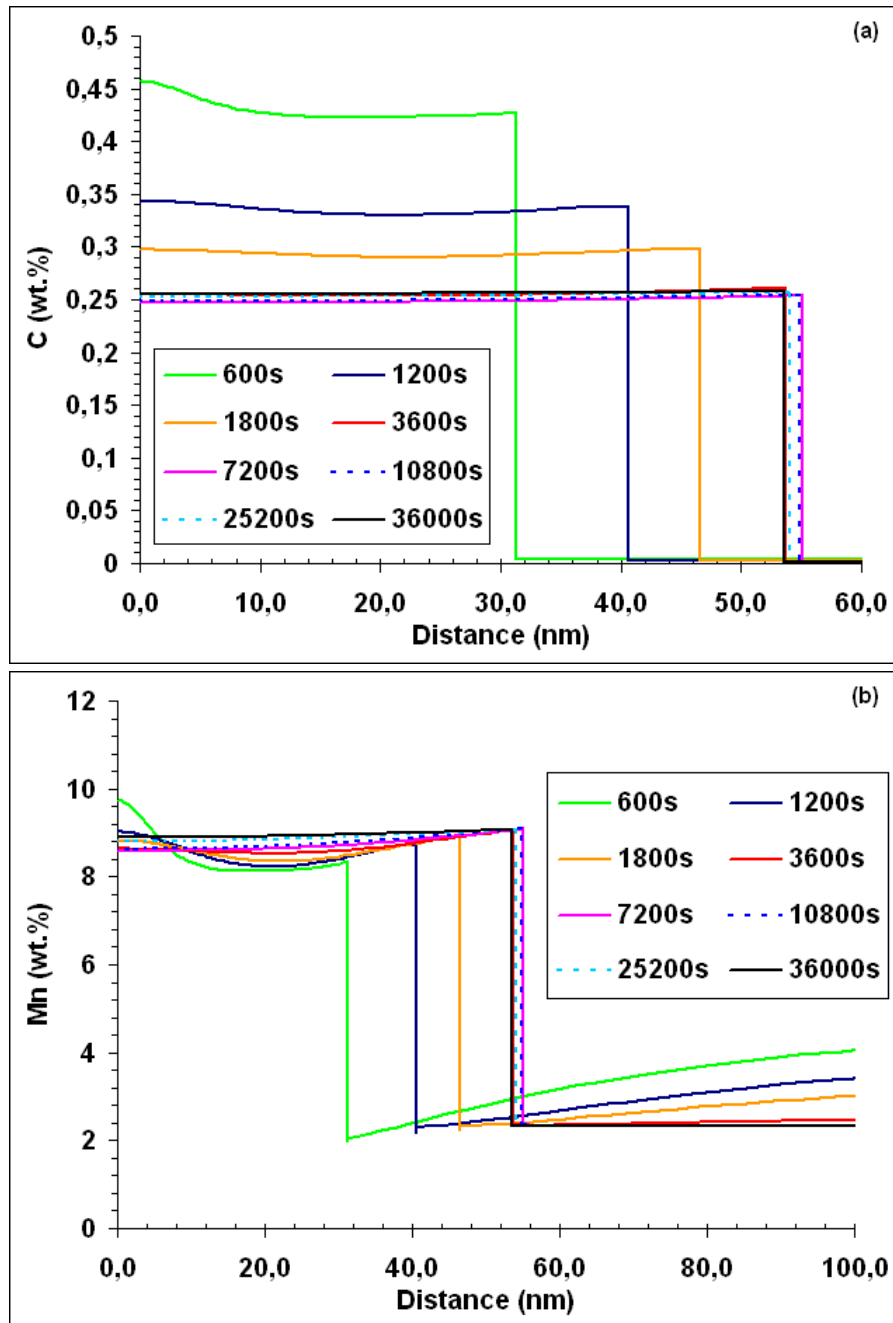
Figure 102 – Simulated with DICTRA time-evolution of both C (a) and Mn (b) profiles during austenite growth at 650°C after cementite dissolution.

As a partial conclusion, the major part of austenite growth is controlled by Mn diffusion in ferrite and by Mn diffusion of austenite for longer times. Although the transformation is not controlled by the carbon diffusion in austenite, the kinetics of austenite is relatively fast and the shrinkage of austenite occurs, surprisingly, for relatively short times. These effects result from both thermodynamic and kinetics process. For instance, it is clearly shown that the high nominal Mn content and the relatively low temperature of transformation lead to a strong decrease of the C chemical potential gradient through the system. Furthermore, the ultra-fine microstructure seems to play a key role on the kinetics of austenite growth: the kinetics of austenite would have been more sluggish (as it is controlled by Mn diffusion) in the case of coarse microstructure.
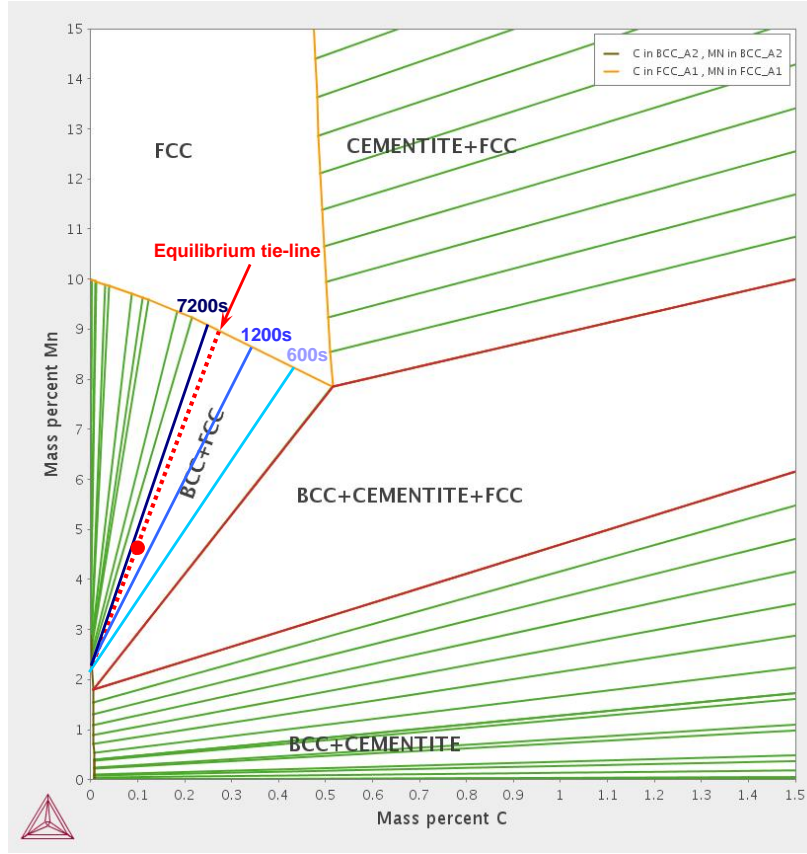
Figure 103 – Time-evolution of tie-line for austenite growth. The equilibrium tie-line passing through the bulk composition (big red point) is given by the red dotted line.

3.3.1.3 Effect of characteristic length L_α size distribution

Further, by combining both effects of cementite size and Mn content, it was possible to compare different austenite kinetics simulated with DICTRA with the experimental values (Figure 104). This figure shows that an increase of both cementite size and its Mn content makes the austenite formation curve smoother. However, taking only the fixed values of cementite size and of its Mn content cannot completely describe the experimental data. Once again, it was supposed that the heterogeneous distribution of size and/or Mn content in the microstructure can explain such an evolution. In the works of Gouné et al. [GOU'10], [GOU'12-2] it was shown that the dispersions existing in microstructure play an important role in the kinetics of phase transformations and that taking into account such heterogeneities can improve the predictions of classical approaches. Based on this, it was decided to perform calculations that will account for the effect of size distribution.

For that purpose, it was assumed that the distribution of the characteristic length L_α can be described by the Log-normal distribution:

$$F(L_\alpha) = \frac{e^{-\frac{1}{2}\left(\frac{\ln(L_\alpha)-\mu}{\sigma}\right)^2}}{L_\alpha \cdot \sigma \cdot \sqrt{2 \cdot \pi}}$$

(43)

where μ and σ are, respectively, the mean value and the standard deviation of the logarithm distribution of the characteristic length L_α.

117
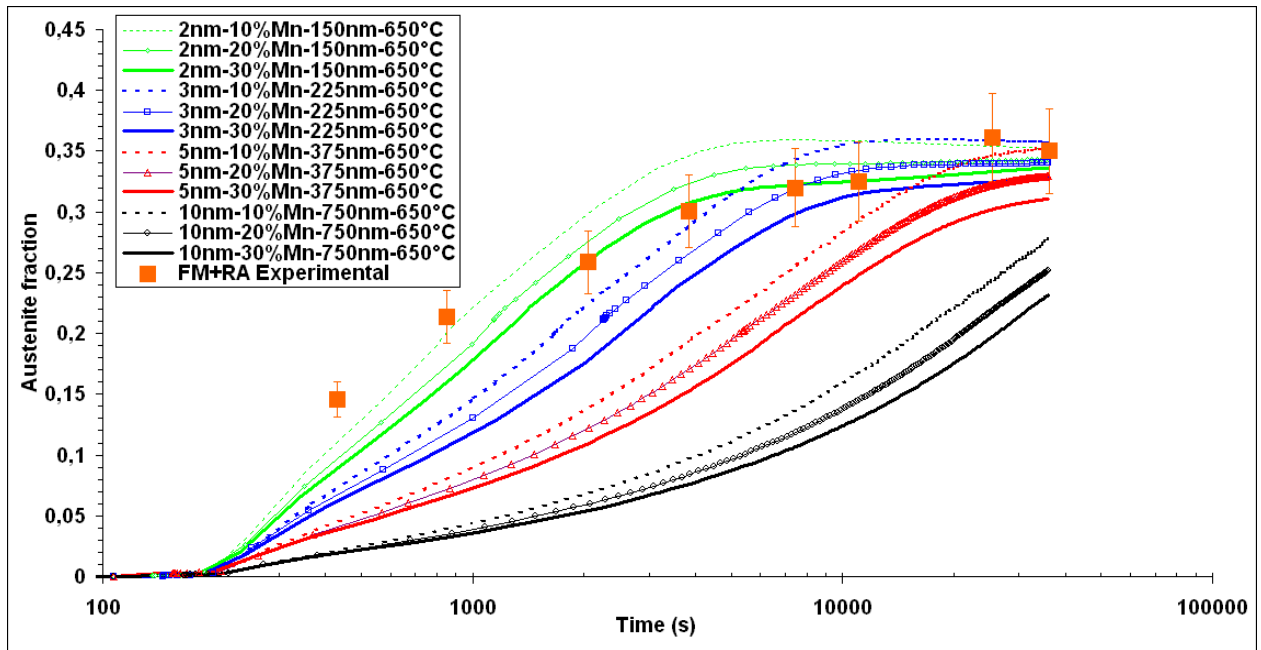
Figure 104 – Austenite kinetics simulated with DICTRA using different size and Mn content of cementite compared to the experimentally measured values (orange squares).

A Log-normal distribution that results in the good fit of austenite kinetics is shown in Figure 105(a). Optimum μ and σ values are, respectively, 4.85 and 0.9. Thus this L_α distribution has a mean value of about 130 nm. Austenite kinetics was estimated in the following manner. For simplicity, only six classes of L_α were considered. Then, the fraction of each class was calculated (Figure 105(b)).
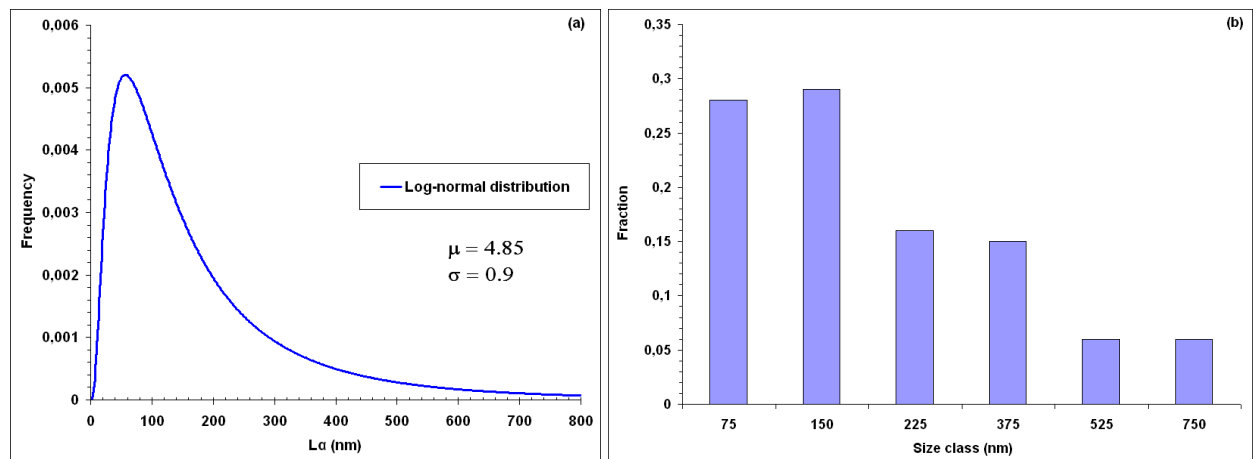
Figure 105 – (a) Calculated L_α Log-normal distribution; (b) Fractions for chosen classes of size L_α calculated from the Log-normal distribution.

It was supposed that there were no interactions between the features of different size classes. Next, DICTRA simulations were performed for each size class. The obtained from each simulation austenite fraction was then balanced according to the distribution fractions (Figure 105(b)) using following equation:

$$f_A(t) = \sum f_A^i(t) \cdot f_{L_\alpha}^i \qquad (44)$$

where $f_A(t)$ is the average volume fraction of austenite at time t, $f_A^i(t)$ is the volume fraction of austenite calculated using DICTRA for a selected L_α^i and $f_{L_\alpha}^i$ is the fraction of L_α^i class calculated from Log-normal distribution.

The resulted austenite kinetics is presented in Figure 106.
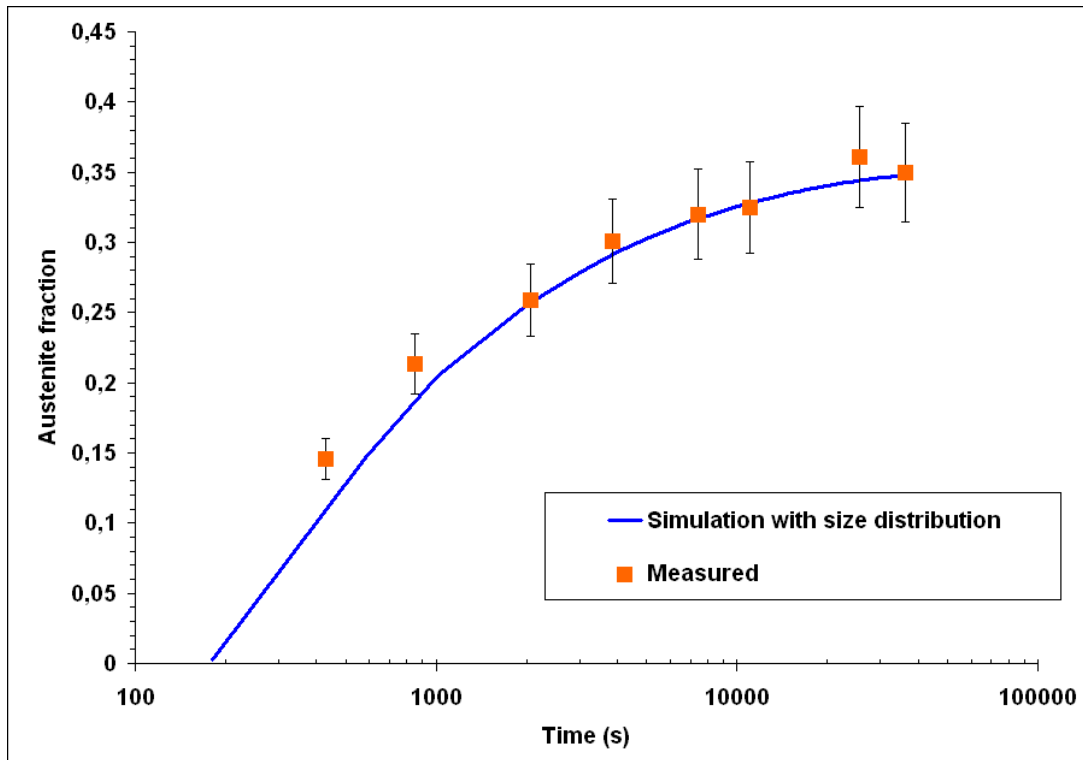
Figure 106 – Austenite kinetics calculated using DICTRA simulations with Log-normal distribution of L_α compared with the experimentally measured values (orange squares).

As it can be seen, very good prediction of austenite kinetics was achieved. The reason of such a good result is the correct selection of the L_α distribution. In fact, high fraction, almost 60%, of small size cells (L_α is less than 200nm) provides a rapid austenite formation during the first 1000s of holding. The austenite fraction generated by the small size cells during this period represents roughly 80% of the global fraction. In the same time, with the increase of holding time the influence of coarser cells increases, thus decreasing the austenite formation rate and making the curve smooth.

An interesting fact is that the calculated fractions for chosen size classes of L_α with the Log-normal distribution is very similar to the measured fractions of austenite size classes for the sample with 3min holding at 650°C (Figure 107). Actually, there is a direct link between L_α and austenite size: a given cell size will result in a certain fraction of austenite with a certain size.

However, to recalculate L_α from the measured austenite size requires a huge number of DICTRA simulations and complex fitting with the experimentally measured austenite fractions.
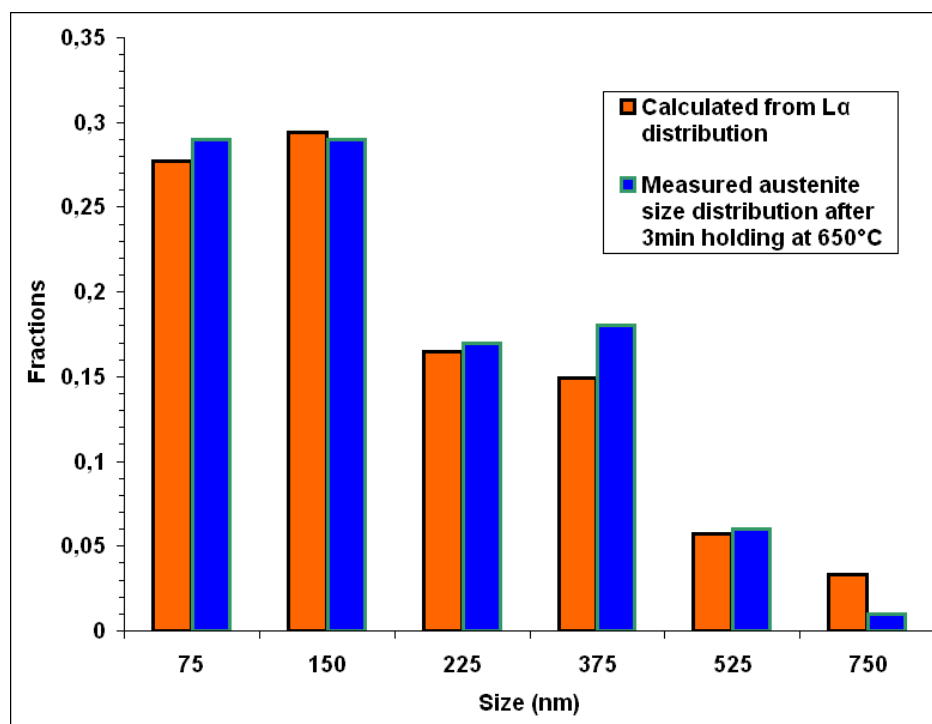
Figure 107 – Comparison of size classes fractions calculated from: L_α Log-normal distribution (orange) and measured distribution of austenite sizes for the sample with 3min holding at 650°C (blue).

On the other hand, this similarity between measured and calculated size classes is a direct proof of the right form of the selected L_α distribution. Indeed, the selected Log-normal L_α distribution should result in the Log-normal distribution of the austenite sizes, which is the observed case in this study.

3.3.2 Factors controlling austenite stabilization at room temperature

In the previous section, it was shown that a relatively high volume fraction of retained austenite can be stabilized at room temperature, although, its carbon composition is much lower than in the classical TRIP steels. The origin of such behavior is controversial as evidenced by some recent lively discussions in [LEE'11], [LUO'12], [LEE'12]. At all events, most agree that the enrichment of alloying elements such as C and Mn are important factors responsible for the room temperature stability of retained austenite in medium Mn steels. However, the effect of grain size on the stability of retained austenite is much more discussed.

In this section, it will be shown that the experimentally obtained evolution of retained austenite is a very valuable dataset for the study of factors governing the stability of austenite in MMS.

Retained austenite fraction at room temperature can be determined using the Koistinen and Marburger empirical equation [KOI'59] presented earlier in the literature review and Chapter 2:

$$f_{RA} = f_A \cdot \exp\left(-\alpha \cdot \left(M_s - T_q\right)\right) \tag{45}$$

where f_{RA} is the volume fraction of retained austenite, f_A is the volume fraction of austenite before martensite transformation (austenite fraction at the end of holding before quenching), T_q is the quenching temperature (T_q=20°C in the present work) and α=0.011 is a fitting parameter.

It is assumed that the effect of chemical composition and other variables is visible in the change of M_s. It can be seen also that the retained austenite fraction (f_{RA}) depends on the initial austenite fraction at the end of holding (f_A). For sake of simplicity, it is suggested to describe the austenite fraction during isothermal holding using the Kolmogorov-Johnson-Mehl-Avrami (KJMA) approach [KOL'37], [JOH'39], [AVR'39]. Obviously, a similar result can be obtained using DICTRA as soon as the kinetics of austenite formation is well described.

In that case f_A can be expressed in the following manner:

$$f_A = f_A^{eq} \cdot \left[1 - \exp\left(-k \cdot t^n\right)\right] \tag{46}$$

where n is so-called "Avrami coefficient", k is a parameter that depends on nucleation and isotropic growth rates, and f_A^{eq} is the volume fraction of austenite under ortho-equilibrium. This value, obtained with ThermoCalc at 650°C, is of 0.36.

A very good agreement with experimental data was obtained for values of k = 0.074 and n= 0.38 (Figure 108).
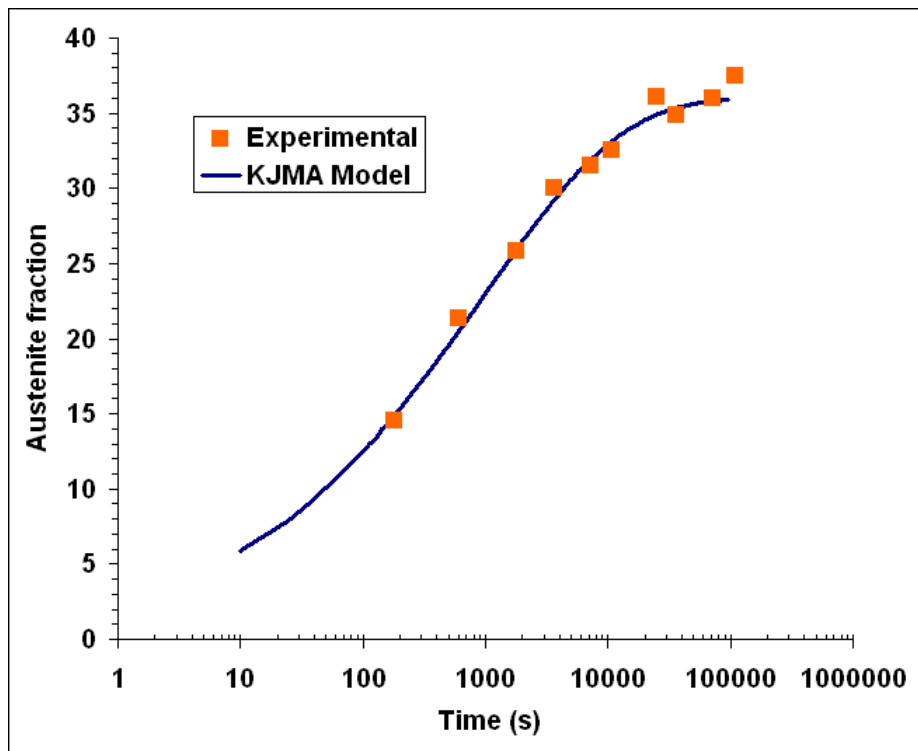
Figure 108 – Experimentally measured and calculated (KJMA model) time evolution of austenite fraction.

121

Then, the time evolution of retained austenite fraction as a function of holding time and M_s temperature is obtained by combining equations (45) into (46):

$$f_{RA} = f_A^{eq} \cdot \left[1 - \exp\left(- k \cdot t^n\right)\right] \cdot \exp\left(- \alpha \cdot \left(M_s - T_q\right)\right) \tag{47}$$

Here, it is highlighted that the time evolution of retained austenite fraction is governed by the competition between the initial volume fraction of austenite before quenching and its stability. The first derivation of equation (47) permits to evaluate the magnitude of retained austenite variation and the inflection points. The following equation is thus obtained:

$$\frac{df_{RA}}{dt} = f_A^{eq} \cdot \exp\left[- \alpha \cdot \left(M_s - T_q\right)\right] \cdot \left(k \cdot n \cdot t^{n-1} \cdot \exp\left(- k \cdot t^n\right) - \alpha \cdot \frac{dM_s}{dt} \cdot \left[1 - \exp\left(- k \cdot t^n\right)\right]\right) \tag{48}$$

This relation shows clearly that the evolution of retained austenite depends on the temporal variation of M_s temperature, which is linked to the austenite stability. For example, when M_s is constant, the derivative from the equation 48 is always positive. Therefore, the retained austenite fraction is expected to be strictly increasing over the considered time-interval.

In this work, it was shown that the retained austenite evolution exhibits a clearly marked maximum (Figure 88). As it was stated previously, three different stages are observed for RA evolution: increase, decrease and, finally, stagnation. First, initial austenite volume fraction is fully stabilized at room temperature, thus, $f_{RA} = f_A$ and it continuously increases till 1h holding time. In that case, it can be easily demonstrated from equations (45) and (47) that this condition is fulfilled for M_s temperatures strictly less than T_q. Second, the time-evolution curve of RA fraction goes through a maximum value and decreases. The peak, that corresponds to the higher volume fraction of retained austenite, is, thus, defined by $M_s = T_q$. As a consequence, the austenite state (chemical composition and size) at the peak, defines the critical point beyond which austenite is unstable, because $M_s > T_q$. From the experimental results, it appears that the peak point corresponds to carbon and manganese contents in austenite of 0.33 wt.% and 9.3 wt.%, respectively. The decrease of f_{RA} can be mainly explained by the concomitant decrease of austenite carbon content and increase of its size during growth. The final stagnation stage is observed simply because of the absence or very slight evolution of austenite: equilibrium fraction and composition are achieved and the effect of size variation is becoming minor. From these considerations it is obvious that the shape of the f_{RA} curve and the position of the peak are fair indicators of the factors controlling austenite stability.

In order to go further, it is important to clarify an important point, which is the chemical contribution to M_s temperature. According to the Andrews empirical relation [AND'65] and in the case of ternary Fe-C-Mn steels, the chemical contribution to M_s can be expressed as:

$$M_s^0 (°C) = 539 - 423 \cdot w_C^A - 30.4 \cdot w_{Mn}^A \tag{49}$$

where w_C^A and w_{Mn}^A are C and Mn contents in austenite taken in the weight percents.

It is important to mention that Andrews collected a huge data base of M_s temperatures obtained from fully austenitic structures with quite large grain sizes. Thus, the effect of austenite grain size on M_s can be reasonably considered as negligible in the resulting data base.

From the measured Mn content in austenite (9.3 wt.%) at peak, this relation predicts that austenite is stable at $T_q = 20°C$ when its carbon concentration of $w_C^A > 0.56$ wt.%. In this study, it was shown clearly that austenite with carbon lower than 0.33 wt.% are expected to transform

into martensite (see the carbon content at peak). This strongly suggests that the empirical relation given in equation 49 has a limited validity for the MMS. In addition, it appears that parameters other than chemical composition may play a significant role in the stability of the austenite.

As already mentioned during literature review, it can be reasonably supposed that the small austenite size affects its stability by lowering the M_s temperature. In other words, an extra driving force that depends on austenite grain size would be added to the change of Gibbs free energy for the austenite to martensite transformation. It was then decided to propose a specific formulation for the influence of austenite size. Actually, it is proposed to introduce an additional term that depends on the volume of austenite as follows:

$$M_s = M_s^0 - \frac{K}{(V_A)^q} \tag{50}$$

where M_s^0 is determined from the equation 49 and represents the chemical contribution, V_A is the volume of austenite features taken as an equivalent volume of cube (D_A^3 in μm^3), and K and q are fitting parameters. As discussed beforehand, at the peak point $M_s = T_q$, therefore, the parameters K and q must satisfy the following first-order condition:

$$K = V_A^q \cdot \left(M_s^{0,\,peak} - T_q\right) \tag{51}$$

In this study, the peak occurs at 1h with carbon and manganese contents in austenite of 0.33 wt.% and 9.3 wt.%, respectively, and a mean size of austenite about 240 nm. Thus, M_s^0 was calculated, using equation 49, to be about 117°C.

The fitting parameters K and q are interdependent and at each value of q is associated an unique value of K (Figure 109). Nevertheless, many pairs of K and q satisfy condition 51 but only a single set of K and q parameters should fit best the time-evolution curve of retained austenite. Using the experimental data of this work, the best agreement was obtained with q=0.039 and K=83.3 (Figure 110). Finally, the new M_s law that accounts for the size effect in the MMS with ultra-fine microstructure takes the following expression:

$$M_s^{new}\,(°C) = 539 - 423 \cdot w_C^A - 30.4 \cdot w_{Mn}^A - 83.3 \cdot \left(V_A\right)^{-0.039} \tag{52}$$

where V_A is given in μm^3.

All the values considered for the calculation of RA fraction and the obtained results are summarized in Table 7. The prediction of RA fraction evolution using new Ms formulae is in a very good agreement with the experimental results. As it was seen experimentally, the fresh martensite starts to form during cooling in case of holding time longer than 2h. This means that for longer holding time, stability of austenite is decreased. Also, the proposed approach predicts correctly the stabilization of RA fraction at very long holding time. Figure 110 shows the comparison between the evolutions of RA fraction calculated using only chemical contribution to M_s (Andrews M_s) and using both chemical and size contributions (new M_s with q=0.039 and K=83.3). These results confirm unambiguously the size effect on austenite stability. It can be also observed that the influence of size effect is quite important. Actually, it brought two things:
    a) delay of the maximum peak to a longer holding time;
    b) global increase of RA fraction (maximum value and values at longer annealing times).
Moreover, the particular peak-like form of the RA fraction time-evolution is the result of concomitant change of C content and size of austenite.
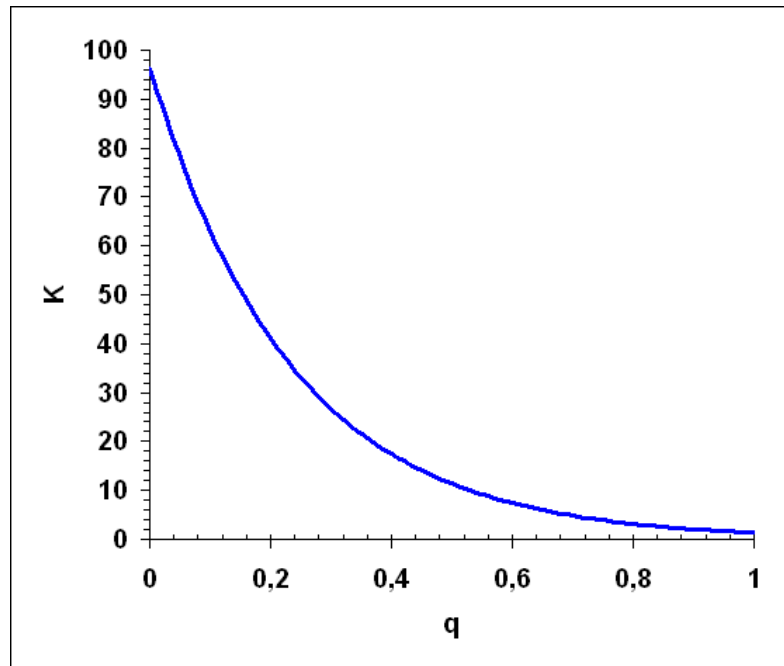
Figure 109 – Interdependence of fitting parameters K and q.
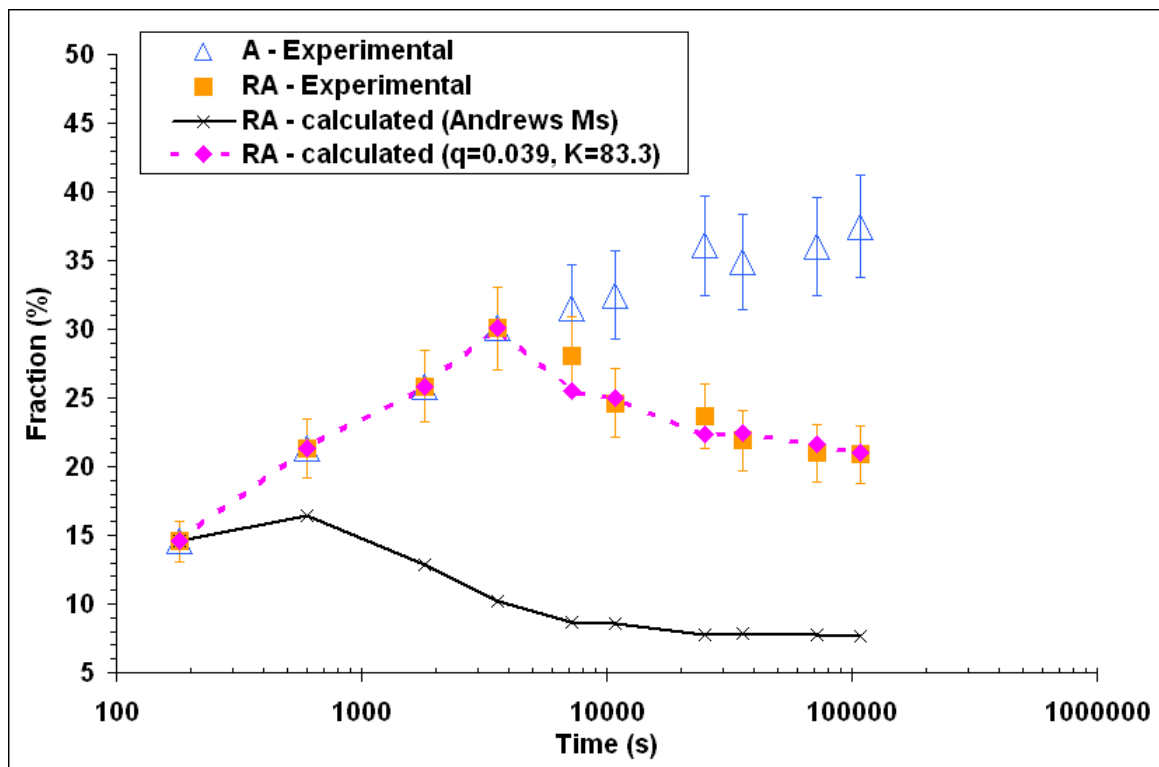
Figure 110 – Evolution of A and RA fractions with the holding time at 650°C: A and RA are experimental fractions of initial, before quench, (blue open triangles) and retained austenite (orange squares); RA-calculated (Andrews M_s) – RA fraction calculated using equations 45 and 49 (black crosses) and RA-calculated (q=0.039, K=83.3) – RA fraction calculated using equations 45 and 52 (pink filled lozenges).

Finally, using the new M_s law it is possible to estimate the critical volume or size of austenite, with a given chemical composition in austenite (in our case C and Mn), necessary for the full stabilization at room temperature:

$$V_A^{critical} = \left(\frac{K}{M_s^0 - 20} \right)^{1/q}$$

(53)

For example, austenite with 0.33 wt.% C and 9.3 wt.% Mn will be fully stabilized at room temperature when its size is lower than 280nm.

Table 7 – The values of all the parameters necessary for the estimation of RA fraction at room temperature and the results of these calculations: M_s^{new} (M_s temperature taking into account the influence of chemical composition and size of austenite), F_{ind}^M (induced martensite fraction) and RA (retained austenite fraction).

Ref.	Time (s)	F_a (%)	D_a (µm)	V_a (µm³)	C_a (wt.%)	Mn_a (wt.%)	M_s^{new}	F_{ind}^M	RA (%)
3min	180	14.6	0.16	0.0041	0.67	10.0	-152.8	0.00	14.6
10min	600	21.4	0.16	0.0041	0.46	9.9	-59.2	0.00	21.4
30min	1800	25.9	0.24	0.0138	0.38	9.7	-14.6	0.00	25.9
1h	3600	30.1	0.24	0.0138	0.33	9.3	20.0	0.00	30.1
2h	7200	31.5	0.26	0.0176	0.31	8.9	39.3	0.19	25.5
3h	10800	32.5	0.27	0.0197	0.30	8.9	43.8	0.23	25.0
7h	25200	36.1	0.30	0.0270	0.27	8.7	63.8	0.38	22.3
10h	36000	34.9	0.31	0.0298	0.28	8.7	60.2	0.36	22.4
20h	72000	36	0.39	0.0593	0.27	8.7	66.4	0.40	21.6
30h	108000	37.5	0.45	0.0911	0.26	8.7	72.5	0.44	21.0

Such stabilization due to the ultra-fine size is apparently contradictory with the classical nucleation model in which more grain boundary area should provide more chances for nucleation of martensite embryos [GHO'94]. This dichotomy was discussed in [FUR'89] and it can be reasonably suspected that a stabilizing mechanism becomes dominant for smaller grain sizes. The results of this work are probably not sufficient in order to determine the mechanism of austenite stabilization by the size effect. However, some discussions about two possible mechanisms are proposed hereafter.

As already seen previously, Yang et al. [YAN'09] suggested that the dependence of M_s on the austenite grain size during the austenite to martensite transformation can be explained quantitatively on the basis of Fisher's original model [FIS'49]. The latter, based on a purely geometrical analysis, claims that the number of plates per unit volume needed to obtain a detectable fraction of martensite increases as the austenite grain volume decreases because the volume transformed per plate is reduced. The adaptations done by Yang et al. [YAN'09] provided the following expression for M_s:

$$M_s = M_s^0 - \frac{1}{b} \ln \left[\frac{1}{aV_\gamma} \left\{ \exp \left(-\frac{\ln(1-f)}{m} \right) - 1 \right\} + 1 \right]$$

(54)

where V_γ is the volume of austenite grain, f is martensite fraction (for M_s calculation $f = 0.01$), m is the plate aspect ratio (m = 0.05 from [CHR'79]) and a = 1mm⁻³, b = 0.2689 and M_s^0 = 363.5°C are three fitting parameters.

Using this M_s law, the critical size of austenite with 0.33 wt.% C and 9.3 wt.% Mn for its full stabilization at room temperature should be lower than ~100nm. This value is almost 3 times lower than that determined previously with the M_s law proposed in this study. One of the possible reasons for this is that the fitting parameters a and b were determined from the grain sizes much higher than those measured in this work (see [YAN'09]). However, by resetting the fitting parameters a, b and m and using M_s^0 of Andrew's it is possible to obtain equivalent results for the retained austenite time evolution. It should be noted that the fitting parameter b and the plate aspect ratio m are not independent. The product is equal to the constant parameter α in the Koistinen-Marburger equation (α being equal to 0.011 here). The values of parameters a and b (m = 0.05) obtained by fitting are 4 mm^{-3} and 0.22, respectively. The obtained results are compared with experimental data in Figure 111. It can be seen that the adapted "geometrical model" fits well the measured retained austenite evolution.
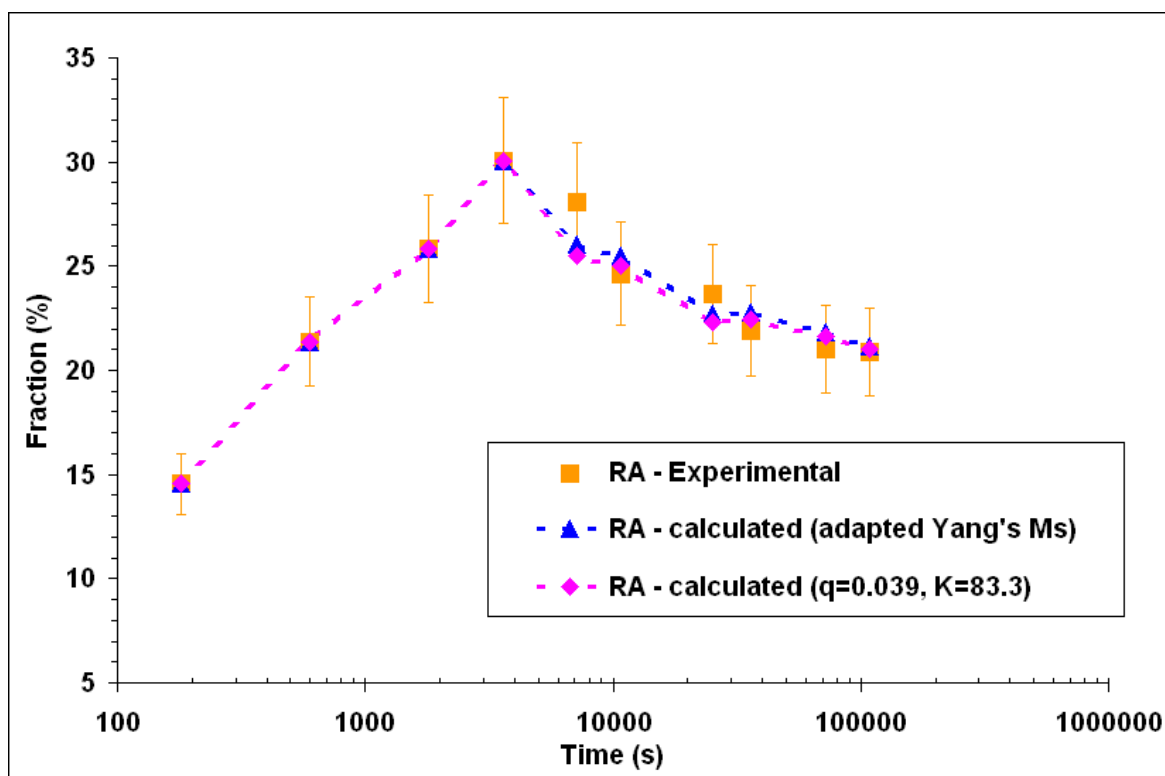
Figure 111 – Comparison of calculated using "geometrical model" RA fraction (RA-calculated (adapted Yang's M_s)) – equations 45 and 54 (blue filled triangles) with the experimental RA fractions (RA –Experimental; orange squares), as well as RA fraction calculated using equations 45 and 52 (RA-calculated (q=0.039, K=83.3); pink filled lozenges).

In the same time, Takaki et al. [TAK'04] recently suggested another theory based on the experimental results of Fe-Cr-Ni steel. It was stated that austenite can be significantly stabilized when the martensitic transformation mode is changed from multi-variant to single variant. Therefore, it can be reasonably suspected that austenite refinement contributes to the change in the transformation mode. The mechanism of grain refinement-induced austenite stabilization can be discussed in terms of increase of elastic strain energy associated with austenite to martensite transformation via a single variant. It was shown that the increase of elastic strain energy due to the development of one single variant of martensite in one single grain of austenite is estimated by the following relation:

$$\Delta E_V = 1276.1 \left(\frac{x}{D} \right)^2 + 562.6 \left(\frac{x}{D} \right) \tag{55}$$

where x is the thickness of martensite plate and D is the austenite grain size.

The plot of elastic strain energy ΔE_v as a function of grain size shows the difficulty for martensite lath to nucleate in austenite which size is smaller than 1 µm [TAK'04]. The quantity ΔE_v can be seen as an excess driving force for martensite nucleation. As a result, it is expected that M_s depends on grain size in the same manner that ΔE_v depends on grain size [GUI'07]. This relation is far from that observed in this work (see equation 52) and would suggest that such mechanisms is not involved.

As it was stated previously, the results of this work do not allow to select or to define the mechanism of austenite stabilization by the size effect, even though geometrical model show a good agreement. It can be imagined that both geometrical and elastic energy constraints can operate together and prevent austenite transformation to martensite. Therefore, more studies are necessary to discriminate the mechanism of austenite stabilization by the size effect.

As a conclusion, austenite stabilization during ART annealing of MMS was provided by two mechanisms: C, Mn enrichment and ultra fine size of austenite (less than 0.5 µm). Mn content and ultra fine size of austenite play an important role for its stabilization; however the prime importance for the austenite stability was attributed to its C content. Both C content and ultra fine austenite size are the key factors for the peak-like form of the RA evolution curve. Moreover, the time-evolution of retained austenite is shown to be a fair indicator of the critical factors governing austenite stability in ultra-fine grained MMS. Particularly, the peak of the curve defines the critical point delimiting stable and unstable austenite. The corresponding critical size was estimated around 280nm.

References

[AND'65] K.W. Andrews, Empirical formulae for the calculation of some transformation temperatures, Journal of the Iron and Steel Institute, 203(7), 1965, 721-727.
[ARL'12-1] A. Arlazarov, M. Gouné, O. Bouaziz, A. Hazotte, G. Petitgand, P. Barges, Evolution of microstructure and mechanical properties of medium Mn steels during double annealing, Materials Science and Engineering A, 542, 2012, 31-39.
[ARL'12-2] A. Arlazarov, A. Hazotte, O. Bouaziz, M.Gouné, F. Kegel, Characterization of microstructure formation and mechanical behavior of an advanced medium Mn steel, Materials Science and Technology (MS&T) 2012, 1124-1131.

[ARL'13] A. Arlazarov, O. Bouaziz, A. Hazotte, M.Gouné, S. Allain, Characterization and Modeling of Manganese Effect on Strength and Strain Hardening of Martensitic Carbon Steels, ISIJ International, 53(6), 2013, 1076-1080.

[AVR'39] M. Avrami, Kinetics of phase change. I General theory. The Journal of Chemical Physics, 7(12), 1939, 1103-1112.

[FIS'49] J.C. Fisher, J.H. Hollomon, D. Turnbull, Kinetics of the austenite → martensite transformation, Transactions of the American Institute of Mining and Metallurgical Engineers, 185(10), 1949, 691-700.

[FUR'89] T. Furukawa, Dependence of strength-ductility characteristics on thermal history in low carbon 5wt.% Mn steels, Materials Science and Technology, 5, 1989, 465- 470.

[GHO'94] G. Ghosh, G.B. Olson, Kinetics of FCC→ BCC heterogeneous martensitic nucleation – I. The critical driving force for athermal nucleation, Acta Metallurgica et Materialia, 42(10), 1994, 3361-3370.

[GOR'62] P. Gordon, R.A. Vandermeer, The Mechanism of Boundary Migration in Recrystallization, Transactions AIME, 224(5), 1962, 917-928.

[GOU'10] M. Gouné, P. Maugis, The role of dispersion in modelling the kinetics of phase transformations, Solide State Phenomena, 172-174, 2011, 279-284.

[GOU'12-1] M. Gouné, P. Maugis, J. Drillet, A criterion for the change from fast to slow regime of cementite dissolution in Fe–C–Mn steels, Journal of Materials Science & Technology, 28(8), 2012, 728-736.

[GOU'12-2] M. Gouné, O. Bouaziz, S. Allain, K. Zhu, M. Takahashi, Kinetics of bainite transformation in heterogeneous microstructures, Materials Letters, 67, 2012, 187-189.

[GUI'07] J.R.C. Guimarães, Excess driving force to initiate martensite transformation in fine-grained austenite, Scripta Materialia, 57, 2007, 237-239.

[HUA'94] H. Huang, O. Matsumura, T. Furukawa, Retained austenite in low carbon, manganese steel after intercritical heat treatment, Materials Science and Technology, 10(7), 1994, 621-626.

[JOH'39] W.A. Johnson, R.F. Mehl, Reaction kinetics in processes of nucleation and growth, Transactions of AIME, 135(8), 1939, 396-415.

[KIM'81] N.J. Kim, G. Thomas, Effects of morphology on the mechanical behavior of a dual phase Fe/2Si/0.1 C steel, Metallurgical Transactions A, 12, 1981, 483-489.

[KOI'59] D.P. Koistinen, R.E. Marburger, A general equation prescribing the extent of the austenite-martensite transformation in pure iron-carbon alloys and plain carbon steels, Acta Metallurgica, 7, 1959, 59-60.

[KOL'37] А.Н. Колмогоров, К статистической теории кристаллизации металлов. Известия Российской академии наук. Серия математическая, 1(3), 1937, 355-359. (A.N. Kolmogorov, Toward Statistical Theory of Metal Crystallization, News of Russian Science Academy, Mathematical Volume, 1(3), 1937, 355-359)

[KOO'76] J.Y. Koo, G. Thomas, Thermal cycling treatments and microstructures for improved properties of Fe-0.12% C-0.5% Mn steels, Materials Science and Engineering, 24, 1976, 187-198.

[KRE'11] B. Krebs, L. Germain, A. Hazotte, M. Gouné, Banded structure in Dual Phase steels in relation with the austenite-to-ferrite transformation mechanisms, Journal of materials science, 46(21), 2011, 7026-7038.

[LAV'49] J.D. Lavender, F.W. Jones, An investigation on banding, Journal of The Iron and Steel Institute, 163, 1949, 14-17.

[LAW'80] N.C. Law, D.V. Edmonds, The Formation of Austenite in a Low-Alloy Steel, Metallurgical Transactions A, 11, 1980, 33-46.

[LEE'11] S. Lee, S.J. Lee, B.C. De Cooman, Austenite stability of ultrafine-grained transformation-induced plasticity steel with Mn partitioning, Scripta Materialia, 65, 2011, 225-228.

[LEE'12] S. Lee, S.J. Lee, B.C. De Cooman, Reply to comments on "Austenite stability of ultrafine-grained transformation-induced plasticity steel with Mn partitioning," Scripta Materialia, 66, 2012, 832-833.

[LUO'11] H. Luo, J. Shi, C. Wang, W. Cao, X. Sun, H. Dong, Experimental and numerical analysis on formation of stable austenite during the intercritical annealing of 5Mn steel, Acta Materialia, 59, 2011, 4002-4014.

[LUO'12] H. Luo, Comments on "Austenite stability of ultrafine-grained transformation-induced plasticity steel with Mn partitioning" by S. Lee, S.J. Lee and B.C. De Cooman, Scripta Materialia, 65 (2011) 225-228, Scripta Materialia, 66, 2012, 829-831.

[LUO'13] H.W. Luo, C.H. Qiu, H. Dong, J. Shi, Experimental and numerical analysis of influence of carbide on austenitisation kinetics in 5Mn TRIP steel, Materials Science and Technology, 30(11), 2013, 1367-1377.

[NEH'50] A.E. Nehrenberg, The Growth of Austenite as Related to Prior Structure, Transactions AIME, 188, 1950, 162-174.

[PET'00] H. Petitgand, H. Réglé, O. Bouaziz, T. Iung, S. Barrois, Modeling of grain growth and mechanical properties of IF steels, Proceedings of ISS Conference IF Steels, 2000, 339-346.

[REI'06] J. Reiter, C. Bernhard, H. Presslinger, Determination and Prediction of Austenite Grain Size in Relation to Product Quality of the Continuous Casting Process, Materials Science and Technology – Association for Iron and Steel Technology, 5, 2006, 805-816.

[SPE'69] G.R. Speich, Tempering of low-carbon martensite, Transactions of the Metallurgical Society AIME, 245(12), 1969, 2553-2564.

[SPE'72] G.R. Speich, W.C. Leslie, Tempering of steel, Metallurgical Transactions, 3(5), 1972, 1043-1054.

[SPE'81] G.R. Speich, V.A. Demarest, R.L. Miller, Formation of austenite during intercritical annealing of dual-phase steels. Metallurgical Transactions A, 12A, 1981, 1419-1428.

[TAK'04] S. Takaki, K. Fukunaga, J. Syarif, T. Tsuchiyama, Effect of grain refinement on thermal stability of metastable austenitic steel, Materials Transactions, 45, 2004, 2245-2251.

[YAN'09] H. Yang, H. Bhadeshia, Austenite grain size and the martensite-start temperature, Scripta Materialia, 60, 2009, 493–495.

CHAPTER 4: CHARACTERIZATION AND MODELLING OF MECHANICAL PROPERTIES AFTER INTERCRITICAL ANNEALING

This chapter presents the experimental characterization of mechanical behavior of studied MMS, the analysis and understanding of the obtained results, and, finally, a modeling approach based on the microstructure observations discussed in the previous chapter. The chapter division on sections is given just above.

4.1 Mechanical properties of annealed samples

Mechanical behavior of the medium Mn steel (0.1C-4.7Mn wt.%) after intercritical annealing was obtained using standard tensile tests. Evolution of mechanical behavior with the holding time at 650°C was mainly studied. Engineering and true stress-strain curves are presented in Figure 112. Engineering and true stress-strain curves were each time separated in two graphs: one corresponding to annealing times going till 3h of holding time and another corresponding to higher holding times. This was done for easier analysis of the curves.
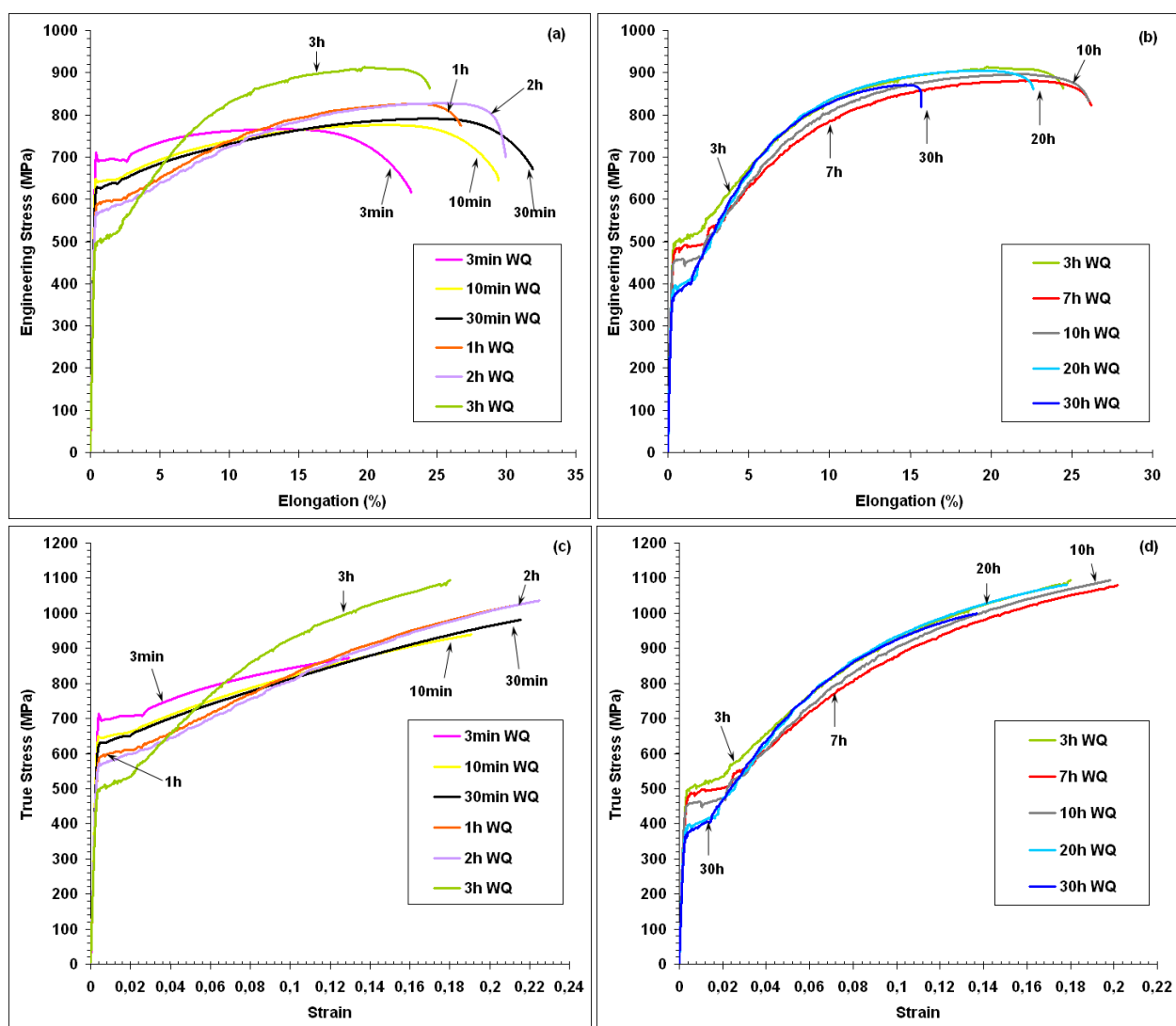
Figure 112 – Engineering (a, b) and true (c, d) stress-strain curves of the samples annealed at 650°C with different holding time.

Figure 112 shows that holding time has an important impact on mechanical behavior. Indeed, a variety of curves were obtained with different strength-elongation combinations and work hardening rates. Mechanical characteristics like yield strength (YS), yield point elongation

131

(YPE), ultimate tensile strength (UTS), uniform (Uel) and total (TE) elongations are summarized in Table 8. Their evolution with holding time was analyzed and presented in Figure 113.

Table 8 – Measured mechanical properties of samples after different annealing treatments, with their corresponding incertitude in the brackets: high and low yield strength (YS$_H$ and YS$_L$ ± 15MPa), yield point elongation (YPE ± 0.2%), ultimate tensile strength (UTS ± 10MPa), uniform (Uel ± 0.5%) and total   (TE ± 1%) elongations, respectively.

Ref.	YS$_H$ (MPa)	YS$_L$(MPa)	YPE (%)	UTS (MPa)	Uel (%)	TE (%)
3min WQ	712	688	2.3	766	13.5	22.8
10min WQ	648	641	1.6	776	20.6	29.1
30min WQ	628	626	1.4	791	23.7	31.6
1h WQ	589	589	2.1	826	23.2	26.3
2h WQ	566	566	0.3	827	24.9	29.6
3h WQ	495	487	1.9	909	19.2	23.6
7h WQ	482	482	1.9	882	21.9	25.8
10h WQ	455	446	1.7	897	21.5	25.7
20h WQ	385	378	1.4	905	19.1	22.2
30h WQ	368	359	1.2	871	14.2	15.2
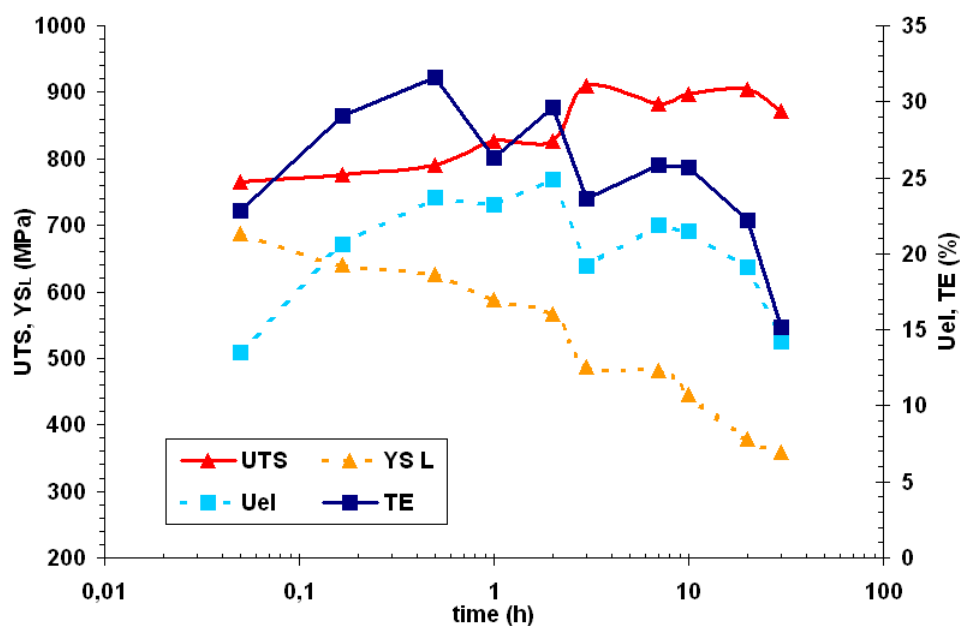
Figure 113 – Evolution of mechanical properties with the holding time for the samples annealed at 650°C.

The obtained mechanical properties are quite attractive: good combination of strength and ductility was produced through a rather large range of holding time. Higher YS (more than 100MPa) with same or slightly better elongation was obtained in comparison with the mechanical properties of classical TRIP800. There is a clear optimum in terms of strength-elongation balance observed for 2h holding at 650°C. It can be seen that increase of holding time till 2h resulted in a small increase of UTS (+60MPa), but in the same time YS showed a decrease in about 150MPa and elongation was improved (+10% of Uel). Further increase of holding time induced a decrease of ductility (elongation), slight increase of UTS and pronounced decrease in YS. Such evolution of mechanical properties correlates well with the microstructure evolution observed in chapter 3. During first holding hours austenite fraction is increasing and carbides are continuously dissolved. C and Mn partitioning into the austenite and its ultra fine size during this

stage are the reasons of improved austenite stability. The retained austenite fraction of 2h sample is close to the maximum observed for 1h sample. Higher RA fraction results in more pronounced TRIP effect which finally gives better elongation. Higher holding time is decreasing the stability of RA, hence fresh martensite is observed in the microstructure, which contributed to the decrease of elongation. Slight increase of UTS till 3h of holding is correlated with the increase of global austenite fraction meaning higher martensite or induced martensite fraction during mechanical loading. The observed permanent decrease of YS is thought to be related with the continuous recovery and recrystallization of initial martensite structure which leads to the lower resistance of matrix phase (ferrite) due to lower density of defects. Low YS can be also attributed to high RA fraction due to the low YS of obtained austenite as it will be shown further in Chapter 4.4.

Strain hardening rate of the samples was also studied. The evolution of strain hardening rate with strain and stress is presented in Figure 114. All samples expose three domains of work hardening (WH) rate evolution: 1) WH rapid decreasing; 2) re-enhancement and stabilization of WH; 3) final drop of WH. These three stages are clearly shown in Figure 115. Such three step behavior was reported to be related to the strain induced transformation of austenite into martensite (TRIP effect) in MMS [SHI'10]. All the samples had a retained austenite fraction higher than 20% thus taking benefit of TRIP effect. However, the rate of strain induced transformation was not the same and, hence, the strain hardening behavior was also singular. The re-enhancement of WH was moderate for the holding times lower than 2h, especially for the 3min holding, but in the same time the final drop of WH appears more as a stagnation or very slight decrease (particularly true for the 1h and 2h samples). Taking into account that the RA fraction was rather high and that stability of RA was increasing, one can suppose that such behavior results from the continuous strain induced transformation of austenite with small increment. It can be even imagined that at the end of the tensile test some RA stays untransformed. On the other hand, for the samples with higher annealing time (>2h) the re-enhancement of WH was more pronounced, but the following decrease of WH was also amplified especially for the 30h sample. It is thought that such behavior was obtained due to the lower stability of RA, thus the rate of strain induced transformation was more rapid and RA was consumed quickly. These aspects of RA stability will be further discussed in chapter 4.6 in relation with the obtained experimental data.
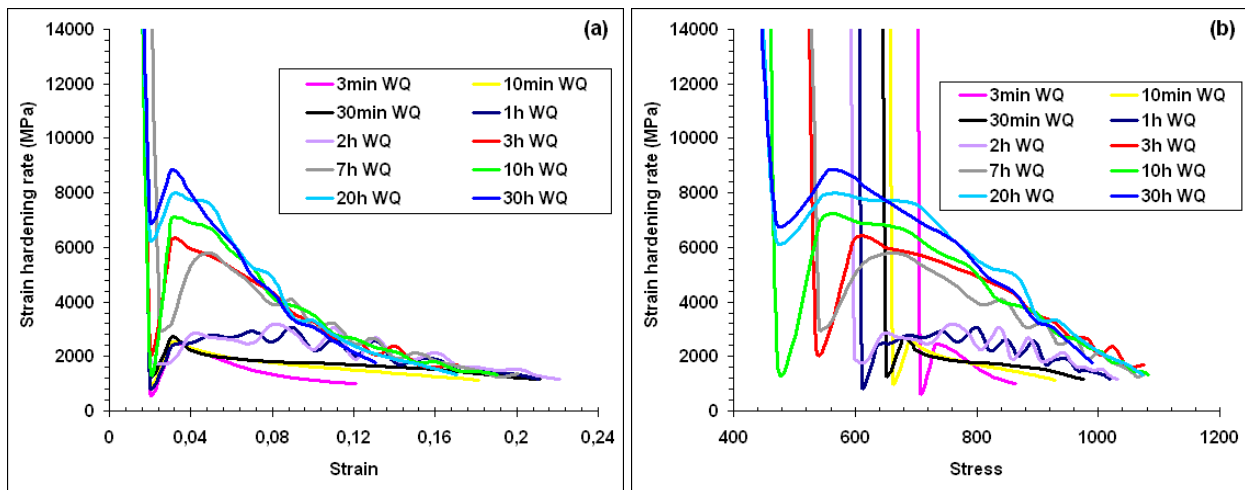
Figure 114 - Strain hardening rate as a function of strain (a) and stress (b).
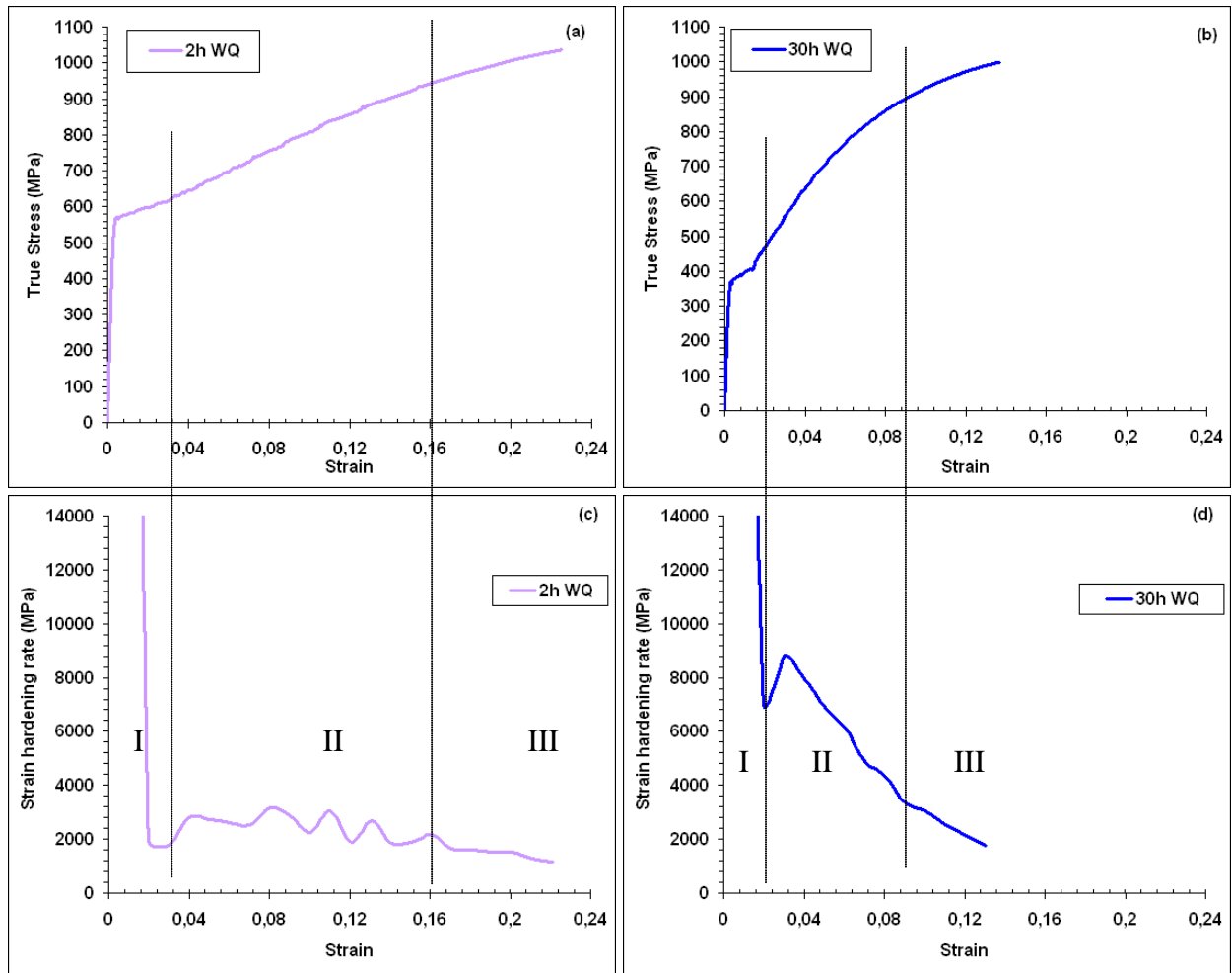
Figure 115 – Examples of 3 stage work hardening rate evolution for the samples annealed at 650°C for 2 and 30 hours. Curves of true stress-true strain (a, b) and of strain hardening rate as a function of true strain (c, d).

Some simple correlations between mechanical characteristics and fractions of constituents were analyzed. Relations between YS_L, Maximum True Stress, Uel and fractions of RA and FM+RA were supposed to be the most interesting, and thus they are presented in Figure 116. It can be seen that RA fraction influence on YS_L and Maximum True Stress is very limited or inexistent, but in the same time it has an impact on Uel, although, it cannot explain the complete evolution. On the other hand, FM+RA fraction has no correlation with Uel, but seems to be an important parameter for the strength of these steels. However, the relation between YS_L and FM+RA fraction appears to be strange in this case. FM+RA represent the hard constituents in the steel. Thus one can expect the increase of YS with the increase of FM+RA fraction, but the observed tendency was opposite. In a particular case when YPE exists, the decrease of YS with the increase of hard phase is possible when the YPE is suppressed. But in this work YPE was found for all the samples. Hence, it was then supposed that this correlation has an indirect link through the holding time at 650°C which represents the annealing (tempering) of initial martensite. Longer holding time results in higher FM+RA fraction, but the degree of initial martensite tempering will be also higher, consequently decreasing YS.

Finally, it can be concluded that, although there are some correlations between mechanical properties and microstructure, they are quite complex and their understanding is incomplete. Hence, to explain and model global tensile behavior of studied steel, more advanced comprehension of the behavior of each constituent and their interactions should be acquired. The

following subsections will present the approach used for the modeling of mechanical behavior and the performed experimental trials to obtain behavior laws of each constituent, when possible. Finally, in the end of the chapter the complete model is presented and discussed.
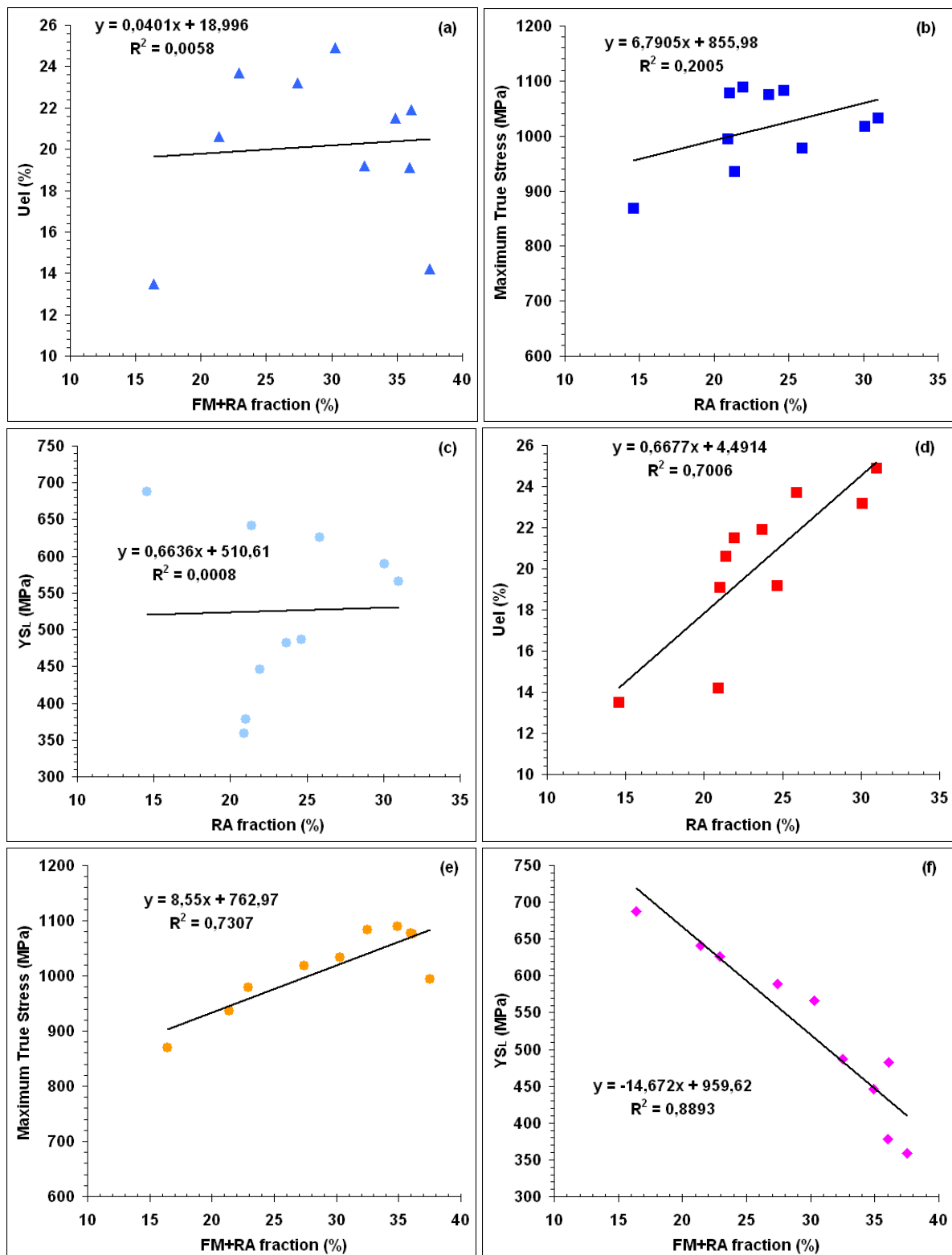
Figure 116 – Tendencies between YS$_L$, Maximum True Stress, Uel and fractions of RA and FM+RA.

4.2 Description of the Iso-W approach

Based on the microstructure analysis and in order to simplify the problem, it was decided to consider a microstructure consisting of three phases: ferrite, retained austenite and fresh martensite. Influence of the carbides, precipitated in the ferrite then dissolved during annealing, was neglected. It is a strong assumption which needs to be confirmed by a complementary detailed study. This point is discussed further in the section concerning mechanical behavior of ferrite.

To predict mechanical behavior law of the three phase mixture without supplementary fitting parameter it was decided to use the so-called "Iso-W" approach proposed by Bouaziz and Buessler [BOU'99]. This approach was already presented in chapter 1. It supposes that in a multiphase microstructure increment of mechanical work is equal in each constituent during the whole mechanical loading. In terms of equation this means that:

$$\sigma_F d\varepsilon_F = \sigma_A d\varepsilon_A = \sigma_{FM} d\varepsilon_{FM} \tag{56}$$

where σ_F, σ_A, σ_{FM} and ε_F, ε_A, ε_{FM} are the stress and strain of ferrite, retained austenite and fresh martensite, respectively.

In order to calculate the increment of strain for each phase the subsequent mixture law was used:

$$d\varepsilon = f_F d\varepsilon_F + f_A d\varepsilon_A + f_{FM} d\varepsilon_{FM} \tag{57}$$

where ε is the macroscopic strain of the material and f_F, f_A and f_{FM} are, respectively, the fractions of ferrite, retained austenite and fresh martensite.

As it can be seen from equations (56) and (57), prediction of the global mechanical behavior of such mixture of phases requires at least two following inputs:
1) mechanical behavior of each constituent: annealed and fresh martensite with medium Mn content, and retained austenite with medium C and Mn content;
2) description of initial microstructure: at least fractions of all constituents.

As well it is necessary to take into account the dynamic evolution of phase fractions under loading, e.g. induced transformation of retained austenite into martensite (TRIP effect), which introduces an additional strain hardening. Hereafter are described the considerations and investigations performed for each phase.

4.3 Mechanical behavior of as-quenched martensite and its simulation

4.3.1 Mechanical behavior of as-quenched medium Mn martensite

Generally, as it was discussed in the literature review, it is considered that the mechanical behavior of as-quenched martensite depends mostly on its C content. Thus, it was decided to obtain experimental stress-strain curves of as-quenched martensite for the studied steel and to model them with the approach proposed by Allain et al. [ALL'12] (already described in the literature review).

Two samples after first complete austenitization at 750°C for 30 minutes followed by water quench as presented in chapter 3 were used. Their microstructure was already investigated in chapter 3.1. Figure 117 presents the main results of this investigation. Microstructure analysis

after Dino etching confirmed the absence of ferrite and X-ray spectra did not revealed any austenite. Hence it was concluded that the structure consists mainly of martensite and only negligible amount of retained austenite, observed in TEM. Then, tensile tests were performed and the obtained tensile curves and mechanical properties are presented in Figure 118 and Table 9, respectively. Figure 118 and Table 9 also illustrates the reproducibility of tensile curves between the two samples.
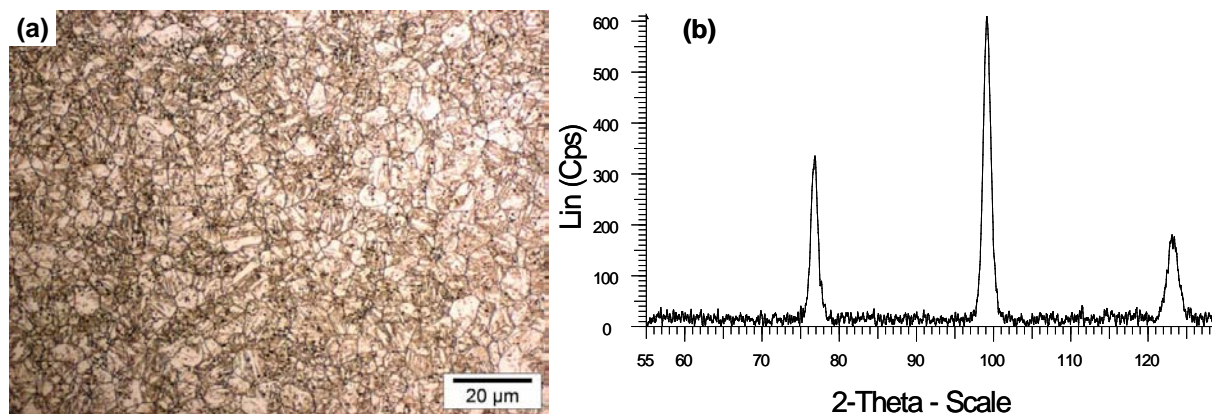
Figure 117 – Structure of medium Mn steel quenched after holding at 750°C for 30min: (a) observation with optical microscope after Dino etching and (b) corresponding X-ray spectrum.
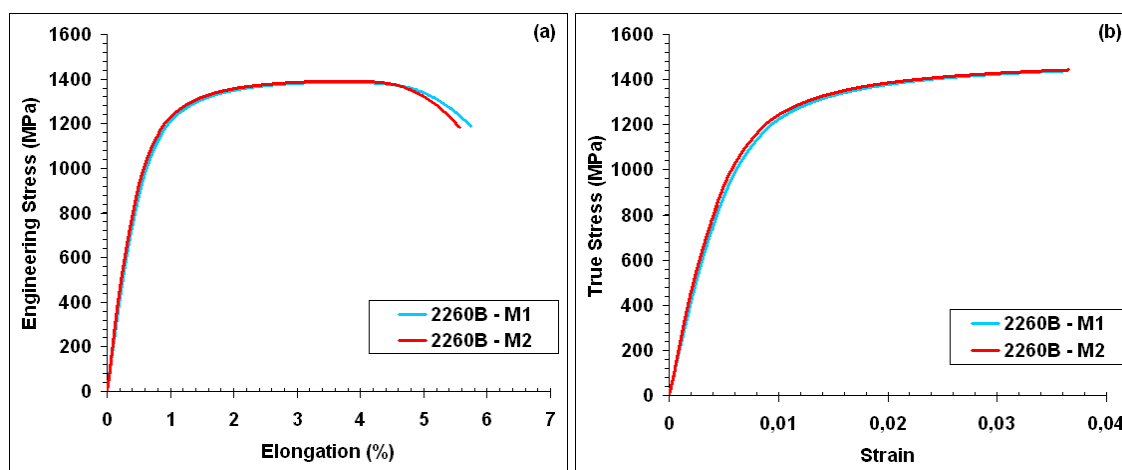
Figure 118 – Engineering and true stress-strain curves of studied medium Mn martensitic samples.

Table 9 – Measured mechanical properties of martensitic samples with the corresponding incertitude in the brackets: yield strength ($YS_{0.2} \pm 15MPa$), ultimate tensile strength (UTS $\pm$ 10MPa), uniform (Uel $\pm 0.5\%$) and total (TE $\pm 1\%$) elongations, respectively.

Ref.	$YS_{0.2}$ (MPa)	UTS (MPa)	Uel (%)	TE (%)
2260B-M1	1049	1387	3.0	5.2
2260B-M2	1067	1391	3	5

It can be stated that the observed strength level and strain hardening rate are quite high for a quenched 0.1C steel which typical UTS value is around 1200MPa. Looking on the obtained data, we were forced to conclude that the mechanical behavior of the obtained martensite depends not only on its C content but also on its Mn content. Moreover, it was not possible to predict the stress-strain curve of such martensite (medium Mn steel) using the CCA model proposed by Allain et al. [ALL'12]. Hence, it was decided to investigate a little more the effect of Mn on the strength and strain hardening of martensite.

4.3.2 Influence of Mn content on the strength and strain hardening of martensite

A database of some selected C-Mn martensitic steels from previously published studies and of some new experimental trials was built. The chemical compositions of these steels are shown in Table 10.

Table 10 – Chemical compositions (wt.%) of some martensitic steels tested in the present study and in previously published works with corresponding references. For each steel first column gives the reference (steel) that will be used further in the text.

Steel	Composition (wt.%)					Source
	C	Mn	Si	Cr	Ti	
0.3C	0.29	1.20	0.25	0.17	0.04	This study
0.36C	0.36	1.22	0.23	0.10	0.04	This study
0.1C-5Mn	0.09	4.6	-	-	-	This study
0.15C-5Mn	0.14	4.6	-	-	-	This study
0.01C-3Mn	0.01	2.92	0.01	0.11	0.04	Zhu et al. [ZHU'10]
0.09C	0.09	1.90	0.15	0.10	-	Allain et al. [ALL'12]
0.15C	0.15	1.90	0.22	0.20	-	Pushkareva [PUS'09]
0.22C	0.22	1.18	0.27	0.21	-	Allain et al. [ALL'12]

"-" means less than 0.01 wt.% for Si and Cr and less than 0.001 wt.% for Ti.

Figure 119 presents the results of experimental tensile tests performed in the present study along with the results collected from the previous works [PUS'09], [ZHU'10], [ALL'12]. The true stress evolution as a function of true strain is shown in Figure 119(a), meanwhile Figure 119(b) shows the related strain hardening rate evolution as a function of true stress (so-called Kocks-Mecking plot [KOC'03], [MEC'81]). For all studied martensitic steels some general highlights can be stated:

- conventional yield stress seems to be a function of martensite carbon and manganese contents;
- high work-hardening rate is observed and it increases up to necking strain in accordance with the carbon and manganese contents.

From Figure 119(a) it can be seen that the true stress-true strain curve of 0.1C-5Mn is almost the same as for 0.15C, and that the true stress-true strain curve of 0.15C-5Mn is in between the curves of 0.22C and 0.3C. The same conclusion can be deduced from Figure 119(b) which demonstrates the strain hardening evolution. The solid solution hardening of Mn cannot explain this difference in the behavior of martensitic steels with high Mn content. Modification of solid solution hardening only shifts the curves to higher stress levels, but in the case of medium Mn steels a clear change in strain hardening of martensite can be found. According to F.B. Pickering and T. Gladman [PIC'63] the solid solution hardening of Mn can be evaluated using following relation: S_{Mn}*Mn wt.%, where $S_{Mn} = 32$. This means that each percent of Mn increases strength of 32MPa and for 4.6wt.% of Mn the strength should increase of about 150MPa. Figure 119(c) shows the experimental curves of 0.15C and 0.15C-5Mn, but also 0.15C curve shifted up at 150MPa. This figure proves that such shift is not sufficient to match with 0.15C-5Mn; there are still about 125 MPa missing. But also the strain hardening rate, which is depicted in Figure 119(b) is not the same. Thus, it is considered that simple additive solid solution hardening cannot explain the behavior of martensite with medium content of Mn. It can be also observed from the Figure 119(a) and (b) that the influence of Mn on stress and on strain hardening is rather limited in the case of small carbon content (0.01C-3Mn). All these facts suggest that Mn content influences the martensite strength and strain hardening in synergy with the carbon content of martensite.
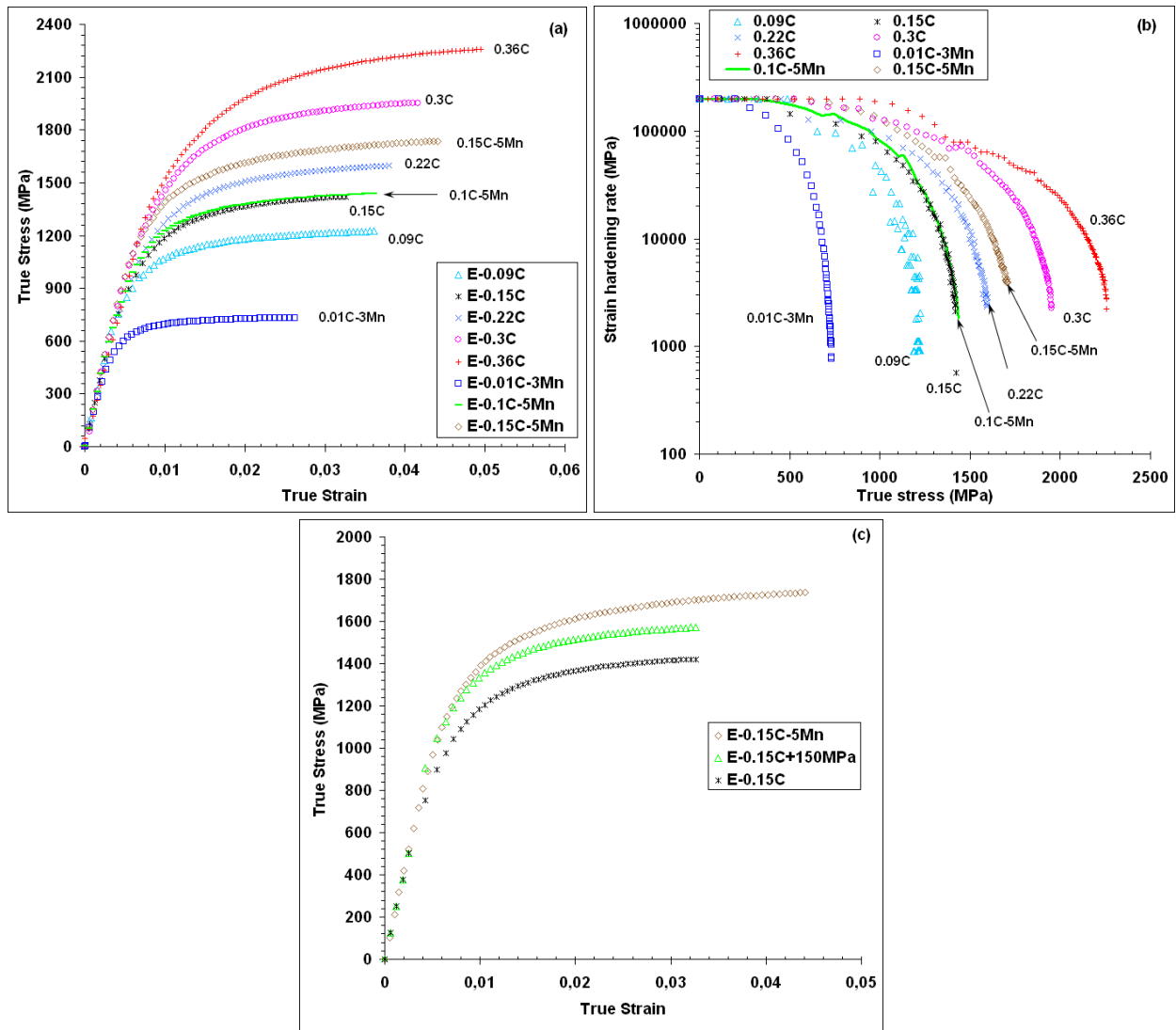
Figure 119 – (a) Experimental true stress-true strain curves of all studied martensitic steels; (b) Strain hardening rate as a true stress function of corresponding tensile tests presented in (a); (c) Comparison of true stress-true strain curves of 0.15C and 0.15C-5Mn steels, and also the curve of 0.15C shifted up at 150MPa, which corresponds to solid solution hardening of Mn.

4.3.3 Model to predict stress-strain behavior of medium Mn martensite

Based on the CCA approach [ALL'12], a simplified behavior law for martensitic steels was proposed. In order to describe the stress-strain curve of martensite as a large elasto-plastic transition the strain hardening can be expressed as the product of Young modulus (Y) by the fraction of elastic zones (1– F):

$$\frac{d\sigma}{d\varepsilon} = (1 - F) \cdot Y \tag{58}$$

where σ and ε are respectively the macroscopic stress and strain of the material.

The plasticized zones fraction F is chosen as a logistic law:

$$F = 1 - \exp\left(-\left(\frac{\sigma - \sigma_{min}}{\sigma_0}\right)^p\right) \tag{59}$$

where σ_{min} is the minimum stress necessary to start to plasticize and, p and σ_0 are the parameters that control the shape of F(σ) curve (Figure 120(a)). In the first stage of tensile test, the macroscopic stress is lower than the elastic threshold ($\sigma < \sigma_{min}$), hence F = 0 and the material exhibits completely elastic behavior. When the applied stress (σ) became more important than σ_{min}, then F starts to increase, meaning that the plasticized zones fraction increases.

Model adjustment with the experimental and literature data showed that σ_{min} and p can be taken as constants for all considered steels, and the following values were found to be optimal: σ_{min} = 450MPa and p = 2.5. Thus, only one variable parameter, σ_0, was used to obtain the best fitting results between model and experiments. It was found that both C and Mn have an important influence on σ_0. A linear dependence between σ_0 and C_{eq} was established in the form of subsequent equation:

$$\sigma_0 = 130 + 1997 \cdot C_{eq} \tag{60}$$

where C_{eq} is the parameter that considers the concomitant influence of C and Mn. It was proposed to take into account this synergy of C and Mn in the following way:

$$C_{eq} = w_C \cdot \left(1 + \frac{w_{Mn}}{K_{Mn}}\right) \tag{61}$$

where w_C and w_{Mn} represent C and Mn (wt.%) contents of martensite, and K_{Mn} is the coefficient of the Mn influence. Finally, from the collected experimental data (Table 10 and Figure 119) it was possible to find the optimum value for K_{Mn} = 3.5.

The σ_0 evolution with C_{eq} is shown in Figure 120(b): experimentally adjusted points were compared to the ones predicted with equation 60.
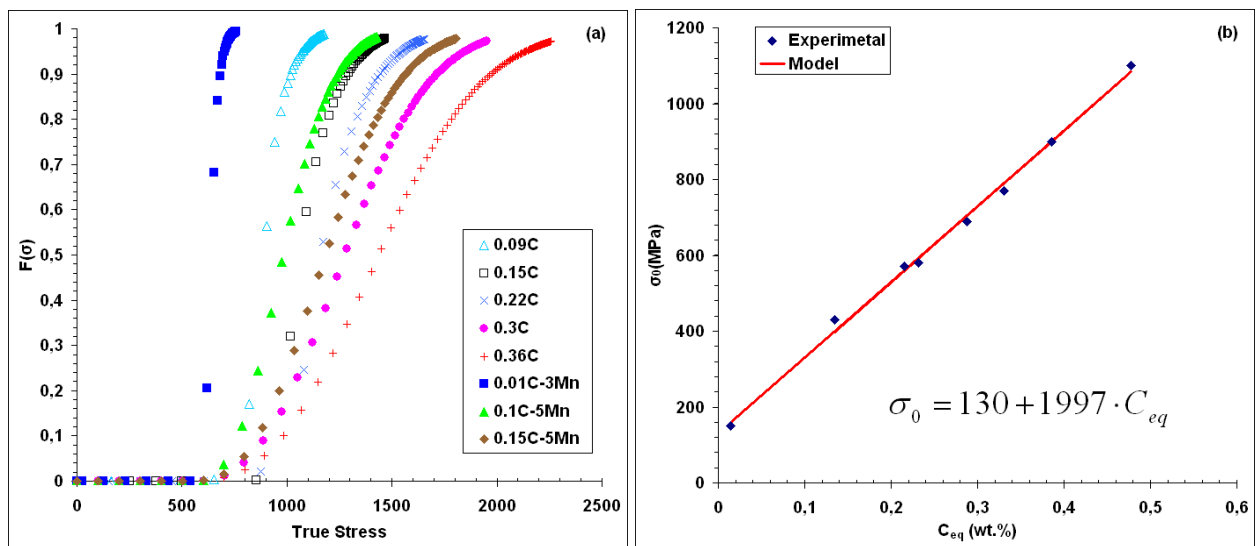
Figure 120 – (a) Evolution of modeled F(σ) with the true stress; (b) Comparison of the σ_0 values: predicted with equation 60 (model) and experimentally adjusted ones.

The final results of the model are presented and compared to the experimental data in Figure 121. The results of stress-strain curves prediction were separated into two graphs (Figure 121(a) and (b)) to have a better vision of medium Mn steels curves. As it can be seen, this simple model accurately predicts the whole stress-strain curves of different martensitic steels with varied C and Mn contents. On the other hand, it can be noticed that the simulated curves are not perfect and there are some mismatches. However, the maximum difference between model and experimental curves in terms of stress is less than 60 MPa and this represent less than 5% of the maximum flow stress.
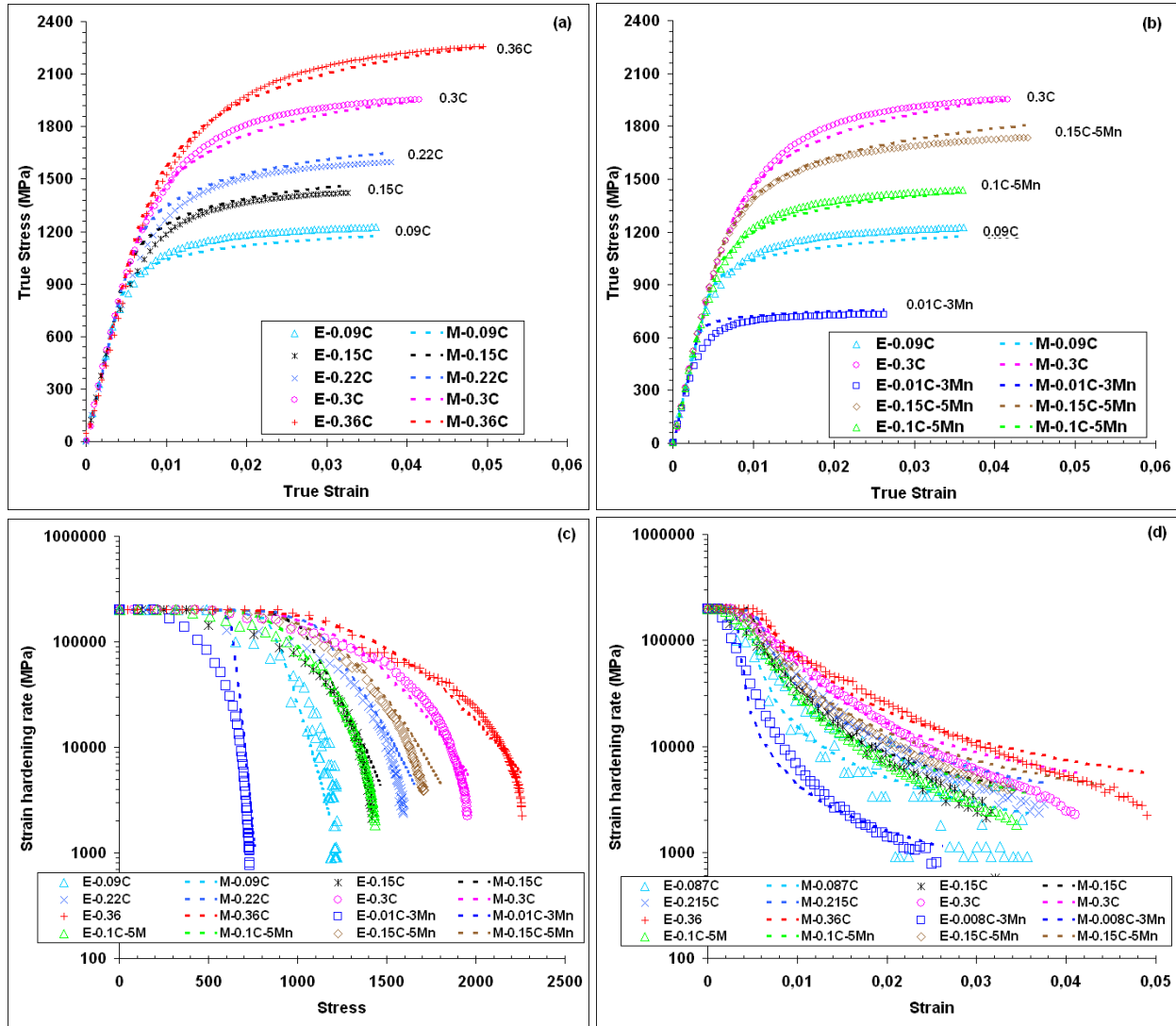
Figure 121 – Comparison of the model and experimental results: (a) and (b) show the stress-strain curves: (a) – steels with varied C content; (b) – steels with higher Mn content and two steels with standard (for AHSS) Mn content for comparison. (c) – evolution of strain hardening rate as a function of stress. (d) – evolution of strain hardening rate as a function of strain. "E" means experimental data and "M" means data from the model.

Figure 121(c) and (d) present the evolution of strain hardening rate as a function of stress and as a function of strain, respectively. Taking into account that modeling of derivative is more complex than modeling of a function itself, the proposed model gives very satisfactory results of strain hardening rate evolution. These figures also show that the model considers correctly the synergy influence of C and Mn on the strain hardening rate evolution.

Even though the results are satisfactory, it is evident that the proposed model is a simplified version of CCA published previously [ALL'12], hence the global description of stress-strain curves is less precise, especially elasto-plastic transition. This can be clearly seen on the stress-strain curves of 0.22C, 0.15C and in particular 0.01C-3Mn steels. The discrepancy of the model is also related to the fact that only one fitting parameter was considered. This was done deliberately in order to simplify the understanding of the observed phenomenon of C-Mn synergy. Model response can be easily improved by relaxing the constraints on σ_{min} making it variable. Nevertheless, more data and studies are needed to obtain good correlation between σ_{min} and some metallurgical or microstructural parameters.

Future works are also necessary to understand physical mechanism of this C-Mn synergy and its relation with the microstructure. The outputs of these further investigations will be probably very helpful for further model improvement.

The work about the effect of Mn on strength and on strain hardening of C-Mn martensite was published in the ISIJ International journal with the reference [ARL'13].

4.4 Mechanical behavior of austenite with medium C and Mn contents

From the microstructure investigations in chapter 3, it was concluded that retained austenite contains about 10 wt.% Mn and a maximum of 0.4 wt.% C. Thus, it was decided to elaborate such composition in order to produce fully austenitic steel and to evaluate its mechanical behavior. However, some technical problems occurred during melting and the obtained steel contained a little higher C content (0.5 wt.%) as well as important quantity of boron. Nevertheless, the work was continued with this steel as it was considered that the increased C content would not change drastically the nature of austenite and the mechanism of its deformation because this composition is in the same domain as targeted one according to the Schumann's diagram (Figure 35).

The obtained 2 kg ingot had the composition given in Table 11. The ingot was then reheated to 1200°C and hot rolled with the finishing temperature around 900°C. Coiling was simulated by a slow cooling in the furnace from 550°C. Microhardness of hot rolled band was evaluated to be around 560 HV.

Table 11 – Chemical composition of steel elaborated for the investigation of austenite mechanical behavior (10^{-3} wt.%).

Ref.	C	Mn	Si	P	Al	B	S	Cr	Cu	N
A193	495	9940	51	11	26	1.4	2	4	6.8	1.1

Hot rolled microstructure was analyzed after Nital etching using optical microscope and SEM. The obtained microstructures are shown in Figure 122.
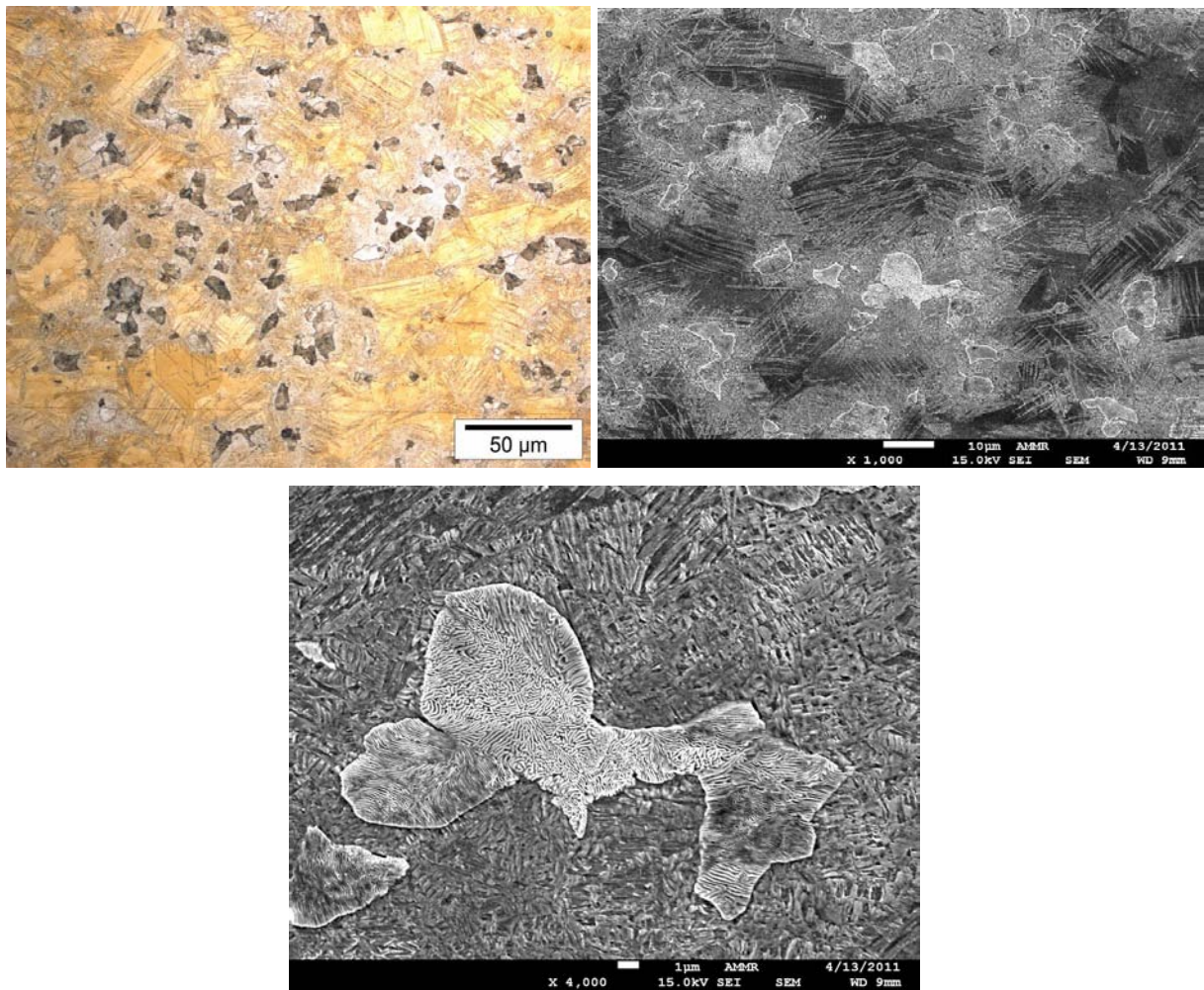
Figure 122 – Optical and SEM images of hot rolled 0.5C-10Mn (wt.%) steel after Nital etching.

From these observations it appears that brown or dark areas on optical image are pearlite islands, which are clearly seen in SEM images. The orange color areas on optical and dark grey on SEM images are supposed to be austenite. Needle like features are supposed to be epsilon martensite. And finally dense areas around pearlite islands are imagined to be alpha prime martensite. X-Ray Diffraction revealed the presence of former three phases: austenite, ε-martensite and α'-martensite. However, deeper microstructure analysis of these phases (like TEM) was not done, thus their morphological appearance on optical and SEM images stays hypothetical.

Cold rolling of such steel was not possible due to high hardness and brittleness of the hot rolled sheet, thus further trials with the objective to produce fully austenitic structure were continued on hot rolled metal. The dilatometer trial presented in Figure 123(a) was performed: heating with ~5°C/s rate to 1000°C, then holding for 10s followed by cooling with ~5°C/s rate. The obtained dilation curve is shown in Figure 123(b). Based on the equilibrium thermodynamic data, at 1000°C the structure is fully austenitic. And according to the dilation curve (Figure 123(b)), there is no phase transformation during slow cooling. Therefore, it was supposed that if the sample is raised into the austenitic domain and then quenched it will be all or mostly austenitic with perhaps some martensite (α' and/or ε). Hence, a new annealing cycle was done on hot rolled sample: it was heated up with ~6°C/s rate to 800°C, soaked for 5min and then water quenched. Hardness of annealed sample was evaluated to be around 270HV. In the same time, low fraction of α'-martensite (less than 7%) was determined from the X-ray and magnetic measurements. It was then supposed that the microstructure was mostly austenitic. Finally, tensile tests were performed on hot rolled and annealed at 800°C-5min samples. The obtained stress-strain curves and mechanical properties are presented in Figure 124 and Table 12, respectively.

Table 12 – Measured mechanical properties of hot rolled and annealed at 800°C-5min samples with the corresponding incertitude in the brackets: yield strength ($YS_{0.2} \pm 15MPa$), ultimate tensile strength ($UTS \pm 10MPa$), uniform ($Uel \pm 0.5\%$) and total ($TE \pm 1\%$) elongations, respectively.

Ref	$YS_{0.2}$ (MPa)	UTS (MPa)	Uel (%)	TE (%)
Hot Rolled	339	572	4.6	4.8
800°C-5min	337	603	3.8	3.9
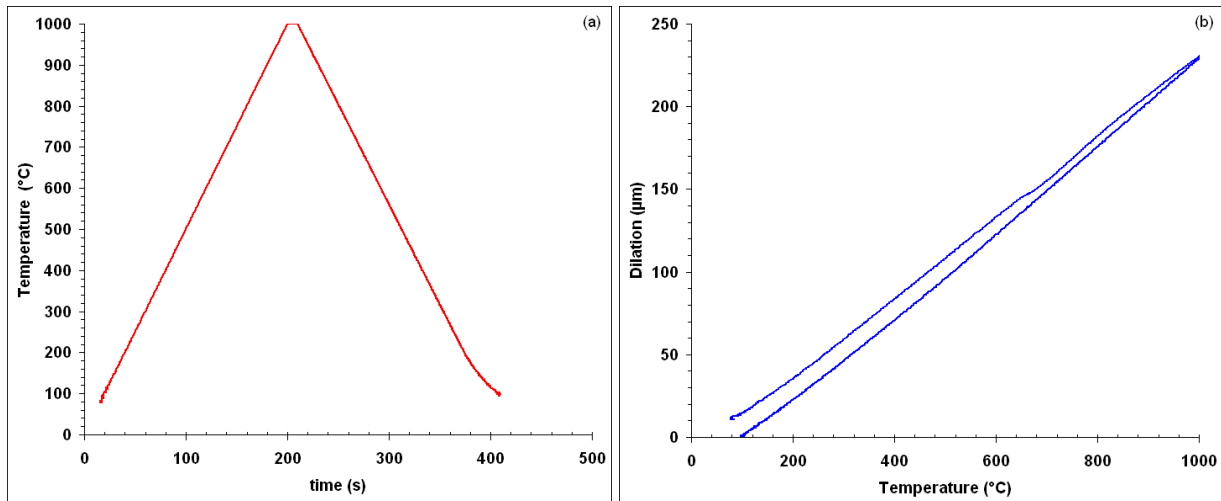
Figure 123 – Dilatometer trial performed on 0.5C-10Mn (wt.%) steel: (a) – temperature versus time curve; (b) dilation curve.
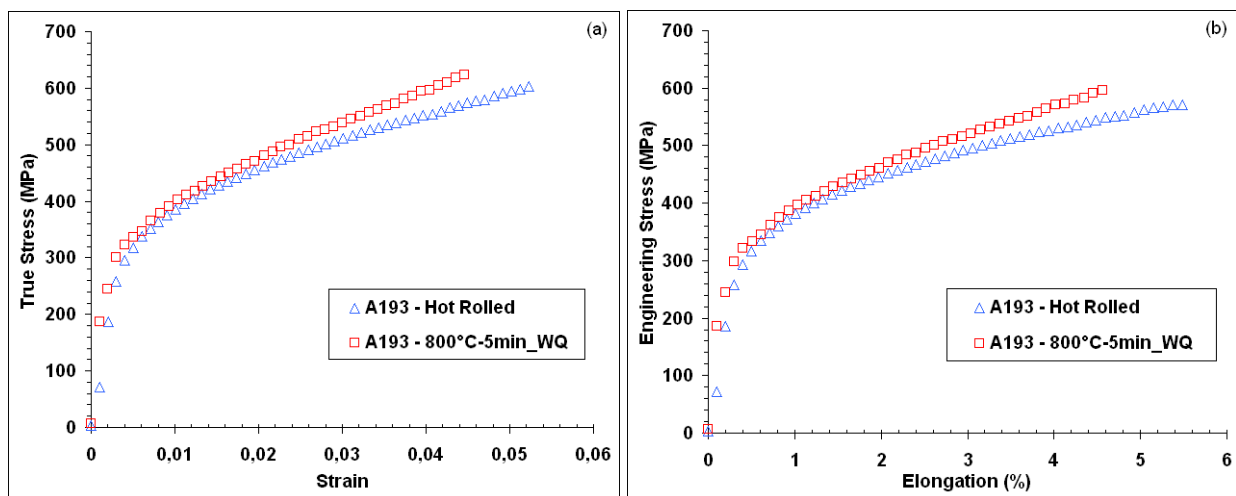
Figure 124 – Engineering and true stress-strain curves of hot rolled and annealed at 800°C-5min samples.

It can be observed that the obtained mechanical properties are rather similar, meaning that the effect of thermal treatment on the properties of this steel is rather limited. In both cases the $YS_{0.2}$ is about 340 MPa, UTS close to 600 MPa and somehow poor elongation (less than 5%) is observed. It is known that the YS is controlled by the softest phase. Hence, taking into account that in the both microstructures the soft phase is austenite, it is assumed that the obtained YS correspond to the YS of austenite. On the other hand, very poor ductility is thought to be due to the very hard initially present or transformation induced α'-martensite that contain high level of C and Mn. Mn segregations can also be the reason for the low elongation values. However this topic was not studied.

144

Finally, considering the observed low YS and relatively high C and Mn content (0.4 wt.% of C and at least 9 wt.% of Mn) of retained austenite in the final microstructure, it appeared to be appropriate to use the law proposed by Bouaziz et al. [BOU'11] for the description of retained austenite mechanical behavior:

$$\sigma_A(\varepsilon_A) = \sigma_{0_A} + K \cdot \left[\frac{1 - \exp(-f \cdot \varepsilon_A)}{f} \right] \tag{62}$$

where σ_A and ε_A are respectively the stress and strain of the retained austenite, $K = 2900$ and $f = 4$ are fitting parameters determined by Bouaziz et al. [BOU'11] and σ_{0A} is the yield stress of austenite that increases with C content and decreases with Mn content in the following manner:

$$\sigma_{0_A} = 228 + 187 \cdot w_C - 2 \cdot w_{Mn} \tag{63}$$

where w_C and w_{Mn} are, respectively, C and Mn contents of austenite in weight percents.

Comparison of the stress-strain curves proposed by the explained model and experimental one is shown in Figure 125. One can state that the simulation differs from the experimental points. Clearly, the strain hardening rate of the experimental curve is higher than the model ones. Of course, by changing the fitting parameters the difference can be decreased. But deeper analysis of the global data (tensile curves and microstructure characterization) brought us to the following conclusions. In fact, initially present or rapidly transformation induced α'-martensite that contain high level of C and Mn would contribute significantly to the strain hardening of the experimental material. Hence, the experimentally obtained curve for the sample annealed at 800°C for 5min is not representative of the fully austenitic structure behavior, but that of an austenite-martensite structure. Taking into account these considerations, it was judged that the proposed model will be appropriate for the mechanical behavior description of austenite with medium C and Mn contents.
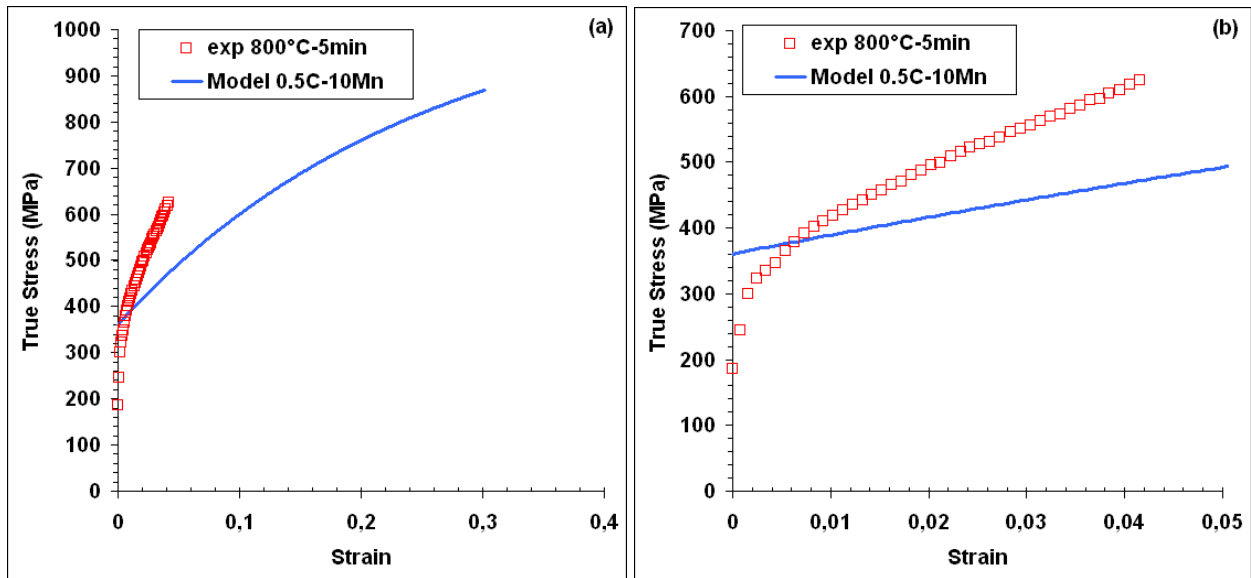
Figure 125 – True stress-true strain curves of the sample annealed at 800°C for 5min (experimental points – open red squares) and model austenite structure (blue curve): (a) – complete curves; (b) – zoom on low strain domain.

4.5 Mechanical behavior of ferrite with medium Mn content

As presented previously in chapters 1 and 3, ferrite (annealed martensite) is the phase that was obtained from the high temperature annealing of fresh martensite. One can say that this is simply a ferrite and from crystallographic point of view this will be true, but the morphology and mechanical behavior of this ferrite (annealed martensite) is different. This was clearly shown in the works of Sugimoto [SUG'02]. In our work in chapter 3 it was also demonstrated that such ferrite contains an important quantity of dislocations which should have a non negligible impact on mechanical behavior. Consequently, in this work it is considered that this ferrite (annealed martensite) has similar properties as an ultra fine lath-like ferrite with some dislocations and/or restorations cells.

Then the question was: how to produce steel with 100% lath-like ferrite structure? This question was quite complex and no trivial answer was found. No way to produce 100% lath-like ferrite structure was determined. However, it was possible to produce microstructure with lath-like ferrite (more than 98%) and some carbides. Then it was decided to study such structure and to look for some approximations.

The studied 0.1C-4.7Mn (wt.%) steel was heated up with ~6°C/s rate to 500°C, held for different times (3min, 1h and 30h) and finally water quenched. Such low temperature was chosen intentionally in order to avoid any austenite formation. However, even at such low temperature after very long annealing, some nucleus of austenite were formed, as it was revealed by microstructure analysis presented further. Microstructure was controlled using SEM after metabisulfite etching; the images are presented in Figure 126. The revealed microstructure shows clearly the ferrite in grey with some carbides (white spots). Prior austenite boundaries can be also easily observed. In the sample with 30h holding time some very small nucleus of austenite were observed (black colored spots in the down left corner of Figure 126(b)) but their fraction was quite limited and thus they can be neglected.
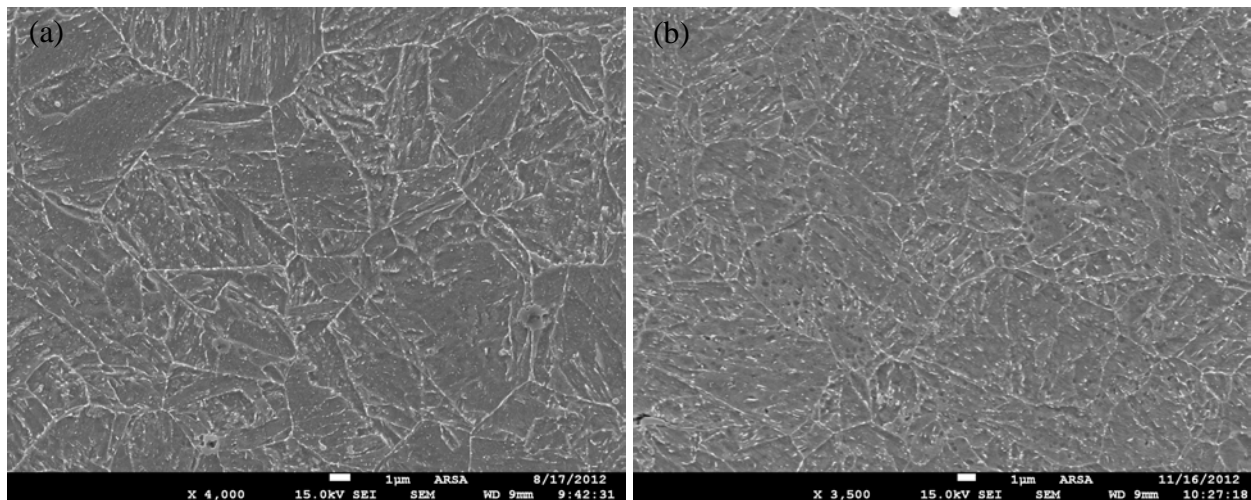
Figure 126 – Microstructure of the studied MMS steel annealed at 500°C for (a) – 1h, (b) – 30h. Grey color is ferrite and white spots are carbides.

The low temperature annealed samples were then submitted to tensile tests. The resulting stress-strain curves and mechanical properties are presented in Figure 127 and Table 13, respectively. Data for one sample with fully fresh martensite structure are also given for comparison.

It can be seen that the obtained tensile curves were quite particular. The yield strength was rather high (more than 750 MPa) and almost no strain hardening was observed (flat curves). Such mechanical behavior corresponds to the revealed microstructure: ultra fine lath-like recovered ferrite and some fine carbides. In the work of Bouaziz [BOU'09] it was already shown that during mechanical loading ultra fine ferrite is characterized by very high strength (for example ~1000MPa for 0.3µm size) and absence of strain hardening. Based on this work it was concluded that the obtained tensile curves and microstructures are in good agreement. In addition, it was noticed that with the increasing holding temperature or time the size of annealed martensite increases, thus decreasing the strength (3min ~1000 MPa; 30h ~800 MPa).
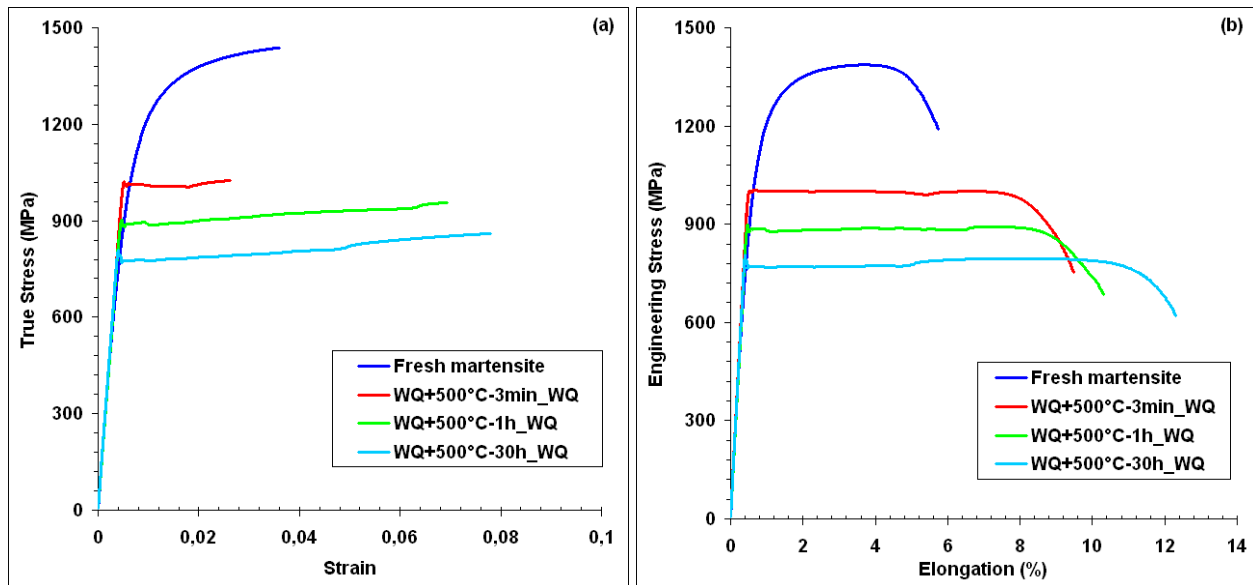
Figure 127 – Engineering and true stress-strain curves of samples annealed at 500°C for different times and one fresh martensite sample for comparison.

Table 13 – Measured mechanical properties of samples annealed at 500°C for different times and one fresh martensite sample. Corresponding incertitude is presented in the brackets: high and low yield strength (YS$_H$ and YS$_L$ ± 15MPa), yield point elongation (YPE ± 0.2%), yield strength (YS$_{0.2}$ ± 15MPa), ultimate tensile strength (UTS ± 10MPa), uniform (Uel ± 0.5%) and total (TE ± 1%) elongations, respectively.

Ref.	YS$_H$(MPa)	YS$_L$(MPa)	YPE (%)	YS$_{0.2}$ (MPa)	UTS (MPa)	Uel (%)	TE (%)
Fresh M	-	-	-	1049	1387	3.0	5.2
3min WQ	1000	990	4.9	-	1001	6.1	9.1
1h WQ	898	878	6	-	892	6.8	10
30h WQ	806	765	4.3	-	795	7.7	12

Considering the fact that there was no strain hardening of such a ferrite and that its morphology was a lath-like one, it was proposed to model its behavior with an elastic perfectly plastic law where the stress level depends only on solid solution hardening and on the mean free path. For that purpose, the law proposed by Bouaziz and Buessler [BOU'02] and inspired from Orowan [ORO'54] theory was used:

$$\sigma_F(\varepsilon_F) = \sigma_{0_F} + \frac{M \cdot \mu \cdot b}{\lambda} \tag{64}$$

where M is the Taylor factor (taken equal to 3), μ is the shear modulus (80000MPa), b is the magnitude of the Burgers vector (0.25 nm), λ is the mean free path (lath size) and σ_0 is the internal friction stress that takes into account solid solution hardening in the following manner:

$$\sigma_{0_F} = 60 + 32 \cdot w_{Mn} + 750 \cdot w_P \tag{65}$$

where w_{Mn} and w_P are Mn and P contents of ferrite, taken in weight percents.

The parameter λ (mean free path) is a fitting parameter and it can represent the influence of both lath size of ferrite and carbides interspacing. Therefore, influence of carbides can be partially included in this fitting parameter λ.

4.6 Retained austenite strain induced transformation (TRIP effect)

As it was discussed in chapter 1, under mechanical loading retained austenite transforms to martensite. Such transformation increases considerably the strain hardening rate of the material, thus delaying necking and increasing elongation. Hence, it is very important to know the factors that control this transformation and to predict properly the induced martensite fraction. With this aim, the evolution of RA fraction with the increase of deformation was measured via the interrupted tensile tests for two different treatments. These two extreme cases are 1h and 30h holding at 650°C. Magnetic saturation measurements were performed in the deformed zone to estimate retained austenite fraction. The increase of induced martensite and the decrease of RA fraction with the strain are presented in Figure 128.

Looking only on the Figure 128(a) one could say that the induced martensite transformation is the same, but this is not really true. In fact, considering Figure 128(b) it is more evident that there is an important difference. In the beginning (till ~0.08 strain) the slope of RA decrease in both cases seems to be the same, but afterward a different behavior is observed. The slope of 1h sample is slightly diminished thus less austenite is transformed, but in the case of 30h sample the transformation continues with the same rate. Finally, it can be found that in 1h sample still ~8% of RA was available at the end of tensile test and in contrary in the 30h sample all austenite was consumed. This means that in the 1h sample a portion of RA was stable enough to avoid the transformation even at rather high strain levels. These observations are also in a good agreement with the strain hardening rate curves presented in Figure 114. Strain hardening rate increase of 1h sample was less pronounced but in the same time a certain value is maintained for a rather high strain levels which corresponds to high stability of RA and continuous induced transformation. On the other hand, for 30h sample the increase of strain hardening is important, but its drop off is as well very quick. Such behavior corresponds to a more rapid induced transformation and signifies lower stability of RA.
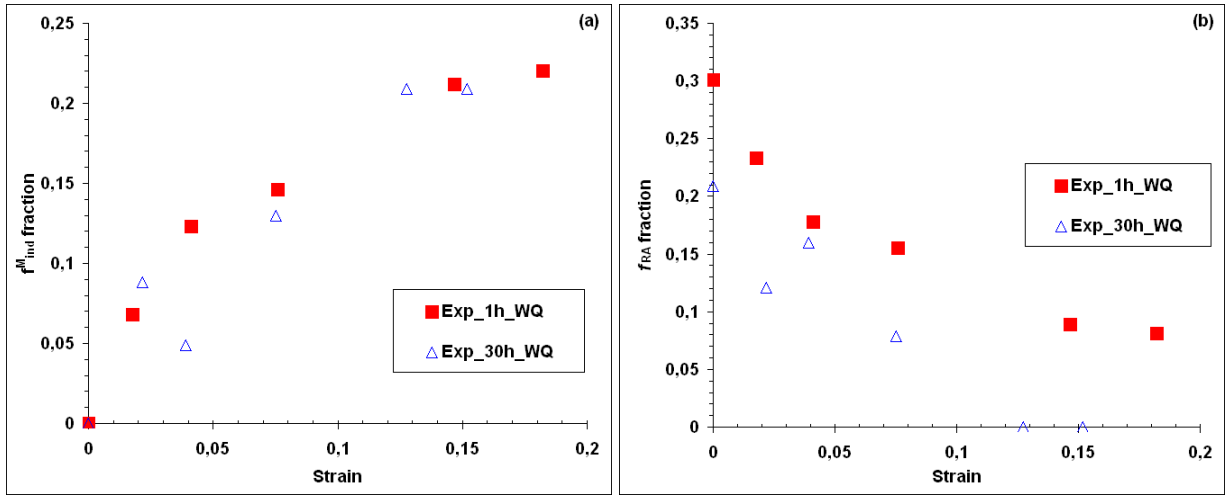
Figure 128 – Evolution of induced martensite (a) and RA (b) fraction with the increase of strain.

Different models describing TRIP effect were presented in chapter 1. The model proposed by Perlade et al. [PER'03] was even tested, but it was rejected (in its actual form) due to the high sensitivity to the austenite size evolution. For simplicity and in the same time good control of the transformation rate, an approach proposed by Olson and Cohen [OLS'75] was selected. This approach is based on simple Kolmogorov-Johnson-Mehl-Avrami [KOL'37], [JOH'39], [AVR'39] law. Nevertheless, the controlling and fitting parameters may differ from author to author. In our case a special form of this phenomenological exponential law was proposed to simulate the evolution of RA fraction with the increase of strain:

$$f_{ind}^{M} = f_{ini}^{RA} \cdot \left(1 - \exp\left(-\left(\frac{\varepsilon_{RA}}{\varepsilon_0} \right)^{n} \right) \right) \tag{66}$$

where f_{ini}^{RA} and f_{ind}^{M} are the fractions of initial retained austenite and induced martensite, respectively, ε_{A} is the strain of the retained austenite and ε_0 and n are the fitting parameters. Using the experimental data from Figure 128, ε_0 and n were obtained for the two samples with different holding time at 650°C: 1h (ε_0=0.12; n=1) and 30h (ε_0=0.07; n=2). Comparison of the simulated and experimental evolution of martensite induced transformation is shown in Figure 129.
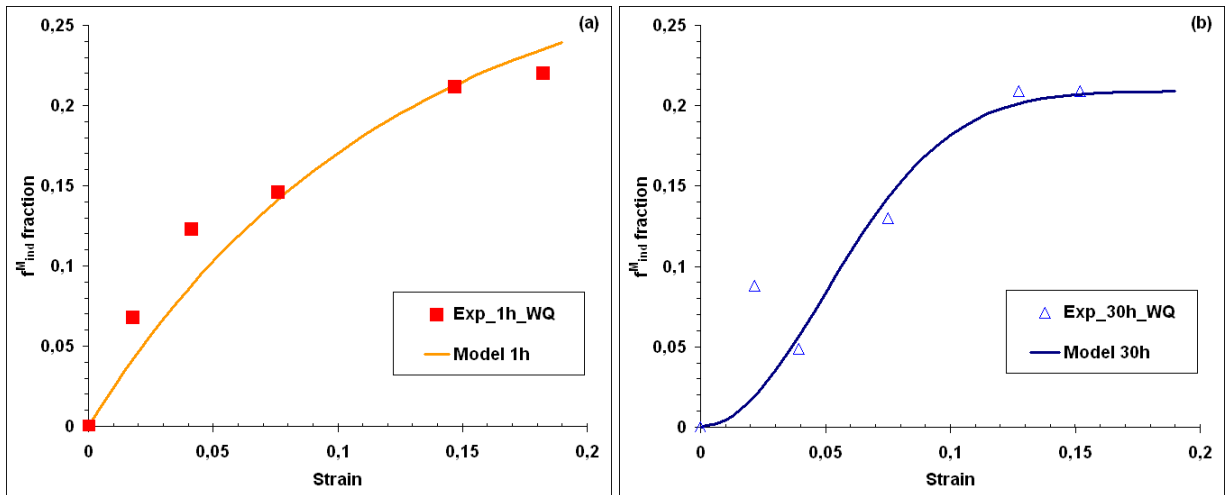
Figure 129 – Induced martensite fraction (f^{M}_{ind}) as a function of strain. Proposed model compared to experimental results for two samples annealed at 650°C for: (a) – 1h; (b) – 30h.

As it can be seen, the proposed model accounts well the differences in the stability of RA discussed above. As a perspective for this model, the parameters that govern the induced transformation rate (ε_0 and n) can be related to some physical parameters controlling the stability of retained austenite (C, Mn composition, grain size and/or others).

Before starting the description of the obtained results with the global model, some additional considerations for the model should be discussed. In fact, during strain induced transformation, fraction of RA decreases and new induced martensite appears. Hence, the effect of such transformation on strain hardening and also the difference between the flow stress of two phases (transformed and induced) should be taken into account. As proposed by Embury and Bouaziz [EMB'10] the strain hardening law for such multiphase mixture can be written in the following manner:

$$\frac{d\sigma}{d\varepsilon} = f_F \frac{d\sigma_F}{d\varepsilon} + f_A \frac{d\sigma_A}{d\varepsilon} + f_{FM} \frac{d\sigma_{FM}}{d\varepsilon} + \frac{df_A}{d\varepsilon}\left(\sigma_M - \sigma_A\right) \tag{67}$$

where f_F, f_A, f_{FM} are the fractions of ferrite, retained austenite and fresh martensite, respectively, σ_M is the flow stress of induced martensite and σ and ε are respectively macroscopic stress and strain.

$\dfrac{df_A}{d\varepsilon}\left(\sigma_M - \sigma_A\right)$ part in equation 67 demonstrates explicitly the contribution of strain induced transformation on the work hardening and also the difference between the flow stress of retained austenite and induced martensite. As the observed C and Mn contents of retained austenite were rather high   (~0.3 wt.% C and at least 9 wt.% Mn) the flow stress of induced martensite will be also high, hence it was decided to take a constant value of $\sigma_M = 2500$ MPa. This value of 2500MPa represents roughly the maximum flow stress that can be measured for fully martensitic steel with high C content (~0.5 wt.%). Krauss [KRA'99] showed, for example, such a value for a 0.5C (wt.%) steel tempered at 150°C. For such high C content martensite a brittle fracture is expected without tempering. For higher C values, a high amount of retained austenite is present after quench, hence, it seems impossible to evaluate properly the flow stress of such martensite.

4.7 Global Iso-W model

As the behavior of each constituent was determined and simulated, it was then possible to predict the stress-strain curves of samples with different holding times at 650°C and various multiphase microstructures. All the parameters used in the model which are necessary for the description of each phase behavior are presented in Annex 4.1. As it was determined experimentally in chapter 3, martensite appears only for the samples with holding time superior to 2h. The values for C content of retained austenite and martensite were taken from the calculations performed in section 3.3.2 (Table 7). C_{eq} calculated for martensite was close to 1 wt.%, however, as it was discussed above, mechanical behavior of such martensite cannot be determined. Thus in the case when C_{eq} was more than 0.5, it was limited to the value of 0.5, which gives $\sigma_{0FM} = 1129$ MPa.

True stress-true strain (only plastic strain is considered) curves simulated with the model and obtained experimentally are compared in Figure 130. This figure is divided in four couples for the easy judgment of the model performance (avoid intermixture between curves): (a) – 3min and 1h samples; (b) – 10min and 3h samples; (c) – 30min and 10h samples; (d) – 2h and 30h samples. Curves of the samples 10h and 20h were not represented as their behavior is very close to the 7h and 30h samples, respectively.
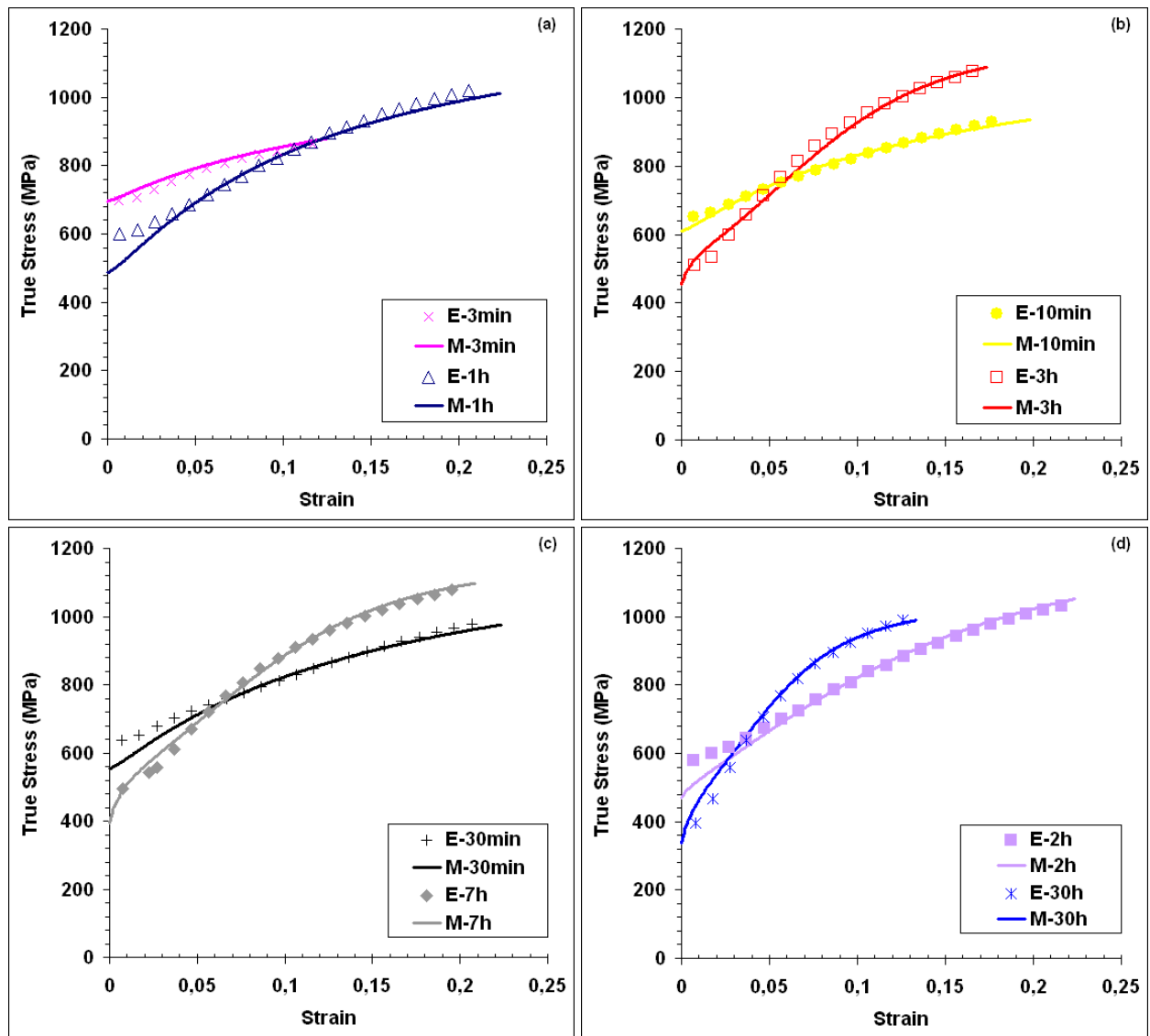
Figure 130 – True stress-true strain curves resulting from the proposed model compared to the experimental ones: (a) – 3min and 1h samples; (b) – 10min and 3h samples; (c) – 30min and 7h samples; (d) – 2h and 30h samples. "E" means experimental data and "M" means data from the model.

As it can be seen, the model provides quite reasonable results: accurate prediction of the whole stress-strain curves is obtained for the samples with different holding times at 650°C. This also means that good description of two phase and three phase microstructures was achieved, as the samples with holding time lower than 2h contained only ferrite and retained austenite (of course the carbides were neglected) while samples with higher holding time contained in addition fresh martensite. However, it can be seen that the beginning of certain curves (1h and 2h samples) was not well predicted. This was supposed to be linked to the pronounced YPE, which was not accounted at all in the model. Description of Lüders plateau is rather complex, thus it needs a specific study which was not in the scope of the present work.

Strain hardening of the different samples is correctly described and the variation of different mechanical parameters was well predicted. Table 14 shows the comparison between experimental and model mechanical properties. Differences between experimental and model values of UTS and Uel (ΔUTS and ΔUel) were rather limited and their values were comparable with the experimental errors. On the other hand, prediction of YS appeared to be more difficult.

In the case of samples with high volume fraction of RA (30min, 1h and 2h holding) the ΔYS is close to 100MPa, which is rather high. Such a big error is attributed to the three factors:
1. presence of YPE;
2. difficulties to assess the individual values of YS for each constituent;
3. and lack of information about austenite mechanical stability at low strain levels.

However, a more detailed study is necessary to provide precise reasons of such deviations.

Although the absolute values of YS were not well predicted, the evolution of YS with the holding time was well described.

Table 14 – Comparison between experimental and model mechanical properties of samples after different heat treatments: yield strength (YS), ultimate tensile strength (UTS) and uniform elongation (Uel), respectively.

Ref.		YS (MPa)	UTS (MPa)	Uel (%)	ΔYS	ΔUTS	ΔUel
3min WQ	E	688	766	13.5	9.2	10.2	0.7
	M	697	776	12.8			
10min WQ	E	641	776	20.6	29.1	6.1	2.3
	M	612	770	18.3			
30min WQ	E	626	791	23.7	69.1	8.4	1.7
	M	557	783	22.0			
1h WQ	E	589	826	23.2	98.1	15.4	0.1
	M	491	811	23.3			
2h WQ	E	566	827	24.9	82.7	14.5	0.1
	M	483	842	25.0			
3h WQ	E	487	909	19.2	6.2	6.3	0.1
	M	481	915	19.3			
7h WQ	E	482	882	21.9	52.0	11.0	0.8
	M	430	893	21.1			
10h WQ	E	446	897	21.5	19.6	6.3	1.7
	M	426	891	19.8			
30h WQ	E	359	871	14.2	16.1	4.5	0.2
	M	375	866	14.4			

Globally, the performance of this model with all the taken assumptions and only 3 fitting parameters (λ, ε_0 and n) was considered to be very satisfactory. Good description of mechanical properties and of tensile behavior evolutions with the holding time at 650°C is achieved. As well, sensibility analysis of the model was performed. The detailed description and results of the analysis are presented in Annex 4.2. Figure 131 shows the effect of the most sensitive parameters on the true stress-true strain curve. Globally, the model accounts properly different influence of input parameters and has certain sensitivity to all of the parameters. Consequently, for the good performance of the model a detailed microstructural analysis of such complex microstructures is needed. As it is highlighted in Figure 131, the most sensitive parameters are the fractions of constituents (especially fresh martensite) and the size of ferrite. On the contrary, the impact of retained austenite stability, represented by ε_0 and n, appears to be of the second order.
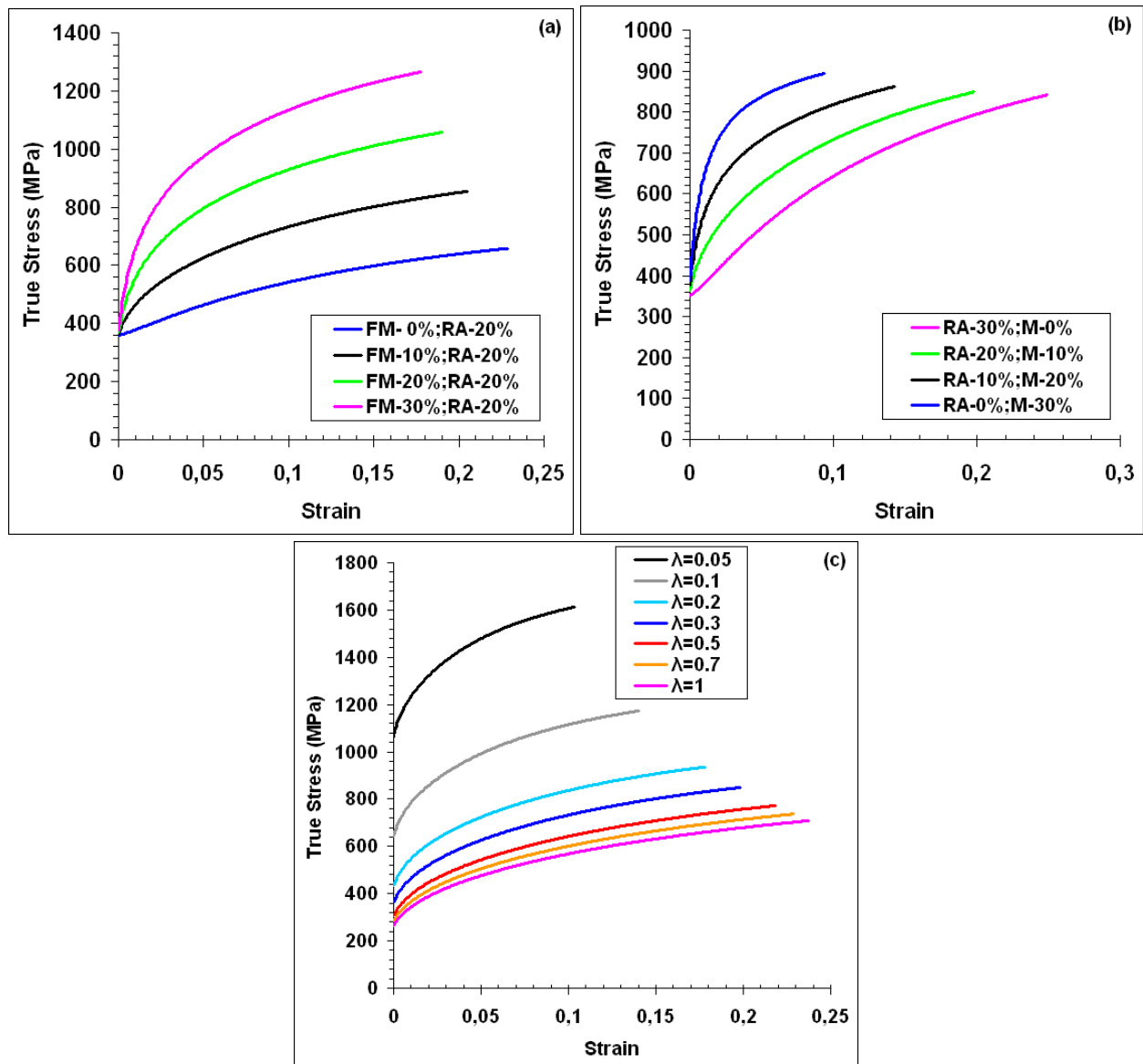
Figure 131 – Influence of the most sensitive parameters ((a) and (b) fractions of fresh martensite and retained austenite, respectively; (c) size of ferrite) on the true stress-true strain curves according to the model.

As a final conclusion, it should be stated that the model demonstrates very good performance and an accurate prediction of the experimental tensile curves is achieved. However, to obtain such a good results of the model a very fine and advanced description of the microstructure constituents and their chemical composition is required. Therefore, additional studies to characterize different microstructure constituents and in particular lath-like recovered ferrite can even further improve the performance of the model. Better understanding of the induced austenite transformation can also contribute to the development of the model.

References

[ALL'12] S. Allain, O. Bouaziz, M. Takahashi, Toward a New Interpretation of the Mechanical Behaviour of As-quenched Low Alloyed Martensitic Steels, ISIJ international, 52 (4), 2012, 717-722.

[ARL'13] A. Arlazarov, O. Bouaziz, A. Hazotte, M.Gouné, S. Allain, Characterization and Modeling of Manganese Effect on Strength and Strain Hardening of Martensitic Carbon Steels, ISIJ international, 53(6), 2013, 1076-1080.

[AVR'39] M. Avrami, Kinetics of phase change. I General theory, The Journal of Chemical Physics, 7(12), 1939, 1103-1112.

[BOU'02] O. Bouaziz, P. Buessler, Mechanical behaviour of multiphase materials: an intermediate mixture law without fitting parameter, Revue de Métallurgie, 99(01), 2002, 71-77.

[BOU'09] O. Bouaziz, The "Ductilities" in Single Phase Steels from Usual to Nano-Scale Microstructures, Materials Science Forum, 633-634, 2009, 205-210.

[BOU'11] O. Bouaziz, H. Zurob, B. Chehab, J.D. Embury, S. Allain, M. Huang, Effect of chemical composition on work hardening of Fe–Mn–C TWIP steels, Materials Science and Technology, 27(3), 2011, 707-709.

[EMB'10] D. Embury, O. Bouaziz, Steel-based composites: driving forces and classifications, Annual Review of Materials Research, 40, 2010, 213-241.

[JOH'39] W.A. Johnson, R.F. Mehl, Reaction kinetics in processes of nucleation and growth, Transactions AIME, 135(8), 1939, 396-415.

[KOC'03] U.F. Kocks, H. Mecking, Physics and phenomenology of strain hardening: the FCC case, Progress in Materials Science, 48(3), 2003, 171-273.

[KOL'37] А.Н. Колмогоров, К статистической теории кристаллизации металлов. Известия Российской академии наук. Серия математическая, 1(3), 1937, 355-359 (A.N. Kolmogorov, Toward Statistical Theory of Metal Crystallization, News of Russian Science Academy, Mathematical Volume, 1(3), 1937, 355-359.

[KRA'99] G. Krauss, Martensite in steel: strength and structure, Materials Science and Engineering: A, 273, 1999, 40-57.

[MEC'81] H. Mecking, U.F. Kocks, Kinetics of flow and strain-hardening, Acta Metallurgica, 29(11), 1981, 1865-1875.

[OLS'75] G.B. Olson, M. Cohen, Kinetics of strain-induced martensitic nucleation, Metallurgical transactions A, 6(4), 1975, 791-795.

[ORO'54] E. Orowan, Dislocations and mechanical properties, chapter 3 of the book "Dislocations in metals", Ed. M. Cohen, AIME, 1954, 69-195.

[PER'03] A. Perlade, O. Bouaziz, Q. Furnémont, A physically based model for TRIP-aided carbon steels behaviour, Materials Science and Engineering A, 356, 2003, 145-152.

[PIC'63] F.B. Pickering, T. Gladman, Metallurgical Developments in Carbon Steels, Iron and Steel Institute, Special Report No. 81, 1963, 10.

[PUS'09] I. Pushkareva, PhD report, Evolution microstructurale d'un acier Dual Phase. Optimisation de la résistance à l'endommagement, Institut National Polytechnique de Lorraine (INPL), 2009, http://pegase.scd.inpl-nancy.fr/theses/2009_PUSHKAREVA_I.pdf.

[SHI'10] J. Shi, X. Sun, M. Wang, W. Hui, H. Dong, W. Cao, Enhanced work-hardening behavior and mechanical properties in ultrafine-grained steels with large-fractioned metastable austenite, Sripta Materialia, 63, 2010, 815-818.

[SUG'02] K.I. Sugimoto, A. Kanda, R. Kikuchi, S.I. Hashimoto, T. Kashima, S. Ikeda, Ductility and formability of newly developed high strength low alloy TRIP-aided sheet steels with annealed martensite matrix, ISIJ international, 42(8), 2002, 910-915.

[ZHU'10] K. Zhu, O. Bouaziz, C. Oberbillig, M. Huang, An approach to define the effective lath size controlling yield strength of bainite, Materials Science and Engineering: A, 527(24), 2010, 6614-6619.

CONCLUSIONS

The so-called "Medium Mn" steel (MMS) is a promising solution to get high strength steels with good formability. An attractive combination of strength and ductility is the result of pronounced TRIP effect in these steels. The latter is obtained due to the high amount of retained austenite in the final microstructure at room temperature. There are several reasons for such a high retained austenite fraction: for example, Mn partitioning and ultra-fine microstructure. This type of ultra-fine microstructure can be obtained using a particular heat treatment, named ART-annealing that consists of two subsequent heat cycles: first austenitization followed by rapid cooling to get a fully martensite structure, then intercritical annealing of this martensitic Medium Mn steel. During the second treatment, the formation of austenite occurs according to the so-called "Austenite Reverted Transformation" (ART) mechanism. The main goal of this PhD was to better understand the mechanism of microstructure formation and the link between microstructure parameters and the mechanical properties of Medium Mn steels.

First of all, the chemical composition of the steel studied during this PhD work was Fe-0.1C-4.7Mn wt.%. It was chosen from a large analysis of literature data assisted by thermodynamic calculations. The temperature for the second intercritical annealing was determined according to the thermodynamic simulations and, in the same time, by combinatory experimental heat treatments. It was found that there is an optimum domain of temperatures (between 640 and 660°C) where a good balance between strength and ductility can be achieved. Based on the obtained results, the selected heat treatment was double annealing with first austenitization at 750°C for 30min followed by intercritical batch annealing at 650°C. Using this type of treatment the time-evolution of microstructure and mechanical properties during intercritical annealing at 650°C was studied.

Microstructure evolution during intercritical annealing

The initial state before intercritical annealing (after austenitization at 750°C for 30min followed by water quench) was characterized using different experimental techniques: optical (OM), scanning electron (SEM) and transmission microscopes (TEM), X-ray diffraction (XRD) and electron probe microanalyzer (EPMA). Majority of the microstructure was found to be lath martensite.

Next, the microstructure evolution during intercritical annealing at 650°C was characterized using the before mentioned techniques as well as saturation magnetization measurements and NanoSIMS analysis. First, the evolution of Mn microsegregations was investigated. It was found that a significant redistribution of Mn happens during a long intercritical annealing. Such a long-range diffusion of Mn supposes that Mn should diffuse in both ferrite and austenite, meaning that the effective diffusivity of Mn may be different from that in ferrite and in austenite. It was found that homogeneization was controlled by diffusivity close to those in ferrite. In the same time, both the small segregated band spacing and the ultra-fine size of microstructure constituents were supposed to enhance this phenomenon. On the other hand, another type of Mn diffusion was observed at smaller scale. This Mn partitioning is mainly linked to the interactions between Mn and migrating α/γ interface during austenite growth.

Second step was the characterization of cementite precipitation state evolution during heating and holding at 650°C. In this work, the evolution of carbides during heating process was not very significant, probably due to relatively high heating rate ~5°C/s. The most important information

from this analysis was the mean Mn content of carbides at the beginning of holding (650°C-0s). Its value was estimated to be about 10 wt.%. Then, the time evolution of carbides during holding was analyzed on four samples: 3min, 1h, 2h and 3h. In the beginning of holding (3min), carbides with both two types of morphology (rod and polygonal) and Mn content (15 and 30 wt.%) were observed. Samples after 2h holding time still presented a small amount of carbides with high Mn level (~25 wt.%). Finally, sample after 3h holding was completely carbide free. Existence of cementite after 2h holding at 650°C contrasts with equilibrium thermodynamic calculations predicting complete cementite dissolution at around 610°C. This indirectly highlights the role of kinetics effects.

Third stage was the analysis of austenite and ferrite time-evolution. SEM characterizations shown that the final microstructures contained at least three phases: ferrite, retained austenite and fresh martensite. Double morphology (lath-like and polygonal) was revealed for both austenite (retained austenite and fresh martensite) and ferrite. At longer holding times (more than 3h) a clear presence of fresh martensite was observed and most of this martensite was polygonal. From image analysis of SEM pictures, it was also found that the kinetics of austenite transformation was very rapid in the beginning and then becomes smoother. Mn distribution between austenite and ferrite as a function of time was evaluated using local TEM-EDX measurements and TEM-EDX hypermaps. Unexpectedly, the system reaches the equilibrium after a relatively short time of 10h. The experimental volume fractions of phases and the respective compositions were in agreement with those calculated with Thermo-Calc software: 36% of austenite with 9.1 wt.% Mn and 64% ferrite with 2.3 wt.% Mn. At last, the carbon content in austenite for the samples with 1h and 30h holding time at 650°C was measured by NanoSIMS technique. The C content of austenite was estimated by comparison of the obtained SIMS intensities between the analyzed samples and the reference one using image analysis. This methodology was employed for the first time in this work and was considered to be adapted for such type of studies. The measured mean carbon contents of 1h and 30h samples were close to 0.36 wt.% and 0.27 wt.%, respectively. These values correspond very well to the C content calculated from the mass balance neglecting the presence of cementite and thus confirms that a major part of carbides are dissolved after one hour treatment at 650°C.

Fourth step was the study of retained austenite and martensite time-evolution. Here it is important to note that a preliminary comparison between two experimental techniques (XRD and Sigmametry) for retained austenite fraction measurements was performed. This was done due to the observed discrepancies in the RA fraction values obtained with two mentioned techniques. It was then found that RA fraction is underestimated by XRD measurements due to preceding mechanical polishing. Such an important effect of mechanical polishing is particular to the MMS and probably results from the lower mechanical stability of RA. As in the standard TRIP steels, RA stability is assumed to be controlled by the austenite composition (C, Mn in this work) and its size. The effect of austenite size on its thermal stability is quite important in the case of MMS. However, according to some very recent work of Matsuoka et al. [MAT'13] the size effect on the mechanical stability of RA is quite low or even absent. Based on these results, Sigmametry technique was considered to be more adapted for this study. Then, the time-evolution of volume fraction of retained austenite was evaluated. A particular peak-type form of the RA time-evolution curve was observed. It can be divided in three stages:

- ➢ full stabilization of growing austenite resulting in the increase of RA fraction till the maximum value;
- ➢ decrease of RA fraction and appearance of martensite due to the decrease of austenite stability (lower C, Mn contents and bigger size)
- ➢ a final stage where RA seems no longer to evolve, probably because the state close to the equilibrium one is achieved.

In the end, TEM analysis of several samples with different holding time was performed. Depending on the holding time at 650°C, the four possible phases, cementite, ferrite, retained austenite and fresh martensite, were distinguished using Convergent Beam Electron Diffraction (CBED) in STEM mode (Scanning TEM). The double morphology (lath-like and polygonal) of the observed features was confirmed.

The next point was the austenite size measurements and discussion of the observed morphology. The mean austenite size was found to vary from 0.16 µm to 0.45 µm for the studied range of time. These values correspond well to those found in the literature. According to the overall microstructure characterizations, a complete vision on the sequence of carbide precipitation and austenite nucleation and growth in connection with the microstructure topology was proposed.

The next part of the work consisted in the analysis of the main results using coupled experimental/modelling approach. The kinetics of phase transformation in ultra-fine lath-like microstructure was studied, including both cementite dissolution and austenite formation, with DICTRA simulations. It was found that in this specific case of Medium Mn steel with ultra-fine microstructure the major part of austenite growth is controlled by Mn diffusion in ferrite and by Mn diffusion in austenite for longer times. It was also clearly shown that standard DICTRA simulations based on a mean filed approach disclose limitations for the prediction of the observed kinetics of cementite dissolution and austenite formation. However, prediction of austenite fraction evolution can be improved by taking into account the dispersions. These dispersions come from the prior processing conditions and play an important role in the kinetics of phase transformations. In this work, DICTRA simulations that account for the effect of size distribution were performed. Very good prediction of austenite kinetics was achieved using such methodology. The reason of such a good result is the correct selection of the size distribution which is coherent with the experimental observations. Finally, the important role of the initial ultra-fine size for the overall kinetics was highlighted.

In last section of this part, the critical factors controlling thermal austenite stability, including both chemical and size effects, were determined and discussed, based on the analysis of the retained austenite time-evolution. In an original manner, it was shown that the time-evolution of retained austenite is a fair indicator of the critical factors governing austenite stability in the MMS with ultra-fine microstructure. Particularly, the peak of the curve defines the critical point in terms of composition and size delimiting stable and unstable austenite. The effect of austenite size on its stability was clearly demonstrated and a critical size of about 280 nm was estimated. Finally, an adapted formulation of M_s temperature law applicable to the medium Mn steels with ultra-fine microstructure was proposed.

Characterization and modeling of mechanical properties

Tensile properties of the steel were measured as a function of holding time at 650°C and the relation between microstructure and mechanical behavior was analyzed. The continuous increase of ultimate tensile strength (UTS) and decrease of yield strength (YS) was observed with the increase of holding time. In the same time, uniform (Uel) and total (TE) elongations have a hill-like time-evolution with the maximum values corresponding to the range of times between 30min and 2h. The increase of UTS is clearly related to the increase of global austenite fraction (retained austenite plus fresh martensite). The observed permanent decrease of YS was supposed to be related with the continuous recovery and recrystallization of initial martensite structure which lead to the lower resistance of matrix phase (ferrite) due to lower density of defects. Finally, it was seen that time-evolution of ductility (Uel and TE) is somehow linked to the RA fraction, but this relation is not straightforward, since it requires to take into account the

mechanical stability of RA. As well recovery and recrystallization of initial martensite structure can affect the ductility. Analysis of the work hardening rate (WH) curves supports the thoughts about the significant influence of RA on both ductility and strength. Indeed, all the samples exhibited transformation induced plasticity (TRIP) effect, however the rate of strain induced transformation was not the same and, hence, the strain hardening behavior was also singular. Advanced analysis of the individual behavior of the three major constituents (ferrite (annealed martensite), fresh martensite and retained austenite) was done in order to better understand the behavior of such multiphase medium Mn steels.

Mechanical behavior of ferrite with medium Mn content

From the microstructure characterizations, it was shown that the ferrite (annealed martensite) is the matrix phase of the steel. This ferrite was obtained during the annealing of initial martensite structure and, thus, it has a double specificity. Firstly, the majority of the ferrite has a lath-like morphology. Secondly, it has an important dislocation density issued from the recovery process. No simple way to produce such type of microstructure (100% of lath-like dislocated ferrite) was found. Hence, it was approximated that microstructure with lath-like ferrite (more than 98%) and some carbides has the similar mechanical behavior. Such type of microstructures was obtained by the annealing of initial martensite at 500°C. Three different holding times were considered. The obtained tensile curves were particular, but in accordance with the literature data. The yield strength was rather high (more than 750MPa), but almost no strain hardening was observed (flat curves). Taking into account the fact that there was no strain hardening of such a ferrite and that its morphology was a lath-like one, it was proposed to model its behavior with an elastic perfectly plastic law, where the stress level depends only on solid solution hardening and on the mean size of laths.

Mechanical behavior of as-quenched medium Mn martensite

Experimental stress-strain curves of as-quenched martensite for the studied steel were obtained. It was observed that the strength level and the strain hardening rate are higher than the levels classically seen in the literature for the 0.1C (wt.%) steel. Also, it was not possible to predict the stress-strain curve of such martensite using the Continuous Composite Approach (CCA) model [ALL'12]. Therefore, it was supposed that there is an effect of Mn on the strength and strain hardening of martensite. To investigate this effect, a database of 8 C-Mn martensitic steels from previously published studies and of some new experimental trials was built. The stress-strain curves and the strain hardening rate versus true stress were analyzed. An important influence of Mn content on the strength and strain hardening of fresh martensite was confirmed. Moreover, it was found that Mn content influences the martensite strength and strain hardening in obvious synergy with the carbon content of martensite. In addition, a more pragmatic behavior law, based on the CCA approach, was proposed for modeling the stress-strain curve of medium Mn martensite. The revealed synergy between carbon and manganese was taken into account in a specific way and the coefficient of the manganese influence was adjusted. The results of the adjusted model with only one fitting parameter showed very satisfactory agreement with the experimental data. Influence of Mn content on the mechanical behavior of as-quenched martensite and its synergy with C content of martensite was clearly evidenced in this work.

Mechanical behavior of austenite with medium C and Mn content

Mechanical behavior of austenite was assessed on the steel with 0.5 wt.% C and 10 wt.% Mn. This composition was chosen based on experimental characterization of austenite. The investigations were performed on the hot rolled steel (~4 mm thick) because cold rolling was not possible. A specific annealing treatment was determined in order to avoid α'- and/or ε-martensite formation and to produce almost fully austenitic steel. The final microstructure was mostly austenitic and contained less than 7% of α'-martensite. The obtained tensile curves were rather particular. High strain hardening, low YS and low ductility were observed. It was considered that low YS is intrinsic to the austenite matrix, which is in accordance with the literature data. On the other hand, poor ductility and high strain hardening was supposed to be the result of transformation induced α'-martensite with high level of C and Mn. On the ground of these results, it was proposed to describe mechanical behavior of retained austenite using empirical law proposed by Bouaziz et al. [BOU'11].

Retained austenite strain induced transformation (TRIP effect)

Retained austenite transforms to martensite under mechanical loading. Interrupted tensile tests were performed for two treatments (1h and 30h holding at 650°C) in order to study the evolution of RA fraction with the increase of deformation. It was found that in the 1h sample a portion of RA was stable enough to avoid the transformation even at rather high strain levels and at the end of tensile test still ~8% of RA was available. In contrary, in the 30h sample lower stability of RA was observed and all austenite was consumed. These observations are also supported by the strain hardening rate curves of the studied samples. Based on the Kolmogorov-Johnson-Mehl-Avrami approach, a special form of phenomenological exponential law was proposed for the modeling of RA fraction evolution with the increase of strain. Two fitting parameters, that allow good control of the induced transformation rate, were necessary. These parameters can be related to some physical factors controlling the stability of retained austenite in the future studies.

Iso-W model to predict mechanical behavior of studied medium Mn steel

At last, based on the Iso-W mixture model, a complete model for predicting the true-stress versus true-strain curves of medium Mn steels was proposed. The effect of strain induced RA transformation on strain hardening and also the difference between the flow stress of two phases (transformed and induced) was taken into account in the way proposed by Embury and Bouaziz [EMB'10]. The performance of this model with all the taken assumptions and only 3 fitting parameters was considered to be very satisfactory. Good description of the mechanical properties, stress-strain curves and strain hardening rate evolutions with the holding time at 650°C was achieved. It was found that the most sensitive parameters are the fractions of constituents (especially fresh martensite) and the size of ferrite. In contrast, the influence of retained austenite stability appears to be of second order.

As a general conclusion it can be highlighted that this work contributes to the understanding of microstructure formation and of mechanical behavior of ultra-fine medium Mn steels. Microstructure analysis revealed undoubtedly the influence of austenite size on its thermal stability and the absolute necessity to take this into account for the M_s temperature predictions. On the other hand, studies of mechanical behavior demonstrated the important influence of Mn content on the tensile behavior of as-quenched martensite. Moreover, a complete model for the prediction of mechanical behavior of complex multiphase medium Mn steels was build utilizing the inputs from microstructure investigations. Clearly, this model is a helpful tool for the further developments of medium Mn steels.

PERSPECTIVES

Although this work proposed the answers on several important questions, there are still a certain number of topics for further investigations and improvements. Furthermore, this work put on the table some new questions, hence there are even more questions now than in the beginning of this study. Possible subjects for the further studies are summarized hereafter.

Microstructure formation and evolution

In this work, it was shown that ferrite recrystallization from initial not deformed martensite structure can happen rather rapidly. The first ultra-fine grains of ferrite were detected already after 30min of annealing at 650°C. In the literature, there are certain works about ferrite recrystallization from not deformed martensite, however the observed times are much longer. From a scientific point of view, ferrite recrystallization from not deformed martensite can be a very interesting subject for further investigations.

As it was stated before, a long-range diffusion of Mn happens during a long intercritical annealing. This suggests that the effective diffusivity of Mn may be different from that in ferrite and in austenite. Therefore, it can be of interest to think about the method for calculating the diffusivity of Mn in a two-phase or multiphase structure.

Characterization of cementite precipitation state and further DICTRA simulations highlighted the importance of cementite dissolution for the austenite transformation and stabilization. Besides, stability of austenite and its fraction are both very significant parameters for the mechanical behavior of steel. In particular, different thermal paths can provide different carbides and austenite evolutions, and thus result in various mechanical properties. Therefore, the control of cementite precipitation state and its influence on the austenite transformation and stabilization can be a very valuable topic for future studies.

In this study, austenite size was shown to have an important influence on its thermal stability. However, the mechanism of austenite stabilization by the size effect is still the subject of discussions. Thus, it can be interesting to continue the work on this topic. Moreover, some results pointed out the low or even non-existing effect of size on the mechanical stability of austenite. This issue requires deeper investigations.

Finally, it was clearly demonstrated that standard DICTRA simulations based on a mean field approach disclose limitations for the prediction of the observed kinetics of cementite dissolution and austenite formation. Nevertheless, prediction can be improved by taking into account the dispersions, for example, in form of size distribution. It seems to be important to work on the characterization and modeling of different dispersions (size, morphology, topology, etc…) and further to introduce them in the kinetics simulations. This aspect is of particular importance for the 3rd generation AHSS grades due to their higher sensibility to the heritage effects.

Mechanical properties and behavior

It was discussed that producing 100% of lath-like dislocated ferrite structure is a very complex issue. It is thought to be challenging to produce such type of microstructure and to measure its mechanical response.

Significant influence of Mn content on the tensile behavior of as-quenched martensite was revealed. It was also emphasized that there is a synergy between C and Mn. However, to understand the physical mechanism of this Mn influence and its synergy with C requires further deeper studies. It is also of interest to look if there is any effect on the microstructure of as-quenched martensite and its link with the mechanical behavior.

Finally, the improvement of characterization and modeling of austenite induced transformation (TRIP effect) is supposed to be very relevant. At least two ways to improve the modeling of TRIP effect are possible. One is to modify the already existing physical model proposed by Perlade et al. [PER'03] in order to decrease its exaggerated sensitivity to the austenite grain size. Another possibility is to introduce some physical factors controlling the retained austenite stability in the empirical law used in this work.

References

[BOU'11] O. Bouaziz, H. Zurob, B. Chehab, J.D. Embury, S. Allain, M. Huang, Effect of chemical composition on work hardening of Fe–Mn–C TWIP steels, Materials Science and Technology, 27(3), 2011, 707-709.
[EMB'10] D. Embury, O. Bouaziz, Steel-based composites: driving forces and classifications, Annual Review of Materials Research, 40, 2010, 213-241.
[MAT'13] Y. Matsuoka, T. Iwasaki, N. Nakada, T. Tsuchiyama, S. Takaki, Effect of Grain Size on Thermal and Mechanical Stability of Austenite in Metastable Austenitic Stainless Steel, ISIJ International, 53, 2013, 1224-1230.
[PER'03] A. Perlade, O. Bouaziz, Q. Furnémont, A physically based model for TRIP-aided carbon steels behaviour, Materials Science and Engineering A, 356, 2003, 145-152.

FINAL STATEMENT OF AUTHOR

Головою думая, человек мудрость приобретает !

Но если в сердце нет Бога, а значит любви,

От мудрости этой он только страдает !

En réfléchissant, une personne acquiert la sagesse !

Mais sans Dieu dans le cœur, et donc sans l'amour,

Cette sagesse n'apporte que l'ennui et la tristesse !

Mind thinking develops the men's wisdom and cleverness !

But without God in the heart, meaning without love,

This wisdom brings sorrow and sadness !

Artem ARLAZAROV

ANNEXES

Annex 1: Data base of mechanical properties of MMS

The following table presents the data set, collected from the literature and used for the analysis of mechanical properties of Medium Mn Steels. It contains the following information (when available):

> ➢ composition (major alloying elements);
> ➢ process parameters (hot rolling, cold rolling, annealing);
> ➢ mechanical properties;
> ➢ microstructure description (fractions, sizes and contents of C and Mn).

Table 15 – Data base of mechanical properties collected from the literature.

| N | Ref | Composition | | | | | Process | | | Thick, mm | Concept | Thold °C | t hold, h | QT, °C | Tp,°C | tp, s | Mechanical Properties | | | | | Microstructure | | | | | | | |
		C, %	Mn, %	Si, %	Al, %	MA %	HR	Tbob	CR								YS, MPa	UTS, MPa	Uel, %	TE, %	Ra%	A, %	M, %	F, %	TM,%	FGS, μm	AGS, μm	C% in A	Mn % in A
1	[MAA71]	0.038	3.5	0.28						Bar d=18	Q	900	5min	0			951	1069		14,2	70								
2		0.034	4.5	0.27						Bar d=23	Q	900	5min	0			931	1029		14,7	70								
3												560	1				952	980		12	66	11				0,33			
4												520	4				933	952		19,5	66,4	10				0,35			
5	[MIL72]	0,11	5,7				YES		~60-85%	2,5	lab BA	600	1				880	910		18,5	70,9	23				0,4			
6												640	1				792	1150		30,5	49	30				0,45			
7												600	16				723	880		34	69,2	29				0,55			
8												640	16				600	1200		18,5	20	30				0,9			
9		0.005	5.06								QT				630	4h	410	600	15,8	25,8		11	89						
10	[KOB'84]										QLT	1050	1	0	1) 710 2) 630	1) 5h 2) 4h	340	560	14,2	30,8		20	80						
11		0.01	10.14								QT				550	4h	640	920	14,6	22,9		10	50+40 eps						
12											QLT				1) 620 2) 550	1) 5h 2) 4h	400	750	10	14,2		14	32+54 eps						

No.	Ref						Specimen		Temp	Treatment	V1	V2	V3	V4	V5
13												725	5		
14									600			600	7,5		
15	[FUR'89]								625			600	8,5		
16		0.011	5.22						650	1HFC		590	10		
17									675			600	10		
18									700			825	5		
19	[FUR'94]								650	3HFC	450	800	13		8,6
20									625	3HWQ	520	800	10		4
21												1075	3		
22									600			625	10		
23	[FUR'89]								625			625	13,5		
24		0.075	5.24						650	1HFC		615	20		
25									675			775	19,5		
26									700			950	9,5		
27	[FUR'94]								650	3HFC	350	875	16		22,3
28									650	3HWQ	425	875	18		18
29												1250	4		2
30									600		620	750	10	17	
31									625		600	800	12	18,5	
32									650	1HFC	540	830	25	32	
33									675		300	950	22	26	
34									700		120	1150	15,5	22	
35	[FUR'89]								800		800	1180	4,5	11,5	
36									600		660	760	8,5	16,5	
37									625		620	780	10,5	17,5	
38		0.12	5.1						650	1HWQ	480	800	29	32,5	
39									675		180	1000	17	22,5	
40									700		700	1200	10	17	
41									800		1160	1400	4	8	
42									650	3HFC	500	1050	23,3		31
43									675		460	1050	13,3		24,3
44	[HUA'94]					4mm	NO	Machined to 2mm tensile specimens · lab BA	700		450	1175	7,8		10
45									650	3HWQ	450	1025	22,8		28
46									675		475	1225	10,6		20
47									700		500	1200	6,7		8,9
48									675	3HFC	375	1355	15,2		31,2
49	[FUR'94]								675	3HWQ	475	1588	21,3		44,1
50		0.3	5.06						675	3H-FC550°C-WQ		1543	18,5		43,9
51									675	3H-FC500°C-WQ		1461	15,7		40
52									600			1000	7,3		
53									625			990	8		
54	[FUR'89]								650	1HFC		980	13		
55		0.4	5.17						675			1125	14		
56									700			1325	5		
57	[FUR'94]								675	3HFC	350	1525	10		14,8
58									675	3HWQ	500	1675	20		55,7
59									600		760	860	13,5	19	
60									625		720	880	14	20	
61									650	1HFC	680	940	21,5	29,5	
62									675		660	1030	27	32,5	
63									700		580	1140	17,5	22	
64									800		820	1360	7,5	12	
65									600		740	880	12,5	20	
66									625		740	900	13,5	21	
67	[FUR'89]								650	1HWQ	720	960	28	38	
68		0.1	5.25	2.09					675		540	1040	24	30	
69									700		480	1220	16,5	24	
70									800		1220	1580	4	8	
71									600		920	1000	9,5	16,5	
72									625		840	920	11	17,5	
73									650	5minWQ	800	960	14,5	23	
74									675		720	1120	24,5	30	
75									700		640	1240	13,5	18	
76									750		940	1440	3	5	

#							Group				no/510/...			C1	C2	C3	C4		
77											no			885	1254	4,1	9,7		
78											510			852	884	5,6	13,4	0,2	
79											538			808	853	7,7	16,5	1	
80							538				566			815	854	6,7	15,9	0,5	
81											593			643	750	12,2	26,5	9	
82											621			648	751	14,4	27,6	12,1	
83											649			611	897	26,7	33,8	24,8	
84											no			789	944	4,6	10		
85											510			850	894	7,7	16,4	0,7	
86											538			783	838	7,3	16,9	2,3	
87		0,1	5,18	0,12	0,03	oui	593				566			795	850	7,1	15,3	0,6	
88											593			650	756	10,2	20,7	10,7	
89											621			675	772	12,8	24,9	14,3	
90											649			630	886	24,7	30	15,6	
91											654			590	772	30,3	39,7		
92											677			360	1013	16,7	20,9		
93											no			810	1155	4,1	9,2		
94											510			833	885	7,2	15,2	0,9	
95											538			779	829	7,1	16,3	1,5	
96							649				566			774	820	7,1	16,4	0,9	
97											593			652	752	12,6	25,1	7,1	
98											621			659	750	14	27	8,2	
99											649			567	897	24,3	31,3	9	
100											no			859	1222	3,7	8,4		
101											510			855	917	7,4	14,7	1	
102											538			808	877	9,2	18,8	5,2	
103							538				566			834	890	8	16,7	6,1	
104											593			708	813	13,1	26,8	15,1	
105											621			687	797	15,2	30	14	
106											649			596	953	28,2	36,3	17,7	
107											no			776	954	5,6	11,8		
108											510			883	918	6,1	15,3	0,8	
109											538			785	859	8,3	17,4	3	
110											566			793	862	8,9	17,9	3,7	
111	[MER'06]	0,095	5,8	0,13	0,03	oui	593				593			716	819	11,4	24,8	8,6	
112											621			744	830	12,2	24,4	11,3	
113											649			606	912	29,3	37,1	13,5	
114											654			625	842	31,2	39,5		
115											677			365	1117	15,9	19,4		
116											no			882	1316	4,1	10,4		
117											510			858	923	7,5	15,5	1	
118											538			786	866	8,4	18,9	5,5	
119							649				566			793	864	8,5	19,3	5,2	
120											593			698	813	12	25,3	14,3	
121											621			718	820	12	24	14,7	
122											649			615	932	28	37,2	18,4	
123											no			866	1413	4,7	10,3		
124											510			922	1014	8,3	16,7	2,7	
125											538			885	992	8,5	16,3	8,9	
126							538				566			872	975	9,4	17,1	8,7	
127											593			764	915	18,7	28,6	22,5	
128											621			817	942	18,6	27,8	19,8	
129											649			638	1083	26,6	28,7	12,7	
130											no			771	978	8,2	15,6		
131											510			934	983	7,8	16	2,9	
132											538			847	967	9,5	18,2	9,2	
133											566			871	939	9,9	19,3	10	
134		0,099	7,09	0,13	0,03	oui	593				593			780	888	15,9	28,5	17,4	
135											621			810	904	17,4	30,3	12,1	
136											649			649	1057	25	27,2	9,7	
137											654			706	950	25,6	30,2		
138											677			389	979	3,5	3,5		
139											no			841	1425	6	11		
140											510			938	1029	8	16,7	2,3	
141											538			822	967	9,5	19,1	9,1	
142							649				566			838	967	10	19,6	8,6	
143											593			754	918	16,8	27,7	12,8	
144											621			763	918	17,8	28,9	14,2	
145											649			660	1074	27,6	33,6	19,6	

146										571			545	667	13,4	22,1		6							
147										599			442	564	14,6	23,6		10							
148										624			440	565	16	24,8		9							
149		0,1	5,2	0,13						652			404	725	24,2	28,7		17							
150										635			503	694	19,8	27,3		9							
151										663			411	980	20,1	24,6		12							
152										654			412	629	22	29		15							
153										677			295	934	13,3	16,1		9							
154										571			733	764	8,8	14,8		8							
155										599			621	670	14,4	24,1		21							
156										624			607	667	23	29,4		20							
157	[MER'07]	0,1	5,8	0,13		YES	~67%	1	real BA	652	40		490	864	21,7	24,6		14							
158										635			667	816	28,1	34		24							
159										663			381	1126	15,8	18,1		8							
160										654			539	739	26	29,4		28							
161										677			387	1115	10,2	12		3							
162										571			937	1206											
163										599			735	736		35,6									
164										624			771	797	26,2	32,7		31							
165		0,1	7,1	0,13						652			524	1054	14,2	14,5		7							
166										635			871	1018	29,3	31,7		37							
167										663			341	1433	10,5	11,5		8							
168										654			682	936	25,4	29		38							
169										677			500	1320	8,5	10,1		2							

#	Ref															
170								600			670	30s		830	920	21,3
171											670	63s		836	1082	29,6
172											670	180s		831	1080	29,1
173											670	1200s		843	1092	30,2
174		0,025	6,69	0,98	1,56	TiBSb		610	30-60%	?	770	60s		989	1280	16,3
175								600			650	0,5		830	920	25,3
176											650	1		736	982	35,2
177											650	5		731	980	37,1
178											650	12		743	992	36,2
179								610			750	1		789	880	24,3
180								630			720	30s		842	940	20,2
181											720	63s		841	1087	30,8
182											720	180s		852	1190	29,9
183											720	1200s		849	1098	30,2
184		0,053	6,75	1	1,53	TiBSb		628	30-60%	?	640	60s		819	992	15,1
185								630			670	0,5		842	940	24,2
186											670	1		741	987	36,8
187											670	5		752	990	35,9
188											670	12		749	1001	35,3
189								628			600	1		798	852	25,1
190								578			740	30s		851	966	22,4
191											740	63s		867	1196	30,6
192											740	180s		878	1112	30,1
193											740	1200s		879	1098	29,8
194		0,109	6,71	0,96	1,57	TiBSb		590	30-60%	?	600	60s		810	922	17,9
195								578			680	0,5		851	966	22,4
196											680	1		767	996	37,6
197											680	5		781	1012	36,1
198											680	12		779	998	36,4
199								590			740	1		780	882	24,9
200	[JIN'09]						yes	580			680	60s		882	1109	30,7
201		0,151	6,74	0,94	1,57	TiBSb		583	30-60%	?	610	60s		824	1056	20,4
202								580			660	5		782	1009	39,9
203								583			610	5		764	956	29,4
204								620			690	60s		828	1089	29,7
205		0,021	6,44	0,45	1,48	TiBSb		610	30-60%	?	780	60s		938	1162	16,9
206								620			690	5		728	989	34,5
207								610			750	5		778	962	26,9
208								600			700	60s		839	1097	30,6
209		0,045	6,43	0,45	1,48	TiBSb		624	30-60%	?	760	60s		953	1124	15,7
210								600			700	5		739	991	35,6
211								624			760	5		753	953	27,8
212								634			680	60s		842	1053	28,9
213		0,098	6,57	0,49	1,52	TiBSb		627	30-60%	?	600	60s		792	929	17,5
214								634			640	5	FC	842	943	26,4
215								627			600	5	FC	792	919	28,5
216								583			670	60s		898	1032	30,2
217		0,144	6,56	0,5	1,49	TiBSb		692	30-60%	?	600	60s		804	952	18,9
218								583			630	5	FC	798	932	25,7
219								692			600	5	FC	834	952	27,9
220								610			700	60s		922	1199	28,9
221		0,025	6,23	0,95	0,04	TiBSb		602	30-60%	?	780	60s		983	1223	14,4
222								610			650	5		752	999	27,3
223								602			750	5		783	923	26,4
224								605			680	60s		889	1103	30,9
225		0,102	6,54	0,98	0,04	TiBSb		595	30-60%	?	600	60s		852	972	19,8
226								605			630	5		789	1103	36,9
227								595			600	5		852	972	27,8
228								630			710	60s		897	1174	29,2
229		0,149	6,12	0,56	0,06	TiBSb		638	30-60%	?	630	60s		912	1053	22,9
230								630			700	5	FC	797	934	25,8
231								638			640	5	FC	812	951	24,9

#	Ref										Temp	Time		YS	UTS								
232											660			936	988	11,5	16,7	6					
233		0.12	4.6	0.55	1.1	1.1					720			766	1204	12,9	15,9	28			0.47	0.26	6.2
234	[SUH'09]						4.5mm	~75%	1mm	CAL	780	2min		940	1461	6,2	8,6	6					
235											720			814	854	14,7	21,7	26			0.42	0.22	
236		0.12	5.8	0.47	3.1	3.1					780			714	994	23,8	27,5	31			0.43	0.29	7.2
237											840			444	1161	11,2	12,4	18					
238											640			919	1014	20	22,8	20					
239	[COO'10]	0.05	6.15	1.5			3mm	~67%	1mm	CAL	660	3min		801	1099	13,8	17,4	15			~0.2-0.3		
240											680			447	1213	9,5	12,7	30					
241											700			727	1348	6,9	10,2	0					
242		0.2	5				1250°C 2h + FORGING	NO	rods with d=16	ART	650	6		620	950		44,5	34,1					
243	[SHI'10]	0.26	5											595	1020		42	35					
244		0.4	5											545	1190		32,5	40					
245		0.2	7											530	1420		31	44,7					
246										ART (1st cycle 750°C-30min)	650	1minAC		829	932		20	4,54			0.4	0.1	7.4
247												5minAC		766	894		27	8,4			0.3	0.15	7.8
248	[WAN'11],											10min		753	875		29	13,9					
249	[LUO'11],											30min		682	883		35	18,3					
250	[CAO'11-1],											1		663	918		35	22,5			0.3	0.2	7.7
251	[DON'11]											6		600	908		44,5	30,9			0.3	0.25	8.6
252												12		587	910		44,5	33,7			0.3	0.3	7.9
253												48						31,9			0.4	0.3	9.1
254												144		500	960		38,5	32,7			0.4	0.33	9
255							Homo 1250°C 2h + FORGING	NO	rods with d=16	ART (1st cycle 675°C-30min)	650	1minAC		650	950	30,7	35,7						
256												5minAC		633	1000	31,4	37,1						
257		0.2	4.72									10min		633	1033	32,1	38,6						
258												30min		625	1025	28,6	34,3						
259												1		645	917	27,1	35,0						
260												3		584	967	32,1	37,1						
261	[XU'12]											6		650	1000	31,9	37,9						
262										ART (1st cycle 1050°C-30min)	650	1minAC		708	867	10,7	22,9						
263												5minAC		683	867	11,4	22,5						
264												10min		683	877	15,7	25,7						
265												30min		675	857	15,7	26,4						
266												1		667	867	20,7	30,0						
267												3		590	933	30,7	33,6						
268												6		550	965	31,9	37,1						
269							Homo 1200°C 2h + FORGING	Yes	1mm (12.5x25mm)	CAL	700	5minWQ		908	964		38,0						
270											750			727	998		67,0						
271	[CAI'13]	0.18	11		3.8						800			544	1131		37,0						
272											850			344	1327		20,0						
273											900			550	1531		13,0						
274							Homo 1250°C 2h + FORGING	Yes	1.5	CAL	650 without 1st cycle	1minAC		907	937		33,5	19,7					
275												5minAC		871	956		43	19,8					
276	[CAO'11-2]	0.14	5									10min		839	996		44,5	19,7					
277												30min		763	957		40						
278												1		746	993		38						
279												6		562	1075		32						

280	[LI'11]	0.088	4.8	0.18			4mm	62.5	1.5	lab BA	590	18					650	26,5	5					
281											630						670	30	16,4					
282											650						740	23,2	17,9					
283											680						910	12						
284											710						1050	9						
285											730						1010	6						
286		0.081	5.76	0.15							590						720	35,5	15					
287											630						880	26	23,9					
288											650						1000	14,8	28,6					
289											680						1210	10,3						
290											710						1255	6,5						
291											730						1170	6						
292		0.08	6.72	0.15							590						800	37,5	19,3					
293											630						960	25,5	26,8					
294											650						1090	19,3	32,5					
295											680						1350	8,7						
296											710						1325	7						
297											730						1290	8,5						
298	[HAN'11]	0.18	12		3	3				CAL	840	2min				600	850	45						
299	[BHO'11]	0.18	5.48	0.92	2.64	2.64	6mm			as HR Q&T						1003	1443	5,84						
300											900	30min	0	350	1h	1209	1462	5,49						
301													350	350	1h	1007	1282	6,4						
302	[HANA'11]	0.1	5.02	1.96			38mm FORGED D		Small machined dilato	CAL	675	2min	0	400	300 He Q	846	1150	19,5	27,5					
303	[GIB'11]	0.1	7.1	0.13			4mm	50%	1.5	lab BA	575	168h WQ				769	800	34	26	0	76	0.9		
304											600					710	876	42	33	18	49			
305											625					503	954	22	40	6	54			
306											650					276	1219	10	43,5	22.5	34			
307											675					759	1360	5	1,4	78.6	20	~2.4		
308	[AYD'13]	0.12	4.98	3.11	3.05	3.05	6mm	NO	ASTM E-8M	HR CAL	950	15min WQ					726	14,3	15,2	10.8	74		1.04	6.32
309		0.19	4.96	3.09	2.99	2.99					1020						826	11,6	9	34	57		1.27	6.9
310		0.22	7.15	3.11	3.21	3.21					1155						802	19	13	30	57		1.09	8.5
311		0.2	10.02	3.17	3.19	3.19					1240						793	28	53	0	47		1.1	11.2

#	Ref					El				T1	proc				Rm	A%					
312										680					1200	23,1	14	8	68	8	1,2
313										700					1240	22	19	9	60	10	1
314							oui		1,4	720					1310	20,6	22	10	55	12	0,9
315										680		temp	360	500	1000	28,1	13	2	70	14	0,9
316										700	500s		360	500	1040	27,4	17	3	62	17	1,1
317										720			360	500	1070	26,9	20	3	58	18	1
318		0,125	4,22	1,21	0,79		oui	non	2	700					1210	23,4	18	8	61	11	1,4
319										510					1270	13,9	2	4	79	4	0,3
320										830					1480	11,8	6	46	26	18	0,2
321										700	10s				1280	13,9	4	4	70	4	0,3
322								oui	1,4	700	500s		700	1800	1090	15,4	2	8	63	11	0,3
323										700	500s		450	3600	1120	14,8	3	10	64	10	0,2
324										670	900s				1090	27,8	17	6	70	6	1,1
325										670	900s	GA	560		1080	28,2	16	6	71	6	1
326										670	900s				1120	30,1	20	5	70	5	0,8
327										660					1260	34,5	25	9	52	12	1
328							oui		1,4	680	300s				1320	32,4	29	10	45	14	0,9
329										700					1370	30,2	32	11	39	16	0,8
330		0,089	5,92	1,05	0,74			non	2	680					1230	32,2	26	9	48	14	1,1
331										650					1240	35,2	26	12	52	9	0,9
332							oui		1,4	650	1200s	GA	560		1250	34,9	27	11	53	8	1
333										650					1320	35,2	31	7	54	7	1,2
334										680					1140	18,4	6	18	71	3	3,3
335	[KAW'12]	0,37	2,85	0,72	0,028				1,4	700	300s				1260	16,6	5	23	67	3	2,9
336										720					1380	14,9	6	32	57	3	3,2
337										645					970	24,8	16	18	63	2	2,8
338		0,112	4,42	0,48	0,026				1,4	665	500s				1130	21,7	19	26	51	3	2,9
339										685					1300	18,9	21	38	36	4	2,7
340		0,092	5,03	1,05	0,92				1,4	700	300s				1190	23,2	24	9	53	12	1,1
341										740	300s				1300	21,5	31	11	40	16	0,9
342		0,124	4,98	1,29	0,88	V			1,4	680	300s				1200	23,3	22	10	52	14	1
343										720					1320	21,2	28	11	39	19	1,2
344		0,089	4,55	1,51	0,732	Mo			1,4	680	400s				1210	22,9	22	9	56	11	1,1
345									1,4	720	400s				1320	21,1	29	10	43	15	0,8
346		0,085	5,56	1,14	0,791	Nb			1,4	680	300s				1240	22,2	20	9	58	11	0,9
347									1,4	720	300s				1360	20,4	27	10	45	14	1,1
348		0,151	5,22	1,32	1,04	Ti+B			1,4	700	300s				1190	22,9	19	10	58	11	1,1
349									1,4	740	300s				1300	21,5	25	9	44	19	1,2
350		0,121	4,55	1,18	0,72				1,4	700	500s				1210	22,9	18	10	53	16	1,1
351									1,4	740	500s				1320	21,1	24	10	40	22	0,8
352										650		GA	550		990	27,8	12	10	70	6	1
353										670		GA	550		1030	26,5	14	11	69	6	1
354		0,096	4,43	1,01	0,041				1,4	690	300s	GA	550		1080	24,8	13	11	70	6	1
355										650	300s				1000	27,6	11	10	71	6	1,1
356										650		temp	360	500	980	28,4	11	6	70	12	1
357										650					1040	29,1	16	9	69	6	1,1
358		0,32	1,77	1,48	0,039				1,4	760	300s				920	21,8	3	6	68	2	0,4

359													650				1038	1105	0,6	1,1		3							
360													665				1018	1094	14,2	15,9		18							
361													675				996	1084	17,3	19,1		23,7						0.31	6.11
362													685	3min + SC			945	1187	15,1	15,9		29,6							
363													700				528	1465	8,6	8,8		12,9							
364	[JUN'11]	0.16	3.95	0.5			3mm		50	1.5	CAL	725				1145	1726	5	5,1		2,3							
365													750				1307	1694	4,5	6,2		0							
366														3min			926	1046	17,8	22		17,7	14.9				0.48	0.57	
367														1			580	973	21,6	24,7		19,9	13.4				0.68	0.53	
368													675	3			482	1031	20,2	21,5		24,8	12.7				1.01	0.48	
369														6			443	956	23,6	25,2		26,5	11.2				1.08	0.42	
370														26			383	922	15,2	17,5		10,7	28.4				1.4	0.38	
371														1			460	950	16	18,2	40	15	22,1	62,9					
372														2			448	951	17,5	20,5	36	15,7	22,3	62					
373														3			354	1002	12,8	14,9	36	6,4	32,3	61,3					
374														4			377	933	15,2	17,6	35	19,9	19,6	60,5					
375														5			395	959	15,5	17,2	34	19,2	21	59,8					
376	[ARL'11]	0.092	4.6				4mm		~70%	1mm	ART	670	6	AC		392	926	16,5	19,3	37	10	30,5	59,5					
377														7			432	868	21	25,2	50	22,6	18,3	59,1					
378														8			326	977	13,2	13,5		17,2	24	58,8					
379														9			322	961	14,4	16,2		12,1	29,4	58,5					
380														10			292	950	13,1	14		9,2	32,7	58,1					
381														30			316	955	11,9	13,5		3	41,1	55,9					

Annex 2: Mechanical properties after Gradient Batch Annealing

Scheme of applied gradient batch annealing cycle is shown in the left part of Figure 132. The obtained gradient of temperature depending on the position in the sheet is shown in the right part of Figure 132. For each temperature two "mini" tensile samples were tested. The obtained tensile curves and mechanical properties are shown respectively in Table 16 and Figure 133.
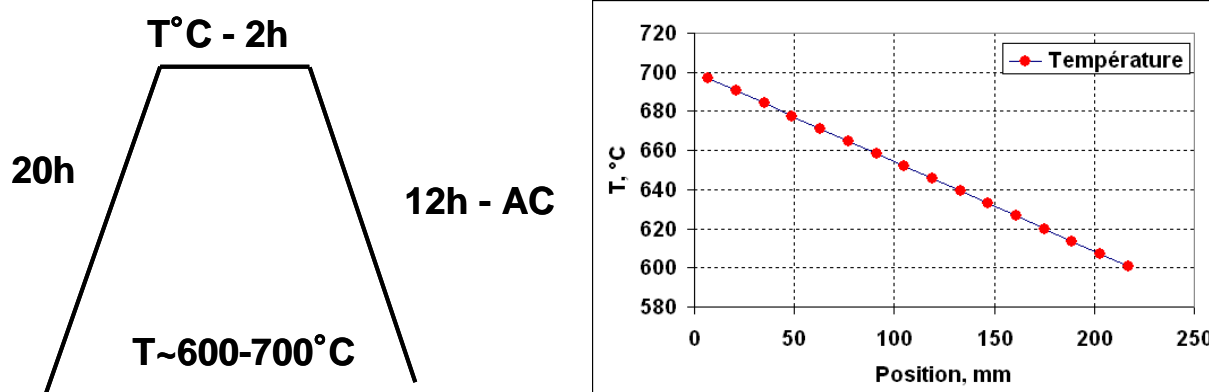
Figure 132 – Scheme of gradient batch annealing cycle (in the left part of the figure) and the obtained gradient of temperature depending on the position in the sheet (in the right part).

Retained austenite fraction was measured by XRD for each holding temperature. The results are presented in Table 16 and in Figure 134.

Table 16 – Measured mechanical properties of samples after gradient batch annealing (different holding temperature), with their corresponding incertitude in the brackets: high and low yield strength (YS_H and $YS_L \pm 15MPa$), yield point elongation ($YPE \pm 0.2\%$), ultimate tensile strength ($UTS \pm 10MPa$), uniform ($Uel \pm 0.5\%$) and total ($TE \pm 1\%$) elongations, respectively. The last column gives also the measured fraction of retained austenite (RA).

T°C	YS_H (MPa)	YS_L (MPa)	YPE (%)	UTS (MPa)	Uel (%)	TE (%)	RA (%)
697	371	371	0.3	961	17.9	23.5	0.20
690	434	434	1.6	926	19.9	25.4	0.28
684	488	488	2.5	895	20.5	26.4	0.28
678	541	518	3.3	858	22.7	28.7	0.27
671	550	535	3.4	826	25.0	31.2	0.30
665	562	562	3.8	804	27.0	33.1	0.27
658	596	570	2.8	761	29.3	36.7	0.25
652	596	581	2.8	722	28.3	36.9	0.24
646	588	581	2.5	707	27.0	34.2	0.22
639	619	596	2.8	697	23.2	32.1	0.20
633	612	612	3.1	697	16.3	25.8	0.17
626	679	630	3.5	700	13.6	25.1	0.14
620	653	653	3.7	711	11.4	21.6	0.09
614	673	659	3.8	722	11.1	19.7	0.06
607	690	671	4.0	725	10.8	20.7	0.03
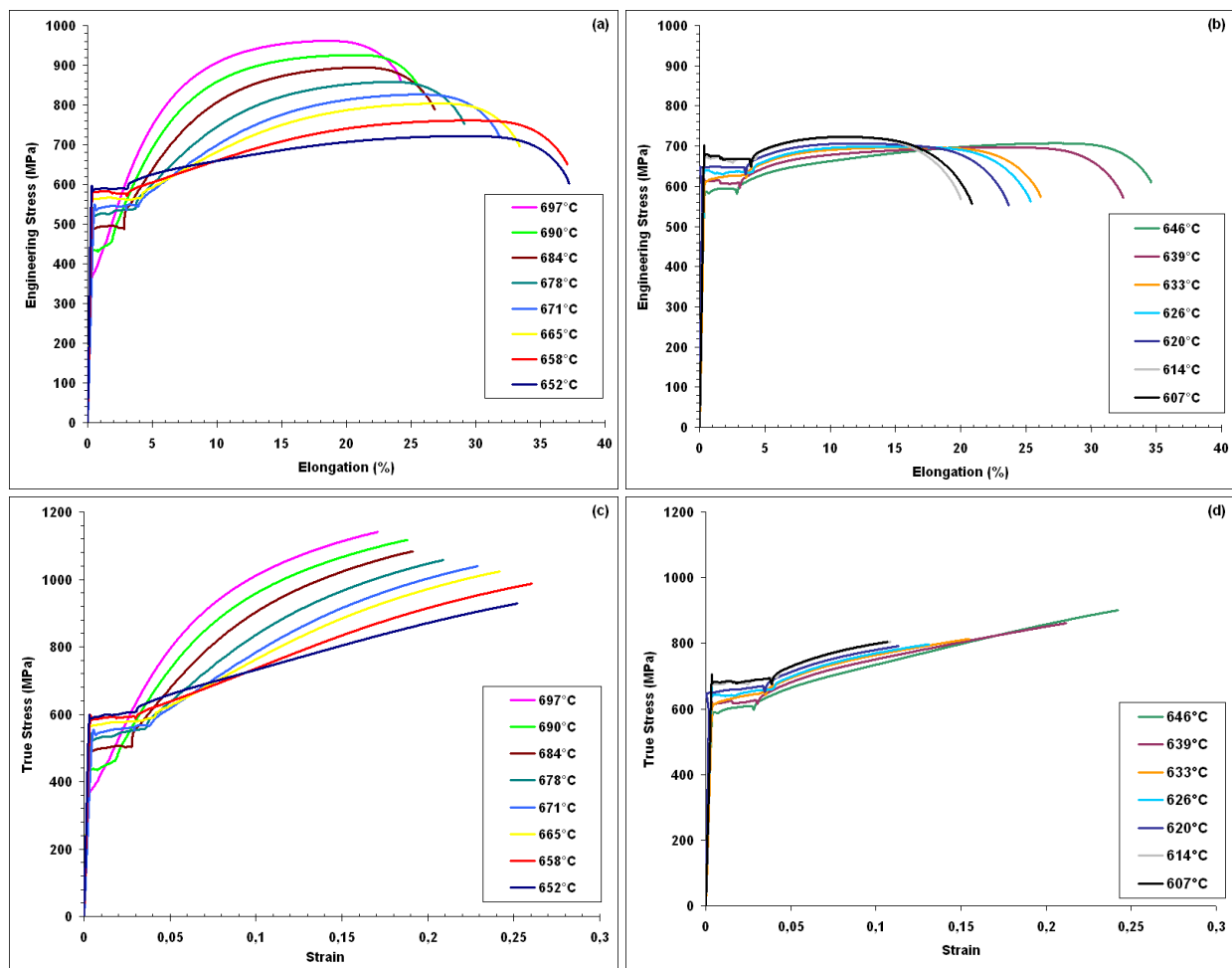
Figure 133 – Engineering (a, b) and true (c, d) stress-strain curves of the samples after gradient batch annealing.
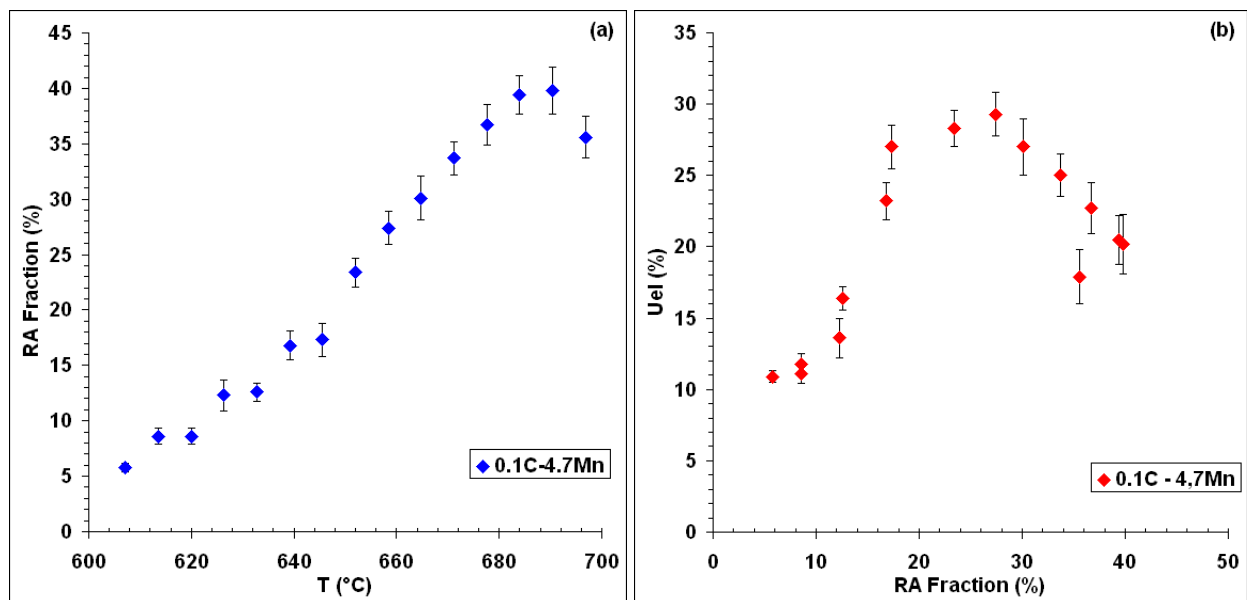
Figure 134 – (a) Evolution of retained austenite fraction as a function of holding temperature (GBA trial). (b) Evolution of Uel as a function of RA fraction.

Annex 3.1: Characterization of Mn microsegregations by EPMA

EPMA analysis was performed for 5 different samples: after austenitization at 750°C for 30min and after ART annealing at 650°C for 3min, 1h, 10h and 30h. The obtained quantitative images of Mn distribution are shown in Figure 135. On several Mn maps some more detailed observations were performed. The obtained individual results are presented in the following sub-sections.
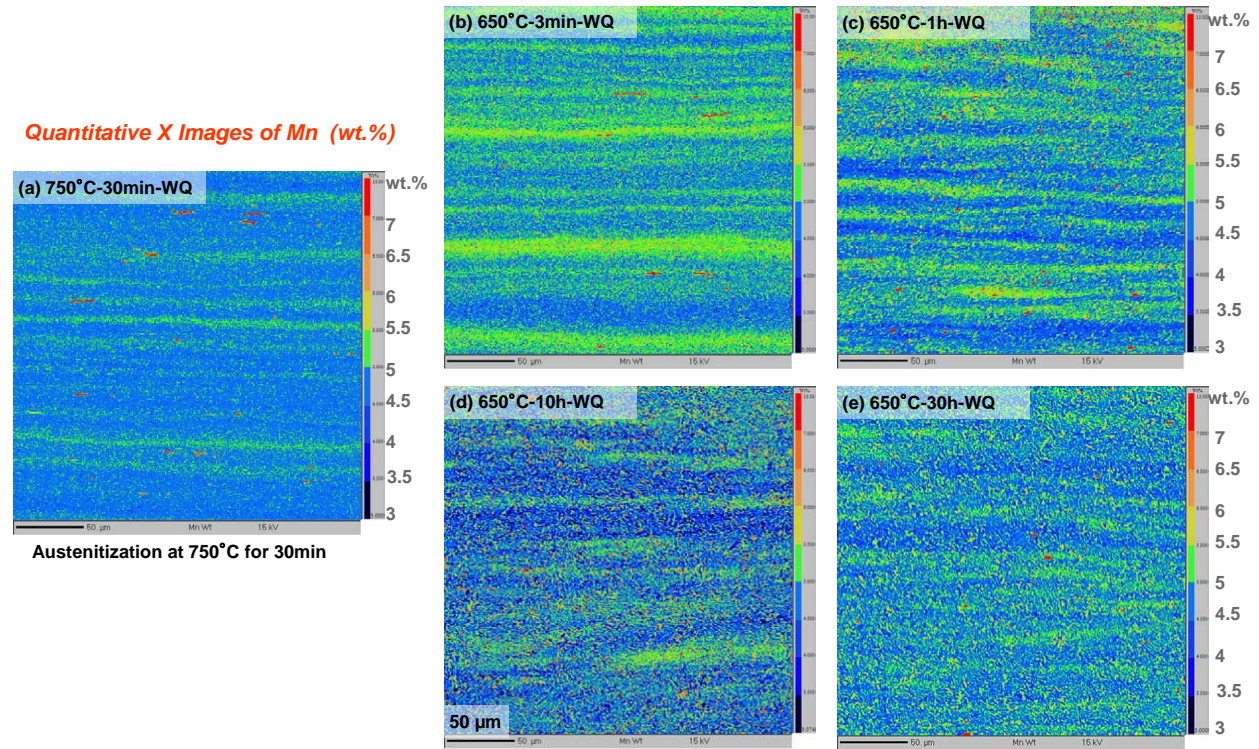
Figure 135 – Quantitative Mn maps obtained with EPMA for the sample after austenitization at 750°C for 30min and for the samples after ART annealing at 650°C for 3min, 1h, 10h and 30h.

Austenitization at 750°C 30min WQ

Figure 136 presents the Mn map analysis performed using Aphelion software: quantitative Mn map and Mn profiles along the lines 1 and 2. Optical observation of microstructure is also included in this figure.
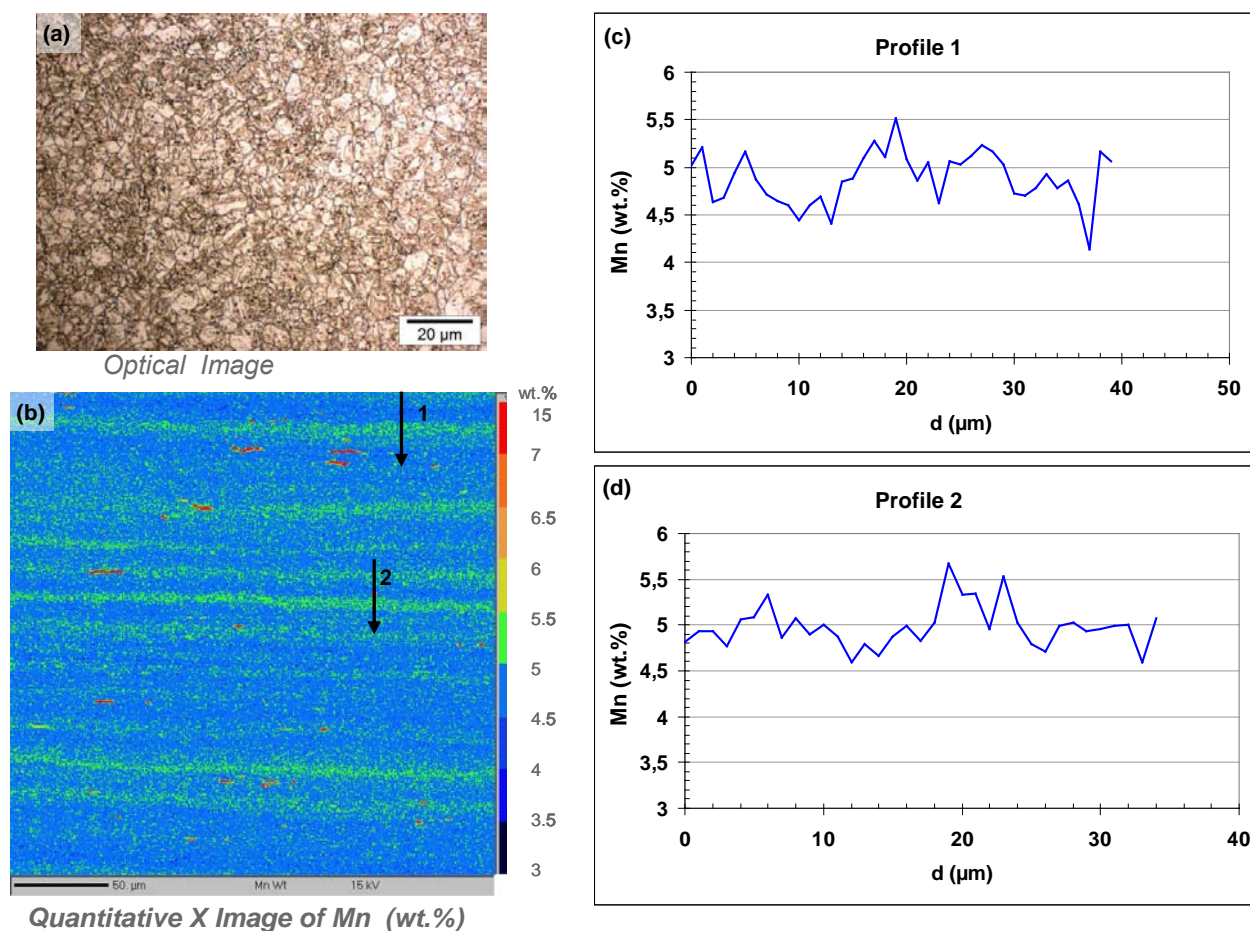
Figure 136 – EPMA quantitative analysis of Mn distribution in the microstructure after first annealing (750°C-30min-WQ): (a) optical micrograph after Dino etching; (b) quantitative Mn map (rolling direction is parallel to abscisse); (c) and (d) Mn profiles along the lines 1 and 2, respectively.

Figure 137 (a), (c) and (e) show another representation of quantitative Mn maps using ImageJ software. In Figure 137 (b), (d) and (f) are plotted the Mn profiles according to the lines in Figure 137(a), (c) and (e).

Locally, Mn composition can be as high as 15 wt.% Figure 137 (a) and (b). However, more globally the Mn content vary in between 4 and 6 wt.%. The calculated mean segregation level corresponds to a partition coefficient of about 1.2.
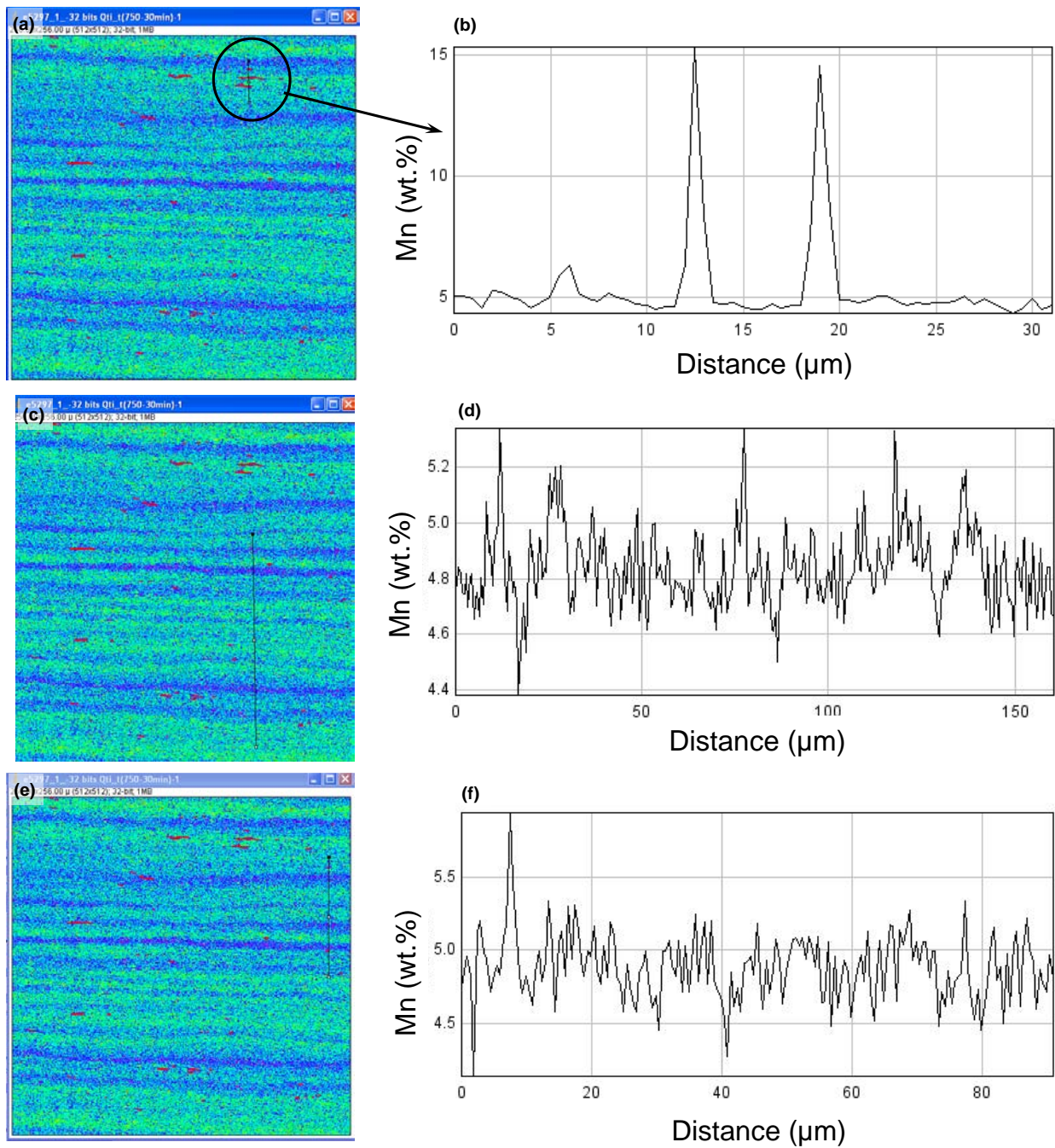
Figure 137 – EPMA quantitative analysis of Mn distribution in the microstructure after first annealing (750°C-30min-WQ) using ImageJ software: (a),(c) and (e) are the quantitative Mn maps and (b), (d) and (f) are the Mn profiles along the lines in (a),(c) and (e).

ART annealing at 650°C for 3min

The microstructure obtained after 3min ART annealing at 650°C is shown in Figure 138. Figure 139 presents the Mn map analysis performed using Aphelion software: quantitative Mn map and Mn profiles along the lines 1 and 2.
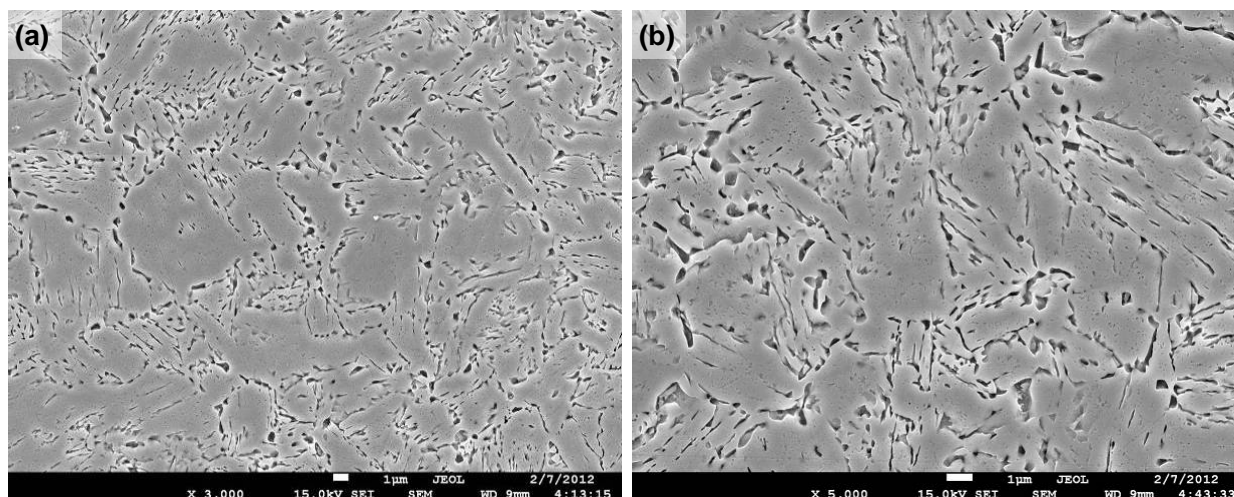
Figure 138 – SEM images of the microstructures obtained after 3min ART annealing at 650°C: (a) ×3000; (b) ×5000.
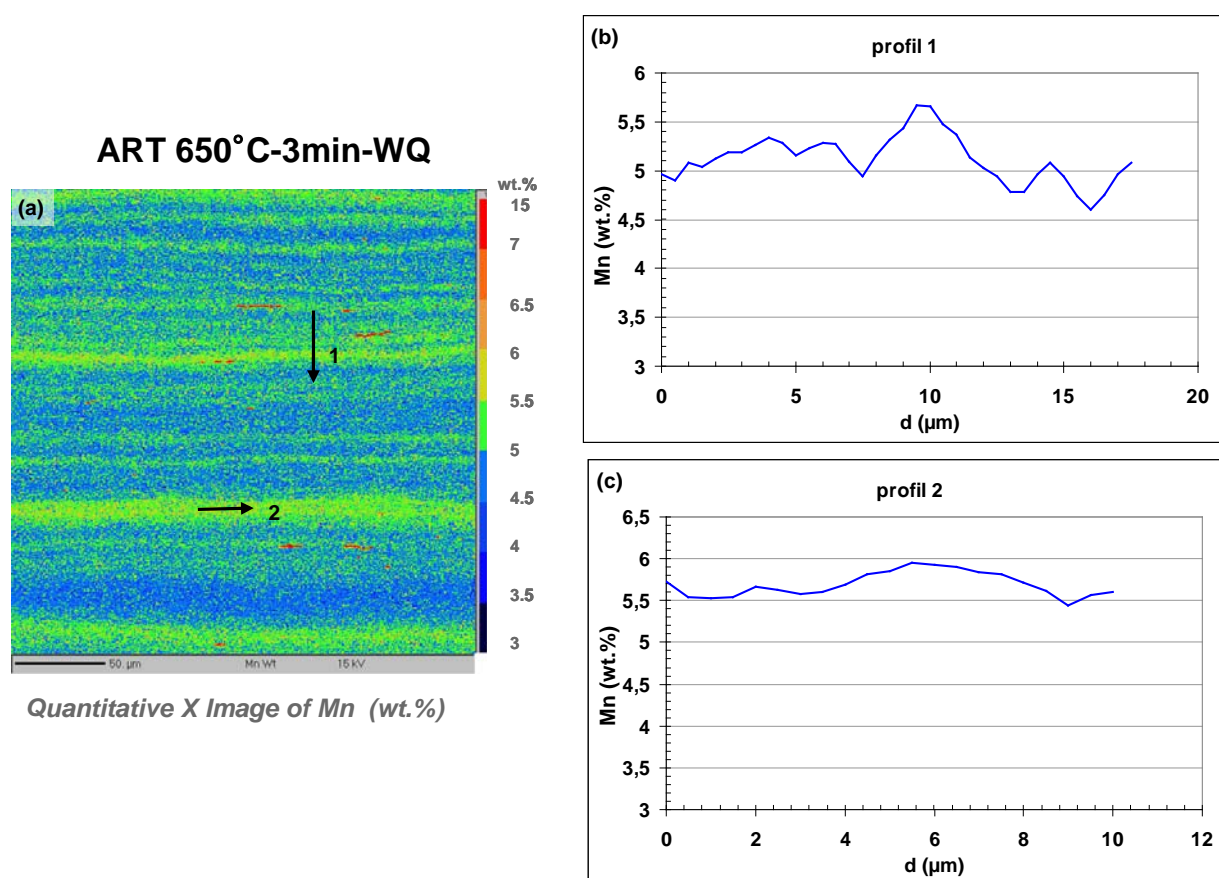
Figure 139 – EPMA quantitative analysis of Mn distribution in the microstructure obtained after 3min ART annealing at 650°C: (a) quantitative Mn map (rolling direction is parallel to abscisse); (b) and (c) Mn profiles along the lines 1 and 2, respectively.

ART annealing at 650°C for 1h

The microstructure obtained after 1h ART annealing at 650°C is shown in Figure 140. Figure 141 presents the Mn map analysis performed using Aphelion software: quantitative Mn map and Mn profiles along the lines 1 and 2.
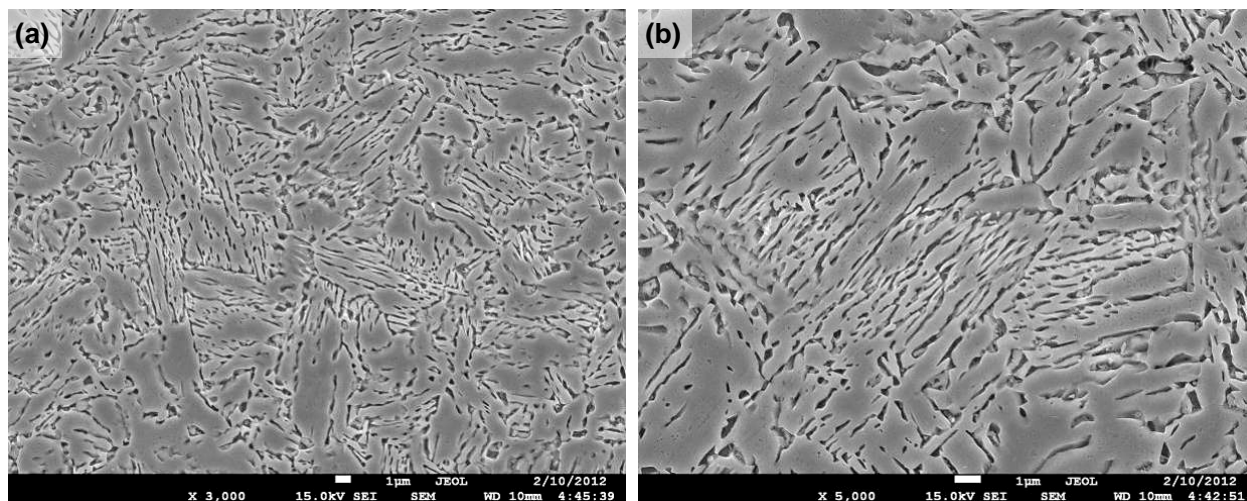
Figure 140 – SEM images of the microstructures obtained after 1h ART annealing at 650°C: (a) ×3000; (b) ×5000.
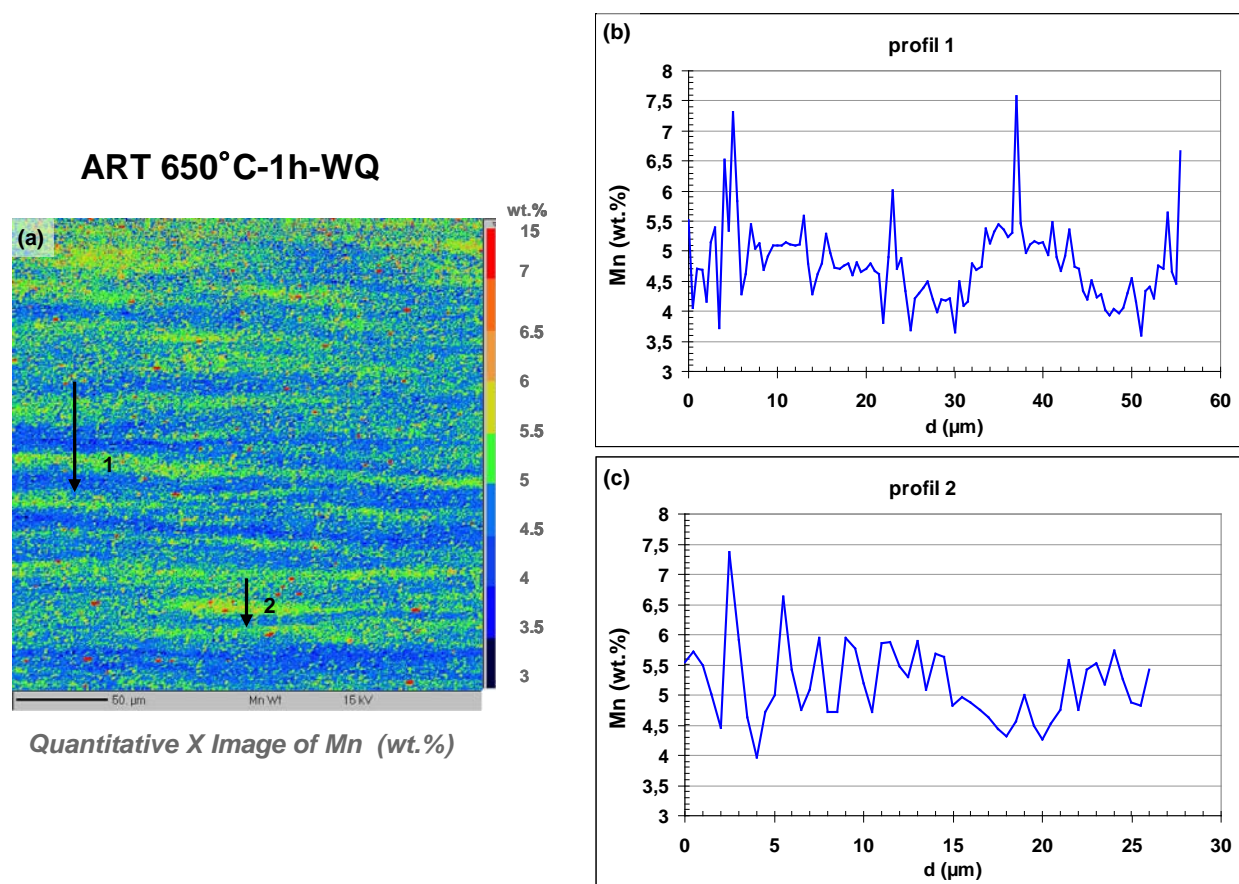
Figure 141 – EPMA quantitative analysis of Mn distribution in the microstructure obtained after 1h ART annealing at 650°C: (a) quantitative Mn map (rolling direction is parallel to abscisse); (b) and (c) Mn profiles along the lines 1 and 2, respectively.

ART annealing at 650°C for 10h

The microstructure obtained after 10h ART annealing at 650°C is shown in Figure 142. Figure 143 presents the Mn map analysis performed using Aphelion software: quantitative Mn map and Mn profiles along the lines 1, 2 and 3.
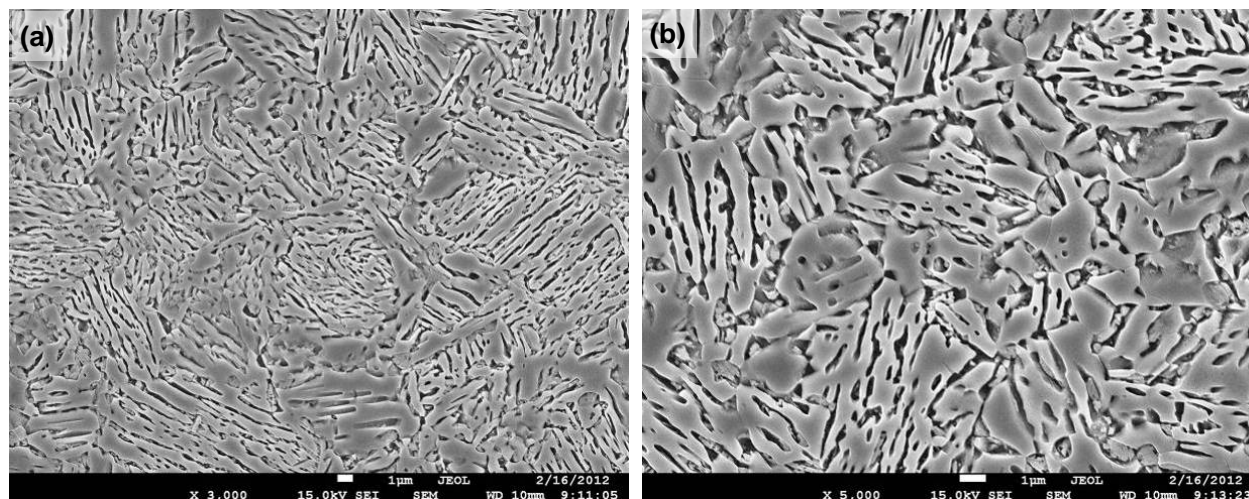
Figure 142 – SEM images of the microstructures obtained after 10h ART annealing at 650°C: (a) ×3000; (b) ×5000.
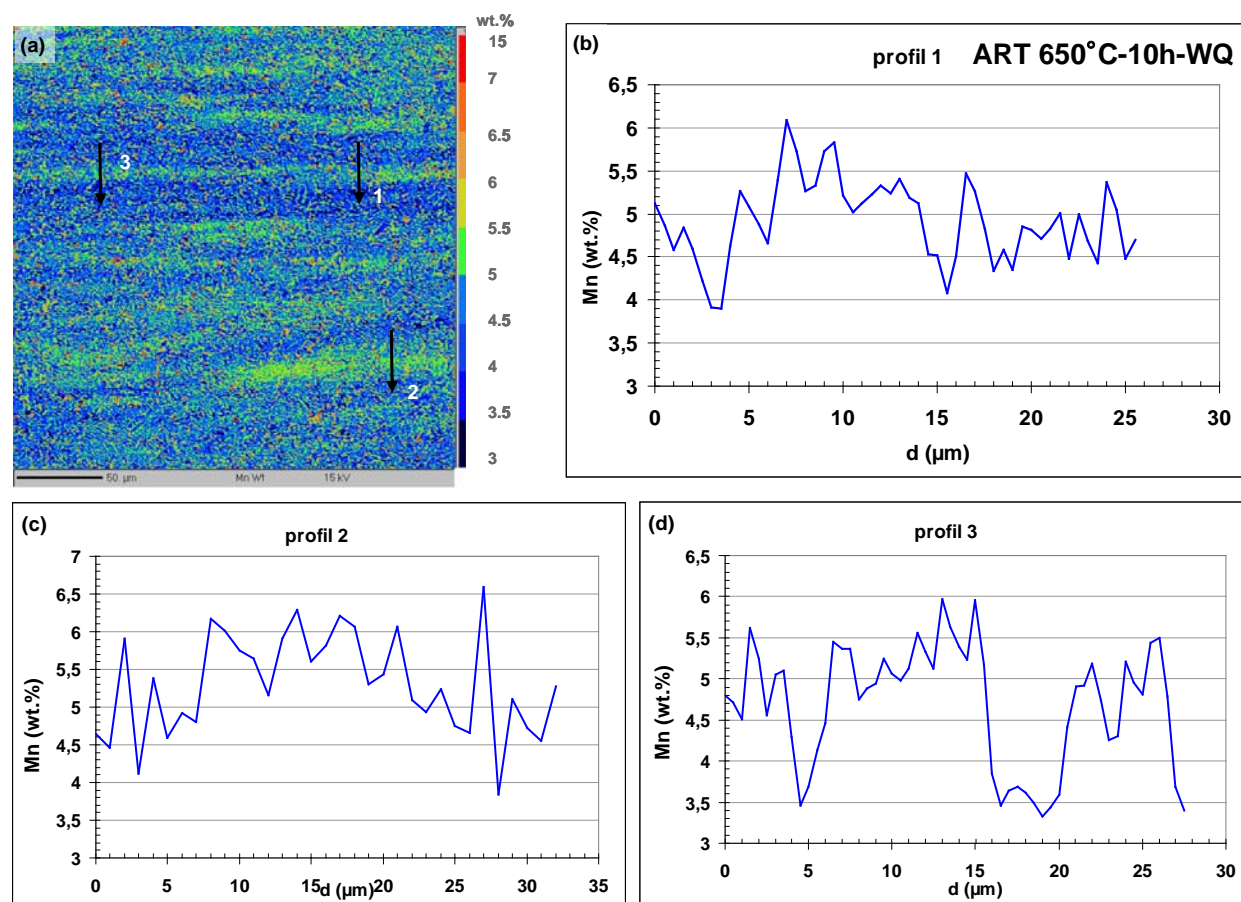
Figure 143 – EPMA quantitative analysis of Mn distribution in the microstructure obtained after 10h ART annealing at 650°C: (a) quantitative Mn map (rolling direction is parallel to abscisse); (b) and (c) Mn profiles along the lines 1, 2 and 3, respectively

ART annealing at 650°C for 30h

The microstructure obtained after 30h ART annealing at 650°C is shown in Figure 144. Figure 145 presents the Mn map analysis performed using Aphelion software: quantitative Mn map and Mn profile along the line 1.
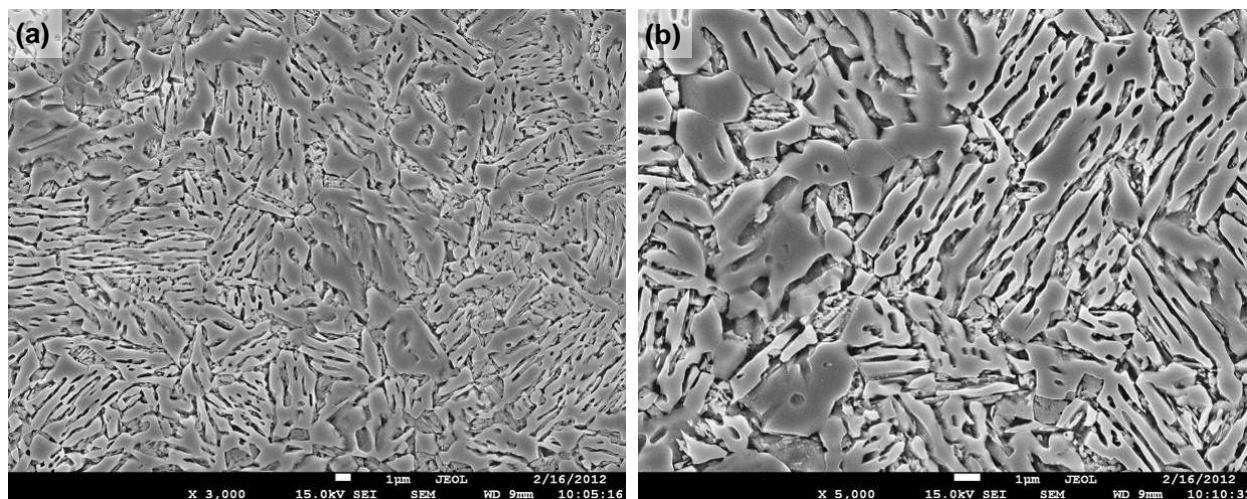
Figure 144 – SEM images of the microstructures obtained after 30h ART annealing at 650°C: (a) ×3000; (b) ×5000.
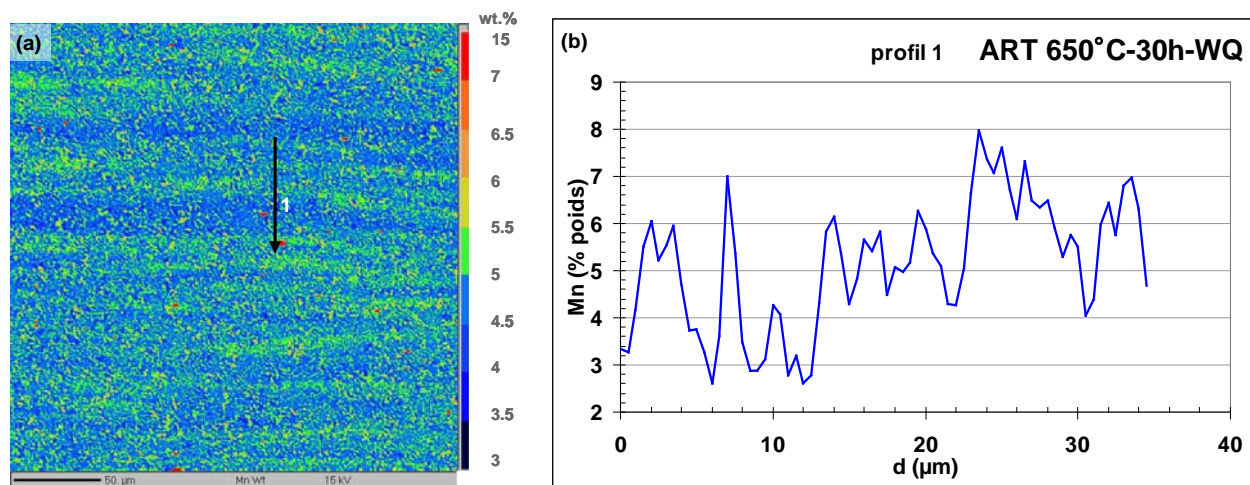
Figure 145 – EPMA quantitative analysis of Mn distribution in the microstructure after 30h ART annealing at 650°C: (a) quantitative Mn map; (b) Mn profile along the line 1.

Annex 3.2: Characterization of carbides by TEM

TEM observations of carbides formed during heating were done using replicas. The heating was interrupted at 550, 600 and 650°C using He quench. For each sample several observations were performed and the obtained results are presented in the following sub-sections.

550°C sample
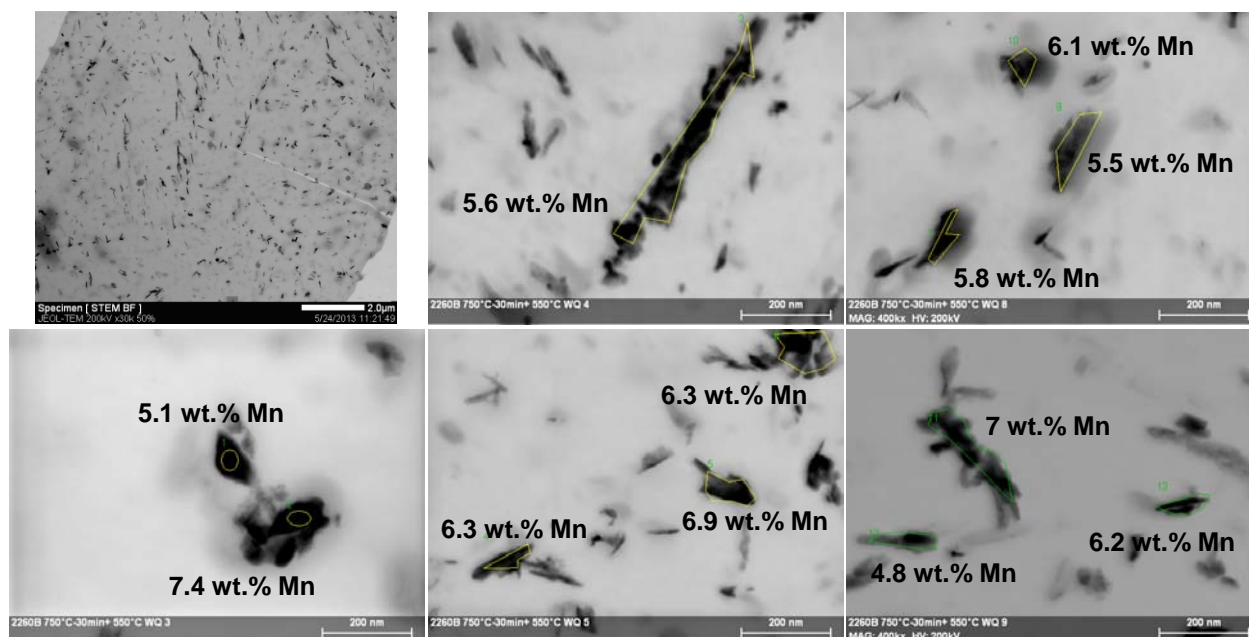
Figure 146 – TEM images obtained using replicas of the sample heated up to 550°C: left up corner - low magnification image of the analyzed zone and the others are images of carbides with their respective Mn content, measured by EDX.

Mean composition of cementite estimated from 12 measurements was 6.1 wt.% Mn

600°C sample
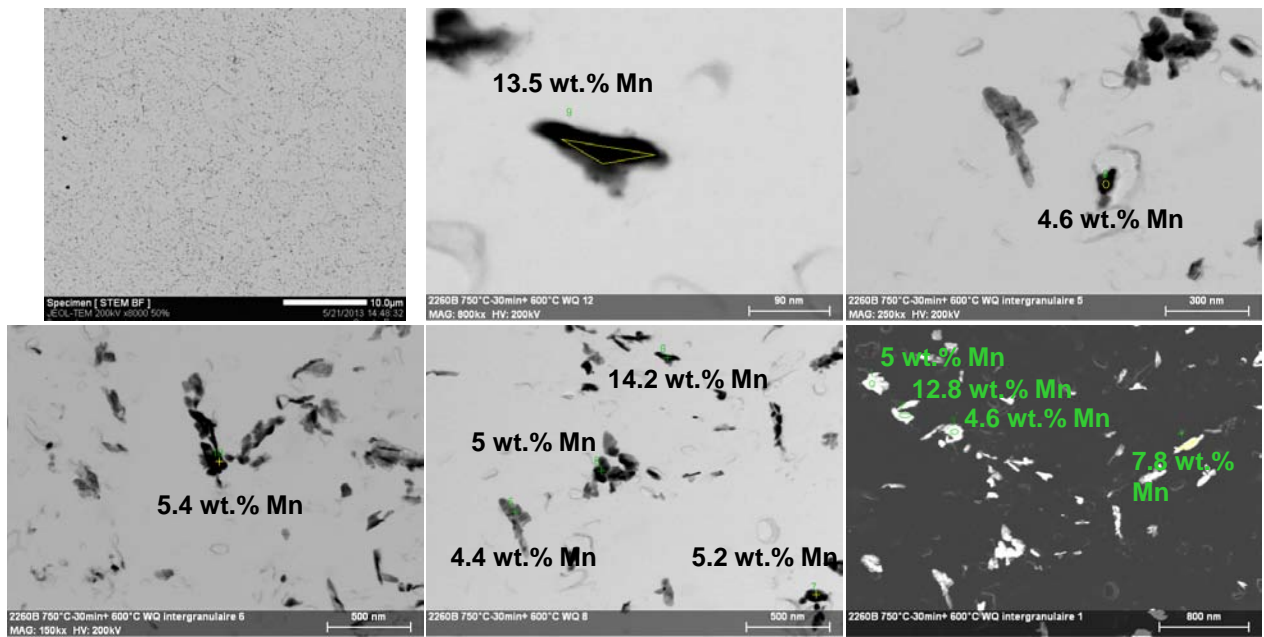
Figure 147 – TEM images obtained using replicas of the sample heated up to 600°C: left up corner - low magnification image of the analyzed zone and the others are images of carbides with their respective Mn content, measured by EDX.
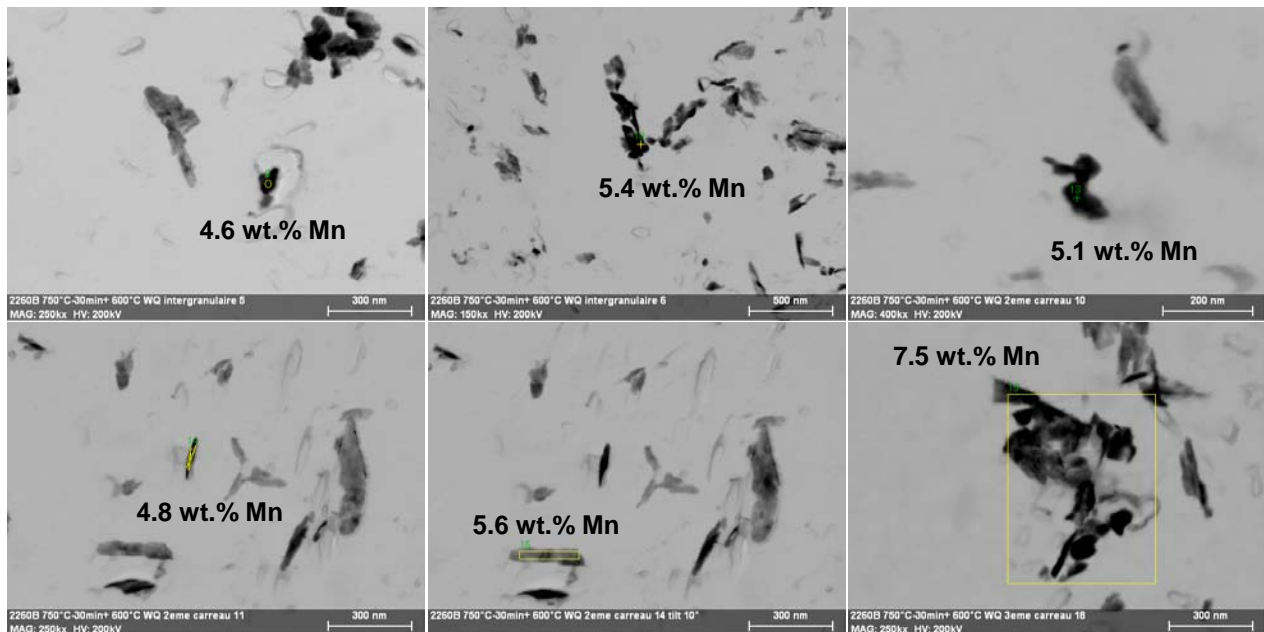
Figure 148 – TEM images of carbides with their respective Mn content, measured by EDX (another zone of 600°C replicas).

Mean composition of cementite estimated from 17 measurements was 6.8 wt.% Mn. However, three levels of Mn content in cementite were observed: first around 5 wt.%, second ~8 wt.% and third about 13 wt.% .

650°C sample
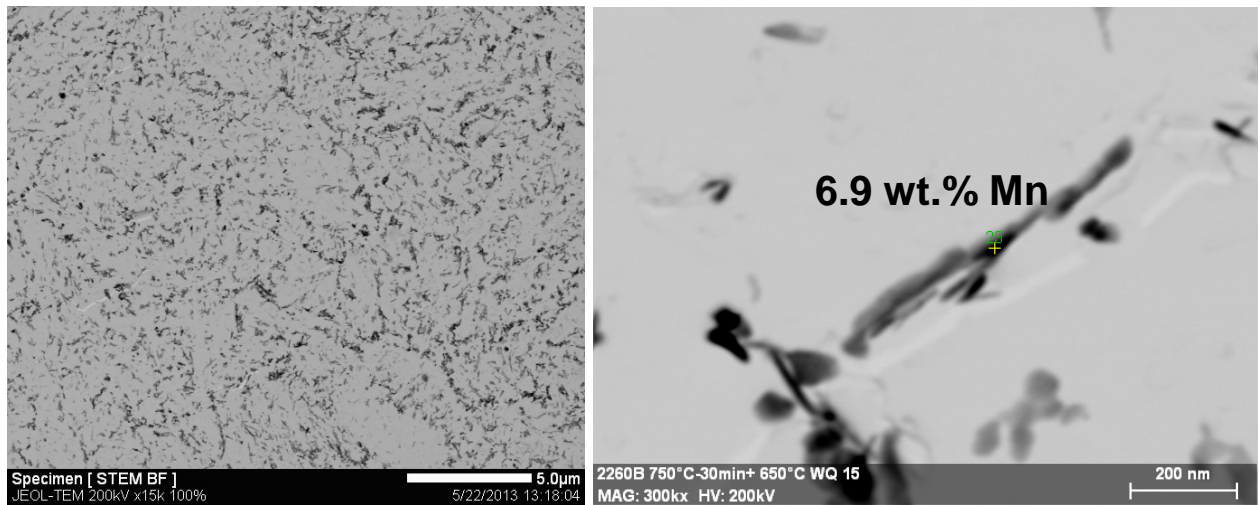
Figure 150 – TEM images obtained using replicas of the sample heated up to 650°C: left up corner - low magnification image of the analyzed zone and the others are images of carbides with their respective Mn content, measured by EDX.
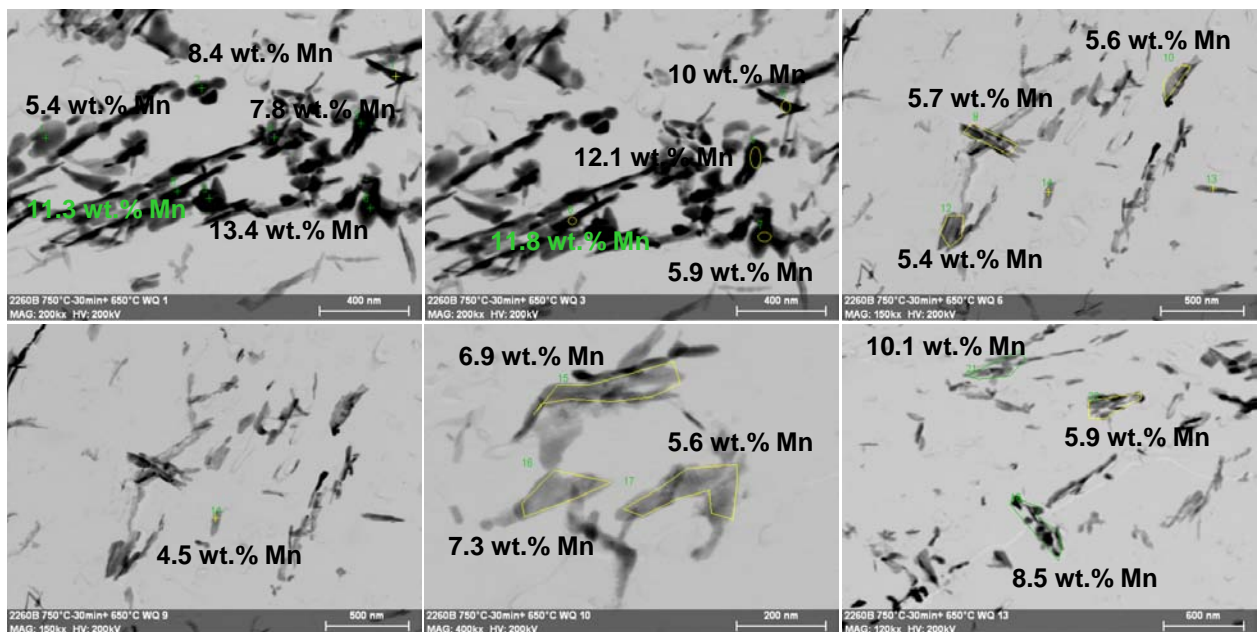
Figure 151 – TEM images of carbides with their respective Mn content, measured by EDX. Replicas of the sample heated up to 650°C and He quenched.

Mean composition of cementite estimated from 20 measurements was ~8 wt.% Mn, but in this sample Mn of cementite varied continuously from 4.5 to 13.5 wt.%.

Annex 3.3: Mn distribution characterization by EDX-TEM

During the TEM observations of samples with different holding time at 650°C (3min, 1h, 2h, 3h, 10h and 30h) EDX direct measurements or EDX-hypermaps were realized. The obtained profiles and hypermaps are presented in the following sub-sections.

<u>3min sample</u>
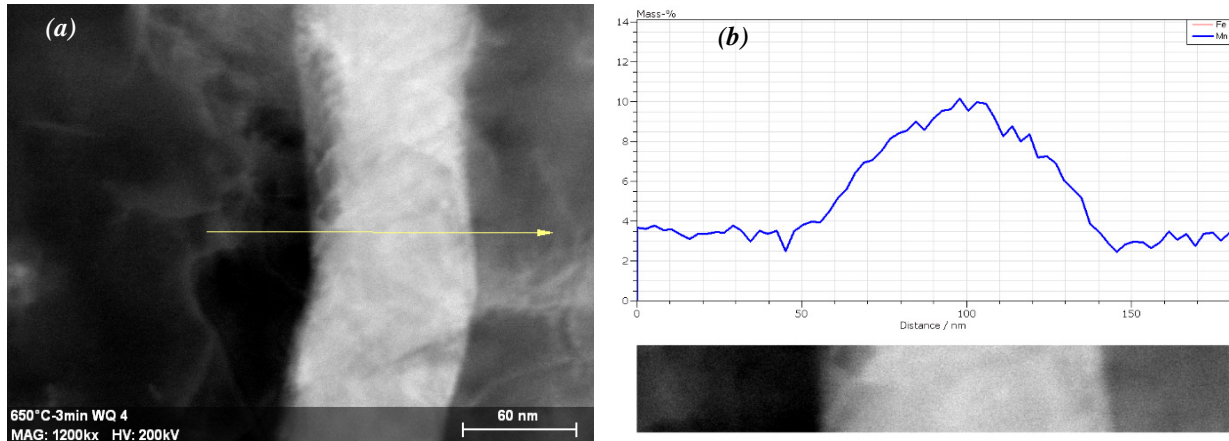
Figure 152 – Mn EDX profile of 3min sample: (a) selected zone; (b) Mn evolution as a function of distance.

<u>1h sample</u>

1st hypermap
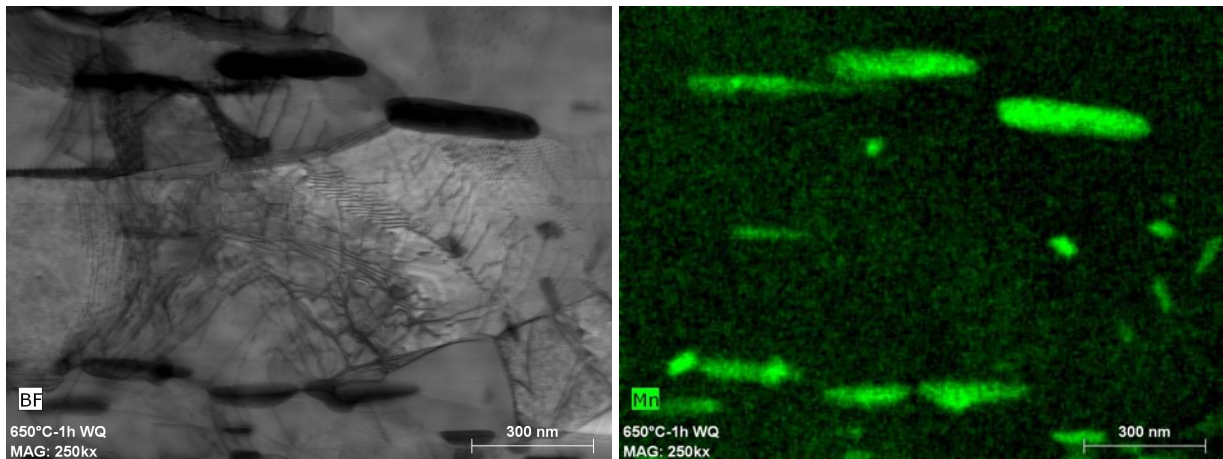
Figure 153 – Bright field TEM image (at left) and the EDX-hypermap of corresponding zone (at right) of 1h sample (1st hypermap).
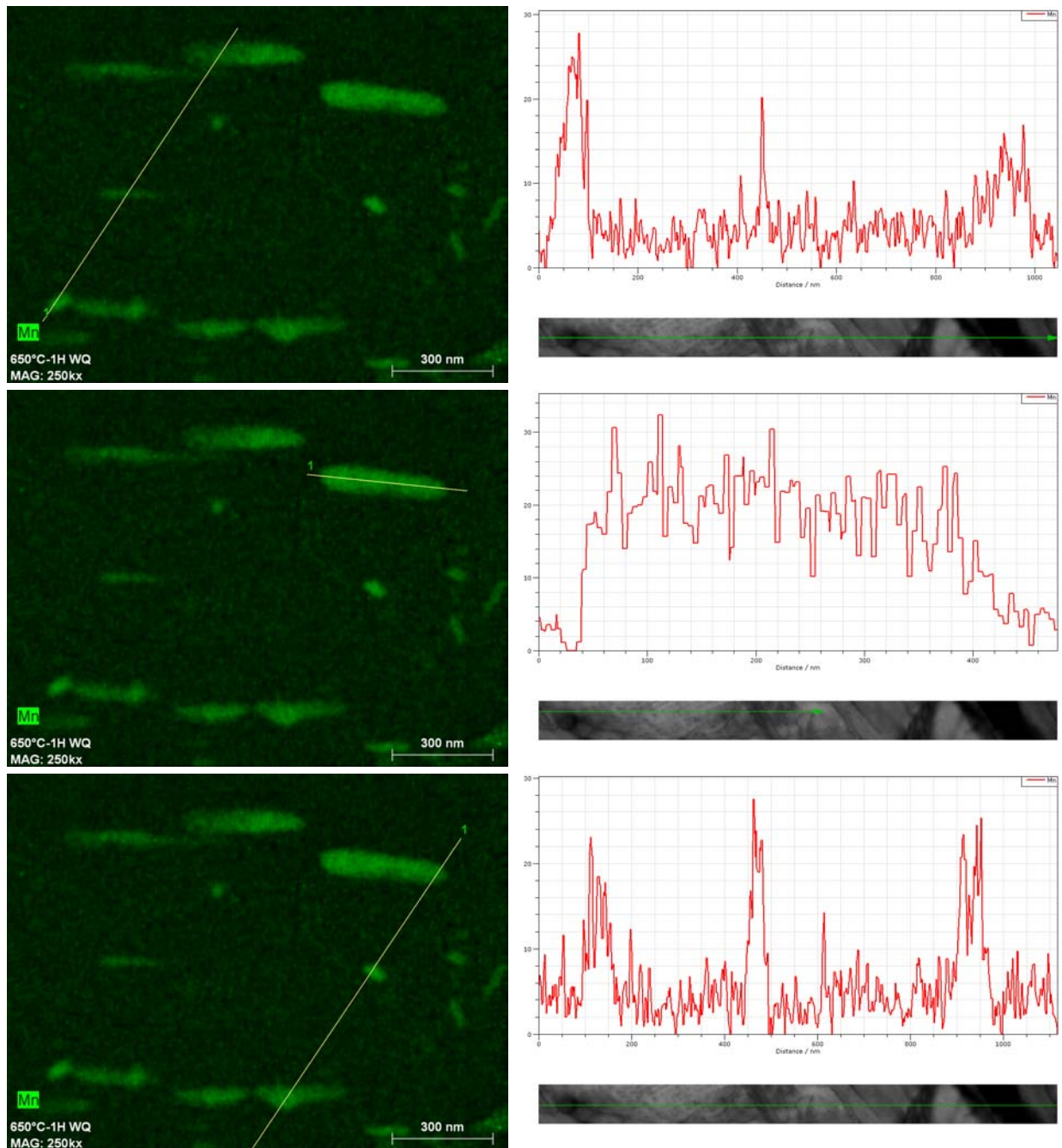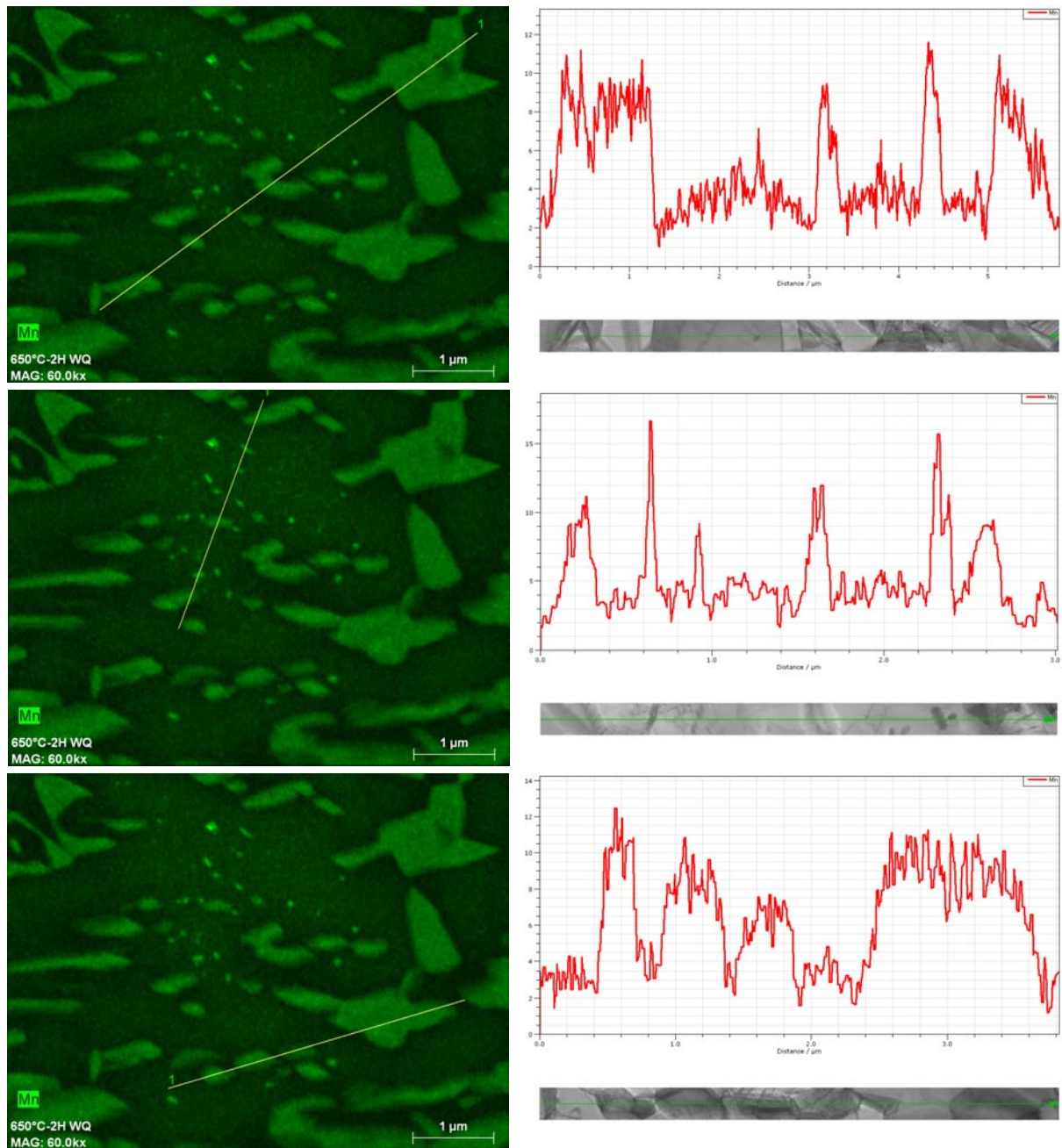
Figure 154 – Mn profiles of 1h sample (1ˢᵗ hypermap): at left are presented selected zones and at right – corresponding Mn evolutions as a function of distance.
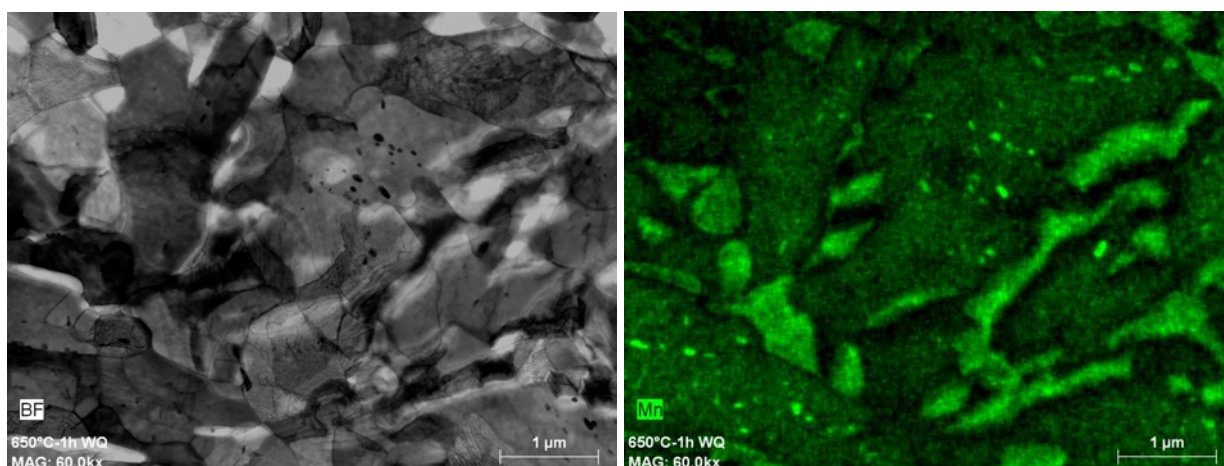
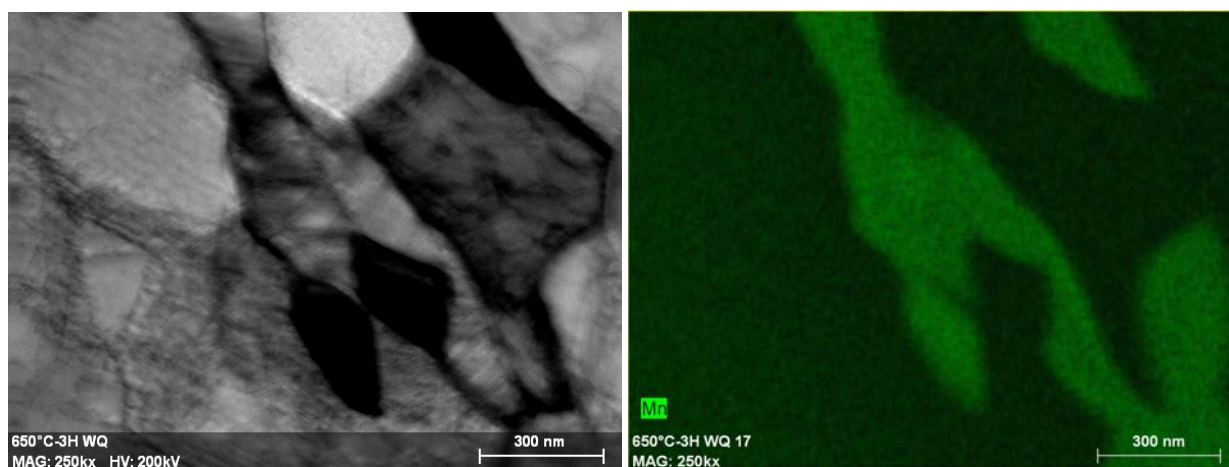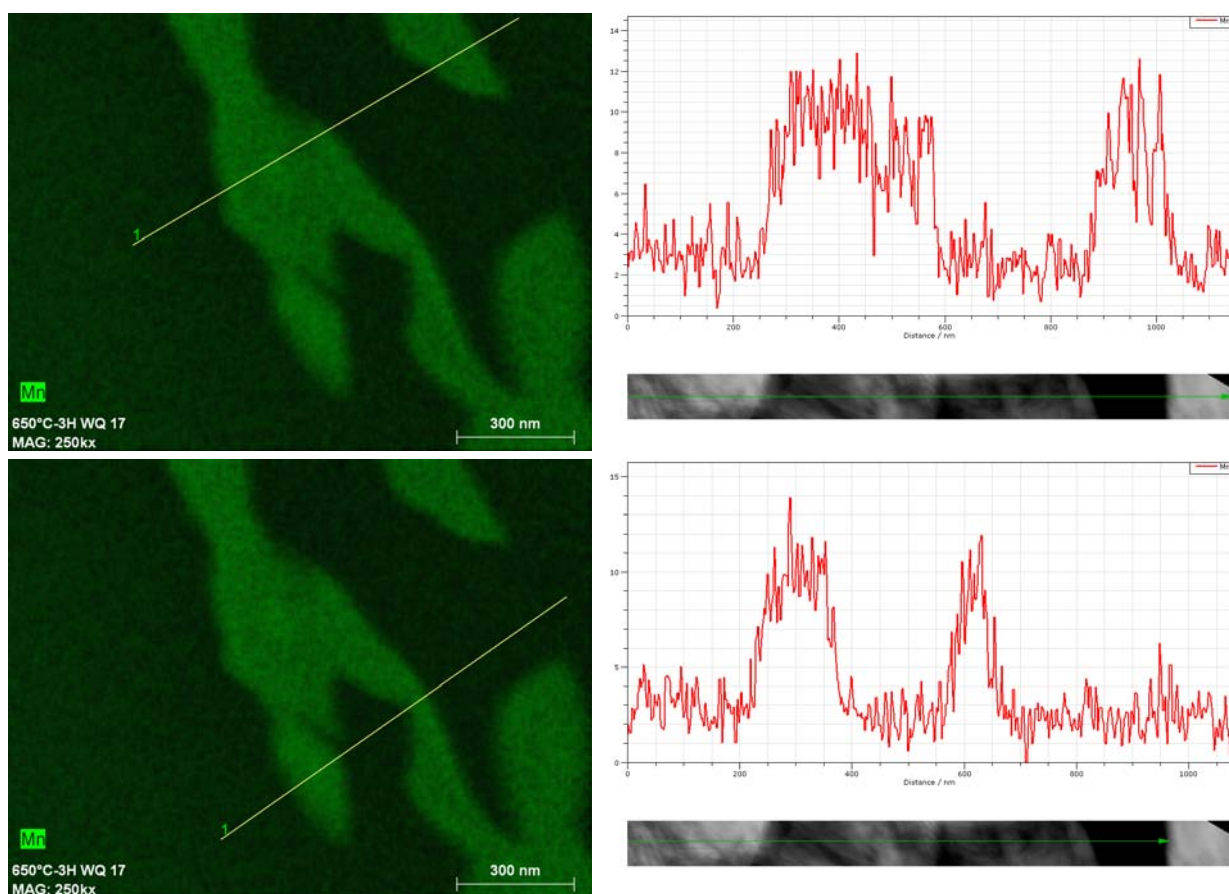2nd Hypermap

Figure 155 – Bright field TEM image (at left) and the EDX-hypermap of corresponding zone (at right) of 1h sample (2nd hypermap).
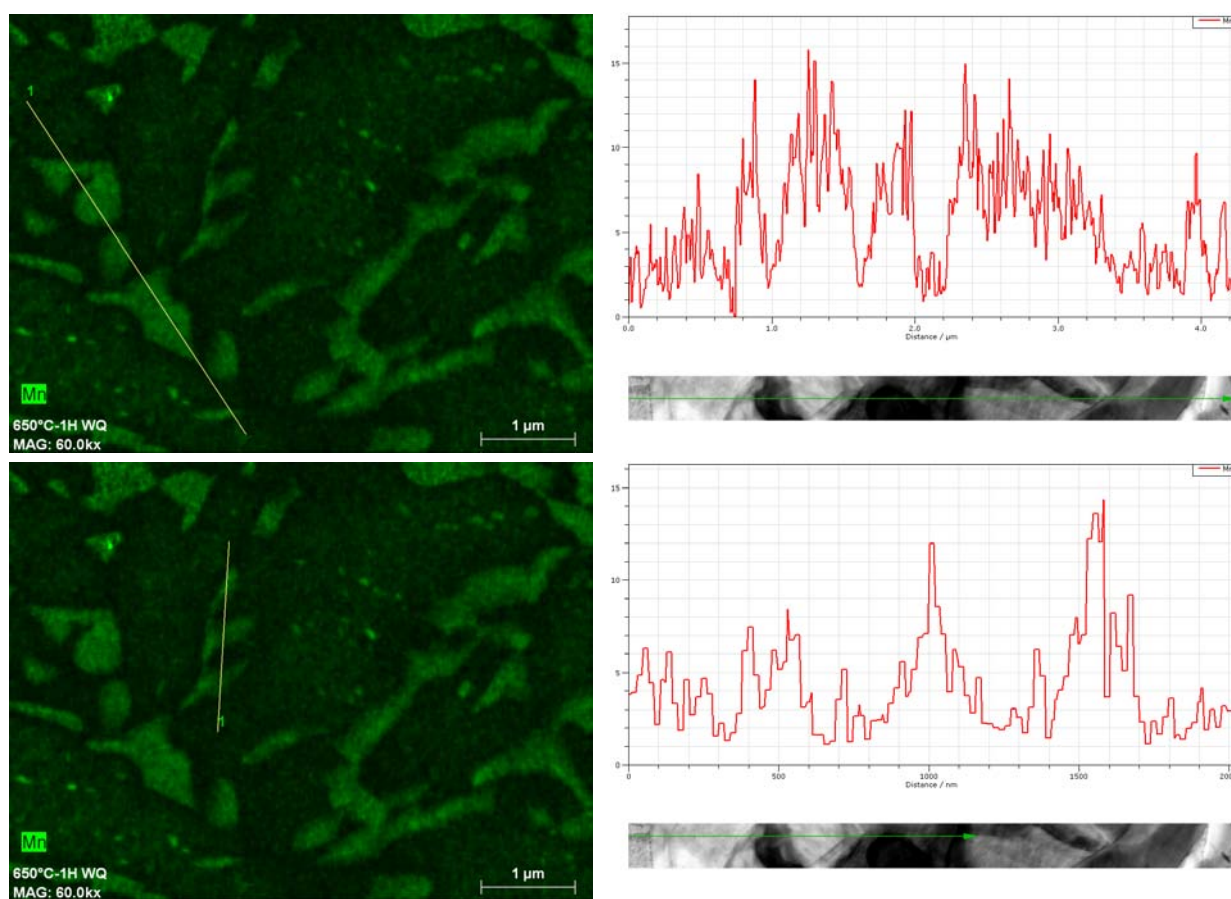
Figure 156 – Mn profiles of 1h sample (2nd hypermap): at left are presented selected zones and at right – corresponding Mn evolutions as a function of distance.
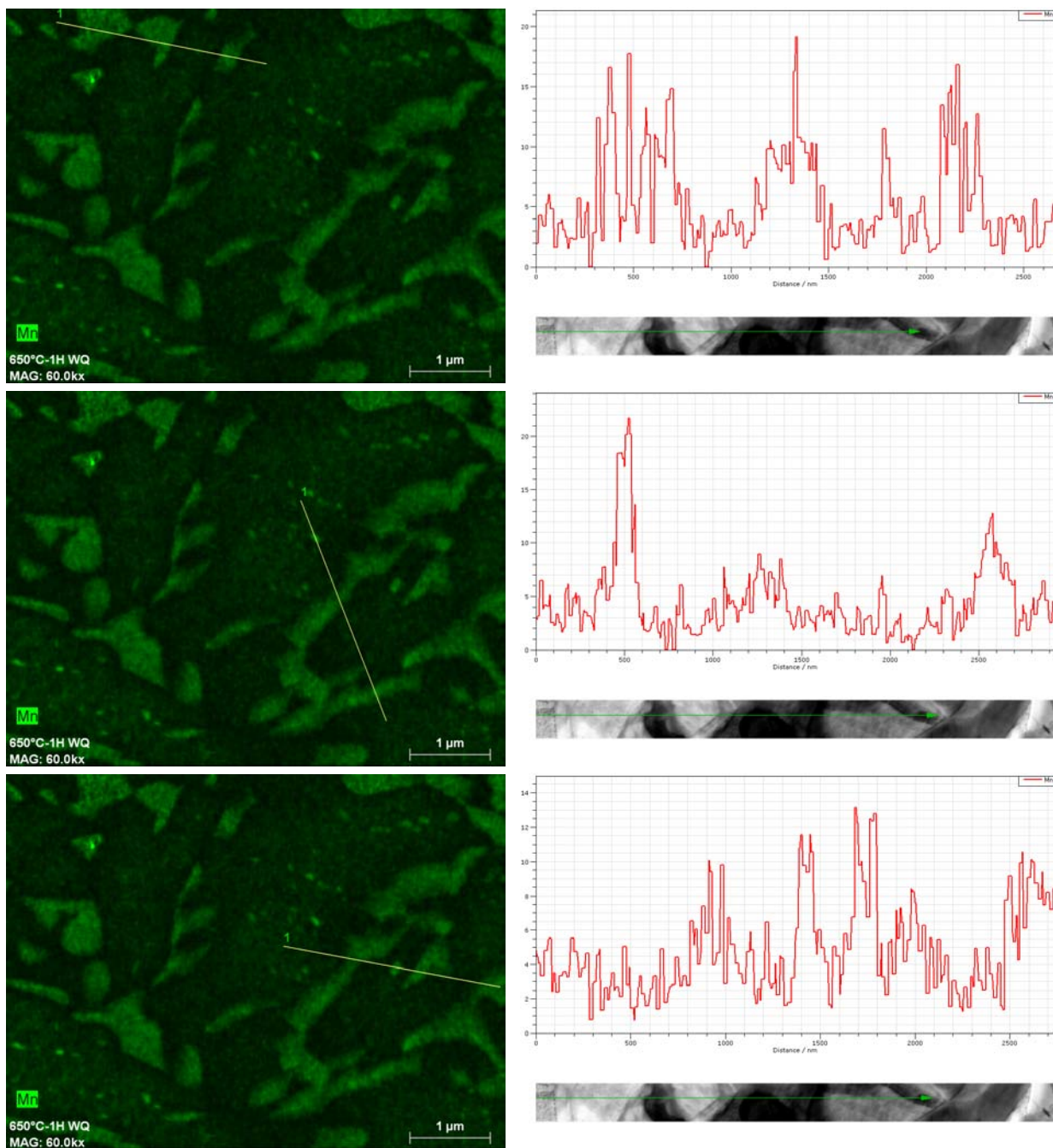
Figure 157 – Mn profiles of 1h sample (2nd hypermap): at left are presented selected zones and at right – corresponding Mn evolutions as a function of distance.
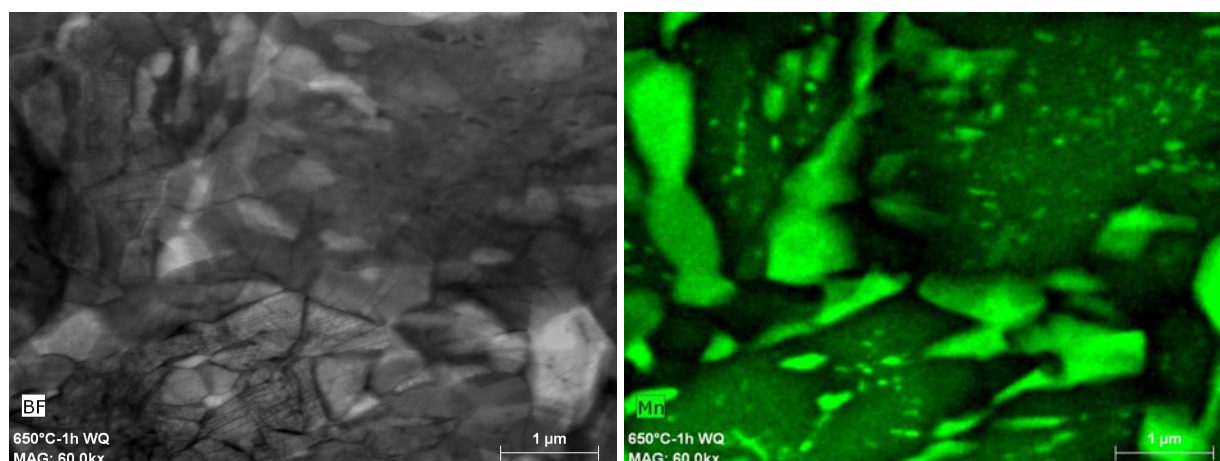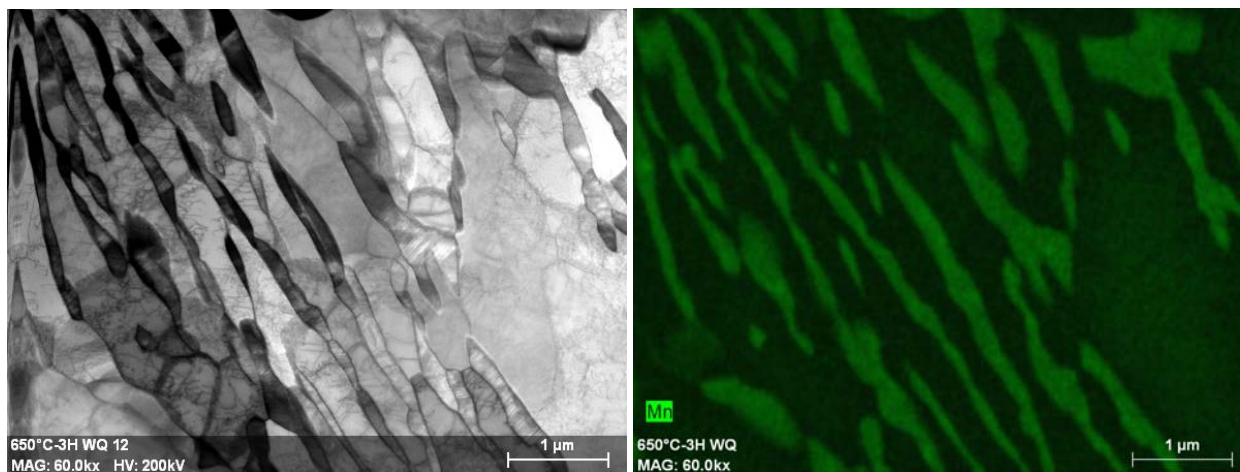
3rd hypermap

Figure 158 – Bright field TEM image (at left) and the EDX-hypermap of corresponding zone (at right) of 1h sample (3rd hypermap).
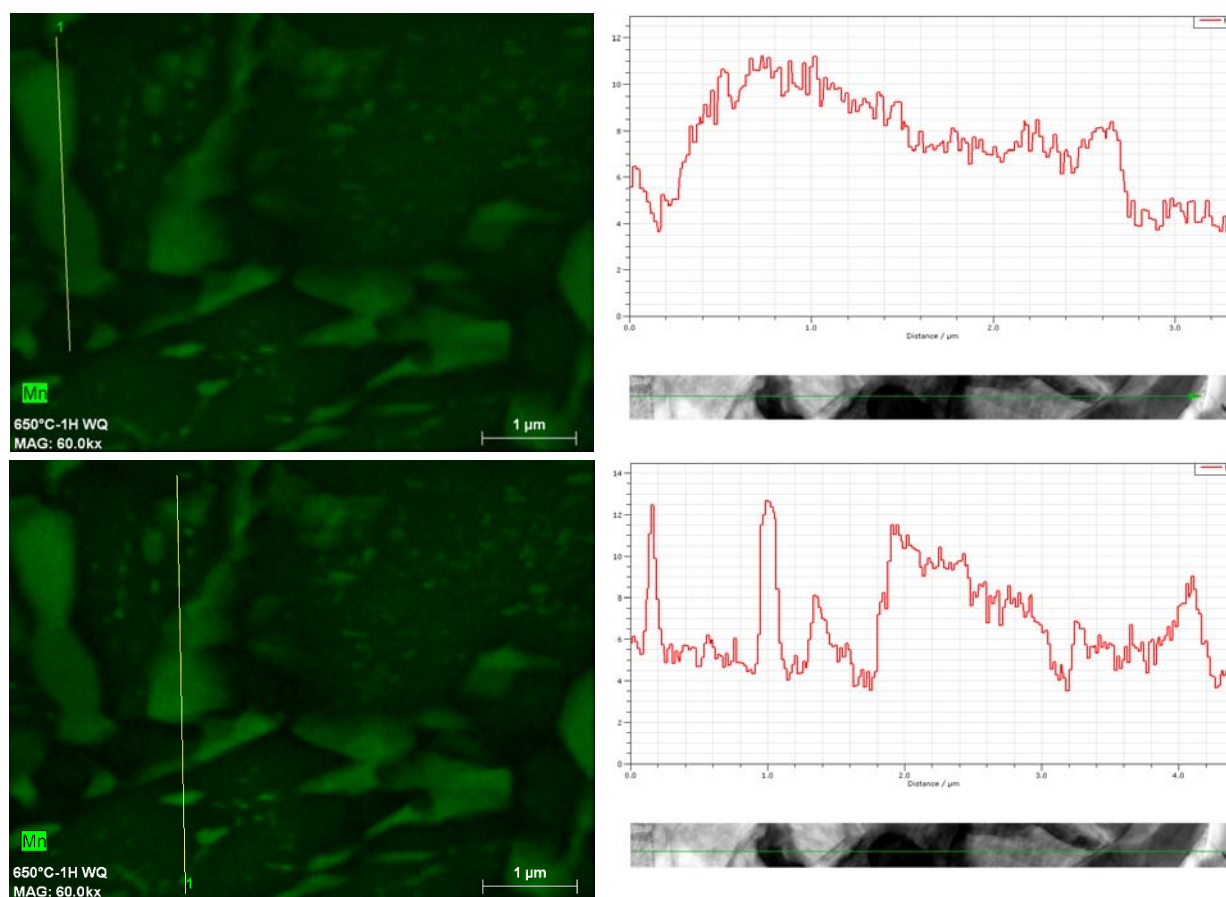
Figure 159 – Mn profiles of 1h sample (3rd hypermap): at left are presented selected zones and at right – corresponding Mn evolutions as a function of distance.
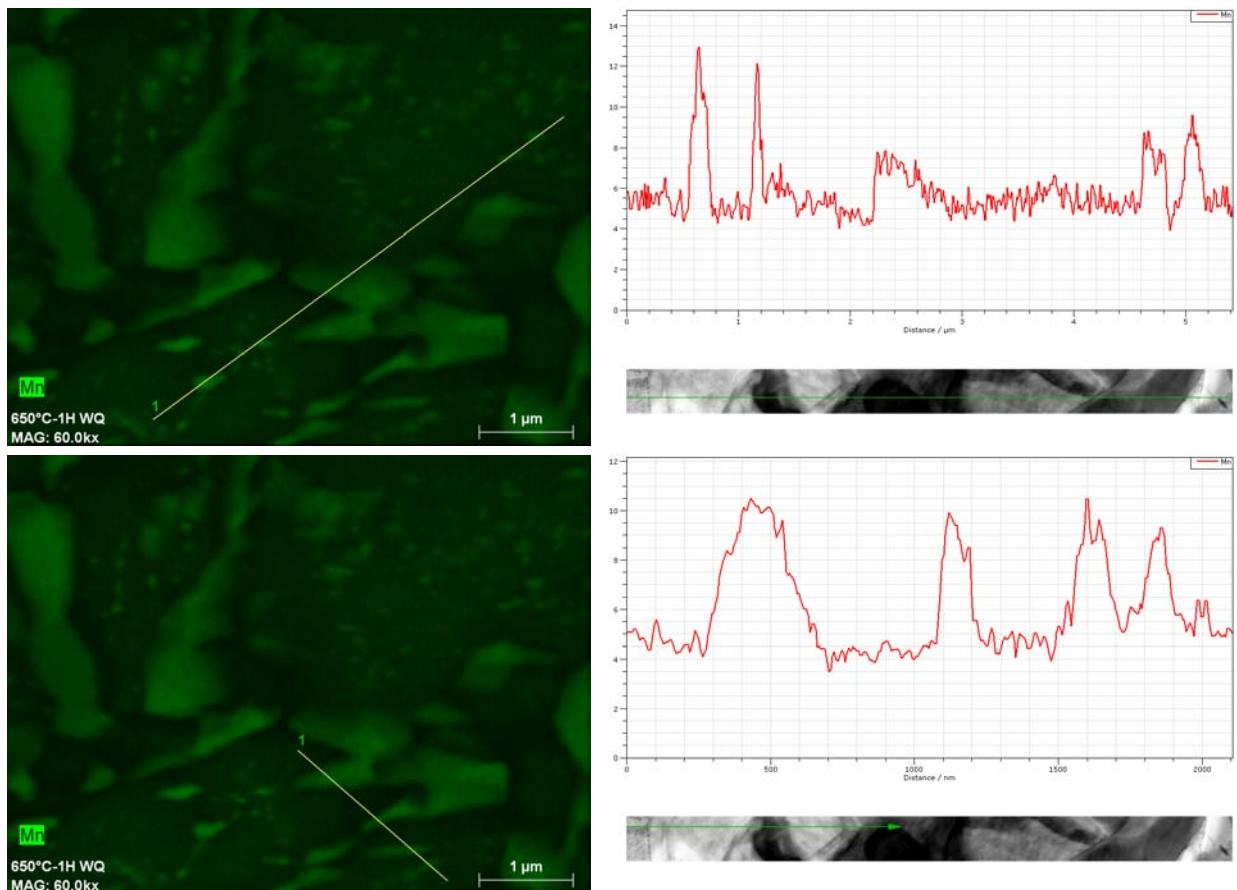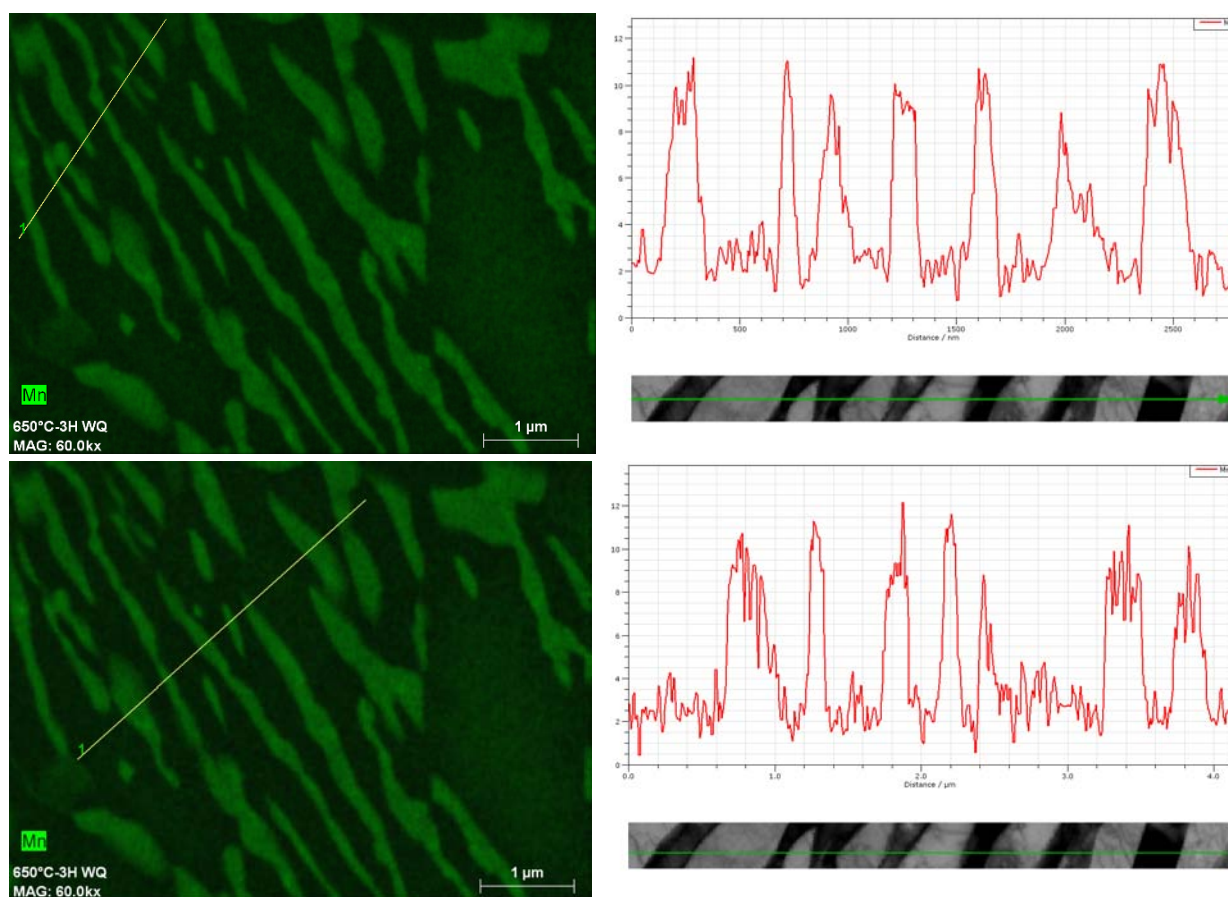
Figure 160 – Mn profiles of 1h sample (3rd hypermap): at left are presented selected zones and at right – corresponding Mn evolutions as a function of distance.
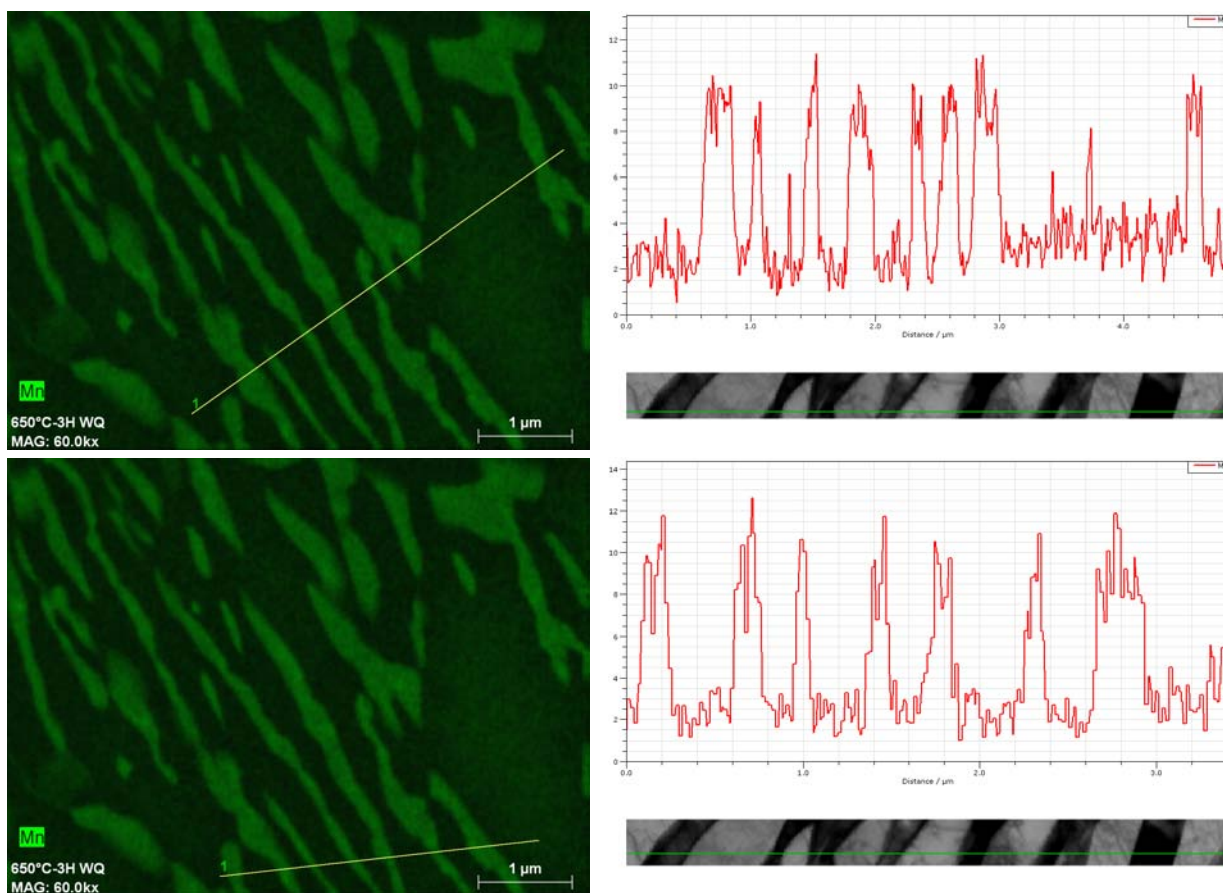
2h sample
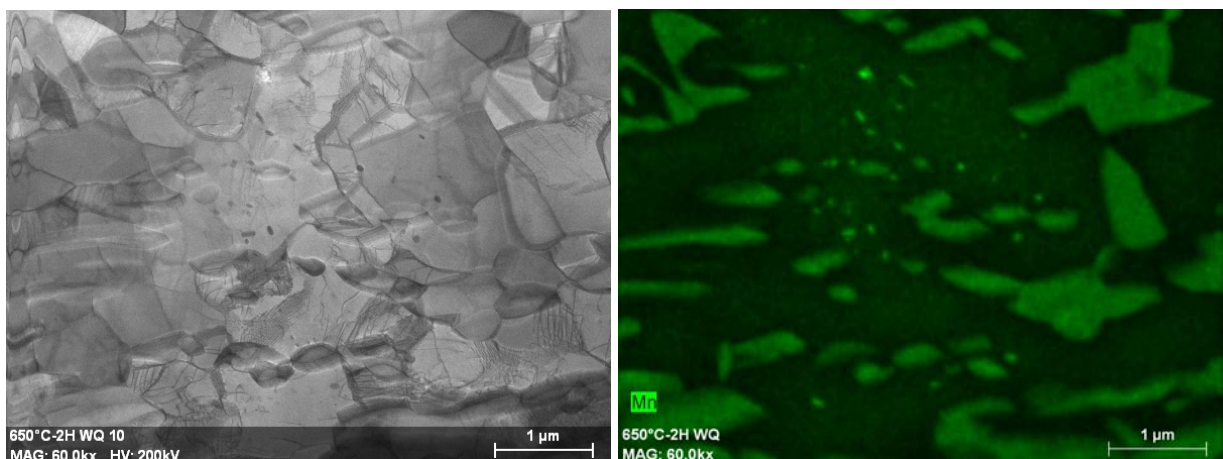
Figure 161 – Bright field TEM image (at left) and the EDX-hypermap of corresponding zone (at right) of 2h sample.
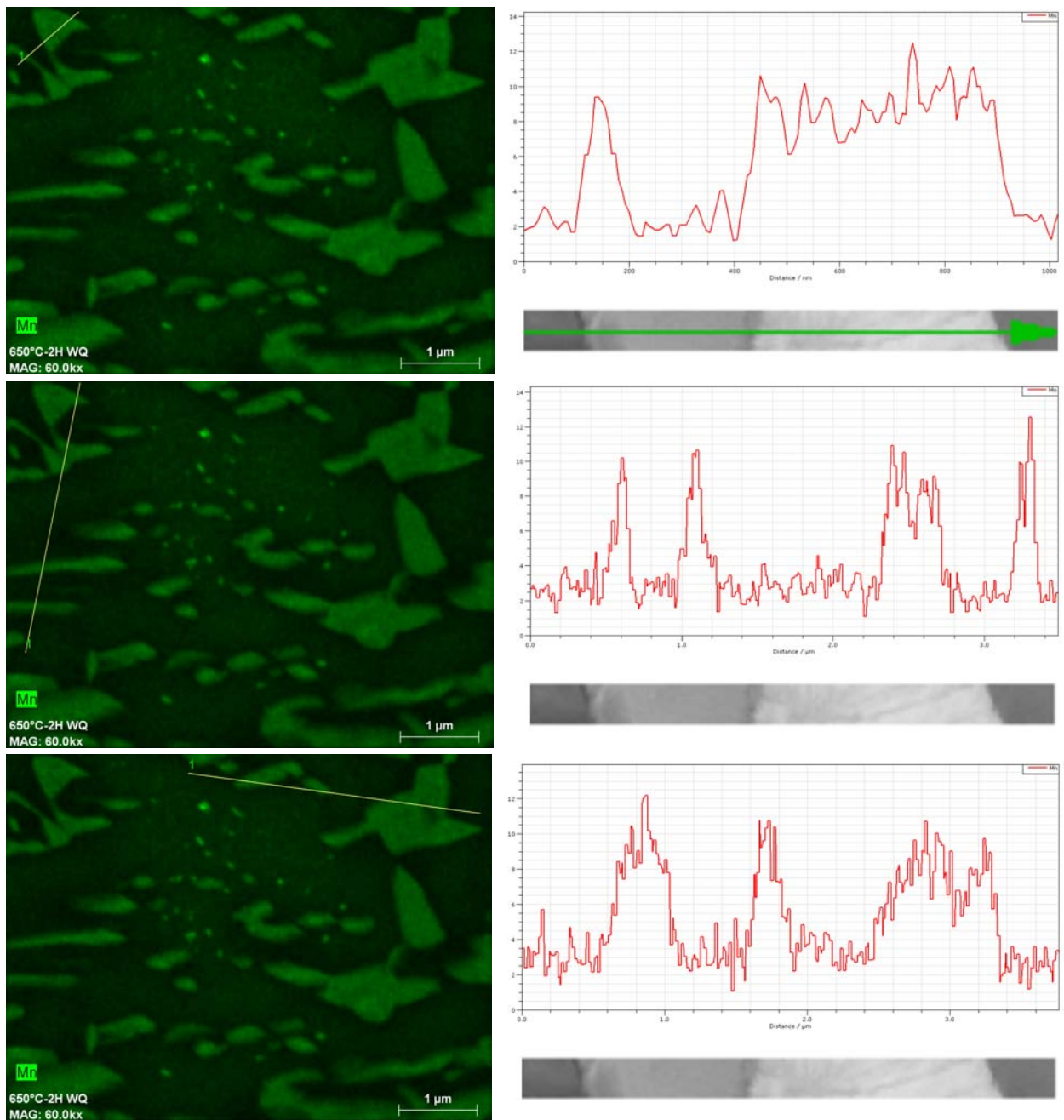
Figure 162 – Mn profiles of 2h sample: at left are presented selected zones and at right – corresponding Mn evolutions as a function of distance.
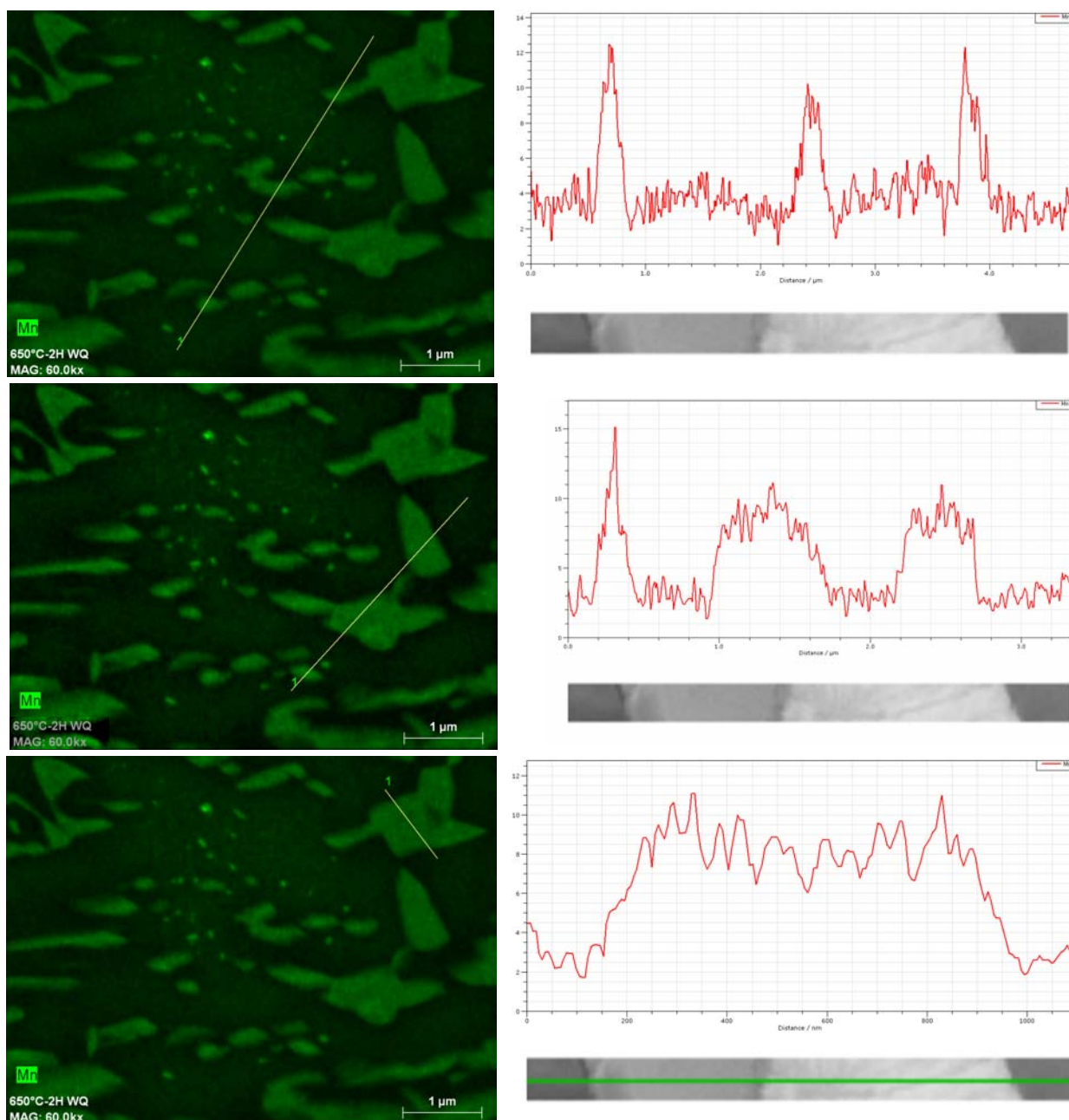
Figure 163 – Mn profiles of 2h sample: at left are presented selected zones and at right – corresponding Mn evolutions as a function of distance.

Figure 164 – Mn profiles of 2h sample: at left are presented selected zones and at right – corresponding Mn evolutions as a function of distance.
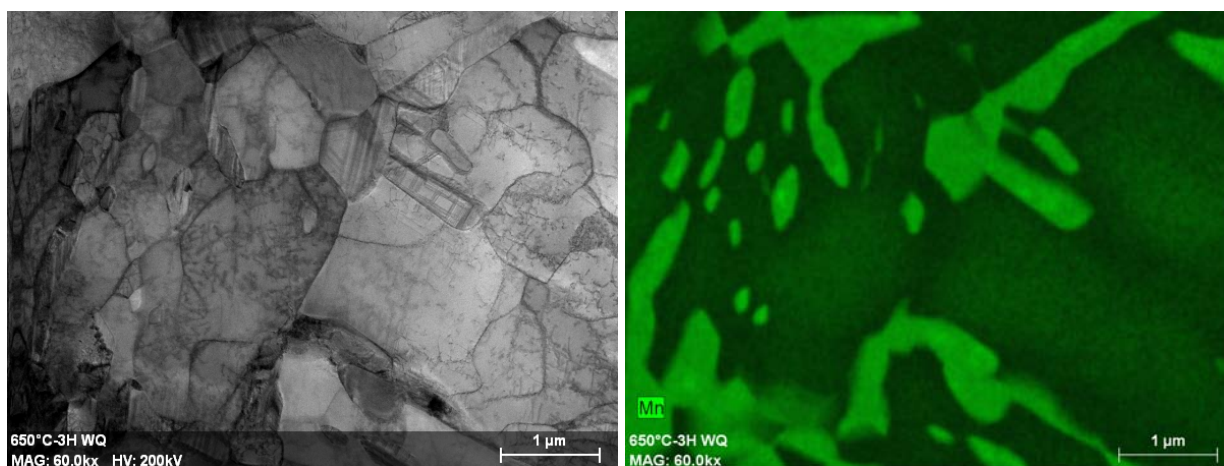
1st hypermap

Figure 165 – Bright field TEM image (at left) and the EDX-hypermap of corresponding zone (at right) of 3h sample (1st hypermap).
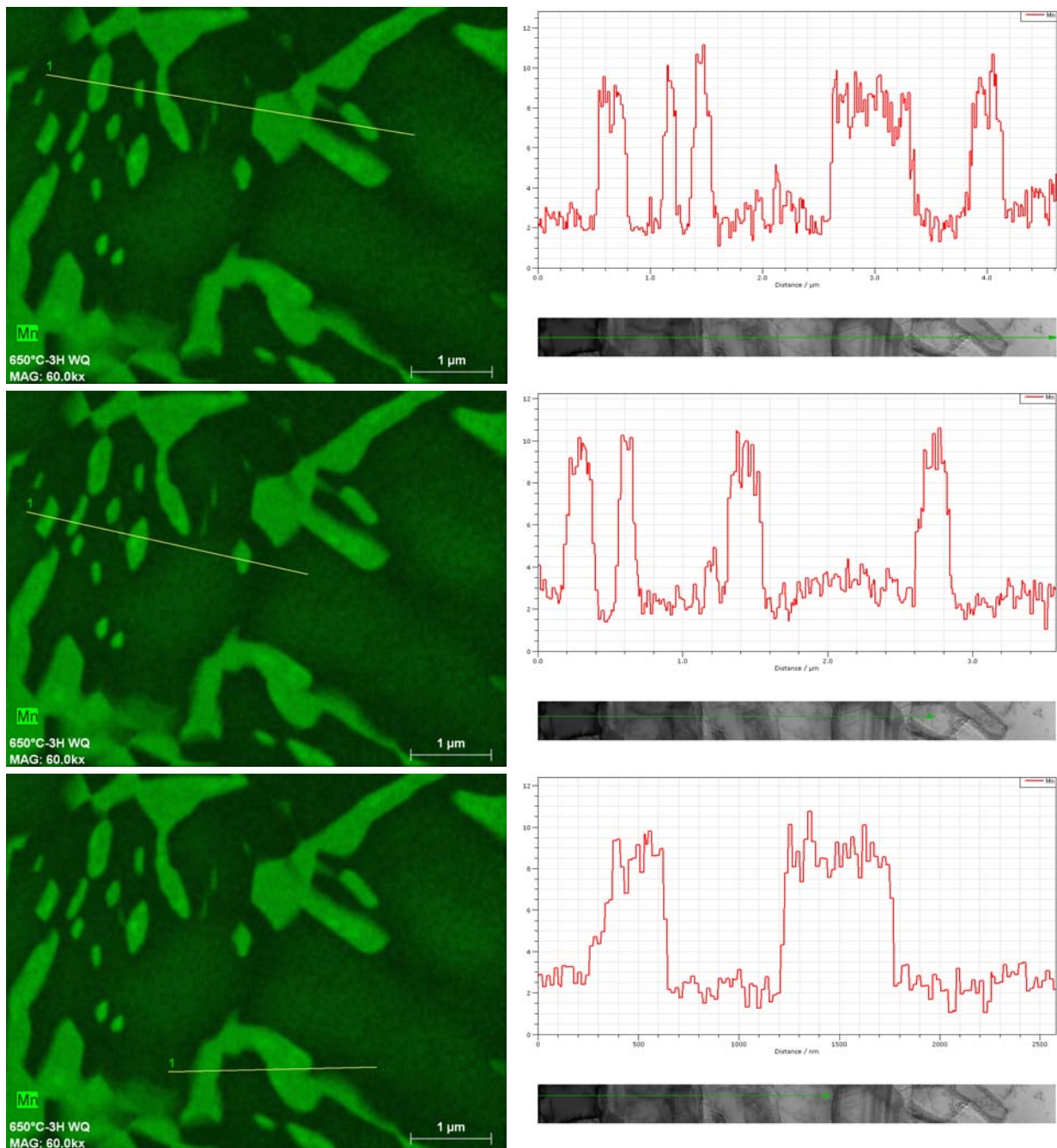

Figure 166 – Mn profiles of 3h sample (1st hypermap): at left are presented selected zones and at right – corresponding Mn evolutions as a function of distance.

2nd hypermap

Figure 167 – Bright field TEM image (at left) and the EDX-hypermap of corresponding zone (at right) of 3h sample (2nd hypermap).

Figure 168 – Mn profiles of 3h sample (2nd hypermap): at left are presented selected zones and at right – corresponding Mn evolutions as a function of distance.
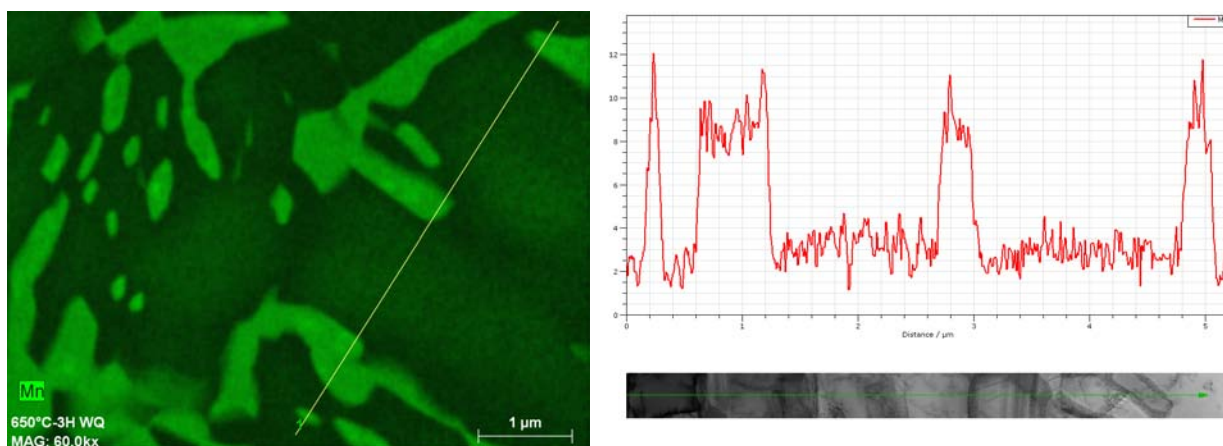
Figure 169 – Mn profiles of 3h sample (2nd hypermap): at left are presented selected zones and at right – corresponding Mn evolutions as a function of distance.

3rd hypermap

Figure 170 – Bright field TEM image (at left) and the EDX-hypermap of corresponding zone (at right) of 3h sample (3rd hypermap).

Figure 171 – Mn profiles of 3h sample (3rd hypermap): at left are presented selected zones and at right – corresponding Mn evolutions as a function of distance.

Figure 172 – Mn profiles of 3h sample (3ʳᵈ hypermap): at left is presented selected zone and at right – corresponding Mn evolution as a function of distance.
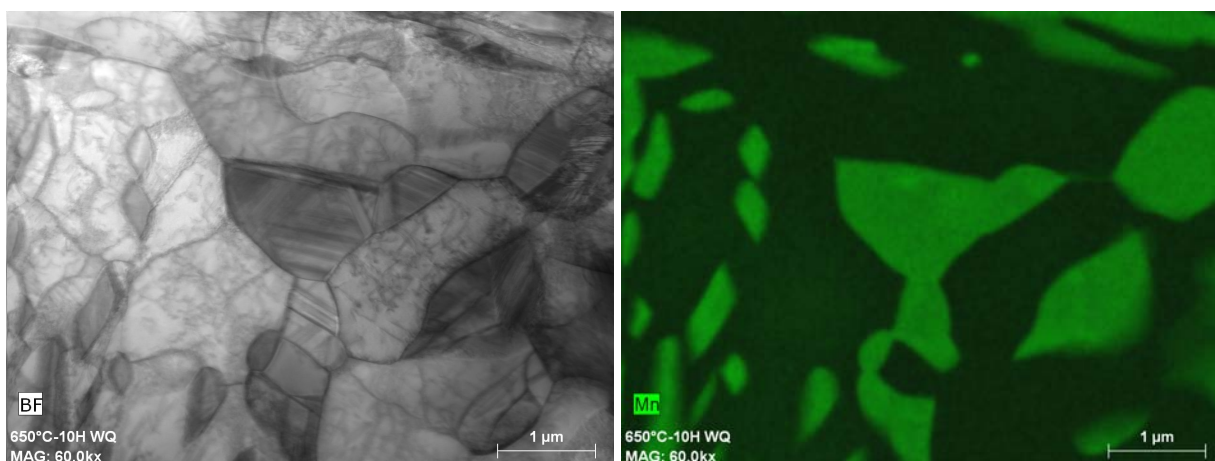
10h sample

Figure 173 – Bright field TEM image (at left) and the EDX-hypermap of corresponding zone (at right) of 10h sample.
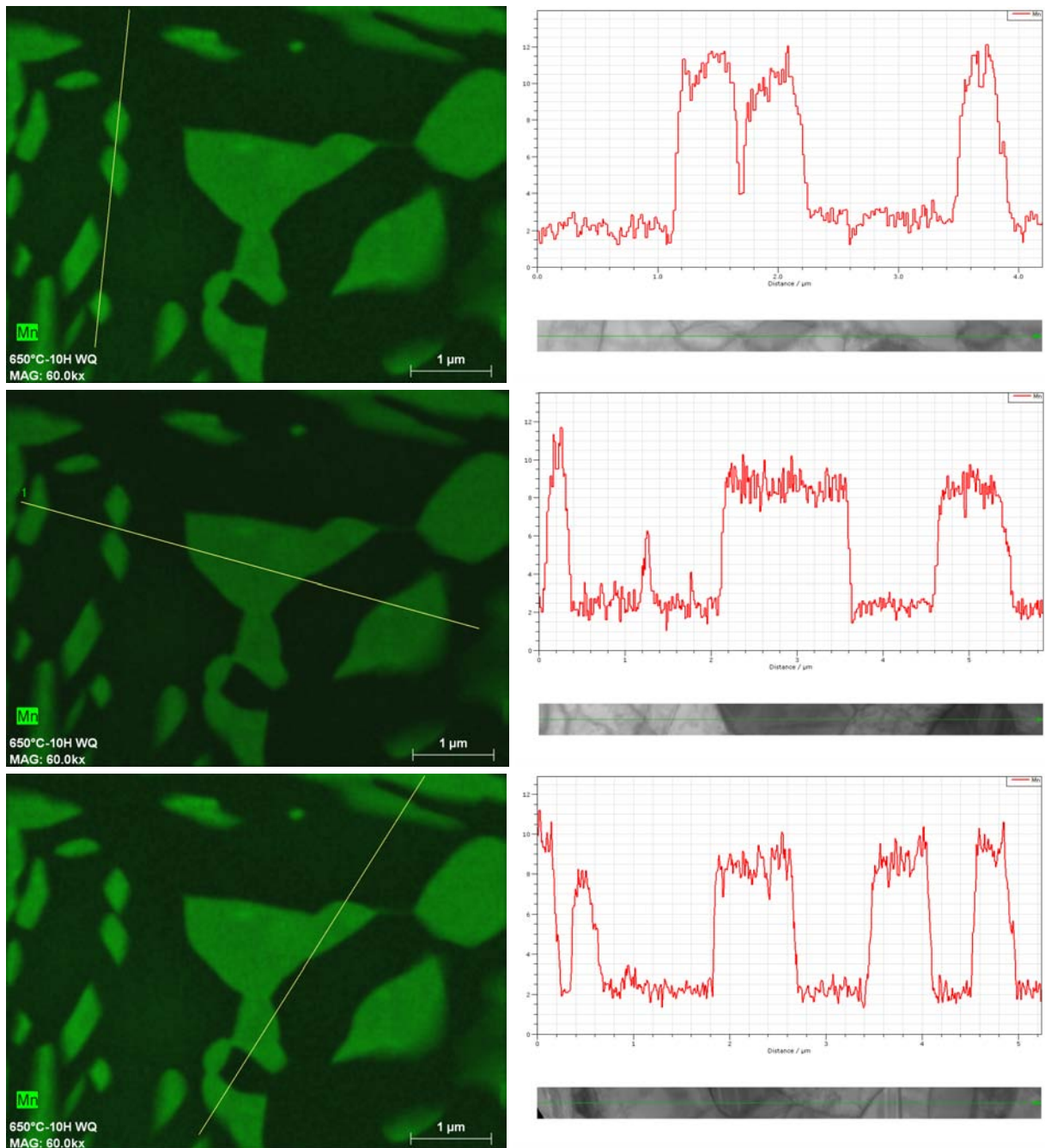
Figure 174 – Mn profiles of 10h sample: at left are presented selected zones and at right – corresponding Mn evolutions as a function of distance.
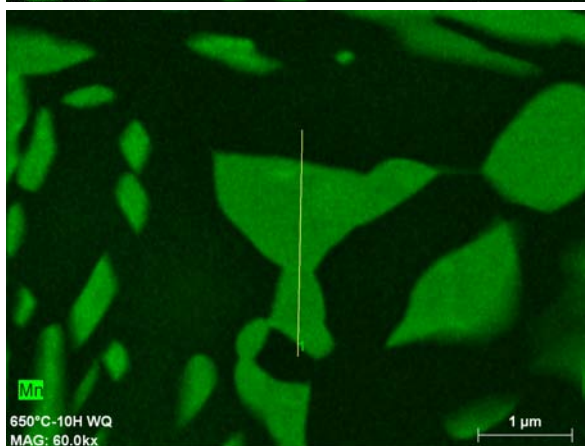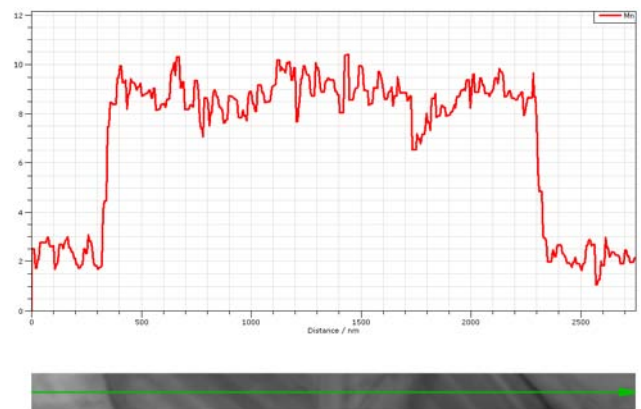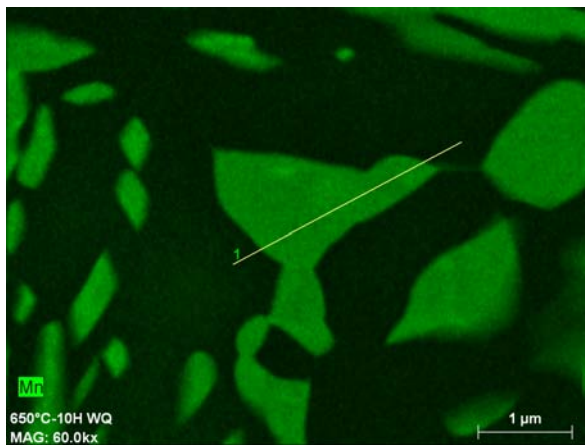
Figure 175 – Mn profiles of 10h sample: at left are presented selected zones and at right – corresponding Mn evolutions as a function of distance.

30h sample

Figure 176 – Bright field TEM image (at left) and the EDX-hypermap of corresponding zone (at right) of 3h sample.

Figure 177 – Mn profiles of 30h sample: at left are presented selected zones and at right – corresponding Mn evolutions as a function of distance.
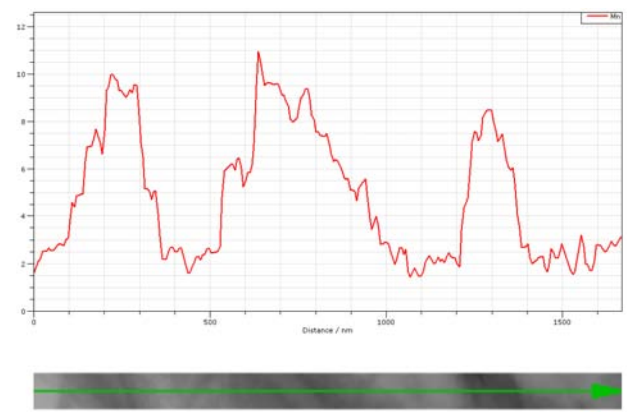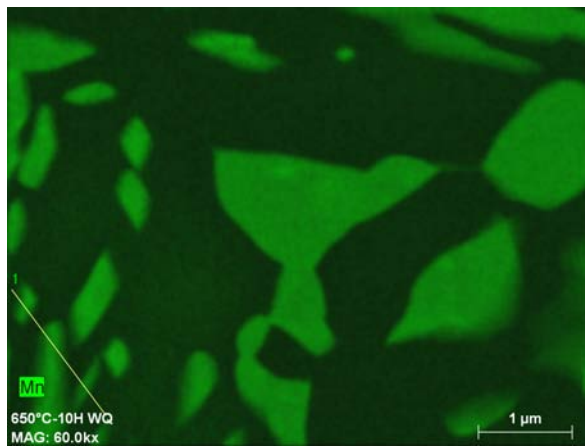
Figure 178 – Mn profiles of 30h sample: at left are presented selected zones and at right – corresponding Mn evolutions as a function of distance.

Figure 179 – Mn profiles of 30h sample: at left are presented selected zone and at right – corresponding Mn evolution as a function of distance.
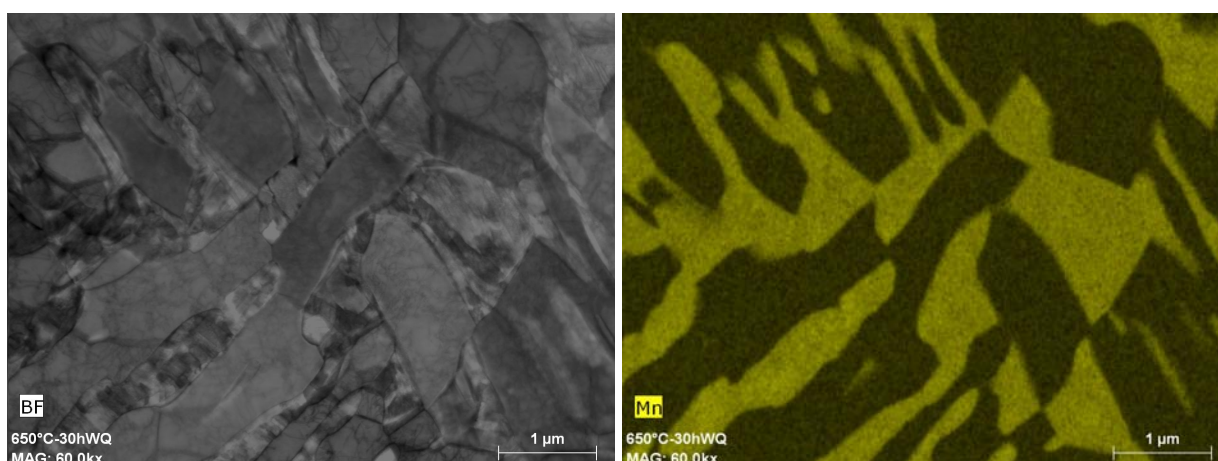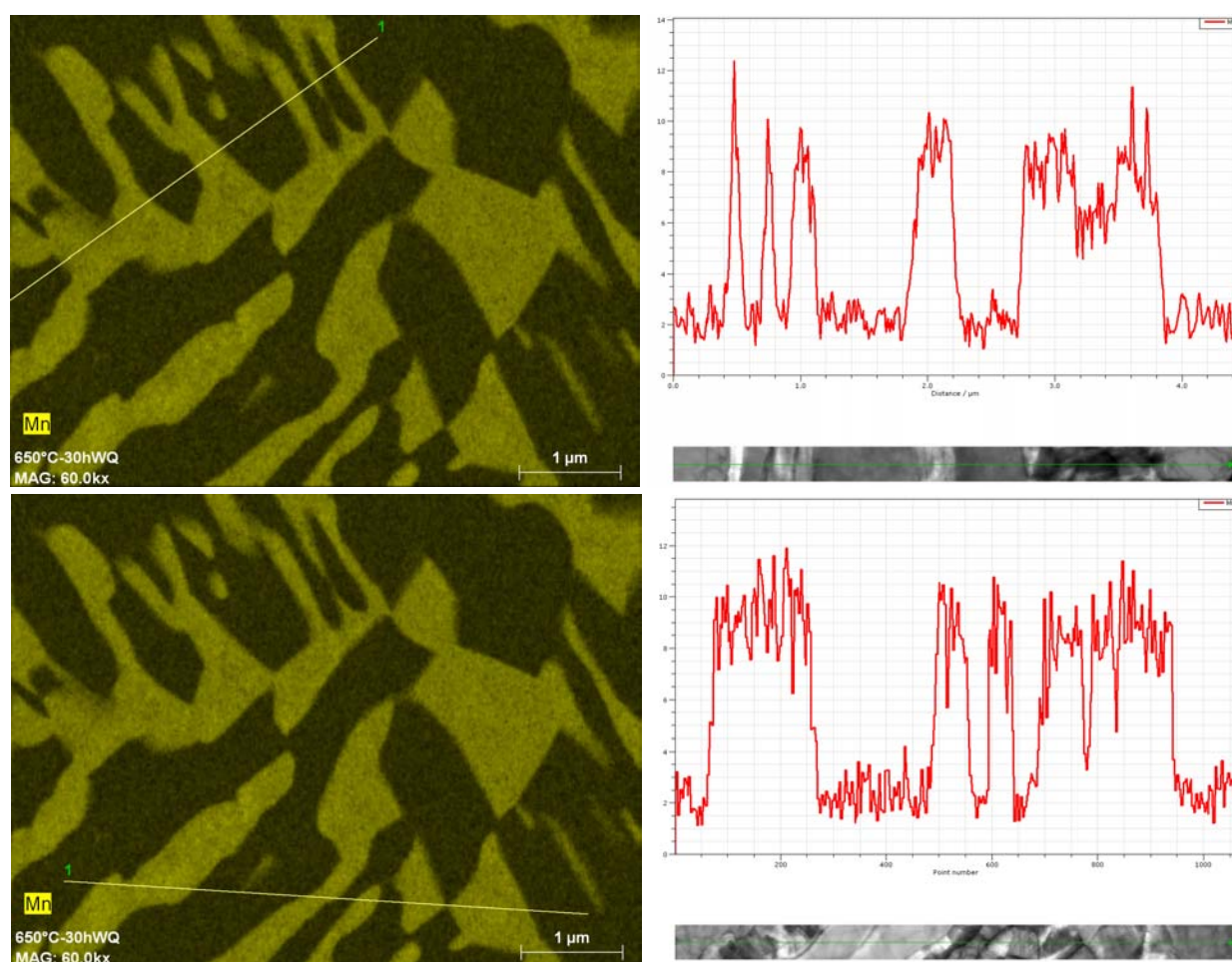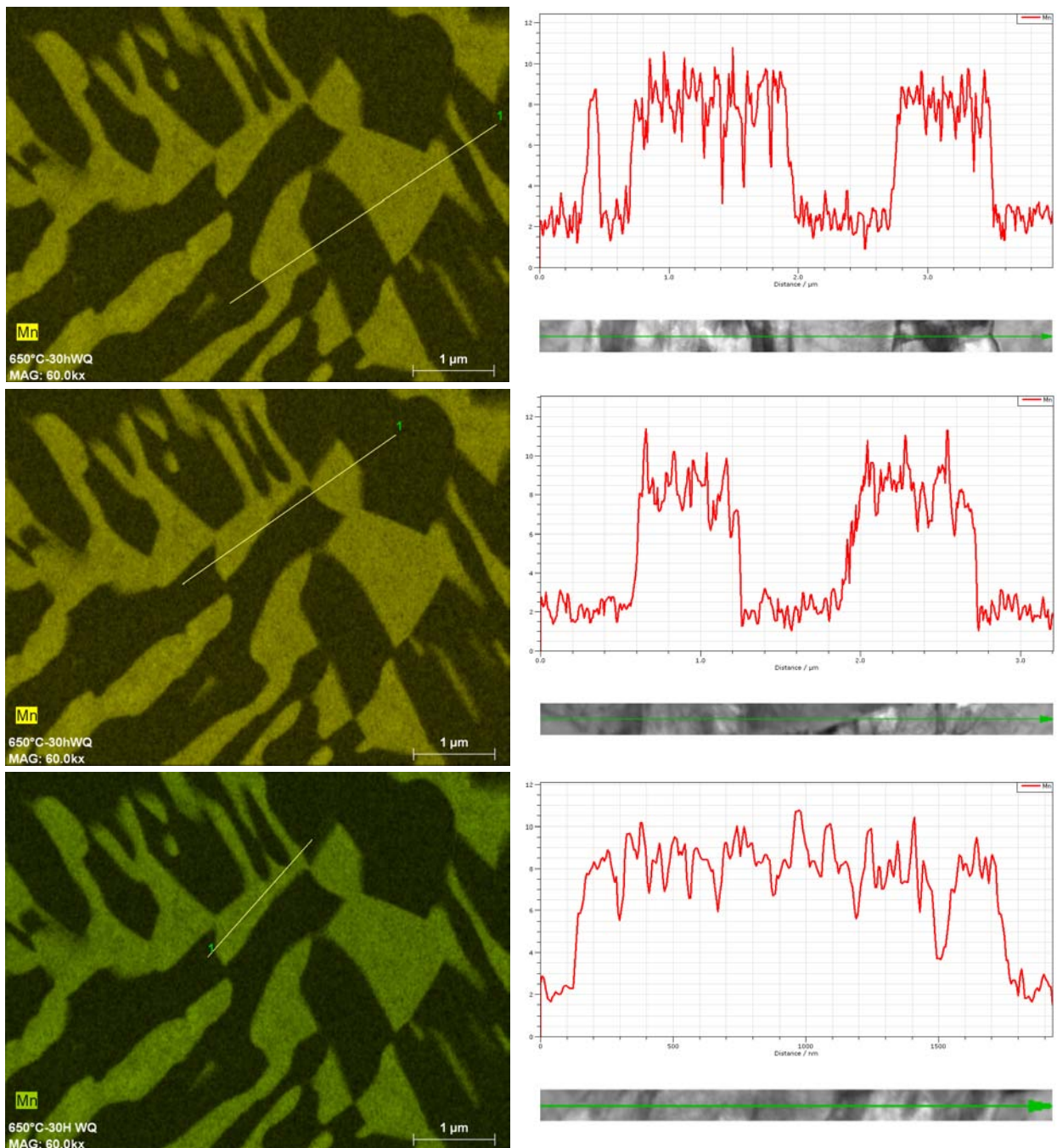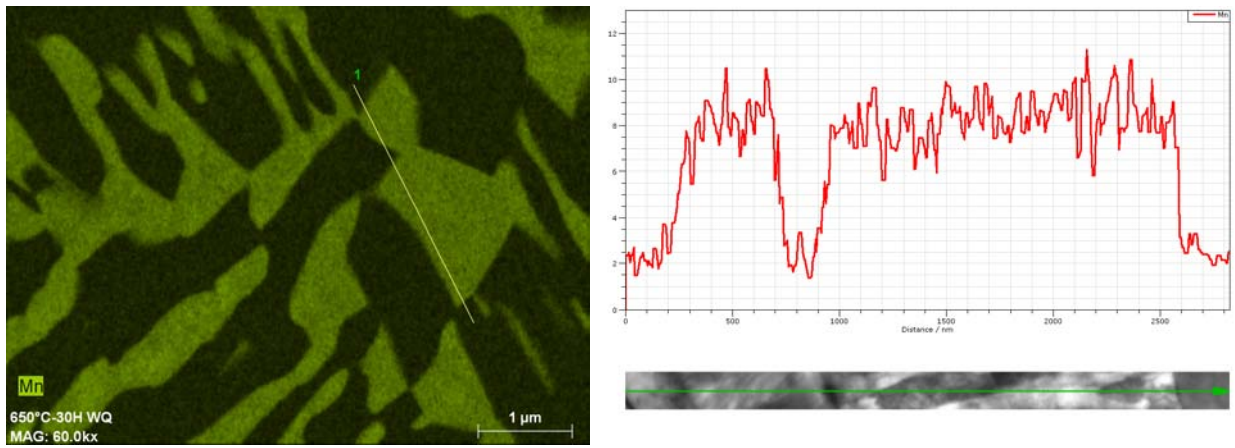
Annex 4.1: Global model parameters.

All the parameters necessary for each phase behavior description are given in the Table 17, 18 and 19.

Table 17 – Identified for Ferrite parameters of mechanical model and their values.

Symbol	Value									Origin
	3min	10min	30min	1h	2h	3h	7h	10h	30h	
M	3									[BOU'02]
μ (MPa)	80000									[BOU'02]
b (nm)	0.25									[BOU'02]
σ_{0F} (MPa)	204	197	194	151	151	145	141	141	141	Eq. (10)
λ (μm)	0.11	0.125	0.135	0.15	0.16	0.17	0.22	0.235	0.34	Fitted
f_F (%)	85	79	74	70	68	67	64	64	64	Exp
Mn_F (wt.%)	4.3	4.1	3.7	2.6	2.6	2.5	2.3	2.3	2.3	Exp

Table 18 – Identified for Fresh Martensite parameters of mechanical model and their values.

Symbol	Value									Origin
	3min	10min	30min	1h	2h	3h	7h	10h	30h	
σ_{min} (MPa)	0	0	0	0	450					[ARL'13]
p	0	0	0	0	2.5					[ARL'13]
σ_{0FM} (MPa)	0	0	0	0	1129					Eq. (5)
f_{FM} (%)	0	0	0	0	4	8	12	14	15	Exp
Mn_{FM} (wt.%)	0	0	0	0	8.9	8.9	8.7	8.7	8.7	Exp
C_{FM} (wt.%)	0	0	0	0	0.31	0.3	0.27	0.27	0.27	Ch.3.3.2
C_{eq}	0	0	0	0	1.1	1.04	0.94	0.94	0.94	Eq. (6)

Table 19 – Identified for Retained Austenite and Induced Transformation (TRIP effect) parameters of mechanical model and their values.

Symbol	Value									Origin
	3min	10min	30min	1h	2h	3h	7h	10h	30h	
K	2900									[BOU'11]
f	4									[BOU'11]
σ_{0A} (MPa)	391	348	334	326	324	322	319	319	319	Eq. (8)
f_{RA} (%)	15	21	26	30	28	25	24	22	21	Exp
Mn_{RA} (wt.%)	10	9.9	9.7	9.3	8.9	8.9	8.7	8.7	8.7	Exp
C_{RA} (wt.%)	0.67	0.46	0.38	0.33	0.3	0.27	0.27	0.27	0.31	Ch.3.3.2
ε	0.2	0.2	0.2	0.15	0.16	0.113	0.113	0.104	0.058	Fitted
n	1	1	1	1	1.5	2	2	2	2	Fitted

Exp – experimentally determined value; Ch.3.3.2 – value calculated in section 3.3.2 (Table 7).

Annex 4.2: Sensitivity analysis of the mechanical model.

Variation of following input parameters of the model was studied:
a) fresh martensite fraction;
b) size of ferrite;
c) retained austenite fraction;
d) mechanical stability of retained austenite (both ε and n).

In order to avoid the interference of different effects several parameters were blocked at a certain values depending on the performed calculations.

Influence of Fresh Martensite fraction

The following parameters were considered with the subsequent constant values:
- $\lambda = 0.3$ (μm)
- $Mn_F = 3$ (wt.%)
- $f_{RA} = 20$ (%)
- $\varepsilon = 0.14$
- $n = 1$

C_{FM} and Mn_{FM} were recalculated according to the global fraction of FM+RA, but the C_{eq} was always superior to 0.5, thus almost no influence on the stress-strain curves. Finally, changing parameters were f_{FM} (0-30%) and f_F fractions (50-80%). The results of the analysis are presented in Figure 180 and Table 20. As it can be seen fresh martensite has an important influence on the mechanical behavior of such a multiphase mixture. UTS has the biggest variation with the FM fraction evolution, on the other hand the change of YS and Uel is less pronounced. It can be also observed that due to the strain partitioning (Iso-W assumption) the induced transformation of RA is slightly modified as well (Figure 180 c).

Table 20 – Results of the model simulations with different fresh martensite fractions.

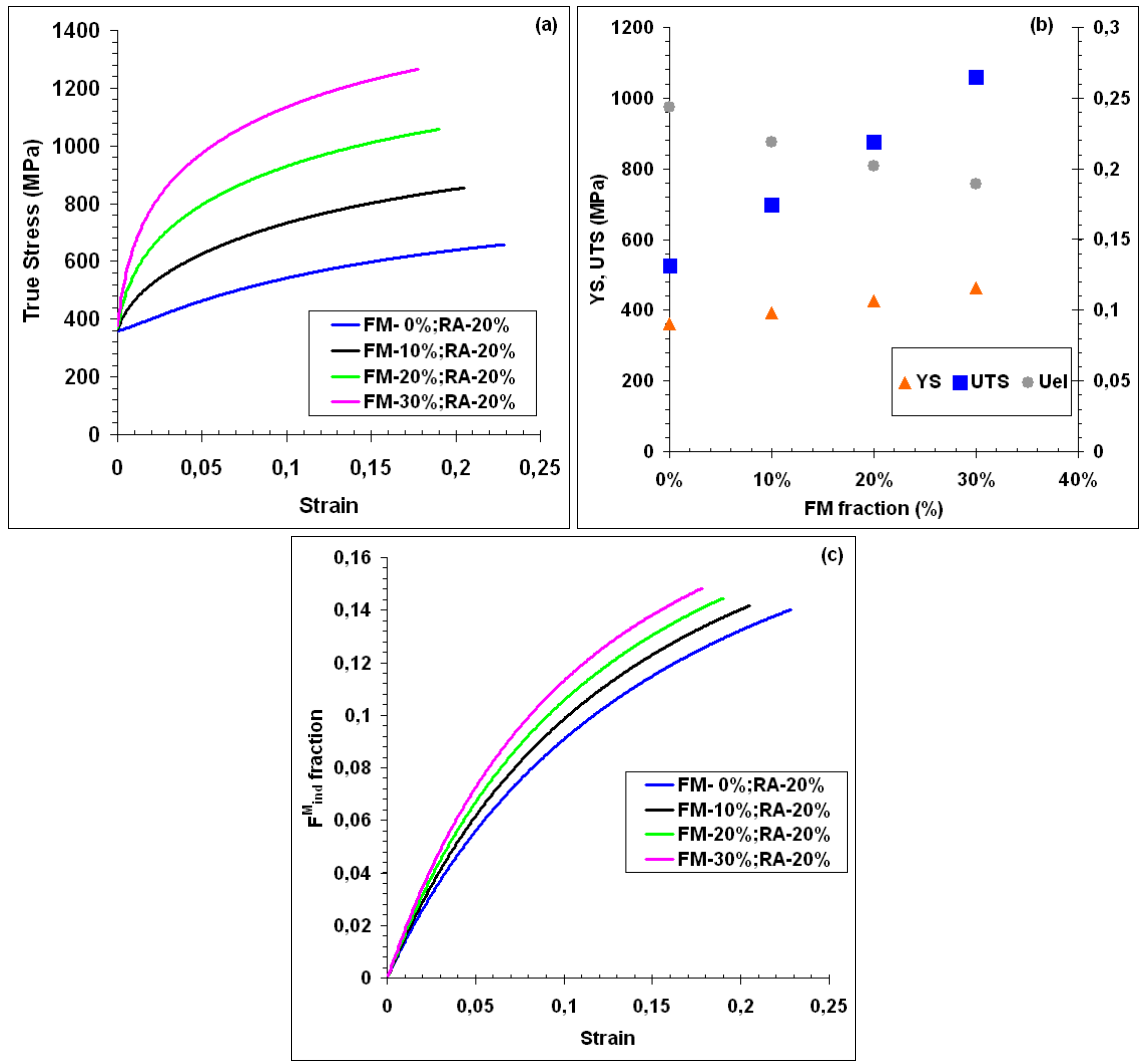|	f_{FM} (%)	YS (MPa)	UTS (MPa)	Uel (%)
	30%	464	1059	18.9%
	20%	427	874	20.2%
	10%	393	696	21.9%
	0%	361	524	24.4%
Variation	30%	102.7	535.6	5.4%
Var / %		**3.4**	**17.9**	**0.2**

Figure 180 – Influence of fresh martensite fraction on the mechanical behavior according to the model: (a) true stress-true strain curves; (b) evolution of mechanical characteristics (YS, UTS and Uel) and (c) stability of retained austenite.

Influence of Ferrite size

The following parameters were considered with the subsequent constant values:
- $f_{FM} = 10 \, (\%)$
- $C_{FM} = 0.31 \, (wt.\%)$
- $Mn_{FM} = 8.3 \, (wt.\%)$
- $Mn_F = 3 \, (wt.\%)$
- $f_{RA} = 20 \, (\%)$
- $\varepsilon = 0.14$
- $n = 1$

The size of ferrite (λ) was varying from 0.05 to 1 (μm). The results of the analysis are presented in Figure 181 and Table 21. The impact of λ evolution appears to be very important for all mechanical characteristics (YS, UTS and Uel). Due to the strain partitioning ferrite size has an important effect on the strain induced transformation (Figure 181c).
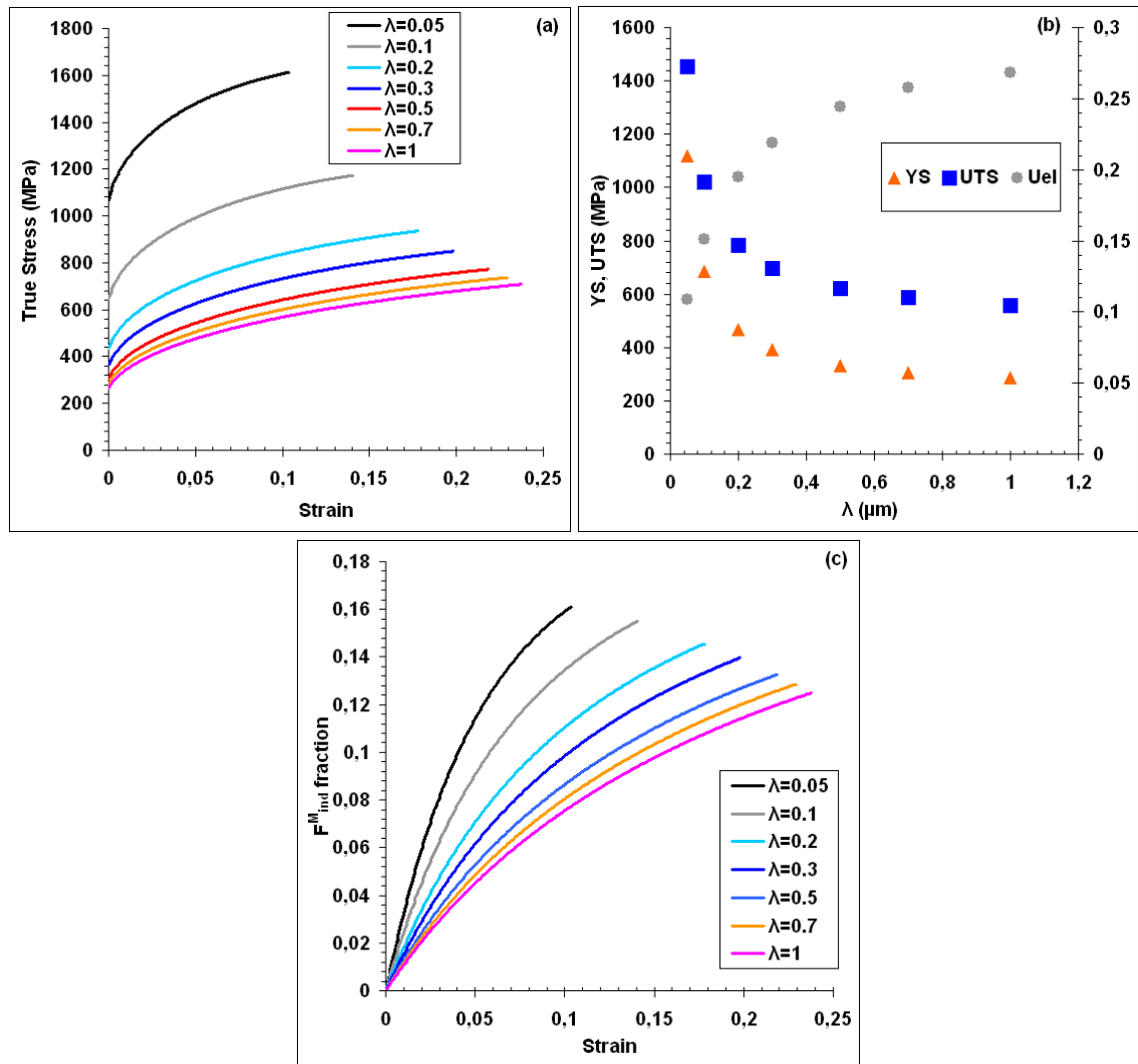
Figure 181 – Influence of ferrite size (λ) on the mechanical behavior according to the model: (a) true stress-true strain curves; (b) evolution of mechanical characteristics (YS, UTS and Uel) and (c) stability of retained austenite.

Table 21 – Results of the model simulations with different sizes of ferrite.

	λ (μm)	YS (MPa)	UTS (MPa)	Uel (%)
	0.05	1118	1454	10.9%
	0.1	687	1020	15.1%
	0.2	467	783	19.5%
	0.3	393	696	21.9%
	0.5	332	621	24.4%
	0.7	306	586	25.7%
	1	286	559	26.8%
Variation	0.95	831.5	895.0	15.9%
Var / 0.1μm		**87.5**	**94.2**	**1.7%**

Influence of Retained Austenite fraction

The following parameters were considered with the subsequent constant values:
- $f_F = 70$ (%)
- $\lambda = 0.3$ (µm)
- $Mn_F = 3$ (wt.%)
- $C_{FM} = 0.31$ (wt.%)
- $Mn_{FM} = 8.3$ (wt.%)
- $\varepsilon = 0.14$
- $n = 1$

Changing parameters were f_{RA} (0-30%) and f_{FM} fractions (0-30%). The results of the analysis are shown in Figure 182 and Table 22. As it can be expected the increase of RA fraction decreases YS and UTS and improves the Uel. The effect on Uel is very significant. On the other hand, on YS and UTS it is less prominent.
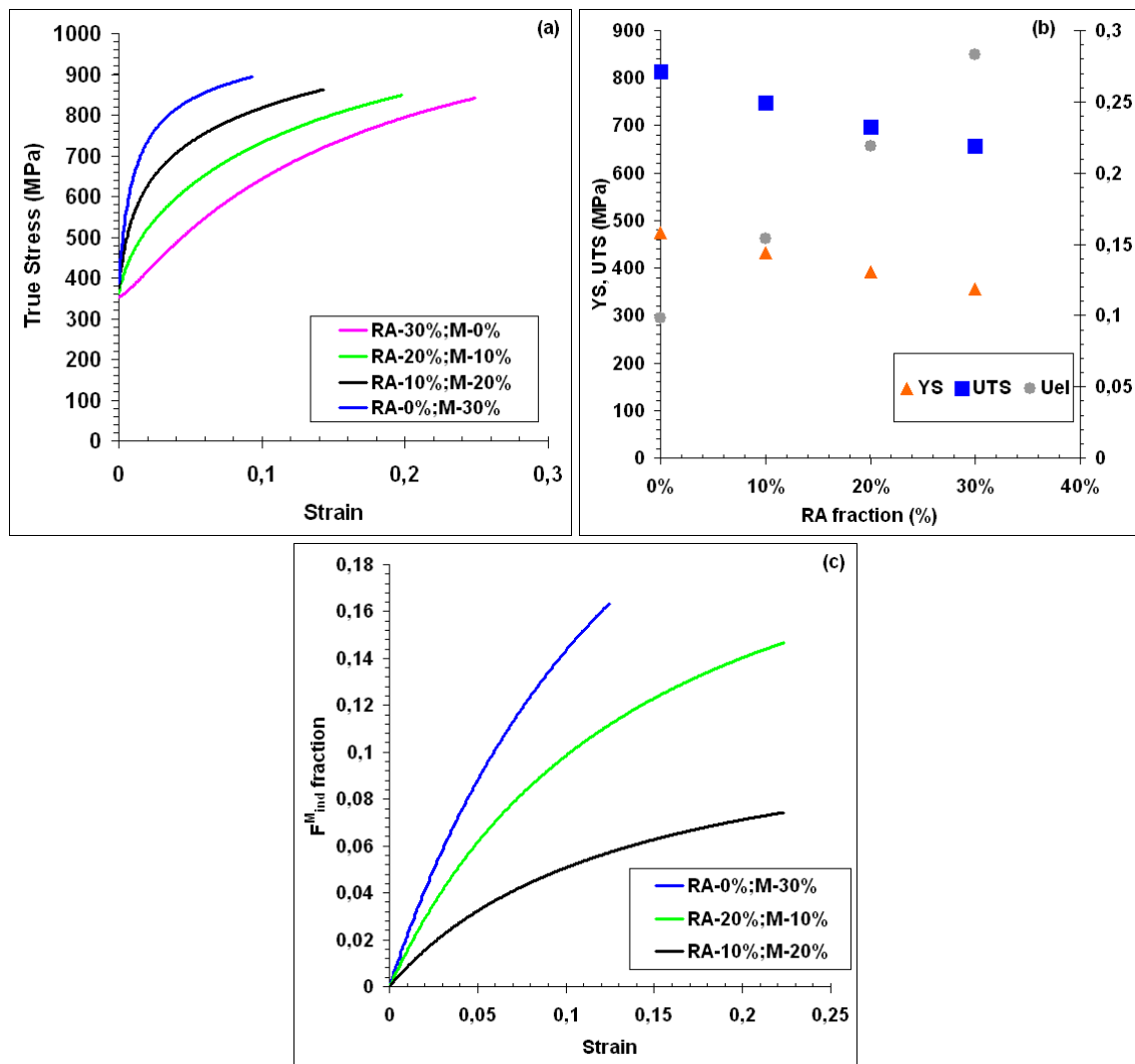

Figure 182 – Influence of retained austenite fraction on the mechanical behavior according to the model: (a) true stress-true strain curves; (b) evolution of mechanical characteristics (YS, UTS and Uel) and (c) stability of retained austenite.

Table 22 – Results of the model simulations with different retained austenite fractions.

	F_{RA} (%)	YS (MPa)	UTS (MPa)	Uel (%)
	30%	355	656	28.27%
	20%	393	696	21.90%
	10%	432	747	15.37%
	0%	474	814	9.80%
Var	30%	118.97	157.90	18%
Var / %		**3.97**	**5.26**	**0.62**

Influence of Retained Austenite stability

The following parameters were considered with the subsequent constant values:
- $f_{AM} = 70$ (%)
- $\lambda = 0.3$ (μm)
- $Mn_F = 3$ (wt.%)
- $C_{FM} = 0.31$ (wt.%)
- $Mn_{FM} = 8.3$ (wt.%)
- $f_{RA} = 30$ (%)

Changing parameters were ε_0 and n. In the case of ε_0 variation (0.03-0.21), the n was blocked at the value of 1. Figure 183 and Table 23 present the obtained results. In contrast, when n was changing, the $\varepsilon_0 = 0.14$ was constant. The results obtained with such simulation are shown in Figure 184 and Table 24. As it can be found both parameters ε_0 and n have low effect on the YS. In the same time the impact of austenite stability on UTS and Uel is quite significant, especially with the variation of ε_0. High values of ε_0 increase the stability of RA thus decreasing induced martensite fraction and subsequently UTS. This effect is also accompanied by the improved Uel. Finally, it can be concluded that the sensibility of ε_0 in comparison with n is more important.

Table 23 – Results of the model simulations with different ε_0 values.

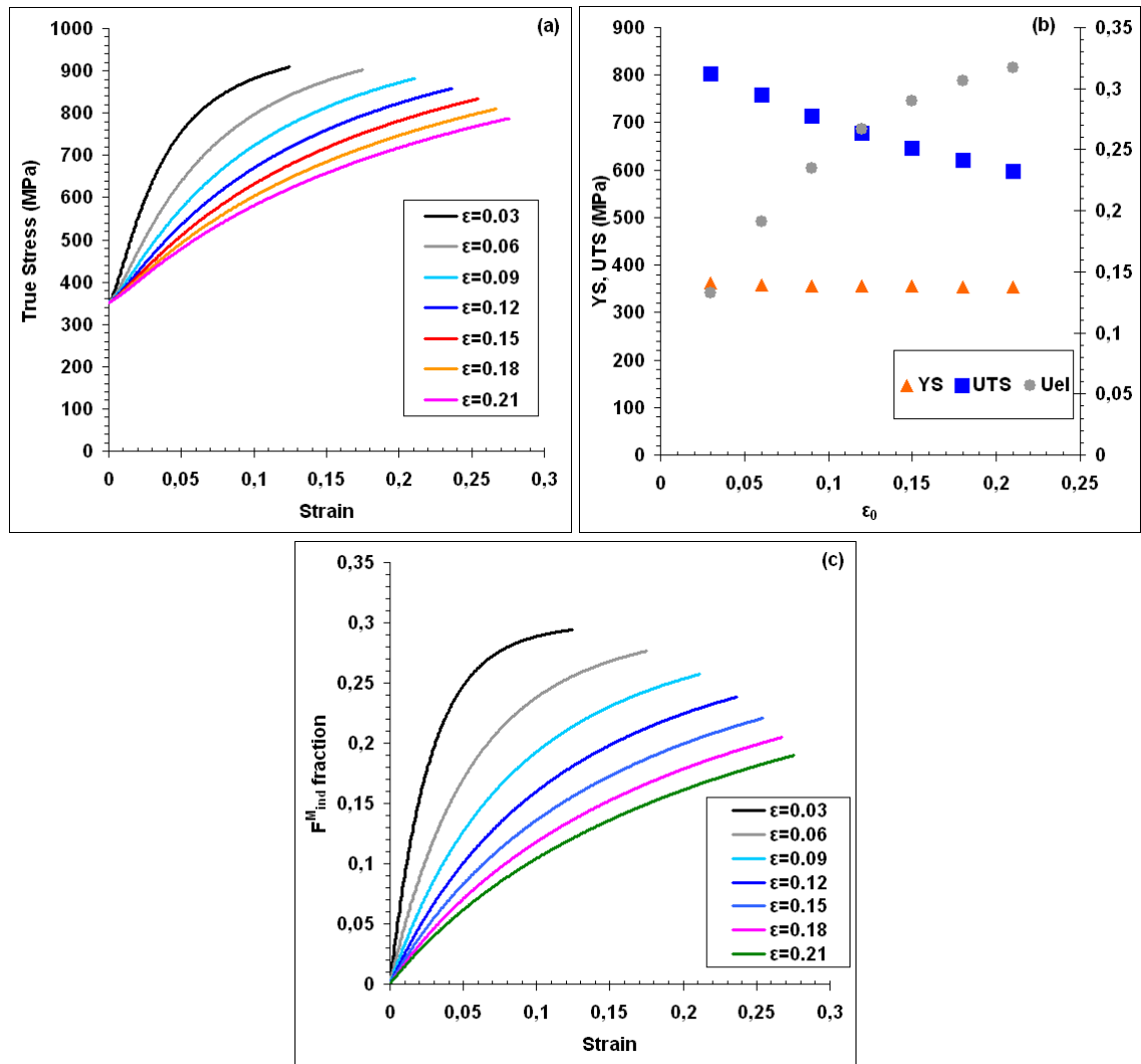|	ε_0	YS (MPa)	UTS (MPa)	Uel (%)
	0.03	362	802	13.3%
	0.06	358	757	19.1%
	0.09	356	714	23.5%
	0.12	355	677	26.7%
	0.15	355	646	29.0%
	0.18	355	620	30.6%
	0.21	354	598	31.7%
Variation	0.18	7.67	204.6	18.5%
Var / 0.01		**0.43**	**11.4**	**1.03**

Figure 183 – Influence of retained austenite stability (ε₀) on the mechanical behavior according to the model: (a) true stress-true strain curves; (b) evolution of mechanical characteristics (YS, UTS and Uel) and (c) stability of retained austenite

Table 24 – Results of the model simulations with different n values

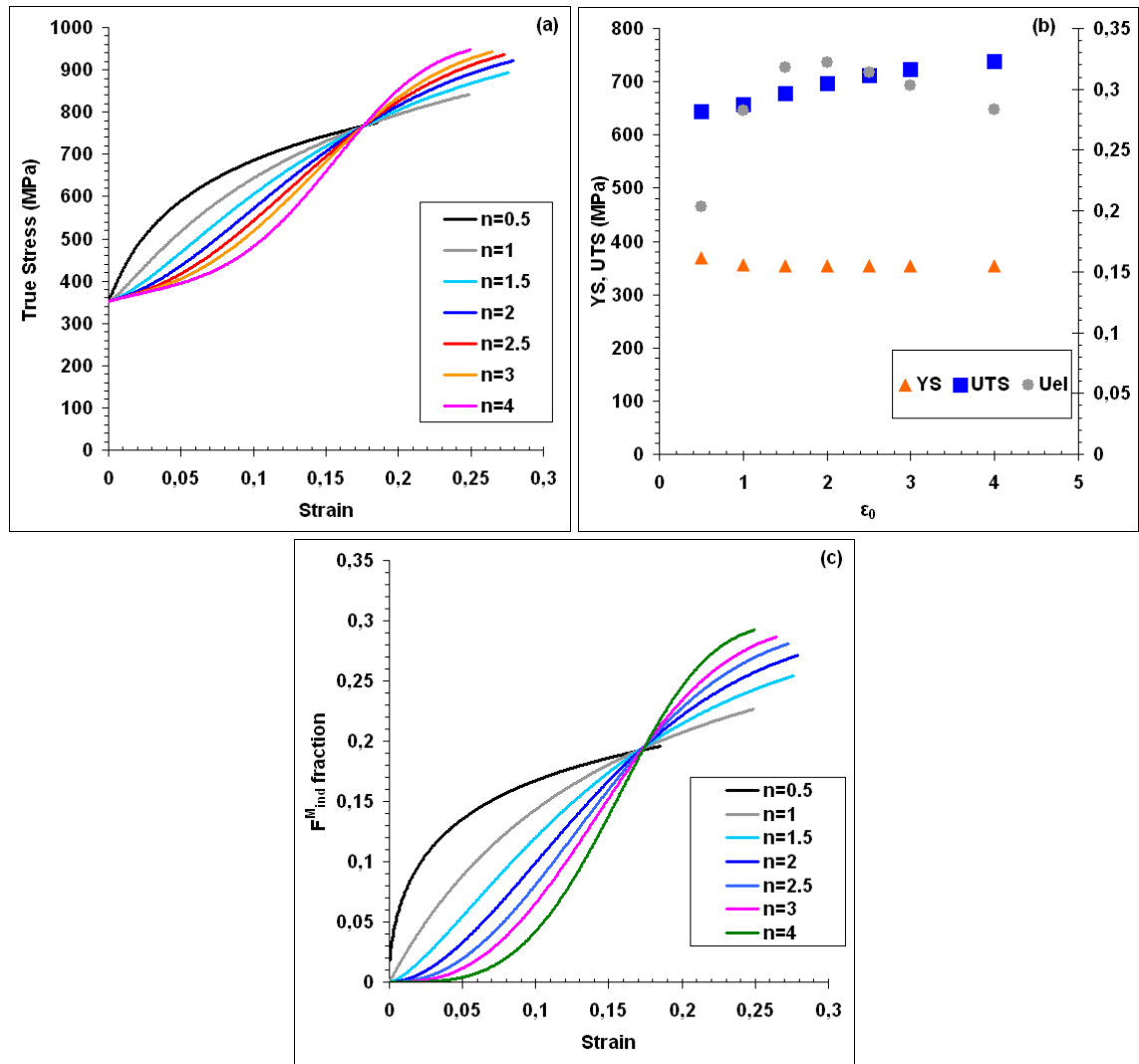|	n	YS (MPa)	UTS (MPa)	Uel (%)
	0.5	368	643	20.4%
	1	355	656	28.3%
	1.5	353	678	31.8%
	2	353	697	32.2%
	2.5	353	712	31.4%
	3	353	723	30.3%
	4	353	738	28.3%
Variation	3.5	15.5	94.3	8.0%
Var / 0.5		**2.2**	**13.5**	**1.1%**

Figure 184 – Influence of retained austenite stability (n) on the mechanical behavior according to the model: (a) true stress-true strain curves; (b) evolution of mechanical characteristics (YS, UTS and Uel) and (c) stability of retained austenite

As a global conclusion of the model sensibility analysis it can be stated that the model accounts well different effects of input parameters and has certain sensitivity to all of them. This proves the necessity of detailed microstructural analysis of such complex microstructures. It can be also highlighted that the most sensitive parameters are the fractions of constituents (especially fresh martensite) and the size of ferrite. In contrast, stability of retained austenite has a lighter impact.